Vrije Universiteit Brussel

FACULTY OF ENGINEERING
Department of Mechanical Engineering

Design and control of a knee exoskeleton powered by pleated pneumatic artificial muscles for robot-assisted gait rehabilitation

Thesis submitted in fulfilment of the requirements for the award of the degree of Doctor in de ingenieurswetenschappen (Doctor in Engineering) by

ir. Pieter Beyl

December 2010

Chair: Prof. Dr. ir. Annick Hubin
Vrije Universiteit Brussel

Vice chair: Prof. Dr. ir. Rik Pintelon
Vrije Universiteit Brussel

Secretary: Dr. ir. Michaël Van Damme
Vrije Universiteit Brussel

Advisor: Prof. Dr. ir. Dirk Lefeber
Vrije Universiteit Brussel

Jury: Prof. Dr. ir. Sunil K. Agrawal
University of Delaware

Prof. Dr. ir. Eugenio Guglielmelli
Università Campus Bio-medico di Roma

Prof. Dr. Romain Meeusen
Vrije Universiteit Brussel

Prof. Dr. ir. Bram Vanderborght
Vrije Universiteit Brussel

Print: Silhouet, Maldegem

Uitgeverij VUBPRESS Brussels University Press
VUBPRESS is an imprint of ASP nv (Academic and Scientific Publishers nv)
Ravensteingalerij 28
B-1000 Brussels
Tel. ++32 (0)2 289 26 50
Fax ++32 (0)2 289 26 59
E-mail: info@vubpress.be
www.vubpress.be

ISBN 978 90 5487 832 2
NUR 978/959
Legal Deposit D/2010/11.161/157

“The mind is like a parachute. It doesn’t work if it’s not open.”

Frank Zappa

Abstract

Research in robot-assisted rehabilitation of gait has known a paradigm shift towards a more "human-centered" approach, focusing on assistance-as-needed, increased functionality and adaptability of the environment displayed by the device. Physical human-robot interaction (pHRI) is a key aspect in this approach. From an engineering viewpoint the improvement of pHRI is sought in wearable design, high performance actuator technologies and dedicated control strategies.

In this dissertation a combination of lightweight, intrinsically compliant actuators with high force output (pleated pneumatic artificial muscles) and safe, adaptable guidance along a target trajectory is investigated for end use in a full lower limb exoskeleton. A powered knee exoskeleton, KNEXO, has been developed for this purpose.

In its design, emphasis was laid on optimising the actuator system configuration and on the adaptability of the human-robot interface.

As for control, two different, but complementary control strategies have been studied by means of simulations and experiments: a torque controller and a trajectory tracking based assistive controller. The torque controller supports an unassisted walking mode, that serves as a baseline for the performance evaluation of robotic assistance and that enables the recording of reference and target trajectories. The assistive controller uses proxy-based sliding mode control (PSMC) in conjunction with a non-model based support torque to provide an assisted walking mode that safely allows for deviations from the target trajectory.

Treadmill walking experiments have been performed in unimpaired subjects wearing KNEXO in order to assess wearability and to investigate controller performance in view of impaired subject testing. Experimental results verified that the combination of intrinsically compliant actuators with proxy-based sliding mode control achieves compliant guidance and at the same time exhibits a safe and tunable response to human-robot interaction torques. Following this positive evaluation, a hemiparetic stroke patient and a multiple sclerosis patient participated in a series of pilot assisted walking experiments. Provided a patient-specific controller tuning, based on experience gained from experiments with unimpaired subjects, KNEXO effectively supports and compliantly guides the subject's impaired knee. Both in unimpaired and impaired subjects gait kinematics measurements and muscle EMG measurements have been performed to quantify human-robot interaction.

Considering these promising results, the methods proposed in this work contribute towards a more human-centered rehabilitation of gait.

Acknowledgements

During my PhD research in the multidisciplinary field of rehabilitation robotics I've found ample opportunity to meet and collaborate with many people. My gratitude goes out to all those who have contributed to this work scientifically, practically, and personally.

First, I would like to thank my advisor, Dirk Lefeber, for providing the opportunity to explore a field that was brand new to the research group and for his suggestions and advise. I owe many thanks to Michael Van Damme for his support in many ways: reading my writings, commenting on my work, and backing me up on object-oriented programming to name just a few. His research on pneumatic muscle modelling and control was of great value for this work. Thanks to Bram Vanderborght for proofreading my thesis and for many useful suggestions. Thanks to Ronald Van Ham for sharing clever design ideas and to Joris Naudet for joining the ride in the early days.

I would like to thank Kristel Knaepen for her many contributions to all the stages of patient testing and for the effort she has put in the ALTACRO project. Also many thanks to Saartje Duerinck for her help with patient testing and gait analysis, and to Friso Hagman for data processing. Thanks to the other research group colleagues, both from R&MM and ARTS, as well. To my office mates, Jelle, Kristof, Pierre, Rino and Victor, thanks for sharing limited space and for lighting up the place at Christmas time.

I would not like to forget the guys from the workshop, Jean-Paul Schepens, Frans Boulpaep and the technical contribution of Xavier Berteele and Koen Buntinx from Cebelor N.V. to the first prototype.

My thanks go out to Dr. Ilsbroukx and Dr. Nagels from the MS rehabilitation center Melsbroek and Dr. Lafosse from rehabilitation center Hof Ter Schelde for patient recruitment. Also, thanks to all volunteers willing to walk many miles with KNEXO.

I would also like to acknowledge the Institute for the Promotion of Innovation through Science and Technology in Flanders (IWT-Vlaanderen) for funding my PhD research.

I am grateful to my brother, my parents, my friends and my family for their support and for encouraging me in my endeavours.

Finally, my last words of gratitude are saved for Liesbeth. Her faith and relentless support I will never ever forget.

Pieter Beyl
Brussels, December 2010

Contents

Nomenclature

List of abbreviations

AAFO	Active Ankle Foot Orthosis
AKROD	Active Knee Rehabilitation Orthotic Device
ALEX	Active Leg Exoskeleton
ALTACRO	Automated Locomotion Training using an Actuated Compliant Robotic Orthosis
ARTHuR	Ambulation-assisting Robotic Tool for Human Rehabilitation
BF	Biceps Femoris
BLEEX	Berkeley Lower Extremity Exoskeleton
BWSTT	Body-Weight Supported Treadmill Training
CAD	Computer Aided Design

C-Leg	Computerised Leg
DCO	Dynamically Controlled ankle-foot Orthosis
DOF	Degrees Of Freedom
EMG	Electromyography
ERF	ElectroRheological Fluid
EXPOS	EXoskeleton for Patients and the Old by the Sogang university
FES	Functional Electrical Stimulation
FF	FeedForward
FSR	Force Sensing Resistor
GA	GAstrocnemius
GBO	Gravity Balancing Orthosis
GUI	Graphical User Interface
HAL	Hybrid Assistive Limb
HO	Heel-Off
IC	Initial Contact
KNEXO	powered KNee EXOskeleton
LR	Loading Response

LOPES	LOwer extremity Powered ExoSkeleton
MOO	Multi-Objective Optimisation
MS	Multiple Sclerosis
MVC	Maximal Voluntary Contraction
NASA	National Aeronautics and Space Administration
NTU	Nanyang Technological University
PAM	Pelvic Assist Manipulator
PD	Proportional Derivative
pHRI	physical Human-Robot Interaction
PI	Proportional Integral
PID	Proportional Integral Derivative
POGO	Pneumatically Operated Gait Orthosis
PPAM	Pleated Pneumatic Artificial Muscle
PSMC	Proxy-based Sliding Mode Control
PSMC IT	Proxy-based Sliding Mode Control with Inner Torque control loop
RF	Rectus Femoris
SCI	Spinal Cord Injury

SERKA	Series Elastic Remote Knee Actuator
SPMS	Secondary Progressive Multiple Sclerosis
SUE	Swing-assist Unmotorized Exoskeleton
TA	Tibialis Anterior
TO	Toe-Off
VL	Vastus Lateralis
ZT	Zero Torque

List of Figures

List of Tables

Chapter 1

Introduction

1.1 Motivation

Gait impairment has a major impact on health-related quality of life. The inability or reduced ability to walk affects a person's ability to perform activities of daily living, induces physical deconditioning and puts strain on his/her psychological and psychosocial well-being. Rehabilitation of gait is essential for promoting recovery and improving quality of life. The physical therapy involved varies greatly depending on the cause and nature of gait disorders. Prevalent causes of gait impairment are neurological disorders and injuries, such as stroke, spinal cord injury, multiple sclerosis and Parkinson's disease. The burden of these disorders on worldwide public health and the related demands for health resources are underestimated and projected to keep rising in the future (World Health Organisation, 2006).

Gait training, over ground or on a treadmill, has become an essential part of rehabilitation therapy in patients suffering from these disorders and its effectiveness is increasingly evidenced by clinical trials and advancements in neuroscience. Seemingly trivial, the notion of "(re)learning to walk by walking" hides some of the key research questions that puzzle not only the field of rehabilitation science. Similar to the neurological principles underlying human walking itself, the principles underlying motor learning and neural recovery are not yet fully understood and subject of ongoing research. By consequence, research efforts in the field are focused on quantifying the rehabilitation process and identifying rehabilitation practice that maximises outcome.

In one of the existing practices, body-weight supported treadmill training (BWSTT), the patient's body weight is partially supported by an overhead harness while his/her lower limb movements are assisted by one up to three physiotherapists. The strenuous physical effort encumbering the therapists and the resulting short training session duration was one of the main reasons for introducing robotics into gait rehabilitation. Although this introduction was envisaged by therapists as well, it was mainly driven by engineering, strengthened by technological advancements in robotics and prior research into powered exoskeletons for humans. The advantages that were initially aimed at by automating therapy, namely enhancing intensity, repeatability, accuracy and quantification of therapy, are indeed easily associated with robotics. However, a robot operating in close physical contact with an impaired human requires an approach to robot performance that differs significantly from the viewpoint of industrial robotics. Accurate repeated motion imposed by a position controlled robot is considered contraproductive for many reasons: a lack of adaptable and function specific assistance, a limitation of the learning environment, reduced motivation and effort by the patient. Nowadays, the field of rehabilitation robotics is increasingly convinced by a human-centered approach in which robot performance is focused on how the robot physically interacts with the patient.

A focus on the human in the robot puts emphasis on the adaptability and task specificity of robotic assistance required to achieve “assistance-as-needed”. At the same time, safety of interaction, preventing harm and discomfort, is mandatory. Variable stiffness or variable impedance is a promising concept in robot design and control that addresses both safety and adaptability of physical human-robot interaction (pHRI). It implies that the robot gives way to human interaction torques to a desired and adjustable extent. This adds to the high requirements that were already posed by the application, for instance with regard to wearability (compact and light weight design, adjustable to the individual) and actuator performance (high torque output, high power-to-weight ratio). Hence, in the development of novel prototypes rehabilitation roboticists are faced with the challenge of combining suitable design concepts, high performance actuator technologies and dedicated control strategies in view of improved physical human-robot interaction. Improvement, that should lead to a better insight into the effects and effectiveness of robot-assisted rehabilitation and ultimately, leads to better therapies.

1.2 Robot-assisted rehabilitation of gait

1.2.1 Gait rehabilitation

In persons with damage to the central nervous system, for instance due to stroke (brain damage) or incomplete SCI (spinal cord damage), task-specific and intensive gait training leads to (partial) recovery of motor function and improved gait (Barbeau and Rossignol, 1994; Dietz et al., 1994; Hesse et al., 1995). In addition, there are several secondary positive effects on the physical and mental condition of these patients (Hidler et al., 2008). Gait training prevents many of the secondary complications that often result from neurological injury and gait impairment (e.g. joint stiffening, muscle atrophy, cardiovascular deterioration, pneumonia, deep venous trombosis). Therefore, treadmill training is a well-established practice nowadays in rehabilitation centers for the neurologically impaired.

The driving force behind neural recovery is neural plasticity, the ability of neural circuits, both in the brain and the spinal cord, to reorganise or change function (Elbert et al., 1994). This process was clearly evidenced in prior animal research, revealing the existence of so called "central pattern generators" at the level of the spinal cord that allow to reinstill animal gait through training following spinal cord leasion. However, neural recovery has proven to be much more complex in humans, as human walking involves both spinal control and brain control (Yang and Gorassini, 2006). For rehabilitation to be successful neural plasticity should thus be maximally promoted. Although the mechanisms underlying neural recovery are not yet fully understood, there is a growing consensus about the major enabling principles. Sensory input from the muscles and joints to the central nervous system (afferent input) is crucial (Ridding and Rothwell, 1999; Harkema, 2001). Also, these sensory cues should match as closely as possible with those normally involved in the task to be relearned. Some critical cues of human locomotion have been established, but are subject of ongoing research (Behrman and Harkema, 2000). Another important requirement for recovery is that training should be intensive and that it should be started as early as possible after the injury to maximise outcome (Sinkjaer and Popovic, 2005).

The need for intensive training and the aim of relieving therapists from the physical strain induced by manually assisted gait training, triggered the application of robotic assistance to gait rehabilitation. The development and use of gait rehabilitation robots both in rehabilitation practice and in research labs has strengthened the validity of some concepts that are believed to underlie gait retraining in general and also to increase the effectiveness of robot-assisted training itself. A key finding is that assisting movements (too much) may result in reduced effort and decreased motor learning (Marchal-Crespo and Reinkensmeyer, 2008). This is evidenced by motor learning studies in unimpaired subjects involving robotic assistance to learn a movement task, and appears to apply to neural recovery as well. Some studies explored the benefits of amplifying movement errors instead of correcting them, which was found to improve short term motor learning, as reported for instance in Reisman et al., 2007. It was also shown that the training should be adapted to the skills of the subject: similar to providing too much assistance, providing too little is counterproductive (Emken et al., 2007). Another important aspect to training is active participation, which is promoted by motivation. The robotic training environment should trigger the subject to self-initiate and actively contribute to the movements and also to sustain efforts (Lotze et al., 2003). The suggestion that effort may be more important than (robotic) assistance, questions the rationale behind the use of robots in movement therapy (Reinkensmeyer et al., 2007). Nonetheless, many rationales for using robotic assistance in gait rehabilitation can be found in literature (Guglielmelli et al., 2009; Marchal-Crespo and Reinkensmeyer, 2009). Previously unexplored movements provide novel sensory information to the patient, assistance makes gait training more safe and intense, and helping the patient accomplish desired movements is an important motivating factor (an extensive overview can be found in Marchal-Crespo and Reinkensmeyer (2009)).

The aforementioned concepts are encompassed by a best practice in assistance-based robotic therapy commonly referred to by "assistance-as-needed", implying that the robot should assist only as much as needed and only where needed. Hence, the level of assistance should be adaptable and task (or function) specific. Newly developed robot technology for gait rehabilitation is increasingly focused on this paradigm. The following section puts emphasis on general concepts and hardware. An overview of control strategies in robot-assisted gait rehabilitation is given in section 3.1.1.

1.2.2 Gait rehabilitation robots

In the course of merely ten years, the number of devices for upper and lower limb rehabilitation, and from a broader perspective, the advancements in assistive technology, have grown remarkably. Hence, the following overview cannot, nor is meant to be exhaustive. Although common challenges are faced in the development of robots for the upper limbs, this overview is limited to devices for the lower limbs.

Similarly to rehabilitation robots for the upper limb, gait rehabilitation robots can be categorised according to their underlying kinematic concept into end-effector based and exoskeleton based robots (Guglielmelli et al., 2009). End-effector based robots interact with the human body in a single point (through their end-effector), whereas exoskeleton based robots interact with the human body in different points across human joints. The latter typically have an anthropomorphic, serial linkage type structure that acts in parallel with the lower limbs. Seldom, there are gait training devices not belonging to any of these two categories. String-man, a device consisting of tensioned wires attached to the body is an example (Surdilovic et al., 2007).

A commercially available end-effector based device is the GT1 Gait Trainer (Rehastim, Germany). It is based on a doubled crank and rocker gear system, driving two programmable footplates, generating gait-like movements of the lower limbs (Hesse and Uhlenbrock, 2000). More recently, a successor is being developed, the HapticWalker, based on the same concept of permanent foot-machine contact (Schmidt et al., 2005a). This concept is also typically found in parallel type rehabilitation

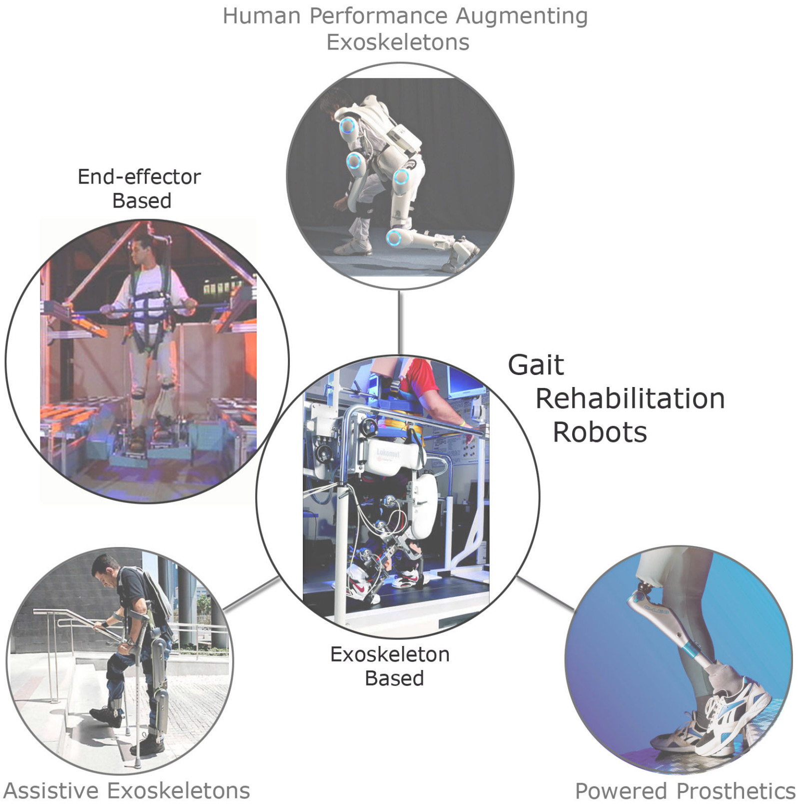

Figure 1.1: Gait rehabilitation robots: end-effector based (e.g. HapticWalker) and exoskeleton based (e.g. Lokomat®). Related applications supporting the development of exoskeleton based gait rehabilitation robots: human performance augmenting exoskeletons (e.g. HAL), assistive exoskeletons (e.g. ReWalk®), powered prosthetics (e.g. C-leg®).

robots with a platform for rehabilitation of the ankle/foot and for balance training as for instance in Saglia et al. (2010); Yoon and Ryu (2005). ARTHuR is a unilateral 2 DOF device using a backdriveable two-coil linear motor and a pair of lightweight linkages to drive a footplate (Emken et al., 2006). It has been used primarily to study motor learning principles and to evaluate a teach-and-replay procedure with impedance adaptation (Emken et al., 2008).

Most gait rehabilitation robots are exoskeleton based and prototype development in this type of devices is often supported and stimulated by advancements in related applications: assistive exoskeletons, human performance augmenting exoskeletons and powered prosthetics (see fig. 1.1). Rehabilitation exoskeletons, assistive exoskeletons and human performance augmenting exoskeletons are the three main types of powered exoskeletons for humans and the past decade has seen a multitude of research prototypes and devices of this sort. As their common rationale is the assistance of human gait, these exoskeletons are not easily categorised and sometimes assistive exoskeletons and human performance augmenting exoskeletons find their way to a rehabilitation setting. Also, from an engineering viewpoint, these applications have common requirements with respect to the performance of the actuators, the weight and compactness of the structure and the wearability of the design. There remains however a clear distinction of basic functionality. Rehabilitation exoskeletons are aimed at recovery of impaired function, whereas assistive exoskeletons assist impaired function and human performance augmenting exoskeletons augment sound function. Powered prosthetics replace lost function. Although acting in series with the human body instead of in parallel, powered lower limb prostheses also inspire the development of gait rehabilitation exoskeletons, as they require high performance actuators, gait phase detection and user-oriented control. An overview of the state-of-the-art in powered lower limb prosthetics can be found in Martin et al., 2010; Versluys et al., 2009a.

To date there are two commercially available exoskeleton-based gait rehabilitation robots: the AutoAmbulator (Healthsouth, US) and the Lokomat (Hocoma, Switzerland). Both devices consist of a treadmill, an overhead suspension system with a harness and a robotic orthosis attached to the patient's lower limbs, assisting the hip and the knee bilaterally. The Lokomat, in particular, has undergone substantial testing with patients and, as opposed to AutoAmbulator, is extensively reported in literature. Lokomat, originally purely position controlled, uses ball screw actuators and joint-space impedance control to achieve naturalistic joint trajectories at the hip and knee. Various patient-cooperative control strategies have been investigated (Jezernik et al., 2004; Duschau-Wicke et al., 2008) as well as a hardware extension of the system with additional actuated DOF (ab/adduction of the hip and lateral and vertical pelvic displacement, see Bernhardt et al., 2005b), but most functionalities were not transferred to the device that is currently on the market and in use in rehabilitation centers.

Several research groups recognised the need for assistance-as-needed control strategies and for more physiological gait movements, both considered essential to increase the effectiveness of robot-assisted gait training. Most research efforts are focused on introducing adaptable compliance (or variable impedance) into the hardware and/or the control of the system and on extending the number of DOF of the exoskeleton, i. e. active DOF (actuated) and/or passive DOF (passive elements or none).

In LOPES, besides flexion/extension of the knee and hip, lateral and forward/backward displacement of the pelvis and abduction/adduction of the hip are assisted (Veneman et al., 2007). Bowden-cable based series elastic actuators are used to power the exoskeleton's joints for reasons of inherent safety and force tracking performance (Veneman et al., 2005). The device is intended for use in stroke patients and focus is on task-specificity of assistance by means of virtual model control (Ekkelenkamp et al., 2007). PAM and POGO use pneumatic cylinders to compliantly assist five out of six DOF of the pelvis and flexion/extension of the knee and hip. Zero-force control and impedance control are used consecutively in a teach-and-replay procedure (Aoyagi et al., 2007). Both LOPES and PAM/POGO are treadmill based devices. The WalkTrainer (Stauffer et al., 2009) is a mobile over-ground walking device, that consists of a mobile base with an active body weight supporting harness, a pelvic orthosis (6 actuated DOF) and two leg orthoses (3 actuated DOF each) (Allemand et al., 2009). It combines task-space impedance control of the orthoses with closed-loop functional electrical stimulation (FES) of the paraplegic patient's leg muscles. The KineAssist (Kinea Design, US), although mobile as well, is not exoskeleton based and primarily intended for adaptable body weight support and walking balance training of stroke patients.

Besides bilateral prototypes, several unilateral rehabilitation exoskeletons, comprising one or more powered joints, have been developed. ALEX is a leg exoskeleton of which the hip and knee joint are actuated by linear drives (Banala et al., 2009). A force field controller is implemented in task-space that displays a position dependent force field acting on the foot. In Sawicki et al. (2005) ankle-foot and knee-ankle-foot orthoses powered by McKibben type pneumatic muscles are investigated for task-specific rehabilitation. This actuator type has also been implemented in, amongst others, a bilateral prototype reported in Costa and Caldwell (2006) and in an ankle rehabilitation device for stroke patients in combination with springs (spring over muscle actuator) reported in Bharadwaj and Sugar (2006). SERKA is an active knee orthosis for gait training focusing on stiff knee gait in stroke patients (Sulzer et al., 2009). It is driven by a rotational series elastic actuator, similar to the actuator type implemented in LOPES, capable of providing low torques during zero-torque control ($1\,Nm$) and considerably high torques (up to $41\,Nm$), while keeping the added mass low by means of remote actuation through Bowden cables. AKROD is a knee orthosis with an electro-rheological fluid (ERF) variable damper component to correct hyperextension of the knee and stiff knee gait in stroke patients (Weinberg et al., 2007). The ERF brake provides only resistive torques (up to $78\,Nm$) and does not introduce any positive power at the knee joint. Entirely passive systems have been developed as well. The gravity balancing orthosis (GBO) compensates the gravitational torques acting at the hip and the knee of the combined system (orthosis and leg) during swing by means of a dedicated spring mechanism (Banala et al., 2006). SUE is a passive bilateral exoskeleton with torsion springs in the hip and knee joints optimised for propulsion of the legs during swing in treadmill walking (Mankala et al., 2007).

Also in the field of assistive exoskeletons, a multitude of devices and prototypes has been developed, some of them also envisaged for use in rehabilitation or performance augmentation. The ReWalk (Argo Medical Technologies, Israel) is a bilateral robotic suit for the mobility impaired that is near to being released to the market. Some exoskeletons are specifically aimed at assisting the elderly, such as the walker based exoskeleton EXPOS reported in Kong and Jeon (2006), others focus entirely on body weight support, such as the Moonwalker (Krut et al. (2010)) and the Bodyweight Support Assist by Honda. A combination of a quasi-passive exoskeleton with functional electrical stimulation (FES) is proposed in Farris et al. (2009). Many single joint exoskeletons have been developed. The DCO (Hitt et al., 2007) and the AAFO (Blaya and Herr, 2004) are examples of active ankle foot orthoses making use of series-elastic actuators to assist in push-off or to correct dropped foot gait.

The majority of human performance augmenting exoskeletons for the lower limbs has been designed for load carrying augmentation (e.g. carrying a backpack) with military applications in mind, such as BLEEX (Kazerooni and Steger, 2006), the Sarcos exoskeleton (Sarcos, US) and NTU exoskeleton (Low et al., 2005). Their control strategies are dedicated to unimpaired users. A quasi-passive leg exoskeleton, using a fraction of the power consumed by the aforementioned devices, is reported in Walsh et al. (2007). The robot suit HAL (Cyberdyne, Japan), of which the control relies on muscle EMG measurements, is currently being evaluated as an assistive exoskeleton for the mobility impaired. For an extensive overview of powered lower limb exoskeletons the reader is referred to Dollar and Herr (2008).

1.2.3 ALTACRO

A five year concerted research action project, ALTACRO (Automated Locomotion Training using an Actuated Compliant Robotic Orthosis), was set out starting from 2008 by a consortium involving three faculties of Vrije Universiteit Brussel with the aim of addressing some of the identified challenges in robot-assisted gait rehabilitation. Engineers, physiotherapists and doctors collaborate on this topic in a multidisciplinary research group ARTS (Advanced Rehabilitation Technology and Science[1]) and conduct research into four aspects of robot-assisted gait training:

- active assistance at the ankle
- balance and load distribution

[1] A consortium of the Robotics & Multibody Mechanics research group (R&MM), the Department of Human Physiology and Sports Medicine (MFYS), the Department of Biomechanics (BIOM), the Department of Rehabilitation Research (RERE), the Department of Experimental Anatomy (EXAN) and the Department of Orthopedics and Traumatology at Vrije Universiteit Brussel

- functional, three dimensional gait kinematics
- physical human robot interaction

The project involves the development of a novel full lower body exoskeleton powered by compliant actuators and the clinical evaluation of its concepts aimed at improving robot-assisted gait rehabilitation in the four aforementioned areas.

The gait rehabilitation devices currently in use in rehabilitation centers do not provide any controlled assistance at the ankle joint. The lack of actuation at the ankle possibly has an adverse effect on the recovery of functional gait, as in normal human walking the largest peak moments of force occur at the ankle joint. Also causes of gait dysfunction like dropped foot or spastic foot extension cannot be adequately countered during therapy. Support of the ankle/foot may even be considered an essential safety requirement for robot-assisted gait training.

A suspension system that lifts a part of the patient's body weight, as used in BWSTT, introduces an unnatural load distribution in the patient's body, since the lower limbs are only subject to a part of the bodyweight. Step rehabilitation training practice indicates sufficient loading of the patient's body is required to generate afferent inputs close to those occurring during unaffected walking (Behrman and Harkema, 2000). The suspension system also hinders the normal balance and postural reactions of the patient that are required for functional walking. As there is currently no consensus regarding the preferred amount of body weight support (Hidler, 2005), a robotic exoskeleton capable of providing full body weight support without any additional suspension system could open up possibilities.

To date, gait assistance in commercial exoskeleton-type robots is restricted to planar motion, resulting in relatively large movements of the body relative to the device (Neckel et al., 2006). However, it is assumed that robot-assisted gait training may benefit from more physiological robotic joints, allowing movements closer to the three dimensional kinematics of human gait. Introducing this principle in a rehabilitation robot may be beneficial to training and recovery of coordination and equilibrium.

A key feature of rehabilitation robotics is the close human-robot interaction involved. The device should be capable of adaptable, compliant behaviour both for reasons of safety and functionality. The envisaged benefits of adaptable compliance (or variable impedance) on the control level (e.g. impedance control with parameter adaptation) and on the hardware level (compliant actuators), which are recently being investigated by some of the research groups active in the field, need to be further explored. For instance, from the safety viewpoint, the need for compliance in the event of spasticity[2] of the leg muscles has not yet been addressed

[2]Spasticity is defined as a motor disorder characterised by a velocity-dependent increase in muscle tone with exaggerated tendon jerks, resulting form hyperexcitability of the stretch reflex (Lance, 1980). It results in increased resistance against passive motion. Spasticity is often diagnosed in neurological disorders as SCI, stroke and multiple sclerosis.

sufficiently. Another topic of research related to safety and functionality is how to set the compliance (or impedance) such that the assistance is as needed, while ensuring safety and continuity of the assisted movements. The shift from stiff position control to strategies involving adaptable compliance (variable impedance) intrinsically implies reduced accuracy of movements and enhanced control over physical human-robot interaction. This dissertation specifically addresses the topic of physical human-robot interaction in robot-assisted gait rehabilitation in the framework of the ALTACRO project.

1.3 Goal and approach

The goal of the work reported in this dissertation is to investigate suitable design and control concepts for a gait rehabilitation robot powered by compliant actuators and in view of safe and adaptable physical human-robot interaction (pHRI).

The compliant actuator used in this work is the pleated pneumatic artificial muscle (PPAM), developed by Daerden (1999). The PPAM is a special type of pneumatic muscle, a contractile device consisting of a thin membrane that is operated by pressurised air. Pneumatic muscles have a high force-to-weight ratio and they are intrinsically compliant, due to the compressibility of air. They are typically coupled to a joint directly, without a complex transmission, and used in antagonistic pairs to power a joint, which fortifies the qualitative analogy with biological muscles. With this configuration of pneumatic muscles one is capable of controlling both the torque and the intrinsic compliance of a robotic joint, which makes them a suitable candidate for the application under study. The nonlinear force-contraction characteristic and the pressure dynamics underlying their performance are two key aspects specific to this type of actuator that need to be dealt with in the design and control of a robotic joint powered by pneumatic muscles.

In order to evaluate the proposed design and control concepts, a knee exoskeleton powered by PPAMs has been developed in this work. In the development of this research prototype several important stages are addressed: actuator system design, mechanical structure design, system modelling and simulation, controller design and control performance evaluation. Since the main objective is to study safe and adaptable pHRI in robotic gait assistance, performing extensive experiments with the prototype in unimpaired subjects before passing on to patient testing was considered of great importance. A pilot robot-assisted walking study with a stroke patient and a multiple sclerosis patient forms the concluding stage of this work.

1.4 Outline

This dissertation describes the design, the control and the evaluation of a compliant powered knee exoskeleton, named KNEXO, in three respective chapters.

Design of KNEXO, a knee exoskeleton powered by PPAMs

After an overview of the fundamental design choices made for the prototype a short introduction to gait terminology and conventions, and to gait analysis focused on the knee is given in section 2.2, as it provides an essential framework for design, control and performance evaluation.

The design of the actuator system is elaborated in section 2.3. Its requirements are defined on the basis of gait analysis data. A detailed overview of the characteristics of the PPAM and its possible configurations in a robotic joint are given. Starting from a trial-and-improvement design of an antagonistic configuration of PPAMs a multi-objective optimisation approach is investigated. An exhaustive search based optimisation method is proposed and applied to two configurations with a different force transmission concept.

Different intermediary prototypes and setups were developed to come to the final prototype, all of them described in section 2.4. The mechanical structure of KNEXO is explained with focus on wearability.

Section 2.5 gives an overview of the instrumentation with emphasis on sensing for control and safety.

Control for safe, compliant and adaptable robotic assistance

This chapter starts by giving an overview of existing assistance-based control strategies (high level control) for gait rehabilitation, focusing on the implementation of “assistance-as-needed”, and an overview of the state-of-the-art in control of pneumatic muscles (low level control). Also in section 3.1, the main challenges regarding control and the approach followed in this work are given.

The simulation models of the combined human-robot system and of the actuator system (torque output, valve dynamics), described in section 3.2, support the implementation of different controllers:

- A torque controller is proposed and experimentally evaluated in section 3.3.
- Section 3.4 elaborates on a trajectory tracking approach to assistance-based control. A trajectory tracking control method is explained and two different implementations are proposed, one of which using the aforementioned torque controller as an inner torque control loop.

Aspects related to the generation and synchronisation of the target trajectory in support of the assistive controllers are discussed separately in section 3.5.

Robot assisted walking with KNEXO

The experiments with unimpaired subjects, covered by section 4.2, address the three main objectives to be met in view of patient testing: unassisted walking, assisted walking with safe guidance, assisted walking with adaptable physical human-robot interaction.

Finally, section 4.3 presents and discusses pilot assisted walking experiments with two impaired subjects: a stroke patient and a multiple sclerosis patient.

1.5 Main contributions

The goal of this dissertation is to contribute to the improvement of physical human-robot interaction (pHRI) in robot-assisted rehabilitation of gait by developing and studying suitable design and control concepts of a gait rehabilitation robot powered by compliant actuators. In addition, this work was aimed at smoothing the way to the development of a novel full lower body exoskeleton within the framework of an ongoing research project ALTACRO (see 1.2.3).

The main contributions with regard to design are:

- a methodical, optimisation based approach to the design of a robotic joint powered by pleated pneumatic artificial muscles (PPAMs).
- KNEXO, a knee exoskeleton powered by PPAMs, as a research prototype for the implementation and evaluation of control strategies for safe and adaptable robotic assistance.

The main contributions with regard to control are:

- a simulation model of KNEXO, comprising an actuator system model and a model of the combined human-robot system.
- a torque controller based on force sensor feedback and on a model-based feedforward.
- a trajectory tracking controller for safe and adaptable robotic assistance using the aforementioned torque controller as an inner torque control loop.

The main contributions with regard to the evaluation of the proposed design and control concepts:

- a study of the effects of compliant robotic guidance by KNEXO in unimpaired and impaired subjects, combining exoskeleton data with gait kinematics analysis and muscle activity measurements.
- pilot experiments with a stroke patient and a multiple sclerosis patient, providing valuable end-user feedback.

A list of publications resulting directly from this work and from related work in collaboration with colleagues can be found after the concluding chapter.

Chapter 2

Design of KNEXO, a knee exoskeleton powered by PPAMs

2.1 Introduction

As emphasized in the introductory section, the main purpose of KNEXO, the knee exoskeleton developed in this work, is the implementation of design and control concepts, smoothing the way towards the development of a novel full gait rehabilitation exoskeleton. The design framework of the prototype can be summarised by the following list of conceptual design choices.

- the exoskeleton is wall grounded and not body grounded
- the mechanical structure is a serial linkage interconnected by a revolute joint, acting in parallel with the human lower limb
- the exoskeleton's knee joint is powered by pleated pneumatic artificial muscles
- the powered joint should be capable of providing a joint torque, a speed and a range of motion comparable to sound human knee joint performance during walking at typical treadmill walking speeds in gait rehabilitation training
- the physical human-robot interface should be adaptable to a wide range of human statures and sizes

The choice for an externally mounted system (see fig. 2.1 left), instead of a portable system (see fig. 2.1 right) adheres to the conventional framework of treadmill based full lower body exoskeletons for gait rehabilitation. The latter are typically externally mounted to allow a compensation of the robot's weight and to maintain balance of the combined human-robot system. This choice does not free the design from the requirement of weight and inertia minimisation, which is one of the major bottlenecks encountered in the design of fully wearable powered exoskeletons.

Figure 2.1: Wall grounded (left) and body grounded (right) exoskeleton

Since the dynamics of the robot cannot be fully compensated by the controlled actuator system, minimising the robot's weight and inertia is hence equally relevant in wall grounded exoskeletons. Energetic autonomy however, another bottleneck in portable robot design, is not an issue.

Recent research in non-anthropomorphic, kinematically redundant exoskeletons reveals promising characteristics in terms of minimisation of undesired interaction forces (Schiele and van der Helm, 2006). These interaction forces are due to misalignments of the robotic joints and the human joints, and typically occur in conventional exoskeleton designs. In addition, alignment of the exoskeleton during fitting is not required or reduced. This kinematic design concept, however, drastically increases design complexity and although successfully applied to an arm exoskeleton for force-feedback tele-operation (EXARM, Schiele, 2008) it is a subject of ongoing research whether it would be as beneficial for powered exoskeletons designed to transfer higher torques (Sergi et al., 2010; Stienen et al., 2009). For the mechanical structure of KNEXO the conventional and most straightforward anthropomorphic kinematic structure with links interconnected by a revolute joint was chosen.

The rationale behind the use of pleated pneumatic artificial muscles (PPAMs) as compliant actuators in this work is threefold. Their high force to weight ratio, their intrinsic compliance, and the adaptability of the compliance of a joint powered by PPAMs make this actuator a suitable and interesting candidate for implementation in a compliantly powered exoskeleton. These advantages and the underlying characteristics of the PPAM are elaborated further in section 2.3.2.

The actuators should provide the exoskeleton with the required torque and power to fully support the function of the knee at moderate walking speeds in the absence of human knee joint torque and power. The approximation of the actuator system's requirements is based on gait analysis data of the sound human knee. Since a prototype design was envisaged, this approach was preferred over a design supporting simulation study involving a multibody model of the human and the robot.

A final conceptual design choice concerns the physical interface between the exoskeleton and the wearer. Unlike a powered exoskeleton intended as an assistive device, a gait rehabilitation exoskeleton for treatment in a facility setting is not customised to a single user. The prototype's interface should be adaptable in order to fit the individual wearer, allowing for a wide range of human statures and sizes in view of experimental studies.

Based on the aforementioned conceptual design choices a prototype design was made. The design process was primarily focused on

- actuator system design
- adaptability of the physical human-robot interface
- weight compensation of the device

In particular, special attention was paid to the investigation of a methodical approach to the design of an actuator system consisting of PPAMs. This approach could then be used for any PPAM-powered joint of a full active lower limb exoskeleton.

The description of the prototype design is structured according to its three main functional components: the actuator system, the mechanical structure and the instrumentation, are covered by section 2.3, 2.4 and 2.5 respectively. For the sake of clarity and completeness, a selective terminology overview as well as a short description of some fundamentals of the biomechanics of human gait with focus on the knee are included in this chapter in section 2.2. This "toolbox" provides a starting point for the actuator system design described in section 2.3. In the final section of this chapter the entire design is summarised in a short overview.

2.2 Toolbox: into the biomechanics of human gait

After a brief overview of basic gait related terminology and conventions used throughout this work, the kinematics and kinetics of the knee joint are brought into focus. The design requirements of the actuator system (chapter 2), as well as the controller design (chapter 3) and the analysis of results of treadmill walking experiments (chapter 4) rely on this framework.

2.2.1 Basic gait terminology

Human gait is a series of cyclic lower limb and whole body movements, characterised by its constituent repeated sequence, the walking pattern or gait cycle. The gait cycle is divided into different gait phases and marked by different gait events, as

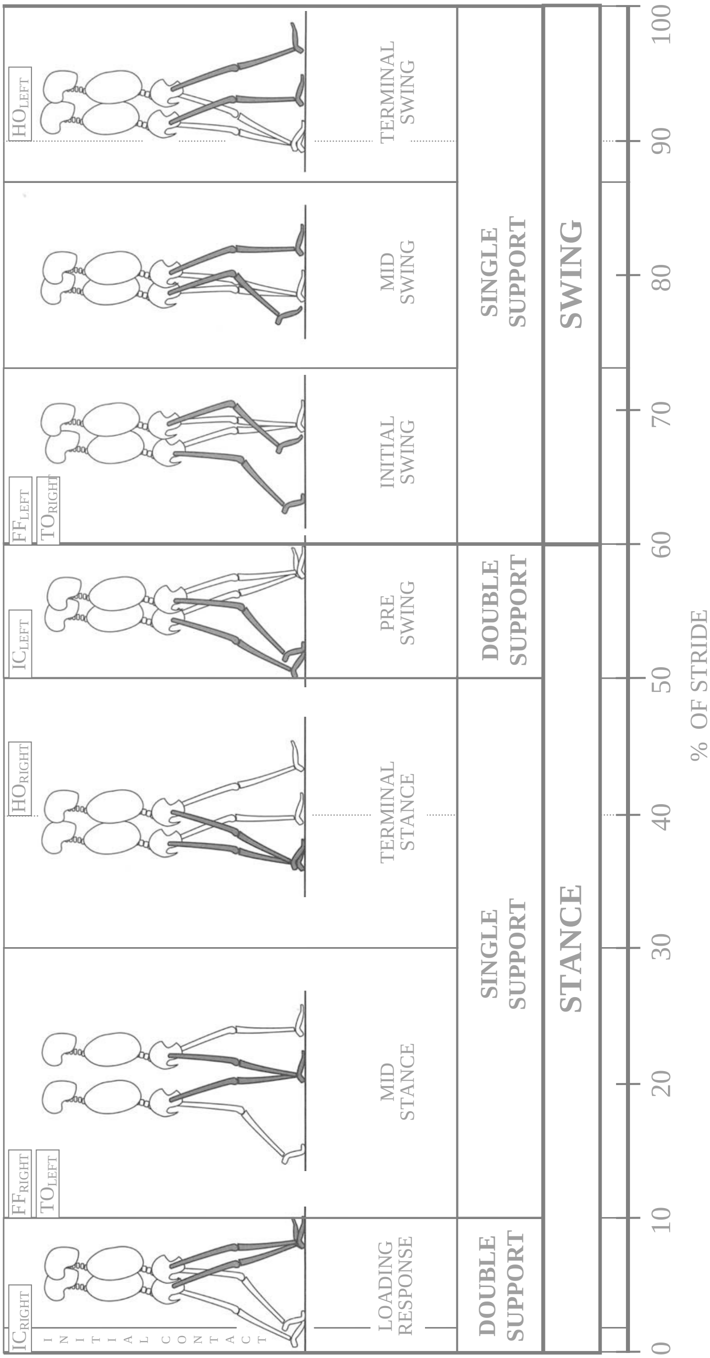

Figure 2.2: The human walking gait cycle: different gait phases and gait events according to Perry (1992). The left and right stick figure correspond respectively with the start and end of each phase (stick figures adopted from Perry (1992)).

illustrated by fig. 2.2. A gait cycle covers a stride, starting from the initial contact with the ground of one foot and lasting till the next initial contact of that same foot. A stride thus consists of two consecutive steps. In normal human gait initial contact corresponds with the heel strike. The different gait events correspond with functional time instances, whereas the gait phases relate to functional time intervals.

The consecutive gait events indicated on fig. 2.2 are: initial contact (IC), foot flat (FF; foot flat on the ground), heel-off (HO; heel is lifted from the ground), toe-off (TO; toes are lifted from the ground). Other gait events, such as midstance and midswing, have been defined and used in literature, but nomenclature and/or definitions vary. The gait phase between heel strike and toe-off of the same foot, during which it is in contact with the ground, is the stance phase. The phase in which the foot is not in contact with the ground is the swing phase. At natural cadence (number of steps per time unit) the stance phase and the swing phase account for about 60% and 40% of the stride period respectively. Combining these phases for both limbs, one infers there is a phase during which both limbs are in stance, called double support phase, lasting about 10% of the stride period and occurring twice in each stride. The single support phase (40% of the stride period for each limb) corresponds with one limb being in stance, while the other is in swing. It is important to note that quantities related to gait timing, such as the stride period and the ratio of stance time to swing time, as well as quantities related to distance, such as the step length, vary with walking speed. Both cadence and step length increase equally with increasing walking speed up to a step length limit. The ratio of stance time to swing time decreases with increasing stride length and with increasing walking speed.

The stance and swing phase can each be subdivided in different functional gait phases (see fig. 2.2). Different gait phase definitions exist in literature. The phases listed below are in accordance with Perry (1992).

- Initial contact: 0-2% stride. The foot makes contact with the ground.
- Loading response: 0-10%. Begins at initial contact and ends at toe-off of the other (contralateral) foot. Covers the first double support period, during which the body weight is shifted from the contralateral leg to the other.
- Mid stance: 10-30%. The first half of the single support interval, starting with contralateral toe-off and ending when the body weight is aligned over the forefoot
- Terminal stance: 30-50%. The body is progressed beyond the forefoot. Ends at initial contact of the contralateral foot.
- Pre-swing: 50-60%. Covers the second double support period and ends at toe-off. Terminates the stance phase.

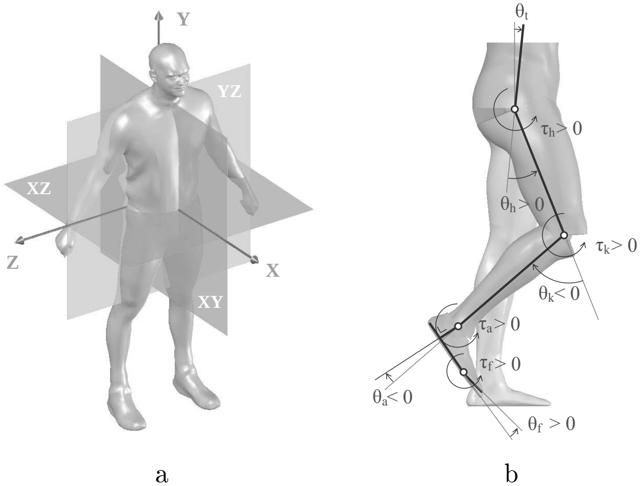

Figure 2.3: Link-segment model: a) Coordinate system, b) Simplified 2D model of the lower limb.

- Initial swing: 60-73%. Starts at toe-off and ends when the swinging foot is opposite the contralateral stance foot.
- Mid swing: 73-87%. The leg is swung further forward. Ends when the lower leg is vertical.
- Terminal Swing: 87-100%. The lower leg advances ahead of the upper leg until the leg is quasi stretched. Ends at initial contact of the foot.

2.2.2 Biomechanical link-segment model and conventions

The analysis of the kinematics and kinetics of human gait requires a three dimensional link-segment or multibody model. Figure 2.3.b shows a simplified 2 dimensional link-segment model of one lower limb and the upper body as a whole. This linkage model is bound to the plane of progression and thus only captures the principal movements in that plane. The plane of progression or sagittal plane is one of three orthogonal planes related to a reference coordinate system placed in the body's center of mass, depicted in fig. 2.3.a. This coordinate system is formed by the direction of progression (X), the vertical axis (Y) and the lateral axis (Z), satisfying the right hand rule. Besides the sagittal plane (XY), it defines the frontal plane (YZ) and the transverse plane (XZ). These coordinate definitons are in accordance with Winter (1991), the sign conventions for joint angles and joint moments explained next differ. In fig. 2.3.b relative angles between adjacent links, joint angles, are defined for kinematics analysis.

Figure 2.4: Gait analysis measurement setup: camera-based motion capture by means of reflective marker tracking and a force plate for ground reaction force measurements.

In gait analysis these relative angles are typically calculated on the basis of a link-segment model and absolute position measurements by a camera-based motion capture system (see fig. 2.4). Relative (in-plane) segment rotation is described with the terms extension and flexion. For the hip (θ_h), flexion implies forward rotation of the upper leg towards the chest, for the knee (θ_k) it implies bending of the knee, for the ankle (θ_k) it implies forward rotation of the foot towards the knee (also called ankle dorsiflexion). Respectively, extension implies backward rotation of the upper leg, stretching of the knee and backward rotation of the foot away from the knee (also called ankle plantarflexion). All counter clockwise angles are defined positive in fig. 2.3.b. The absolute angle of the trunk, denoted by θ_t, is slightly negative and nearly constant in normal walking. The relative angle of the toe segment, denoted by θ_f, is nearly 0° during the entire swing phase and the period of the stance phase between foot flat and heel-off.

A gait kinetics analysis, i.e. an analysis of the forces, moments, energies and powers of gait movements, requires, besides a kinematics model, the knowledge of the inertial parameters of the link-segment model and a convention for joint moment polarity. The joint moment is the total moment of all internal forces (due to muscles, friction, ligaments etc.) acting at that joint. The sign convention has been chosen such that a moment vector and an angular velocity vector have the same sign if the moment and the rotation have the same sense. All counter clockwise moments are hence positive (see fig. 2.3.b). An extension moment and an extension, as well as a flexion moment and a flexion result in positive mechanical power. The instantaneous mechanical power P produced at the joint is the scalar product of the joint moment $\boldsymbol{\tau}$ and the joint angular velocity $\boldsymbol{\omega}$:

$$P(t) = \boldsymbol{\tau}(t) \cdot \boldsymbol{\omega}(t). \tag{2.1}$$

The work W or energy related to joint motion in a time interval $[t_0, t_0 + T]$ is defined as the time averaged instantaneous power:

$$W = \int_{t_0}^{t_0+T} P(t)dt. \tag{2.2}$$

The average power $\widetilde{P}$ over the time interval $[t_0, t_0 + T]$ thus equals

$$\widetilde{P} = \frac{W}{T}. \tag{2.3}$$

In gait analysis human joint moments are calculated from the dynamics equations of a link-segment model, the kinematics (measured by means of a camera-based tracking system, see fig. 2.4) and the external forces, i.e. ground reaction forces (measured by means of a force plate, see fig. 2.4). In this work gait analysis is performed during treadmill walking and it does not incorporate ground reaction force measurements. In order to gain insight in the source of joint moment and power, muscle electromyography (EMG) measurements are performed to capture muscle activity.

2.2.3 Muscle activity

Muscle activity can be measured indirectly by means of electromyography (EMG) measurements, capturing the electrical signals resulting from the electrochemical reactions that take place in activated muscles. The electrical activity of a muscle is the combined result of the activation of several (hundreds of) motor units, i.e. groups of muscle fibers activated by a single motor nerve. It depends on the number and timing of activated motor units, their size and condition (Perry, 1992; Winter, 1991).

Surface electrodes attached to the skin or indwelling needle electrodes, are used to capture this electrical activity. Surface electrodes in particular are most commonly used in gait analysis for measuring activity in larger, superficial muscles over a relatively large area. Integratively recording global activity is an advantage, but also poses difficulties in correctly measuring, processing, analysing and interpreting EMG data, topics extensively discussed in literature (Soderberg and Knutson, 2000). Measurement standards are found for instance in Merletti (1999). Raw EMG data, i.e. voltage signals with peak-to-peak amplitudes in the order of $[100 - 1000]\,\mu V$ and spectral content in a range of $[5 - 500]\,Hz$, are only suitable for the assessment of general muscle activity (on-off).

For a higher level interpretation of the timing and intensity of activation and the relation with muscle force, processing of EMG data is required (see Soderberg and Knutson (2000) for a comprehensive overview). This is especially important when relating electrical activity to muscle tension and joint motion. The processing is mainly concerned with retrieving an estimator of magnitude and with normalization of this magnitude for comparison between measurements (in different muscles or subjects, for instance). The former is typically done by taking the root-mean-square (RMS) or the linear envelope (rectification and filtering) of raw data. Normalisation is done by scaling against a reference value taken from EMG data of static or dynamic effort. The most commonly used reference in unimpaired subjects is maximal voluntary isometric contraction (MVIC or MVC), which provides a measure of maximal effort in static conditions. A time domain analysis of normalised, linear enveloped EMG data benefits from a quantification of timing (on-off) and amplitude (peak, mean) of signal levels in view of a comparison between measurements or a comparison with "normal" EMG patterns reported in literature (see for instance Winter (1991)). In this work, a comparison is made between measurements of unimpaired subjects in different conditions and therefore a discussion of "normal" EMG patterns is outside the scope of this overview.

2.2.4 Knee joint kinematics and kinetics

In view of the design and control of a powered knee exoskeleton, this section is centered on the kinematics and kinetics of the human knee joint. When analysing data originating from gait analyses it is important to bear in mind that besides the error sources residing in the modelled and the measured quantities, large variations are observed due to the natural variability between different individuals and between different data sets of the same individual.

Figure 2.5 shows data originating from Winter (1991), averaged over 19 unimpaired adults, walking overground with a natural cadence ($\approx$ 105 $steps/minute$) and a slow cadence ($\approx$ 87 $steps/minute$). The average walking speeds at these cadences were $4.8\,km/h$ and $3.6\,km/h$ respectively. Joint angle, moment of force, instantaneous power and their corresponding standard deviation curves are plotted against percentage of stride. The moment of force and instantaneous power are normalised with respect to body mass. These data apply only to the sagittal motion of the knee joint and, hence, do not reflect the existing but smaller mobility in the frontal and transverse plane. For an easier interpretation the different phases of gait as listed in section 2.2.1 are indicated: loading response (LR), mid stance, terminal stance, pre swing, initial swing, mid swing and terminal swing.

The two major functions of the knee are providing limb stability during stance and a large mobility (about 60-70°) during swing in order to achieve sufficient clearance of the foot with the ground. The knee is slightly flexed prior to initial contact. At initial contact a flexion moment (negative) stabilises the knee that is

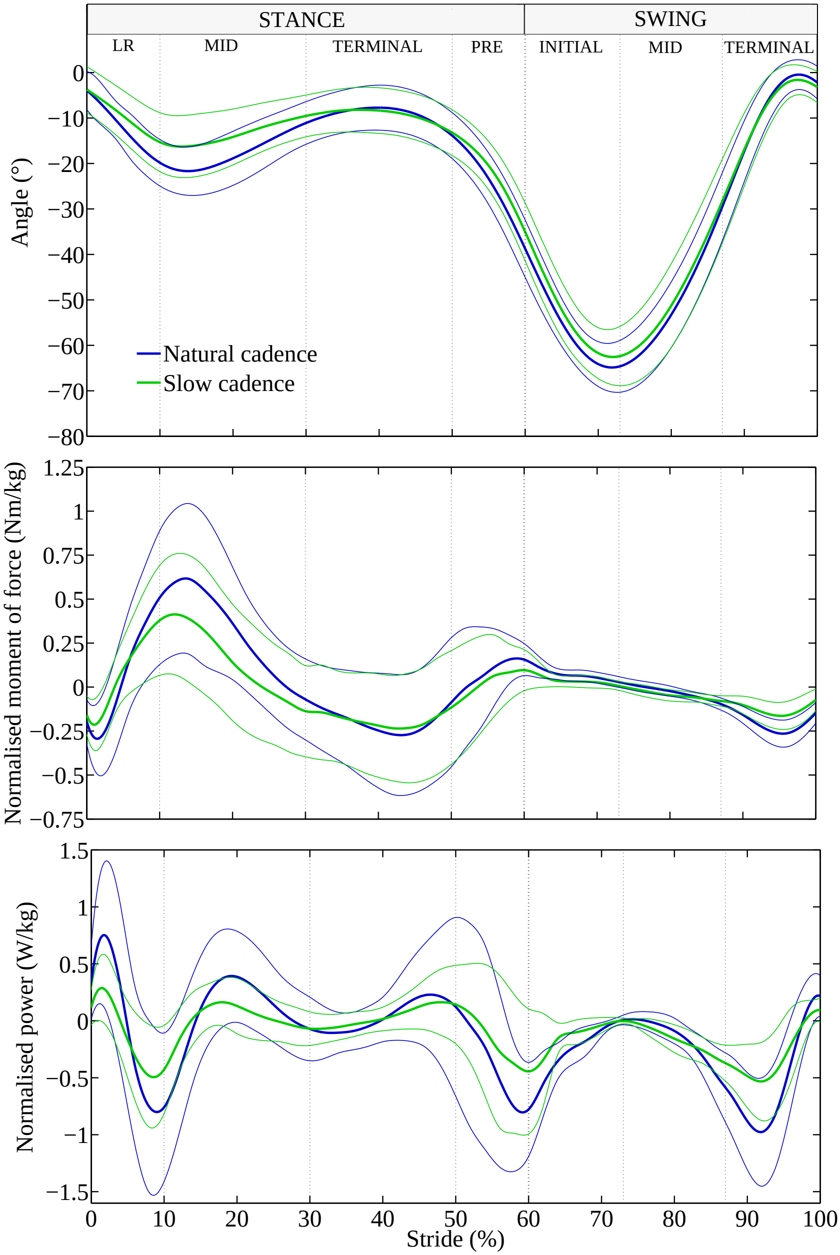

Figure 2.5: Averaged gait analysis data of the human knee joint: angle, normalised moment of force and normalised power with $[-\sigma, +\sigma]$ confidence bounds as a function of stride percentage at natural (blue) and slow (green) cadence (data taken from Winter (1991)).

subject to an external extension moment generated by the ground reaction force. During the loading response phase the knee is flexed and a large extension moment (positive) is built up until the maximum weight bearing load is reached. At the end of the loading response phase this extension moment can reach up to $[0.5 - 1]\,Nm/kg$ at natural cadence. Power absorption takes place as the knee flexes while counteracting gravity. From mid to terminal stance the knee is in single support phase and extended, while the body is progressed over the stationary foot. The knee joint moment grows negatively. During pre swing the limb is being pushed off, while the body weight is transferred to the other limb. A knee flexion occurs prior to toe-off and this is continued during initial swing. Since this knee flexion occurs on average under a small extension moment power is absorbed. From the onset of initial swing (toe-off) on the knee joint moment is close to zero. Maximum flexion is reached and from mid swing on the knee is extended to timely reach a quasi-stretched leg configuration prior to the next initial contact. Maximum extension occurs slightly before initial contact of the next stride and is accompanied by a small flexion moment resulting in power absorption. At slow cadence (lower walking speed) the knee flexion during the loading response phase is less pronounced when compared with natural cadence and it is accompanied by a lower extension moment. Lower moments and/or angular velocities imply lower power magnitudes.

It is important to note that the joint moments are the net result of all internal forces. In the absence of any voluntary muscle force, a so called passive elastic joint moment is observed due to tendons and ligaments. The influence is considerable near full extension of the knee (up to about $-10\,Nm$) and at large flexion angles (up to about $5\,Nm$ at 90°) according to Riener and Edrich (1999).

It is clear from the short overview given in this section that due to the natural variability of gait and due to the model and measurement constraints gait analysis data are prone to large variations. Hence, from an engineering viewpoint, care should be taken when interpreting gait analysis data and translating it into guidelines for the design and control of a powered exoskeleton.

2.3 Actuator system

Given the design choices made in the introductory section (section 2.1) and the basics of gait analysis in section 2.2, the actuator system requirements are specified first. Before selecting and dimensioning the actuator configuration, the actuator itself, the pleated pneumatic artificial muscle (PPAM) and its essential characteristics are presented in detail. The first design, based on an actuator configuration using levers for actuator force transfer to the joint, provides a better insight into the complexity of the design problem. A multi-objective optimisation method is presented as a methodical approach to the design of a joint powered by PPAMs. In order to improve the compactness of the configuration, the second design is based

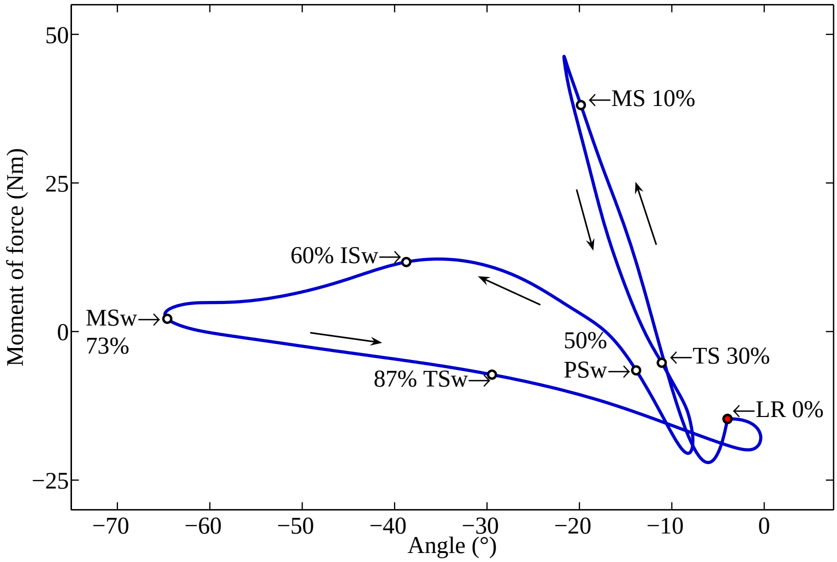

Figure 2.6: Moment of force as a function of knee joint angle for an unimpaired subject (75kg) walking at a natural cadence (4.8km/h). Stride percentage is marked at the indicative start of each phase (see section 2.2.1). Data based on gait analysis data from Winter (1991).

on an actuator force transfer by four bar linkages. By means of the knowledge gained from the first design and the same optimisation method a final design solution is selected and integrated in the design of the exoskeleton described in section 2.4.

2.3.1 Requirements

The actuators should provide the exoskeleton with the required torque and power to fully support the function of the knee at low to moderate walking speeds in the absence of human knee joint torque and power. Gait analysis data from Winter, 1991 of the unaffected knee joint, previously described in section 2.2.4, was used as a reference for the range-of-motion and the torque output of the robotic knee joint. Since gait rehabilitation training of impaired subjects on a treadmill is typically performed at walking speeds in a range of $[1.5 - 3.5]\,km/h$ (Hornby et al., 2005), gait data collected for low walking speeds has been primarily looked into. Data for moderate (natural) walking speeds can be viewed as a maximum rating. The rationale behind the choice of using the gait analysis data provided by Winter, 1991 instead of building a custom made gait database is twofold. First, the data in Winter, 1991 provides sufficient detail to approximate the average knee torque

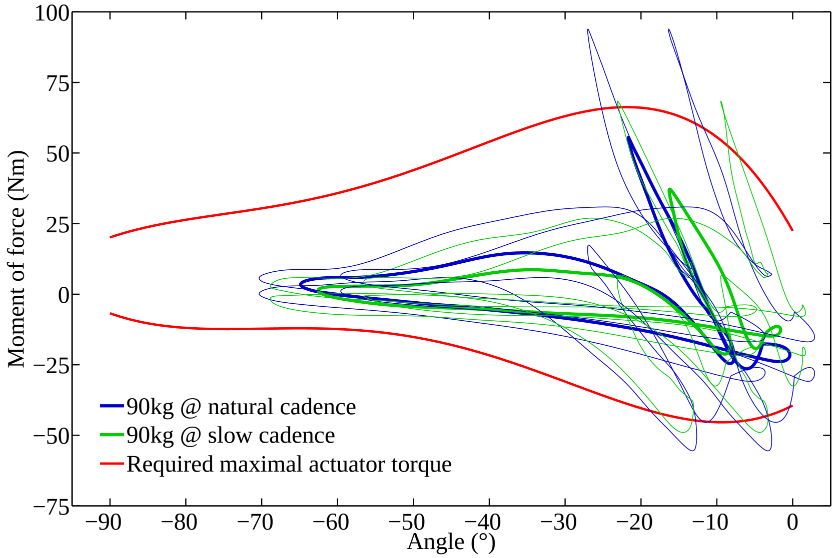

Figure 2.7: Required maximal actuator output torque characteristic (red) compared with typical moment-angle cycles of an unimpaired subject ($90\,kg$) walking at natural ($4.8\,km/h$, blue) and slow cadence (3.6 km/h, green). Data based on gait analysis data from Winter (1991).

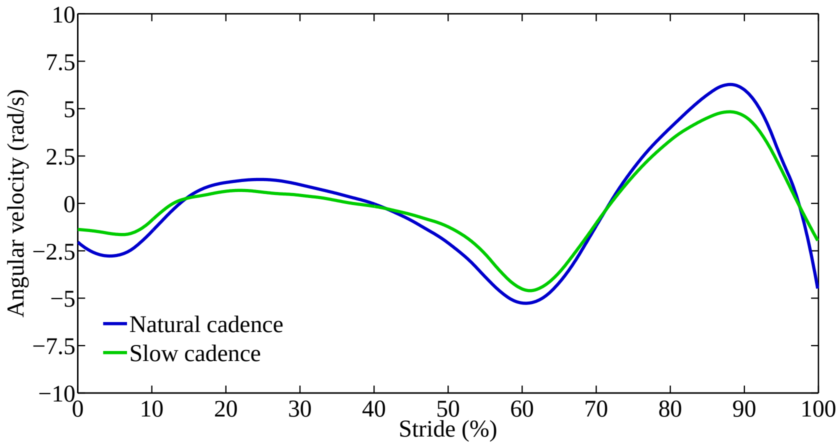

Figure 2.8: Typical angular velocity curves of the knee joint at natural (4.8km/h, blue) and slow cadence (3.6 km/h, green). Data based on gait analysis data from Winter (1991).

and power requirements in the sagittal plane. Second, this data has been used in several other human lower limb exoskeleton designs (see for instance Chu et al. (2005); Veneman et al. (2007)), which provides a reference for comparison.

For easier interpretation, the moment and angle data are combined into a moment-angle cycle, as illustrated by fig. 2.6. Here, the different gait phase transitions (see 2.2.1) and related stride percentages indicate how the cycle elapses in time. Figure 2.7 shows the average moment-angle cycles of an unimpaired subject with a body weight of $90\,kg$ at natural (blue) and slow cadence (green). For both cycles each of the four combinations of $[\theta_k \pm \sigma_{\theta_k}, \tau_k \pm \sigma_{\tau_k}]$ have been added to illustrate the natural variability of the data, where σ_{θ_k} and σ_{τ_k} are the standard deviations of the knee joint angle and of the knee joint moment respectively.

On this basis the required maximal actuator torque has been chosen as an envelope enclosing the majority of moment-angle cycles for slow cadence of a subject with about a 95th percentile body weight ($90\,kg$) of the Belgian population. The actuator system should allow for a joint range of motion of 90°. Angular velocity amplitudes are typically in a range of $[0 - 10]\,rad/s$, as can be seen in fig. 2.8. According to a Fourier analysis of the torque curves depicted in fig. 2.5 the peak torques occurring during limb loading at about 15% of stride can be accurately captured by a fifth order Fourier series, indicating that large knee joint torques have frequencies up to 5 times the fundamental walking frequency. For 95th percentile body weight and slow walking this implies torques up to $50\,Nm$ (peak-to-peak) at frequencies up to $3.5\,Hz$ and for normal walking $70\,Nm$ (peak-to-peak) at $4.5\,Hz$. The actuator system should be capable of generating such torques. Similar torque requirements based on gait analysis are reported in Veneman et al., 2005.

In view of compactness, the actuators should fit in a bounding box of approximately $(0.30\,m \times 0.20\,m \times 0.10\,m)$ along the upper leg between the knee joint and the hip joint. Anthropometric data (NASA, 1978) was used as a reference for human body dimensions and constraints.

2.3.2 PPAM

2.3.2.1 Introduction

A pneumatic artificial muscle (PAM), also called a fluidic muscle, an air muscle or pneumatic muscle actuator, is a contractile linear actuator operated by gas pressure. Its core element is a reinforced closed membrane that expands radially and contracts axially when inflated with pressurised air. Hereby the muscle generates a uni-directional pulling force along the longitudinal axis.

Over the years, different types have been developed. The McKibben muscle (Schulte (1961); Caldwell et al. (1995); Chou and Hannaford (1996)) is the most well known type, and it is commercially available with different companies (Shadow Robot Company, Merlin Systems Corporation, Hitachi Medical Corporation and

Figure 2.9: Second generation pleated pneumatic artificial muscle (PPAM) at three different states of contraction

Festo). It consists of a rubber tube, which expands when inflated, surrounded by a netting that transfers tension. The McKibben muscle has some important drawbacks: moderate capacity of contraction (limited to 20% to 30% of its initial length), hysteresis as a result of friction between the outer sleeve and the rubber tube, and the presence of a threshold pressure, under which no contraction occurs.

Daerden (1999) developed a new PAM, the Pleated Pneumatic Articial Muscle (PPAM, Daerden and Lefeber (2001, 2002)), to remedy some of these disadvantages. The PPAM has a folded membrane that unfolds as it expands. Because of the unfolding, there is virtually no threshold pressure and there is a strong reduction of energy losses in comparison to other muscle types. It can develop higher forces and it can reach higher levels of contraction (up to 40% of the muscle's maximum length). Since it can contract more along its longitudinal axis than a McKibben muscle, the PPAM expands more radially as well, which is a disadvantage, since one generally seeks to maximise the compactness of the actuator system. The main disadvantage of the PPAM is that it is not commercially available, but self-built and mainly handmade. The manual production process is a source of variations in quality and durability. Verrelst et al. (2006a) have developed a second generation of the PPAM to extend its lifespan and to simplify the construction process of the muscles. Figure 2.9 shows three different states of contraction of a (second generation) PPAM. The membrane (black) is made of a flexible, woven polyester fabric, made airtight by a polymer liner. Each pleat contains a strand of high modulus Kevlar® fibre (yellow), a para-aramid synthetic fibre. As the pressure inside the device is increased, the pleats in the membrane unfold and it expands radially. The Kevlar® fibre strands in the pleats, which are being pushed away from the muscle's longitudinal axis by the expanding membrane, translate this radial expansion into a longitudinal contraction. More recently a third generation design has been developed that further reduced the construction time and the complexity of the fabrication process (Villegas et al., 2010).

The PPAMs used in this work adopted the second generation design, but they have integrated end fittings dedicated to the application to cope with restrictions of space.

2.3.2.2 Characteristics

Mathematical models of the PPAM's characteristics have been developed by Daerden and Lefeber (2001) and further refined and experimentally validated by Verrelst et al. (2006a). Although providing a detailed basis, these models are quite comprehensive and their outcome is not readily applicable to the design and control of PPAMs in a black-box fashion. In what follows the most straightforward model, i.e. assuming membrane and fibre inelasticity and neglecting the weight of the muscle's moving parts, will be used to determine the PPAM's characteristics of interest to the design procedure explained in this chapter and the control strategies described in the next chapter.

To obtain the model solution that relates the geometry of the muscle's membrane to muscle characteristics such as the exerted force, the enclosed volume and the maximal diameter, the following set of equations needs to be solved:

$$\frac{E(\varphi_R \setminus m) - \frac{1}{2}F(\varphi_R \setminus m)}{\sqrt{m}\cos\varphi_R} = \frac{l_0}{2R}(1-\varepsilon) \tag{2.4}$$

$$\frac{F(\varphi_R \setminus m)}{\sqrt{m}\cos\varphi_R} = \frac{l_0}{R} \tag{2.5}$$

in which $E(\varphi_R \setminus m)$ and $F(\varphi_R \setminus m)$ stand for elliptical integrals of the first and second kind, l_0 is the muscle's uncontracted length (or maximal length), R is its radius in uncontracted state (or minimal radius) and ε is the muscle contraction - if one denotes the muscle length by l - defined by

$$\varepsilon = \frac{l_0 - l}{l_0} = 1 - \frac{l}{l_0}. \tag{2.6}$$

Note that these geometrical properties are attributed to the muscle membrane and not to the entire PPAM including end fittings. The ratio of maximal length to minimal radius l_0/R, appearing in the equations above, is called "slenderness". The model solution is parameterised in φ_R and m and these model parameters also appear in the analytic expressions that the model provides for muscle force, volume and maximal diameter as will be shown in the following paragraphs. The set of equations 2.4-2.5 needs to be solved numerically for φ_R and m, given a certain muscle geometry defined by the slenderness l_0/R and given a certain contraction ε. The values obtained for φ_R and m can then be substituted into each of the analytic expressions. For a better understanding, consider a characteristic

$$Y = Y(\varphi_R, m, R, l_0) \tag{2.7}$$

that is generally a function of muscle geometry parameters l_0 and R, model parameters φ_R and m, and some other quantities (e.g. internal pressure), depending on the specific characteristic under study, which are not explicitly written here. Since eq.2.4-2.5 holds, eq. 2.7 can be written as

$$Y = Y(\varphi_R(\varepsilon, \frac{l_0}{R}), m(\varepsilon, \frac{l_0}{R}), R, l_0). \tag{2.8}$$

As shown in Daerden and Lefeber (2001), Y can be reformulated by introducing a dimensionless characteristic function y_0, depending exclusively on contraction and slenderness. Regrouping the other quantities in Y' , having the same dimension as Y, leads to

$$Y = Y' y_0(\varepsilon, \frac{l_0}{R}). \tag{2.9}$$

As a result PPAMs with identical slenderness have, apart from the scale factor Y', identical characteristics as a function of contraction. Because the dependency on ε and l_0/R cannot be written directly in analytical form, evaluating the characteristics of a PPAM in the design stage requires numerically solving eq. 2.4-2.5 at each ε for the muscle geometry under study. The design stage aims at selecting the appropriate muscle geometry that meets the requirements expressed in terms of the characteristics of interest. Once the muscle geometry (l_0/R) has been selected, the dimensionless characteristic functions are approximated by $y_0(\varepsilon)$, a sum of power functions. In this work the fitting function has the following form

$$y_0(\varepsilon) = y_1 + y_2\varepsilon^{-2} + y_3\varepsilon^{-1} + y_4\varepsilon + y_5\varepsilon^2 + y_6\varepsilon^3 + y_7\varepsilon^4. \tag{2.10}$$

The coefficients $y_1 \ldots y_7$ are determined by fitting eq. 2.10 to the theoretical $y_0(\varepsilon)$ or to measured data. By doing so, the characteristics are easier to handle and evaluate in the modelling stage and the control stage. The muscle characteristics of interest to this work and explained in what follows are: the muscle's exerted force, the volume enclosed by the muscle, the maximal diameter of the muscle and the muscle's compliance.

Force When neglecting the work needed to deform the membrane's material (very low for a PPAM due to its pleated structure) and the force needed to overcome the inertia of the muscle's moving parts (generally very low compared with the inertia of the load), the force generated by a pneumatic artificial muscle can be written as (Daerden (1999))

$$F = -p\frac{dV}{dl}. \tag{2.11}$$

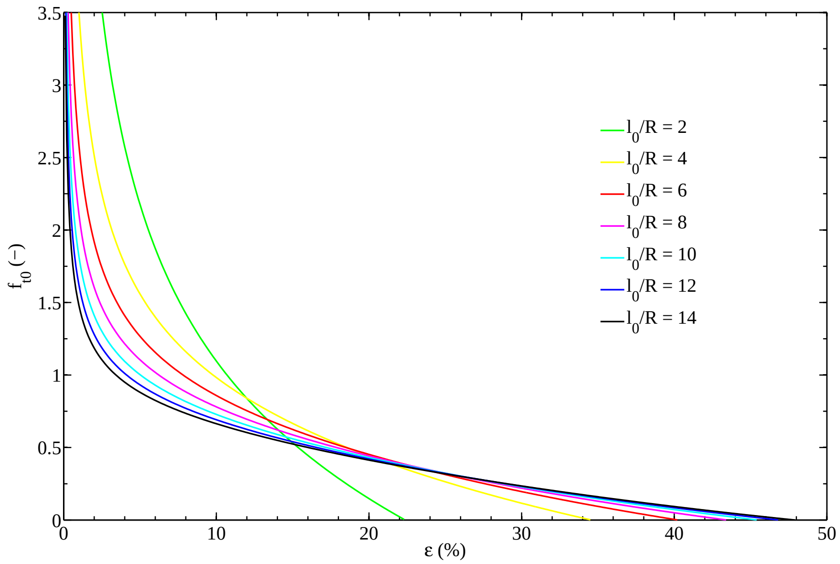

Figure 2.10: Dimensionless force f_{t0} as a function of contraction ε for different values of slenderness l_0/R.

In this expression, p is the gauge pressure inside the muscle, dV the infinitesimal change of the muscle volume (the volume enclosed by the membrane), and dl the change in actuator length. The volume of the actuator increases with decreasing length until a maximal volume is reached. At this point, which corresponds to maximal contraction, the force becomes zero. At low contraction forces tend to be very high. The fact that the force changes as a function of contraction is an essential difference between the pneumatic muscle and the pneumatic cylinder. The force generated by a pneumatic cylinder at gauge pressure p is proportional to the piston area inside the device. Since the piston area is constant, the force does not change with piston position. A pneumatic muscle can be considered as a pneumatic cylinder with varying piston area (equal to $-dV/dl$).

The mathematical model as extended by Verrelst et al. (2006a) yields the following formula for the static muscle force:

$$F = p\frac{n}{2\pi}\sin(\frac{2\pi}{n})R^2\frac{1-2m}{2m\cos^2\varphi_R}. \tag{2.12}$$

In this expression, p is the applied gauge pressure, n the number of fibre strands and φ_R and m are the parameters in which the model solution is parameterised. The influence of the number of fibre strands decreases with increasing n, since $\lim\limits_{n\to\infty}\frac{n}{2\pi}\sin(\frac{2\pi}{n}) = 1$. If n is higher than 30 for instance, its influence comes down to less than 1%. Because of this, the dependence on n is usually not explicitly

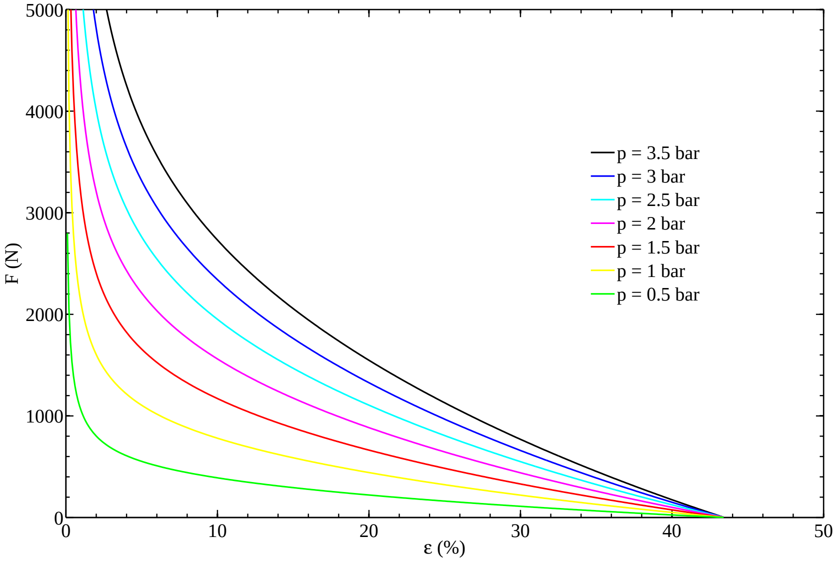

Figure 2.11: Force exerted by a PPAM with $l_0/R = 8$ and $l_0 = 0.1\,m$ as a function of contraction ε for different gauge pressures p.

written. By introducing a nonlinear, dimensionless force function f_{t0} eq. 2.12 is reformulated as

$$F = pl_0^2 f_{t0}(\varepsilon, \frac{l_0}{R}). \tag{2.13}$$

f_{t0} is shown in figure 2.10 for different values of slenderness. As expected, figure 2.10 and eq. 2.13 show there is a varying force-displacement relation at constant gauge pressure, with high forces being generated at low contractions and very low forces at high contractions. This can be seen in fig. 2.11 for a muscle with $l_0/R = 8$, $l_0 = 0.1$ and $n = 32$. For a PPAM with a specific slenderness f_{t0} is approximated by

$$f_{t0}(\varepsilon) = f_1 + f_2\varepsilon^{-2} + f_3\varepsilon^{-1} + f_4\varepsilon + f_5\varepsilon^2 + f_6\varepsilon^3 + f_7\varepsilon^4. \tag{2.14}$$

Since low contractions correspond to very high forces (see fig. 2.11), contraction is kept above a certain minimum - typically about 5% - in order to avoid excessive material loading. For the same reason, and in order to ensure sufficient lifespan for the actuators, gauge pressures have to be limited. Although in this work a conservative limit of $3.5\,bar$ (or $350\,kPa$) is chosen, the PPAM can generally withstand pressures of up to $4.5\,bar$ (or $450\,kPa$), which is lower than the industrially used 6 to $10\,bar$.

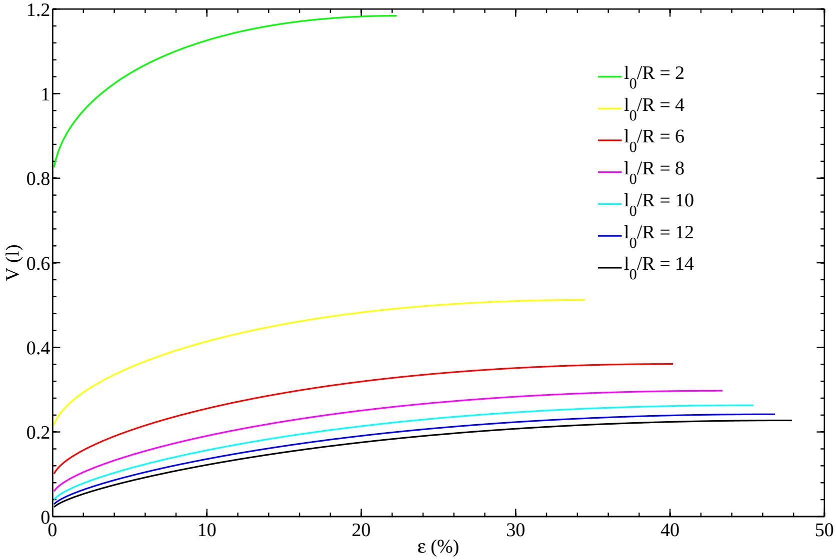

Figure 2.12: Volume enclosed by a PPAM with $l_0 = 0.1m$ as a function of contraction ε for different values of slenderness l_0/R.

Volume Since the enclosed volume of a pneumatic muscle changes with contraction, the pressure regulating servo valves continuously have to adjust the airflow in or out of the muscle in order to keep the gauge pressure at the desired value. In order to model this interaction as well as to calculate additional characteristics such as compliance, it is necessary to know the volume of the muscle. Analogously, by introducing a nonlinear, dimensionless volume function v_0 the formula parameterised in φ_R and m is reformulated as

$$V = l_0^3 v_0(\varepsilon, \frac{l_0}{R}). \tag{2.15}$$

For a PPAM with a specific slenderness v_0 is approximated by

$$v_0(\varepsilon) = v_1 + v_2\varepsilon^{-2} + v_3\varepsilon^{-1} + v_4\varepsilon + v_5\varepsilon^2 + v_6\varepsilon^3 + v_7\varepsilon^4. \tag{2.16}$$

The enclosed volume V as given by eq. 2.15 is shown in fig. 2.12 for a PPAM with $l_0 = 0.1$ and different values of slenderness.

Diameter The central diameter of the pneumatic muscle determines the bounding box to be respected when integrating the actuator in the design of the structure. Contact of the membrane with the surrounding structure should be avoided at the

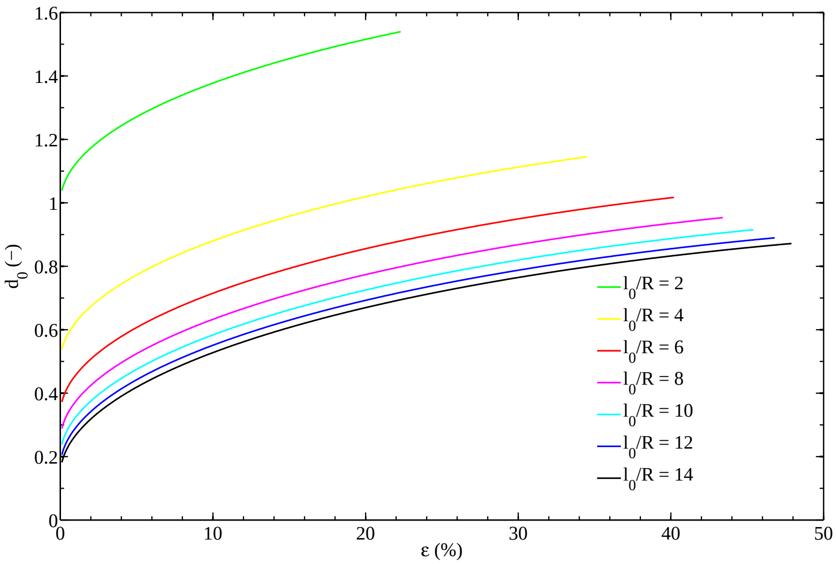

Figure 2.13: Dimensionless diameter d_0 as a function of contraction ε for different values of slenderness l_0/R.

risk of wear and rupture of the membrane. The central diameter is written

$$D = l_0 d_0(\varepsilon, \frac{l_0}{R}) \tag{2.17}$$

and the dimensionless function d_0, relating this diameter to a percentage of the muscle's uncontracted length l_0, is approximated by

$$d_0(\varepsilon) = d_1 + d_2\varepsilon^{-2} + d_3\varepsilon^{-1} + d_4\varepsilon + d_5\varepsilon^2 + d_6\varepsilon^3 + d_7\varepsilon^4. \tag{2.18}$$

Figure 2.13 shows d_0 at different values of slenderness. The characteristics of the different muscle geometries are shown up to their feasible maximal contraction. The overall - i.e. over the entire range of operation - maximal diameter of the PPAM depends on the maximal contraction level attainable in the specific application.

Compliance The compliance, and its inverse the stiffness, of the PPAM can be calculated from eq. 2.13. Defining the mechanical stiffness as the derivative of the amplitude of the restoring force F exerted by the PPAM on its end point with respect to the displacement x of that point, written as

$$k = \frac{dF}{dx},$$

one obtains

$$k = -\frac{dF}{d\varepsilon}\frac{1}{l_0} \tag{2.19}$$

$$= -\frac{dp}{d\varepsilon}l_0 f_{t0} - pl_0\frac{df_{t0}}{d\varepsilon}. \tag{2.20}$$

The sign convention is such that a positive stiffness implies a restoring force amplitude that increases with displacement. Eq. 2.20 shows two distinct contributions to compliance, namely the change of pressure with contraction and the varying force-contraction characteristic. Given a certain muscle geometry the only way to achieve a specific compliance is by controlling the variation of gauge pressure with contraction. The PPAM's passive compliance (or intrinsic compliance) will be observed in the absence of pressure control (e.g. if the valves are closed) or if the air flow dynamics are much slower than the dynamics of the muscle's end point.

If one considers the case of "closed" valves, in which the gauge pressure is not being controlled by inlet or outlet flow, the pressure inside the muscle is related to the muscle volume. In Vanderborght et al. (2008b) and Vanderborght et al. (2006a) a model has been experimentally validated that describes this relationship as a polytropic compression/expansion governed by

$$PV^n = c \tag{2.21}$$

with the absolute pressure denoted by $P = P_{atm} + p$, the polytropic coefficient denoted by n (in isentropic conditions $n = 1.4$ for dry air at room temperature) and c a constant throughout the polytropic process. Starting from eq. 2.21 one obtains

$$\begin{aligned}
\frac{dP}{d\varepsilon} &= \frac{d(cV^{-n})}{d\varepsilon} \\
&= PV^n\frac{dV^{-n}}{d\varepsilon} \\
&= PV^n(-n)V^{-(n+1)}\frac{dV}{d\varepsilon} \\
&= -nP\frac{1}{V}\frac{dV}{d\varepsilon}
\end{aligned}$$

and taken into account that $P = P_{atm} + p$ and that eq. 2.15 holds, this results in

$$\frac{dp}{d\varepsilon} = -n(P_{atm} + p)\frac{1}{v_0}\frac{dv_0}{d\varepsilon}. \tag{2.22}$$

The intrinsic stiffness characteristic of a PPAM is thus defined by

$$k = nl_0 f_{t0}(P_{atm} + p)\frac{1}{v_0}\frac{dv_0}{d\varepsilon} - pl_0\frac{df_{t0}}{d\varepsilon}. \tag{2.23}$$

The derivatives $\frac{dv_0}{d\varepsilon}$ and $\frac{df_{t0}}{d\varepsilon}$ are calculated by taking the derivative of equations 2.4-2.5, solving them for $\frac{d\varphi_R}{d\varepsilon}$ and $\frac{dm}{d\varepsilon}$ by means of symbolic mathematics software, and substituting these expressions in the derivative of $v_0(\varphi_R, m)$ and $f_{t0}(\varphi_R, m)$ (see eq. 2.12 for f_{t0}) with respect to ε. For a PPAM with specific slenderness $\frac{dv_0}{d\varepsilon}$ and $\frac{df_{t0}}{d\varepsilon}$ are approximated by a polynomial function as given by eq. 2.10. It is important to note that eq. 2.23 describes the "intrinsic" stiffness of the PPAM, namely the stiffness that is observed in the absence of pressure control or outside the pressure control bandwidth. Figure 2.14 shows the intrinsic stiffness given by eq. 2.23 as a function of contraction and gauge pressure for a PPAM with $l_0/R = 8$ and $l_0 = 0.1\,m$, while $n = 1.4$ and $P_{atm} = 1\,atm$. As expected, intrinsic stiffness increases linearly with gauge pressure and nonlinearly with decreasing contraction, attaining very high values at low contraction levels. The surface plot gives the instantaneous relationship between intrinsic stiffness on the one hand, and gauge pressure and contraction on the other, but does not show the dependence of gauge pressure on contraction as given by eq. 2.22. The latter is illustrated by the black curve corresponding with starting conditions $p = 1.5\,bar$ and $\varepsilon = 30\%$, and yielding the consecutive intrinsic stiffness values for the PPAM elongated up to 10% contraction under closed valve conditions.

2.3.3 Actuator configuration

Once the characteristics of a single PPAM are known, one should decide on how to configure several PPAMs to power the robotic joint, while taking into account how the configuration of the actuators affects the characteristics of the joint.

2.3.3.1 Series and parallel arrangement

Besides different muscle geometries, one can opt for different arrangements of two or more single PPAMs with the same geometry in series and/or parallel, as illustrated by fig. 2.15a. This option is particularly useful if spatial constraints apply, limiting the maximal diameter and maximal length of the muscles.

The characteristics of the series and parallel PPAMs can be straightforwardly related to the characteristics of their single constituent PPAM. Table 2.1 summarises these relationships, as well as those of a series-parallel combination. The number of single muscles in a series or parallel arrangement is denoted by n_s and n_p respectively and the variables related to the series and parallel PPAM by subscript $\bullet_{n_s}$ and $\bullet_{n_p}$ respectively. Variables without these subscripts are related to the

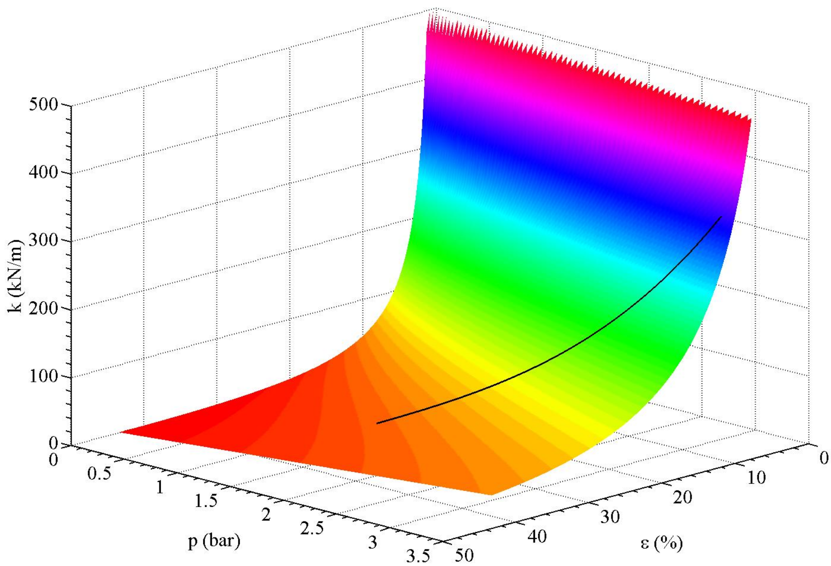

Figure 2.14: Intrinsic stiffness of a PPAM with $l_0/R = 8$ and $l_0 = 0.1m$ as a function of contraction ε and gauge pressure p. The polytropic law relating p to ε is illustrated by the stiffness curve in black for the PPAM elongated from 30% (@ $p = 1.5bar$) up to 10% contraction.

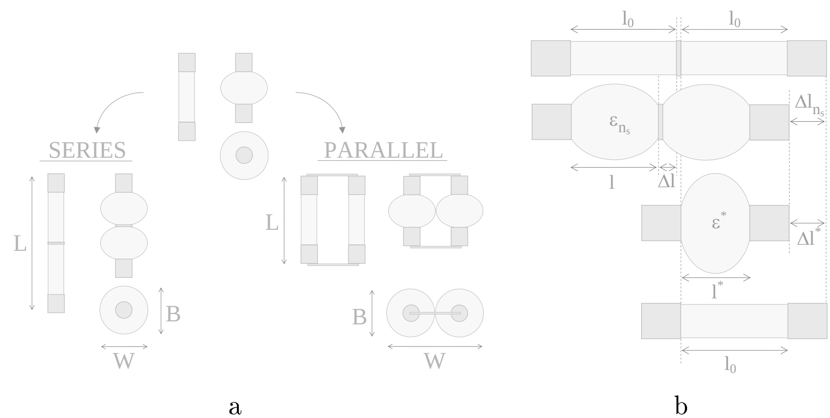

Figure 2.15: a) Series and parallel arrangement of PPAMs, b) series PPAM vs single PPAM at identical stroke ($\Delta l_{n_s} = \Delta l^*$).

	series		parallel	
stroke	Δl_{n_s}	$n_s \Delta l$	Δl_{n_p}	Δl
contraction	ε_{n_s}	$\frac{\Delta l_{n_s}}{n_s l_0}$	ε_{n_p}	$\frac{\Delta l_{n_p}}{l_0}$
force	F_{n_s}	$F(\varepsilon, \frac{l_0}{R})$	F_{n_p}	$n_p F(\varepsilon, \frac{l_0}{R})$
volume	V_{n_s}	$n_s V(\varepsilon, \frac{l_0}{R})$	V_{n_p}	$n_p V(\varepsilon, \frac{l_0}{R})$
stiffness	k_{n_s}	$\frac{1}{n_s} k(\varepsilon, \frac{l_0}{R}, p)$	k_{n_p}	$n_p k(\varepsilon, \frac{l_0}{R}, p)$

	series-parallel	
stroke	$\Delta l_{n_s,n_p}$	$n_s \Delta l$
contraction	ε_{n_s,n_p}	$\frac{\Delta l_{n_s,n_p}}{n_s l_0}$
force	F_{n_s,n_p}	$n_p F(\varepsilon, \frac{l_0}{R})$
volume	V_{n_s,n_p}	$n_s n_p V(\varepsilon, \frac{l_0}{R})$
stiffness	k_{n_s,n_p}	$\frac{n_p}{n_s} k(\varepsilon, \frac{l_0}{R}, p)$

Table 2.1: Formulas relating characteristics of series and parallel PPAMs to the characteristics of their constituent single PPAM.

constituent single PPAM of the arrangement. The most important properties are that a series PPAM exerts the same force as its constituent, having n_s times its stroke, whereas a parallel PPAM exerts n_p times the force of its constituent, while having the same stroke. The advantage of a series PPAM with respect to a single PPAM (with the same geometry as the constituent of the series PPAM) in the case of identical stroke for instance is illustrated by fig. 2.15.b. The series PPAM has the same force-contraction characteristic as the single PPAM (see table 2.1), but at a given stroke it operates at lower contraction levels and thus generates higher forces. This follows from table 2.1:

$$\varepsilon_{n_s} = \frac{\Delta l_{n_s}}{n_s l_0} = \frac{\Delta l*}{n_s l_0} = \frac{1}{n_s} \varepsilon * .$$

At the same time lower contraction levels result in a smaller muscle diameter.

If the application involves spatial constraints in addition to a required force-stroke characteristic, extracting general guidelines for the selection and arrangement of PPAMs becomes considerably more complex. This is due to the dimensions of end fittings and divider rings (depending on muscle geometry and transferred force) and it is also due to the fact that the characteristics of the constituent PPAM depend on muscle geometry. As an example, one can consider a single PPAM and a limit on the muscle's diameter. It can be inferred from eq. 2.17 and fig. 2.13 showing the dimensionless diameter function d_0, that increasing a single muscle's maximal length l_0 by a factor n in order to increase the stroke from $\Delta l \rightarrow n\Delta l$ is only possible at the expense of an increased maximal muscle diameter. Hence, if ε is constant in fig. 2.13 and slenderness l_0/R is increased by n, the decrease of d_0 can not compensate the increase of l_0 in the expression of the diameter D (eq. 2.17). Even if the stroke is kept constant in order to obtain a higher force output

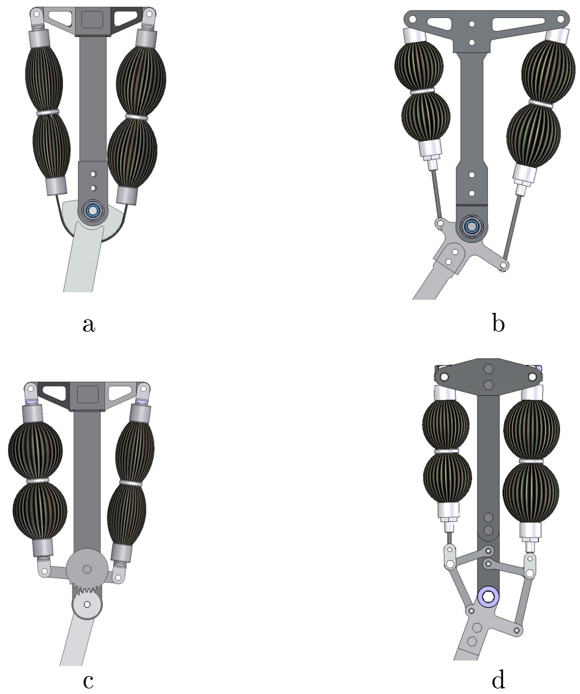

Figure 2.16: Antagonistic configuration of PPAMs with different force transmission mechanisms: a) pulley, b) levers, c) levers and gears, d) four bar linkages.

at the same stroke (dividing ε by n and increasing slenderness l_0/R by n in fig. 2.13), the maximal muscle diameter increases. A series arrangement is the only solution in these cases.

If a limit is imposed on muscle diameter and length, as it is the case in our application, a parallel arrangement is only successful in increasing force output at a given stroke if the bounding box of the muscle arrangement is such that $L \lesssim W$ (see fig. 2.15). If $L \gtrsim W$ holds, a series arrangement is more successful. This follows from the single PPAM generally fitting a cubic bounding box ($L \approx W \approx B$) and from the aforementioned series and parallel PPAM characteristics.

2.3.3.2 Antagonistic configuration & force transmission

Since PAMs are contractile devices, they are single acting actuators. Consequently, to obtain a bidirectionally actuated revolute joint, one has to configure (at least) two single acting PAMs in an antagonistic setup. The actuator force can be transferred to the joint in different ways, determining the characteristics of the powered joint. The two most common and straightforward ways are by using a pulley mechanism (fig. 2.16.a) or a lever (fig. 2.16.b).

In the case of a pulley mechanism, the effective lever arm is constant, equal to the radius of the pulley, so the torque generated by a muscle is proportional to its pulling force. As can be seen in fig. 2.11, the force drops rapidly with contraction, limiting the effective range of operation in which the powered joint produces useful torque. Since the effective lever arm is constant, the muscles exert their force along a fixed direction. This is beneficial for the compactness of the joint, as the muscles can be placed close to the structure.

In the case of a force transmission through a lever a careful selection of the muscle's points of attachment to the structure results in an effective lever arm that increases in length with increasing contraction. In this way the strongly nonlinear force-contraction characteristic can be compensated to some extent and the torque-angle characteristic of the joint can be shaped in a more suitable way. A drawback, however, is that the direction of the force and thus the orientation of the muscles changes with the joint angle. This might raise a conflict with the spatial constraints of the structure, especially if a large angular range of motion is desired.

As mentioned in section 2.3.1 the robotic knee joint should indeed meet stringent requirements, especially the required range of motion (90°) and the bounding box the PPAMs should fit in ($0.30\,m \times 0.20\,m \times 0.10\,m$). It will be shown in the following section that in the particular case of the knee joint using regular levers for force transmission is suboptimal. To ease the trade-off between better matching a required torque-angle characteristic and enhancing compactness the feasibility of an additional transmission was investigated. A simple gear system placed in series as depicted in fig. 2.16.c was not retained for reasons of backlash and friction and because of its fixed transmission ratio. Alternatively, instead of a regular lever combined with an additional transmission mechanism, a four bar linkage placed at either side of the joint was selected as a promising candidate (see fig. 2.16.d). In fact, a four bar linkage can be seen as a regular lever combined with a varying transmission ratio. As will be shown in section 2.3.5, the proposed configuration conveniently combines compactness with good torque shaping capabilities.

2.3.4 Towards an optimised actuator system design

Designing the actuator system boils down to selecting the design parameters of the actuators and the selected actuator configuration such that the characteristics meet the requirements outlined in section 2.3.1. As a best practice, first the antagonistic configuration of PPAMs with regular levers was investigated as an actuator system for a powered exoskeleton. Initially, a suitable design was sought by so called "trial and improvement", relying on the knowledge gained during the design process to find a solution that meets the requirements. This approach may fall short in two aspects:

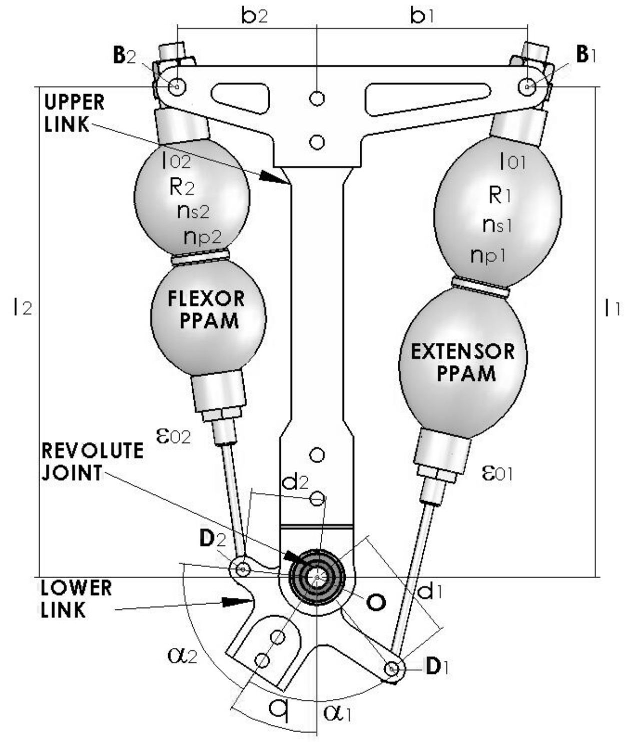

Figure 2.17: Antagonistic configuration of PPAMs with levers: design parameters

- In "challenging" designs, subject to many constraints and involving a large number of design parameters, finding even a feasible solution - if any - is difficult,
- In applications with focus on actuator systems with low weight, slim size and high performance it is worth searching for an optimal design instead of a feasible design.

Therefore the design problem was formulated as a multi-objective optimisation problem and an exhaustive search optimisation technique was used to find an optimal solution.

2.3.4.1 Design by trial and improvement

Design parameters Figure 2.17 shows a schematic drawing of an antagonistic configuration of PPAMs with regular levers. The upper and lower links are interconnected by a revolute joint in O. The actuators operate in a plane perpendicular to the joint axis. For easier interpretation, the actuators are named after their biomechanical counterparts (see section 2.2): "extensor" refers to the actuator on the right side, "flexor" refers to the actuator on the left side. The extensor and flexor PPAM are depicted as series PPAMs ($n_s = 2$), but they can be different series/parallel arrangements in general (see section 2.3.3.1), as long as they are connected with the upper and lower link in the hinging attachment points B_i and D_i respectively ($i = 1$ for extensor side, $i = 2$ for flexor side). For the sake of simplicity, configurations with multiple PPAMs at the same side acting through different sets of attachment points were not considered. Once all mechanical design parameters of the structure are determined, the only remaining degree of freedom is the relative angle between upper and lower link, represented by q. The orientation of the levers $\mathbf{OD_i}$ with respect to the lower link is determined by the angles α_i ($i = 1, 2$). The locations of points B_i and D_i at a certain joint angle q are dependent of the lengths b_i, l_i, d_i and the angles α_i. Hence, the kinematics of the configuration as a function of q is fully defined by the following mechanical parameters: b_i, l_i, d_i, α_i. This leaves the state of the actuators to be determined. As shown in section 2.3.2.2, all characteristics of a single PPAM depend entirely on muscle geometry (l_0, R) and muscle contraction (ε). Series and parallel combinations of PPAMs are defined by n_s and n_p, representing the number of single PPAMs in series and parallel respectively (see section 2.3.3.1). Considering again the antagonistic setup depicted in fig. 2.17, one should note that although the attachment points define the direction of force of each muscle group, their contraction level is still undefined. Setting the contraction levels ε_{0i} at a specific angle q_0 unambiguously defines the relation between ε_i and q. In practice, this is achieved by selecting the appropriate length for each of the connecting rods coupling the muscle group to the attachment points. Thus, contraction ε_i at a certain joint angle q is dependent of ε_{0i} and b_i, l_i, d_i, α_i. In summary, the characteristics of this antagonistic configuration of PPAMs with regular levers are fully defined by the following set of 18 mechanical design parameters, represented by design parameter vector X:

$$X = [l_{01}\ R_1\ n_{s1}\ n_{p1}\ \varepsilon_{01}\ b_1\ l_1\ d_1\ \alpha_1\ l_{02}\ R_2\ n_{s2}\ n_{p2}\ \varepsilon_{02}\ b_2\ l_2\ d_2\ \alpha_2]. \tag{2.24}$$

Torque characteristic As can be seen in fig. 2.17, the extensor PPAM exerts a force, denoted F_1, between point B_1 and point D_1 and hereby generates a moment of force $\mathbf{M}_{O1}$ in O that is given by

$$\mathbf{M}_{O1} = \mathbf{OD}_1 \times F_1\mathbf{e}_1 \tag{2.25}$$

with

$$\mathbf{e}_1 = \frac{\mathbf{OB}_1 - \mathbf{OD}_1}{\|\mathbf{OB}_1 - \mathbf{OD}_1\|}$$

and $\| \cdot \|$referring to the Euclidean norm. Since $\mathbf{OD}_1$ and $\mathbf{e}_1$ are bound to the xy-plane, $\mathbf{M}_{O1}$ only has a z-component, denoted by τ_1 and written as

$$\begin{aligned} \tau_1 &= \mathbf{M}_{O1}\mathbf{1}_z \\ &= F_1(\mathbf{OD}_1 \times \mathbf{e}_1).\mathbf{1}_z \\ &= F_1 r_1 \end{aligned} \tag{2.26}$$

where $r_1 = (\mathbf{OD}_1 \times \mathbf{e}_1).\mathbf{1}_z$ is the lever arm, i.e. the perpendicular distance between the pivot O and the line of action of the actuator force. By substituting F_1 in eq. 2.26 with the general expression of the force exerted by a series-parallel PPAM (see table 2.1 combined with eq. 2.13) one obtains

$$\tau_1 = p_1 l_{01}^2 n_{p1} f_{t01} r_1. \tag{2.27}$$

Since $f_{t01} = f_{t01}(\varepsilon_1(q, \varepsilon_{01}, b_1, l_1, d_1, \alpha_1, n_{s1}), l_{01}/R_1)$ and $r_1 = r_1(q, b_1, l_1, d_1, \alpha_1)$ hold, eq. 2.27 can be rewritten as

$$\begin{aligned} \tau_1 &= p_1 l_{01}^2 n_{p1} f_{t01}(q, l_{01}, R_1, n_{s1}, \varepsilon_{01}, b_1, l_1, d_1, \alpha_1) r_1(q, b_1, l_1, d_1, \alpha_1) \\ &= \tau_1(q, l_{01}, R_1, n_{s1}, n_{p1}, \varepsilon_{01}, b_1, l_1, d_1, \alpha_1), \end{aligned} \tag{2.28}$$

which, once all design parameters have been chosen, simplifies to

$$\tau_1(q) = p_1 l_{01}^2 n_{p1} f_{t01}(\varepsilon_1(q)) r_1(q). \tag{2.29}$$

By introducing a so called "torque function" $m_{\tau 1}(q) = l_{01}^2 n_{p1} f_{t01}(\varepsilon_1(q)) r_1(q)$ eq. 2.29 is further simplified to

$$\tau_1(q) = p_1 m_{\tau 1}(q). \tag{2.30}$$

The function $\varepsilon_1(q)$ can be derived by applying the formula for the contraction of a series-parallel PPAM (see table 2.1):

$$\begin{aligned} \varepsilon_1(q) &= \frac{\Delta l_{n_s, n_p}}{n_s l_0} \\ &= \varepsilon_{01} + \frac{\|\mathbf{OB}_1 - \mathbf{OD}_1\|_{q_0} - \|\mathbf{OB}_1 - \mathbf{OD}_1\|_q}{n_s l_0}, \end{aligned} \tag{2.31}$$

where subscript q_0 and q refer to an evaluation of a function at the respective joint angle.

Analogously, one calculates the torque exerted by the flexor PPAM and, by adding both torque terms, one obtains the total torque $\tau(q)$ exerted by the actuators:

$$\tau(q) = p_1 m_{\tau 1}(q) + p_2 m_{\tau 2}(q). \tag{2.32}$$

Equation 2.32 relates the torque produced by the actuator system at the joint to the gauge pressures of the individual PPAMs. Hence, it is useful if these gauge pressures are considered as the input variables of the system, provided that the torque is the output variable. A key property appearing from this formula is that the output (torque) not only depends on the input (gauge pressures) but also on the joint angle. Alternatively, if one considers the use of the actuator forces as inputs, the torque can be formulated as

$$\tau(q) = F_1 r_1(q) + F_2 r_2(q). \tag{2.33}$$

Since the lever arms change with joint angle, they can be designed such that they compensate the nonlinear force-contraction characteristics of the individual PPAMs. For design purposes, the output torque characteristic, denoted τ_{MAX}, is defined as the maximal torque output provided by the actuator system in both directions. Using the formulation of eq. 2.32, one obtains

$$\tau_{MAX}(q) = \begin{cases} \tau_{1MAX} & = p_{MAX} m_{\tau 1}(q) \\ \tau_{2MAX} & = p_{MAX} m_{\tau 2}(q) \end{cases}, \tag{2.34}$$

where p_{MAX} is the maximal allowable gauge pressure (chosen 3.5 bar in this work).

Compliance characteristic By means of the torque formulas given by eq. 2.33 and eq. 2.32 the stiffness (the inverse of compliance) of the powered joint can be calculated. The mechanical rotational stiffness is defined as the derivative of the amplitude of the restoring torque exerted by the PPAMs on the lower link with respect to the angular displacement of that link and thus given by

$$K = -\frac{d\tau}{dq},$$

which, applied to eq. 2.33, yields

$$K(q) = -\frac{dF_1}{dq} r_1(q) - F_1 \frac{dr_1(q)}{dq} - \frac{dF_2}{dq} r_2(q) - F_2 \frac{dr_2(q)}{dq}. \tag{2.35}$$

The sign convention is such that a positive stiffness implies a restoring torque that increases with angular displacement. The joint stiffness can be related to the stiffness of the individual PPAMs by combining $\frac{dF_i}{dq} = \frac{dF_i}{d\varepsilon_i}\frac{d\varepsilon_i}{dq}$ with eq. 2.19 (see section 2.3.2.2), which yields

$$K(q) = k_1 l_{01} \frac{d\varepsilon_1}{dq} r_1(q) - F_1 \frac{dr_1(q)}{dq} + k_2 l_{02} \frac{d\varepsilon_2}{dq} r_2(q) - F_2 \frac{dr_2(q)}{dq}. \tag{2.36}$$

Equation 2.36 shows two contributions to the stiffness of the joint: the stiffness due to the intrinsic stiffness (k_i) of the PPAMs and the stiffness due to the variation of the lever arms ($\frac{dr_i(q)}{dq}$) with the joint angle. To obtain the stiffness as a function of gauge pressures, one performs an analoguous derivation starting from eq. 2.32, which leads to

$$K(q) = -\frac{dp_1}{dq} m_{\tau 1}(q) - p_1 \frac{dm_{\tau 1}(q)}{dq} - \frac{dp_2}{dq} m_{\tau 2}(q) - p_2 \frac{dm_{\tau 2}(q)}{dq}. \tag{2.37}$$

Considering the case of closed valves, as explained in section 2.3.2.2, in which eq. 2.22 relates gauge pressure to muscle volume, and combining this equation with eq. 2.37 and with $\frac{dp_i}{dq} = \frac{dp_i}{d\varepsilon_i}\frac{d\varepsilon_i}{dq}$ one obtains

$$K(q) = n(P_{atm} + p_1)\frac{1}{v_{01}}\frac{dv_{01}}{d\varepsilon_1}\frac{d\varepsilon_1}{dq} m_{\tau 1}(q) - p_1 \frac{dm_{\tau 1}(q)}{dq} \tag{2.38}$$

$$+n(P_{atm} + p_2)\frac{1}{v_{02}}\frac{dv_{02}}{d\varepsilon_2}\frac{d\varepsilon_2}{dq} m_{\tau 2}(q) - p_2 \frac{dm_{\tau 2}(q)}{dq}, \tag{2.39}$$

where

$$\frac{dm_{\tau i}(q)}{dq} = l_{0i}^2 n_{p1}\left(\frac{df_{t0i}(\varepsilon_i)}{d\varepsilon_i}\frac{d\varepsilon_i}{dq} r_1(q) + f_{t0i}(\varepsilon_i(q))\frac{dr_1(q)}{dq}\right)$$

and, since eq. 2.31 holds,

$$\frac{d\varepsilon_i}{dq} = -\frac{1}{n_s l_0}\frac{d\|\mathbf{OB}_i - \mathbf{OD}_i\|_q}{dq}.$$

By introducing so called “stiffness functions”, namely K_1, K_2 and K_{ATM}, and regrouping terms containing p_1, p_2 and P_{ATM} in eq. 2.38, a more concise formula for the stiffness $K(q)$ can be derived:

$$K(q) = p_1 K_1(q) + p_2 K_2(q) + P_{ATM} K_{ATM}(q). \tag{2.40}$$

As it is the case for the torque $\tau(q)$ (see eq. 2.32), the stiffness of the joint $K(q)$ not only depends on gauge pressures, but on joint angle as well. Equations 2.32 and 2.40 form a set of equations to be solved in order to obtain the required gauge pressures that produce the desired torque and stiffness. Provided an output torque, the joint stiffness is thus adaptable within a certain range, limited by the torque requirement on the one hand and the gauge pressure limit on the other. This adaptable stiffness is a key property of the antagonistic configuration of PPAMs. For design purposes the feasible stiffness range of the powered joint is defined by $K_{MAX}\mid_{\tau_{REQ}}$ and $K_{MIN}\mid_{\tau_{REQ}}$, respectively the maximum and minimum of

$$K = p_1 K_1 + p_2 K_2 + P_{ATM} K_{ATM}$$

subject to

$$\begin{aligned} \tau_{REQ} &= p_1 m_{\tau 1} + p_2 m_{\tau 2} \\ 0 \leq \; p_1 &\leq p_{MAX} \\ 0 \leq \; p_2 &\leq p_{MAX} \end{aligned}$$

which leads to

$$\begin{aligned} K_{MIN} \mid_{\tau_{REQ}} &= \max(0, \frac{\tau_{REQ}}{m_{\tau 1}}).(K_1 - \frac{m_{\tau 1}}{m_{\tau 2}} K_2) + \frac{\tau_{REQ}}{m_{\tau 2}} K_2 \\ &+ P_{ATM} K_{ATM} \qquad (2.41) \\ K_{MAX} \mid_{\tau_{REQ}} &= \min(\frac{\tau_{REQ} - p_{MAX} m_{\tau 2}}{m_{\tau 1}}, p_{MAX}).(K_1 - \frac{m_{\tau 1}}{m_{\tau 2}} K_2) \\ &+ \frac{\tau_{REQ}}{m_{\tau 2}} K_2 + P_{ATM} K_{ATM} \qquad (2.42) \end{aligned}$$

If the required torque τ_{REQ} is equal to the maximal torque output τ_{MAX}, as defined by eq. 2.34, the minimal and maximal stiffness characteristic coincide. Hence, the stiffness range at a given required output torque depends on how close the required torque is to the maximal output torque.

Design procedure To facilitate the design by trial and improvement, a graphical user interface (GUI) was considered indispensable for easy design parameter selection and visualisation of characteristics of the selected muscle arrangement and joint configuration. The GUI was conceived to be also used for joints (e.g. ankle, hip) other than a powered robotic knee joint. Figure 2.18 shows the main GUI window containing:

A PPAM input fields: $l_{01}, R_1, n_{s1}, n_{p1}, l_{02}, R_2, n_{s2}, n_{p2}$ determine PPAM geometry

B PPAM numeric output : construction parameters for the selected PPAM geometry, i.e. required number of fiber strands, fibre radius, fibre bond length in the end fittings, membrane fold depth

C PPAM graphical output : dimensionless force function $f_{t0}(\varepsilon)$, individual muscle diameter $D(\varepsilon)$, total volume $V(\varepsilon)$, dimensionless stress function $s_0(\varepsilon)$

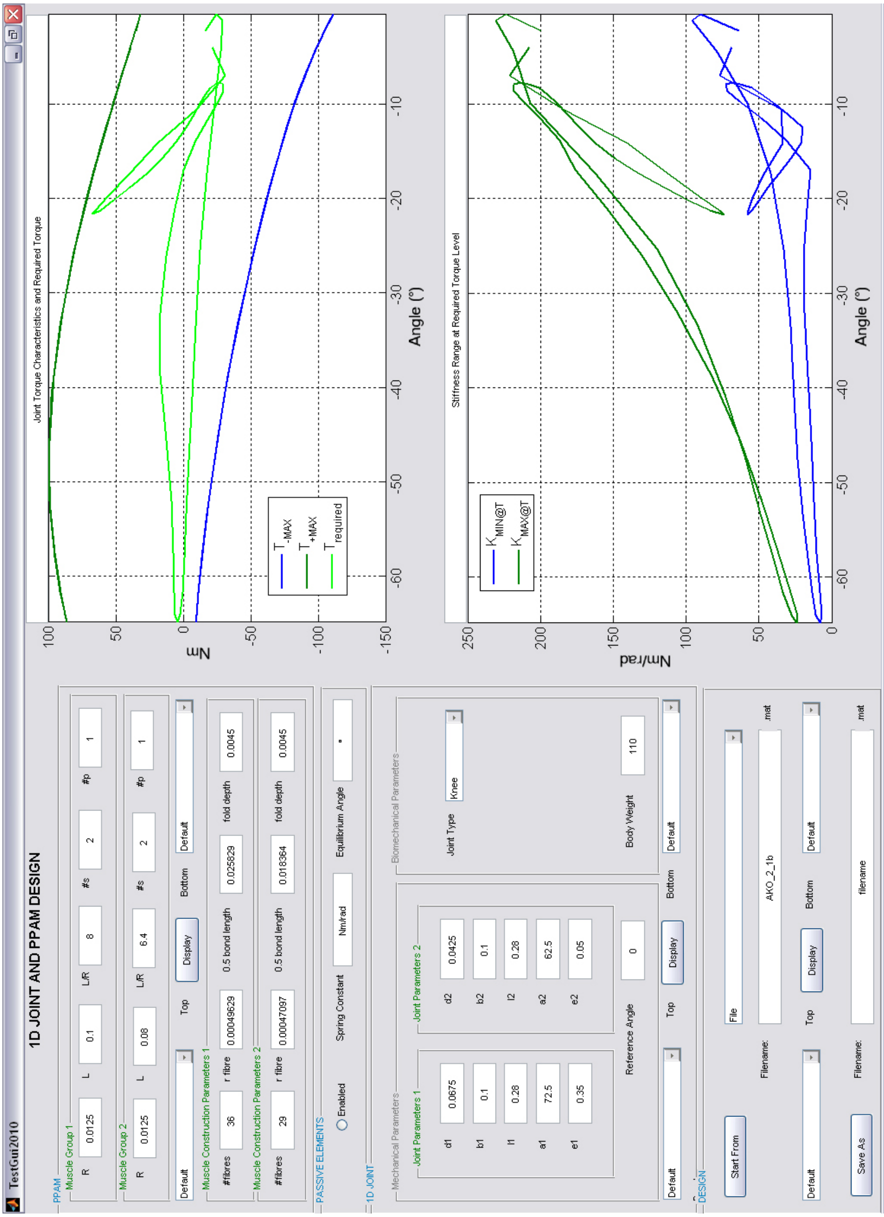

Figure 2.18: Graphical user interface for design by trial and improvement of a PPAM actuator system with levers.

D PPAM optional input fields: spring constant and reference angle of a linear torsion spring to investigate the benefit of a passive element in parallel with the PPAMs

E Configuration input fields: $\varepsilon_{01}, b_1, l_1, d_1, \alpha_1, \varepsilon_{02}, b_2, l_2, d_2, \alpha_2$ and the reference angle q_0 related to ε_{0i} determine the configuration of the PPAMs

F Configuration graphical output: torque functions $t_i(q)$, lever arms $r_i(q)$, contraction levels $\varepsilon_i(q)$, stiffness functions $K_i(q)$ and $K_{ATM}(q)$, $d\varepsilon_i(q)/dq$, $dr_i(q)/dq$

G Actuator system input fields: required torque-angle characteristic based on normalised gait analysis data (Nm/kg) from Winter (1991), body weight (kg).

H Actuator system graphical output: torque characteristic (see eq. 2.34), stiffness characteristic (see eq. 2.41-2.42)

Alongside the use of this GUI a CAD model of the configuration is used to verify practical feasibility and to check for spatial constraints. It became clear from this process that finding a design solution that merely complies with the constraints is a challenge. Also, feasible solutions can possibly be improved. The configuration displayed in fig. 2.18 shows a high extensor torque output at large flexion angles, where it is indeed not required. An optimisation approach based on design objectives and taking into account design constraints would lead more quickly to feasible design solutions and also better solutions in terms of the objectives. Since different design objectives are relevant here, the design problem is formulated as a multi-objective optimisation problem.

2.3.4.2 Design as a multi-objective optimisation problem

The multi-objective optimisation (MOO) problem related to the configuration with regular levers is formulated as follows:

Find $X = [l_{01}\ R_1\ n_{s1}\ n_{p1}\ \varepsilon_{01}\ b_1\ l_1\ d_1\ \alpha_1\ l_{02}\ R_2\ n_{s2}\ n_{p2}\ \varepsilon_{02}\ b_2\ l_2\ d_2\ \alpha_2]$

To minimise $O(X) = [O_1(X)\ \ldots\ O_n(X)]$

Subject to $C(X) = [C_1(X)\ \ldots\ C_m(X)]$,

where X is the vector of design parameters (see eq. 2.24), $O(X)$ is the vector of n objective functions and $C(X)$ is the vector of m constraint functions. The following objective functions to be minimised were considered:

- $O_1(X) = (\tau_{MAX} - \tau_{REQ})$: the root mean square of the difference between the required and the maximal torque output characteristic. By minimising torque overdimensioning, one can scale down actuator dimensions and decrease structural loading for those areas of operation where the actuator systems shows overperformance.

- $O_2(X) = (D_i)_{MAX}$: the maximal diameter of the PPAMs over the range of operation. Minimising the maximal diameter should increase compactness of the configuration and penalise operation of the PPAMs at large contraction levels, corresponding to low output forces.
- $O_3(X) = (F_i)_{MAX}$: the maximal force exerted by the PPAMs over the range of operation. Since the maximal load on the structure determines the minimal cross section of its components, minimising this load should decrease the weight of the structure and increase compactness.
- $O_4(X) = 1/(K_{MAX})_{MEAN}$: the compliance based on the maximal joint stiffness averaged over the range of operation. Since the use of compliant actuators is rather new in the field of rehabilitation robotics, no detailed guidelines exist on how to design actuators for compliance in such applications. Moreover, these guidelines should address the passive compliance, intrinsic to the actuator, as well as the active compliance resulting from control. Rather than investigating this topic in a prior simulation study, it was decided to address it in a more pragmatic way in actual experiments with the device in test subjects. Therefore, maximising the stiffness range of the powered joint, regardless of any torque requirement, was considered a sensible choice.

Several constraints, mainly spatial in nature, have to be taken into account. The following constraint functions were considered:

- $\| \tau_{MAX} \| \geq \| \tau_{REQ} \|$: the maximal torque characteristic should exceed or at least coincide with the required torque characteristic.
- $\| r_i \| \geq r_{min}$: singular actuator configurations ($r_i = 0$) may not occur in the range of operation and, more conservatively, the lever arm should be large enough to prevent spatial obstruction.
- $\varepsilon_{i,MIN} \leq \varepsilon_i \leq \varepsilon_{i,MAX}$: contraction has a lower and upper bound. The lower bound is typically about 5% , the upper bound, at which forces drop too low, depends on muscle slenderness, as can be seen in fig. 2.10 in section 2.3.2.2.
- other spatial constraints: e.g. the PPAMs should fit in a predetermined bounding box and may not be obstructed. These constraints were also verified with the CAD model of the configuration.

The fact that there are multiple objectives and constraints, generally nonlinear in the design parameters, make this MOO problem complex and hard to solve.

Typically, optimisation techniques for solving MOO problems are based on scalarisation of the objective function vector $O(X)$ (Miettinen, 1999). The different objectives are combined into one single objective, for instance by linear combination,

	l_{01}	R_1	n_{s1}	n_{p1}	ε_{01}	α_1	d_1	l_1	b_1
	(m)	(m)	(-)	(-)	(%)	(°)	(m)	(m)	(m)
Δx_k	0.002	0.001	1	1	1	1	0.001	0.001	0.001

Table 2.2: Parameter resolution values as used in sensitivity calculations shown in fig. 2.19.

after which single objective optimisation techniques can be used. A drawback of scalarisation is that it requires prior knowledge of the designer about the problem (on what basis will preferences between objectives be pointed out ?) and that problem simplification comes at the cost of loss of information (potential solutions might be missed out). Another aspect of importance is the discrete nature of the design parameters. The solution of a continuous MOO problem might provide parameter values for muscle geometries that are difficult to realize in practice. Discretisation of these parameters gives the designer control over the feasible solutions. For each combination of discrete parameters a continuous optimisation problem in the remaining parameters could then be solved. Although it comes at the cost of reduced optimality, it was decided to discretise the entire solution search space in order to avoid prior scalarisation and the MOO problem was solved by means of exhaustive search optimisation.

2.3.4.3 Exhaustive search optimisation

Exhaustive search, also known as brute-force search or direct search, is a straightforward technique that consists of generating all possible solutions to a problem defined in a discretised search space. Unlike metaheuristics (e.g. genetic algorithms, simulated annealing, differential evolution (Blum and Roli, 2003)), techniques that are used for combinatorial optimisation in a discrete search space, exhaustive search is not aimed at iteratively trying to find a more optimal solution, but at enumerating all optimal solution candidates. This technique is computationally expensive as computation time is roughly proportional to the number of solutions. For large size problems, characterised by a large (number of parameters) and dense (parameter resolution) search space, and for problems with costly objective function evaluations, reducing the search space is mandatory. Here, this was done in three ways: by reducing the number of parameters, narrowing the parameter bounds and adapting the discrete step size.

Search space reduction Close inspection of the objective and constraint functions reveals that the MOO problem, as formulated in section 2.3.4.2, can be reformulated as two separate MOO problems, one for the extensor side and one for the flexor side of the actuator system. This can be inferred from the fact that minimising $(\tau_{MAX} - \tau_{REQ})_{RMS}$ is equivalent to minimising $(\tau_{1,MAX} - \tau_{1,REQ})_{RMS}$ together with $(\tau_{2,MAX} - \tau_{2,REQ})_{RMS}$, and that minimising $1/(K_{MAX})_{MEAN}$ is

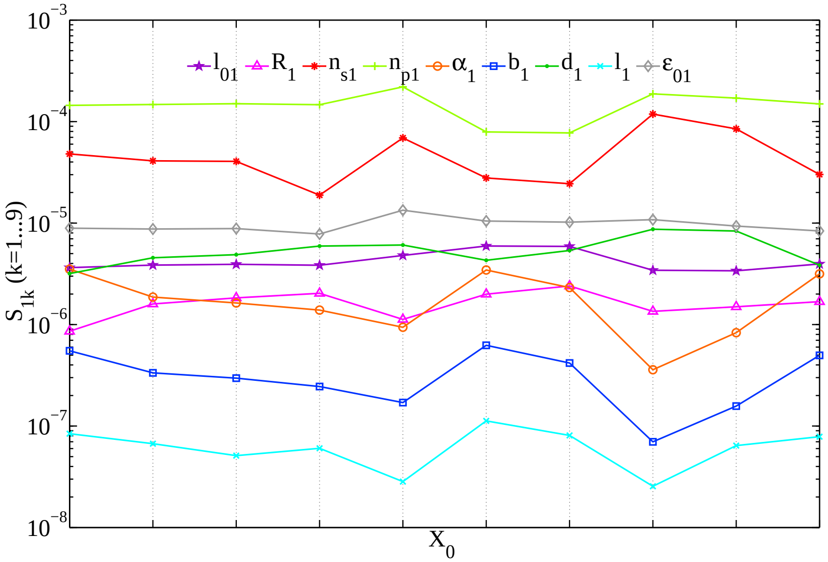

Figure 2.19: Scaled sensitivity S_{1k} of objective function O_1 with respect to the design parameters x_k $(k = 1\ldots9)$ in different points X_0 of the search space.

equivalent to minimising $1/(K_{1,MAX})_{MEAN}$ together with $1/(K_{2,MAX})_{MEAN}$. The constraint $\| \tau_{MAX} \| \geq \| \tau_{REQ} \|$ becomes $\| \tau_{i,MAX} \| \geq \| \tau_{i,REQ} \|$. If one considers the original number of points of the 18 dimensional discretised search space, N_{18}, and assumes a fixed parameter step size, one indeed obtains a significant search space reduction by splitting the problem in two subproblems defined in a 9 dimensional search space. Hence, the new number of points $N_{2\times9}$ relates to N_{18} as given by $N_{2\times9} = 2\sqrt{N_{18}}$. Each MOO subproblem is now designated to a design parameter vector $X_i = [l_{0i}\ R_i\ n_{si}\ n_{pi}\ \varepsilon_{0i}\ b_i\ l_i\ d_i\ \alpha_i]$. The remaining procedure, explained in what follows, applies to each of the subproblems, unless noted otherwise.

After problem decomposition a sensitivity analysis was performed to evaluate the relative effect of design parameter changes on the objective functions and eliminate non-dominating parameters from the parameter vector. The sensitivity of the objective functions to parameter variations can be assessed locally by observing the partial derivatives of the objective function with respect to those parameters, evaluated in a fixed point in the search space. To enable mutual comparison, the partial derivatives are multiplied by a scale factor, the design parameter resolution, which yields a "scaled" sensitivity. This scaled sensitivity, denoted by S_{jk}, of the objective function O_j $(1 \leq j \leq n)$ to variations of design parameter x_k $(x_k \in X)$ at a point X_0 of the search space is thus given by:

$$S_{jk} = \Delta x_k \left| \frac{\partial O_j}{\partial x_k} \right|_{X_0}, \tag{2.43}$$

with Δx_k the resolution of design parameter x_k and $|\cdot|_{X_0}$ denoting evaluation at point X_0. In the case of O_1, O_3 and O_4 the partial derivative in eq. 2.43 was calculated by means of symbolic mathematics software. In the case of O_2 a first order approximation was calculated numerically. Figure 2.19 shows the scaled sensitivities of objective function O_1 in ten different points of the search space, based on the parameter resolution values listed in table 2.2. Based on these results, l_i and b_i have been excluded from the parameter vector X_i. Parameters n_{si} and n_{pi} were also excluded for two reasons. They can only take a limited number of integer values because of spatial constraints and more importantly their value greatly affects feasible bounds for the remaining parameters l_{0i}, R_i , ε_{0i} , d_i , α_i. These parameter bounds can thus be tailored to each specific subproblem.

In summary, after problem decomposition and search space reduction, an exhaustive search needs to be performed, given a feasible parameter set $[n_{si} n_{pi} b_i l_i]$, for the set of remaining parameters $[l_{0i}\, R_i\, \varepsilon_{0i}\, d_i\, \alpha_i]$. Since all dimensionless characteristics of the PPAM depend on the muscle's slenderness l_0/R the set $[l_{0i}\; l_{0i}/R_i\; \varepsilon_{0i}\; d_i\; \alpha_i]$ was used instead. By approximating these characteristics by fitting functions (see eq. 2.10 in section 2.3.2.2) for each value of slenderness prior to optimisation, the computation time of the optimisation routine is drastically reduced.

Exhaustive search procedure In the exhaustive search process, parameter combinations are generated iteratively, according to the step size and within the parameter bounds. Each combinatorial candidate is checked for constraint violations. Afterwards, the obtained set of valid solutions can be searched for solutions that are optimal in terms of the objectives. In the field of multi-objective optimisation various definitions of optimality exist (Ehrgott and Gandibleux (2000)). Here Pareto optimality was used as a criterion. A solution is Pareto optimal if no other solution exists that is at least better at one objective and not worse at the other objectives. The set of Pareto optimal solutions thus contains only "non-dominated" solutions, that cannot be improved in one of the objectives, without hurting one or more of the other objectives. Since each single objective optimum is a Pareto optimal solution, the set of optimal solutions contains at least n $(= \dim(O(X)))$ solutions. Out of the set of Pareto optimal solutions the "most optimal" solution is selected. Alternatively, the designer redefines the optimality criterion and/or the objectives in order to change or reduce the set of optimal solutions. Possible strategies for the latter include transforming objectives into constraints or merging objectives by means of linear combination (scalarisation). The knowledge gained from the distribution of the set of valid solutions and the set of optimal solutions helps the decision maker in this process. The entire procedure is summarised by the flow chart shown in fig. 2.20.

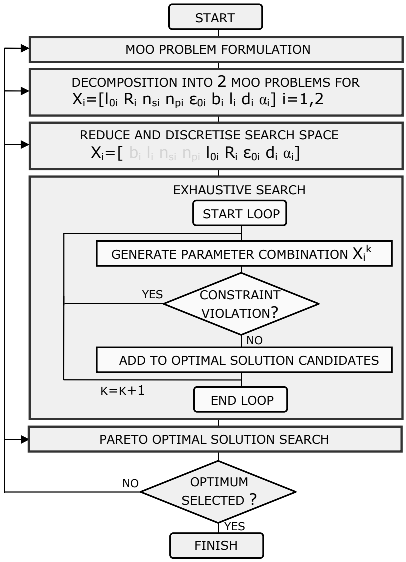

Figure 2.20: Flow chart of the optimisation procedure for the configuration with levers.

	l_{01}	l_{01}/R_1	ε_{01}	d_1	α_1	b_1	l_1	$n_{s,1}$	$n_{p,1}$
	m	-	%	m	°	m	m	-	-
lower bound	0.08	5	15	0.03	30	0.10	0.30	2	1
Δ	0.005	0.5	1	0.001	1	0.02			
upper bound	0.14	10	45	0.10	150	0.12			

Table 2.3: Design parameter ranges and step sizes for the extensor side of the configuration with levers corresponding with the feasible solution sets depicted in fig. 2.21.

	l_{01}	$\frac{l_{01}}{R_1}$	ε_{01}	d_1	α_1	O_1	O_2	O_3	O_4
	m	-	%	m	°	Nm	m	kN	rad/Nm
$\min(O_1(X))$	0.125	10	32	0.049	116	108			
$\min(O_2(X))$	0.125	10	28	0.044	124		0.100		
$\min(O_3(X))$	0.13	10	32	0.049	120			5.81	
$\min(O_4(X))$	0.14	9.5	28	0.066	130				$1.39\,10^{-3}$

Table 2.4: Parameter values corresponding with the single objective optima of the extensor side (see fig. 2.22).

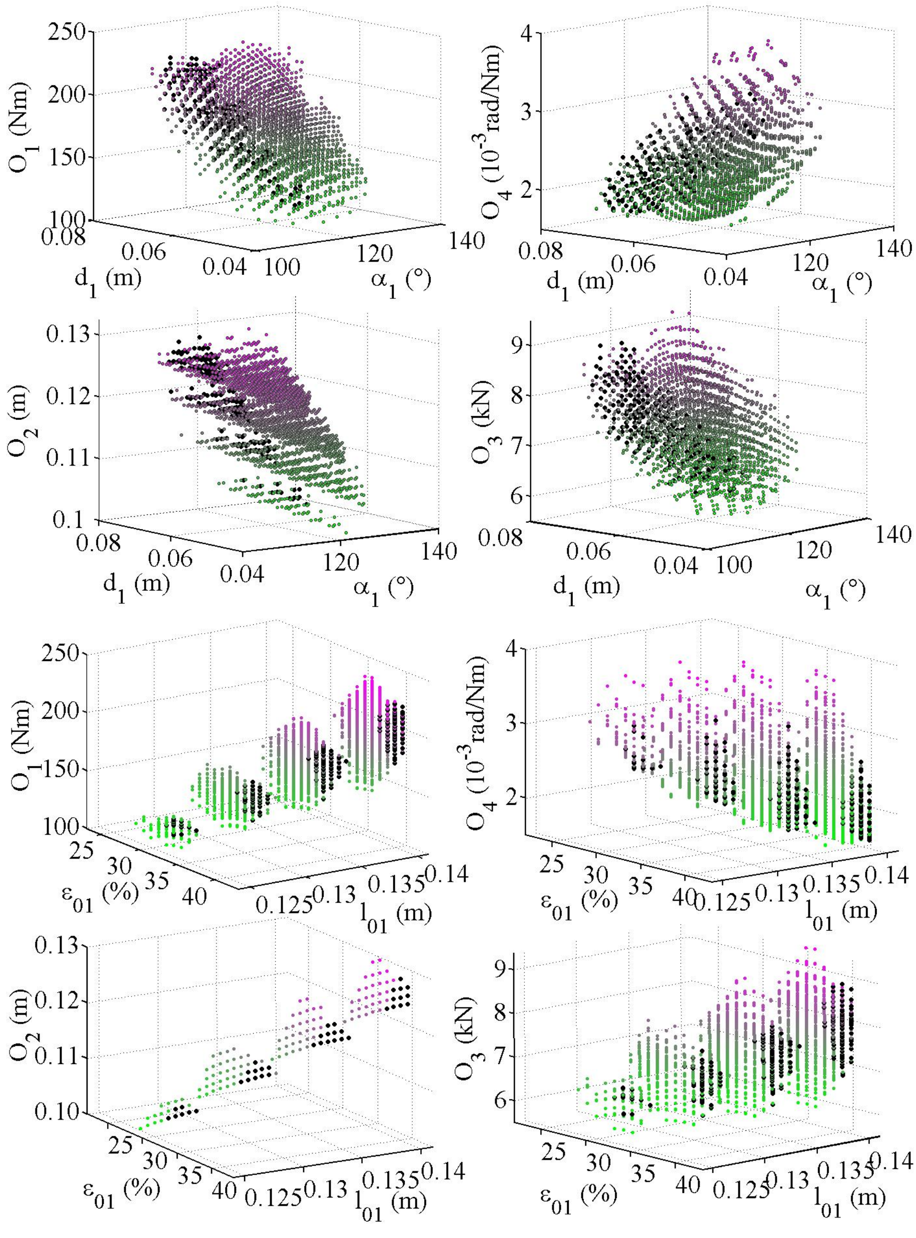

Figure 2.21: Feasible solution sets for the extensor side of the configuration with levers: solution set for $b_1 = 0.12m$ (coloured dots) and for $b_1 = 0.10m$ (black dots). Colour map (purple→green) indicates closeness to optimality.

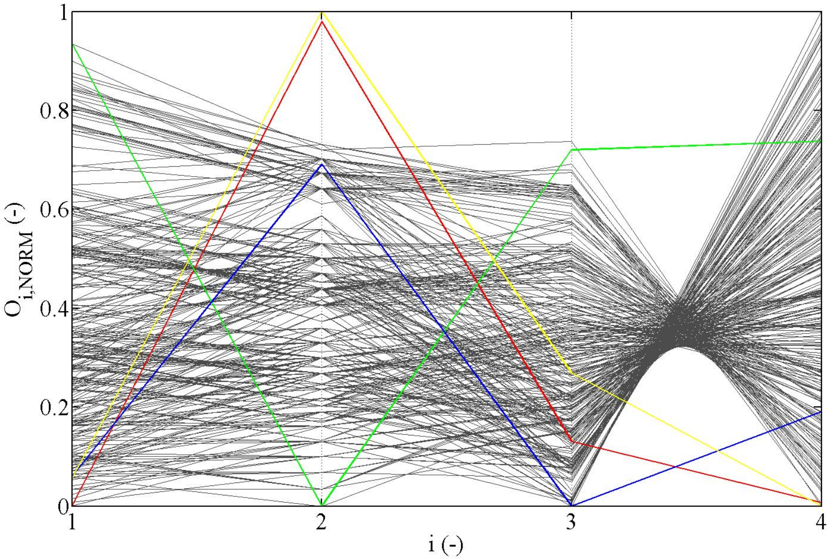

Figure 2.22: Value path illustration of the set of Pareto optimal solutions for the extensor side of the configuration with levers with $b_1 = 0.12m$. Single objective optima are coloured (O_1 red, O_2 green, O_3 blue, O_4 yellow).

Figure 2.21 shows two sets of feasible design solutions for the extensor side of the configuration with levers. The corresponding design parameter ranges and step sizes are listed in table 2.3. Each graph in fig. 2.21 depicts one of the objective functions $O_1 \ldots O_4$ as a function of the parameters α_1, d_1 or ε_{01}, l_{01}. The solution set corresponding with $b_1 = 0.12\,m$ is represented by coloured dots according to the objective function value (green (minimum) $\rightarrow$ purple (maximum)), the solution set corresponding with $b_1 = 0.10\,m$ by black dots. Parameter b_1 has a major effect on the size of the solution space. For values below $b_1 \approx 0.10\,m$ no feasible solution is found that complies with the spatial constraints, while providing sufficient torque. Larger values generate better solutions in terms of the objectives, but decrease compactness. No solutions were found for $n_{s,1} > 2$ and for $n_{s,1} = 1$ only bulky solutions were found with $b_1 \gtrapprox 0.12\,m$ and $l_{01} \gtrapprox 0.16\,m$.

From these graphs one can infer how to narrow down the search space to an optimal solution region and how the objectives are affected by parameter changes. According to the four top graphs in fig. 2.21 for instance, keeping torque overdimensioning (O_1), maximal diameter (O_2) and maximal muscle force (O_3) low, requires small values for d_1, whereas a design for maximal stiffness (O_4) requires large values for d_1. The influence of l_0 also indicates the conflicting nature of O_4 with respect to the other objectives. Figure 2.22 shows a so called "value path illustration" of Pareto optimal solutions, extracted from the full set of solutions for $b_1 = 0.12\,m$.

	l_{01}	l_{01}/R_1	ε_{01}	d_1	α_1	b_1	l_1	$n_{s,1}$	$n_{p,1}$
	m	-	%	m	°	m	m	-	-
lower bound	0.06	5	5	0.025	0	0.06	0.30	2	1
Δ	0.005	0.5	1	0.001	1				
upper bound	0.12	10	20	0.07	90				

Table 2.5: Design parameter ranges and step sizes for the flexor side of the configuration with levers.

	l_{02}	$\frac{l_{02}}{R_2}$	ε_{02}	d_2	α_2	O_1	O_2	O_3	O_4
	m	-	%	m	°	Nm	m	kN	rad/Nm
$\min(O_1(X))$	0.09	9	9	0.036	38	14.5			
$\min(O_2(X))$	0.085	8	5	0.036	39		0.077		
$\min(O_3(X))$	0.09	9	9	0.037	36			2.28	
$\min(O_4(X))$	0.12	10	5	0.036	60				$2.12\,10^{-3}$

Table 2.6: Parameter values corresponding with the single objective optima of the flexor side.

The objective function values have been normalised, i.e. transformed to a range of $[0\ldots1]$, by means of the minimal and maximal single objective values for easier interpretation and comparison of solutions. The normalised objective vector is given by

$$\begin{aligned} O_{NORM}(X) &= [O_{1,NORM}(X)\ \ldots\ O_{n,NORM}(X)] \\ &= [\frac{O_1(X)-\min(O_1(X))}{\max(O_1(X))-\min(O_1(X))}\ \cdots\ \frac{O_n(X)-\min(O_n(X))}{\max(O_n(X))-\min(O_n(X))}]. \end{aligned}$$

Each single objective optimum (coloured value paths in fig. 2.22) is a Pareto optimum. The parameter values corresponding with the single objective optima are listed in table 2.4. In spite of the relative gain that can be achieved by optimisation the optimal design solutions for the extensor side are not satisfying the need for compactness. This appeared to be less the case for the flexor side, as the required flexion torque is lower and the placement is more favourable with respect to the range of motion of the link, reducing the risk of obstructions. Feasible solutions have been found up to $b_2 \approx 0.06$ for $n_{s,2} = 2$. Table 2.6 lists the parameter ranges and the single objective optima of a representative optimisation run for the flexor side with $[b_2 = 0.06\,m,\ l_2 = 0.30\,m,\ n_{s,2} = 2,\ n_{p,2} = 1]$ as the fixed parameter set.

The exhaustive search optimisation method generates optimal solutions in a straightforward and intuitive way, while providing a better insight into the nature of the design problem. The major bottlenecks appearing from the analysis are the large range of motion of the joint for the flexor side, and the high extension torque peak

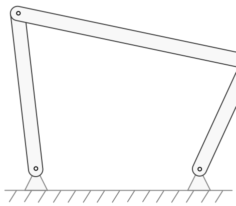

Figure 2.23: Four bar linkage.

and the spatial constraints for the extensor side, resulting in moderate compactness. To further improve on the different objectives, the benefits of a different force transmission are investigated in the following section.

2.3.5 Antagonistic setup of PPAMs with four bar linkages

The same methodical approach as previously explained is applied to the design of a configuration using four bar linkages instead of levers for force transmission. The four bar linkage (see fig. 2.23), the most simple planar 1 DOF closed kinematic chain, is commonly found in biological systems (e.g. skeletal systems, ligaments) and it is used in machine design to generate relatively complex motion (with a relatively simple mechanism) or to introduce a mechanical advantage in force or torque transmission. The linkage is proposed here in order to increase the range of motion of the powered joint, while avoiding mechanical obstruction, and in order to benefit from the mechanical advantage for a better matching of the required torque characteristic. The design parameters, the characteristics and the optimisation problem are formulated and a final design solution is presented.

2.3.5.1 Configuration

Figure 2.24 shows a schematic drawing of an antagonistic configuration with four bar linkages. The upper and lower link are interconnected by a hinge joint in O and their relative angle is denoted by q as it is the case for the previously studied configuration depicted in fig. 2.17. The extensor PPAM and flexor PPAM are connected to the upper link in hinging points B_i and to the lower link, unlike the configuration with levers, through planar four bar linkages with hinging points O, F_i, D_i and G_i with subscript i denoting the extensor side ($i = 1$) and flexor side ($i = 2$). The link connecting O and F_i is referred to as the fixed link. The link connecting F_i and D_i is referred to as the input link, since the actuator acts directly on this link. The output link is part of the lower link and it connects O and G_i. Its orientation with respect to the lower link is defined by the angle α_i. The coupler link, connecting D_i and G_i, transfers forces between the input link and the output link. Since a planar four bar linkage has one degree of freedom and both linkages have their output link fixed to the lower link of the joint, the only remaining degree of freedom of the configuration, once all design parameters have been determined, is the joint angle q.

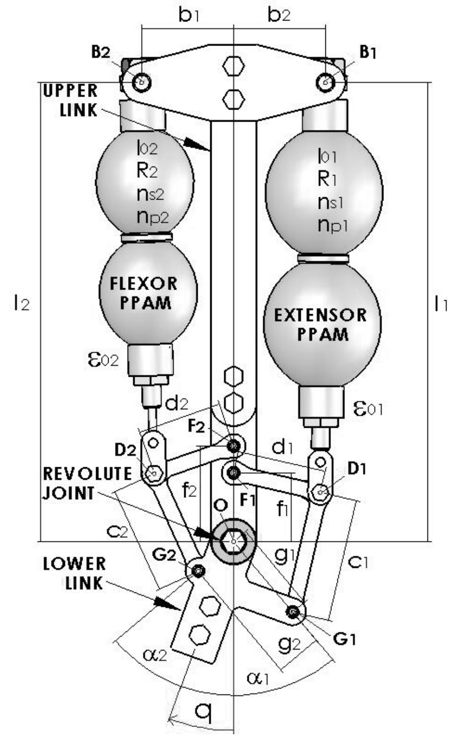

Figure 2.24: Schematic drawing and determining mechanical parameters of an antagonistic configuration of PPAMs with four bar linkages

Hence, the kinematics of the configuration as a function of q are defined by linkage link lengths f_i, d_i, g_i, c_i, lengths b_i, l_i and angles α_i. As explained in section 2.3.4.1, the characteristics of the PPAMs depend on muscle geometry (l_{0i}, R_i), the number of single PPAMs in series and parallel (n_{si}, n_{pi}), muscle contraction (ε_i), and the contraction level ε_{0i} at a specific angle q_0. In summary, the characteristics of this antagonistic configuration with four bar linkages are fully defined by the following set of 24 mechanical design parameters:

$$X = [l_{01}\, R_1\, n_{s1}\, n_{p1}\, \varepsilon_{01}\, b_1\, l_1\, f_1\, d_1\, c_1\, g_1\, \alpha_1\, l_{02}\, R_2\, n_{s2}\, n_{p2}\, \varepsilon_{02}\, b_2\, l_2\, f_2\, d_2\, c_2\, g_2\, \alpha_2]. \quad (2.44)$$

2.3.5.2 Characteristics

The derivation of the characteristics of the configuration with four bar linkages is analogous to the steps taken in section 2.3.4.1 treating the configuration with levers. The major difference resides in the transmission ratio introduced by the linkages. Detailed calculations related to the analysis of the four bar linkages can be found in appendix A.

Torque characteristic The extensor PPAM, as can be seen in fig. 2.24 generates a moment of force $\mathbf{M}_{F_1 1}$ in point F_1 that is given by

$$\mathbf{M}_{F_1 1} = \mathbf{F}_1\mathbf{D}_1 \times F_1\mathbf{e}_1 \tag{2.45}$$

with $\mathbf{e}_1 = (\mathbf{OB}_1 - \mathbf{OD}_1)/\|\mathbf{OB}_1 - \mathbf{OD}_1\|$. The z-component of $\mathbf{M}_{F_1 1}$, representing the torque produced by the extensor PPAM at the input link of the four bar linkage, and denoted by $\tau_{1,IN}$, is written as

$$\begin{aligned}
\tau_{1,IN} &= \mathbf{M}_{F_1 1}\mathbf{1}_z \\
&= F_1(\mathbf{F}_1\mathbf{D}_1 \times \mathbf{e}_1)\mathbf{1}_z \\
&= F_1 r_1'
\end{aligned} \tag{2.46}$$

where $r_1' = (\mathbf{F}_1\mathbf{D}_1 \times \mathbf{e}_1)\mathbf{1}_z$ is the lever arm. The torque $\tau_{1,OUT}$ at the output link of the four bar linkage is related to the torque $\tau_{1,IN}$ at its input link. Their ratio represents the mechanical advantage or the transmission ratio of the linkage, denoted by r_{t1} (see appendix A):

$$r_{t1} = \frac{\tau_{1,OUT}}{\tau_{1,IN}}. \tag{2.47}$$

Since the linkage output torque $\tau_{1,OUT}$ equals the torque τ_1 applied by the extensor PPAM onto the lower link, the latter is written as

$$\tau_1 = F_1 r_1' r_{t1} \tag{2.48}$$

Substituting F_1 in eq. 2.46 with the force formula for a series-parallel PPAM (see table 2.1 combined with eq. 2.13) leads to

$$\tau_1 = p_1 l_{01}^2 n_{p1} f_{t01} r_1' r_{t1}. \tag{2.49}$$

Since $f_{t01} = f_{t01}(\varepsilon_1(q, \varepsilon_{01}, b_1, l_1, f_1, d_1, c_1, g_1, \alpha_1, n_{s1}), l_{01}/R_1)$,
$r_1' = r_1(q, b_1, l_1, f_1, d_1, c_1, g_1, \alpha_1)$ and $r_{t1} = r_{t1}(q, f_1, d_1, c_1, g_1, \alpha_1)$ hold, eq. 2.49 is a function of the design parameters related to the extensor side:

$\tau_1 = \tau_1(q, l_{01}, R_1, n_{s1}, n_{p1}, \varepsilon_{01}, b_1, l_1, f_1, d_1, c_1, g_1, \alpha_1)$. Once all design parameters have been chosen the torque is written as

$$\begin{aligned}\tau_1 &= \tau_1(q) \\ &= p_1 l_{01}^2 n_{p1} f_{t01}(\varepsilon_1(q)) r_1'(q) r_{t1}(q) \\ &= p_1 m_{\tau 1}(q), \end{aligned} \qquad (2.50)$$

with the torque function $m_{\tau 1}(q) = l_{01}^2 n_{p1} f_{t01}(\varepsilon_1(q)) r_1'(q) r_{t1}(q)$ and $\varepsilon_1(q)$ as defined previously by eq. 2.31.

By combining an analogous derivation of τ_2 with eq. 2.50 one obtains the total torque $\tau(q)$ exerted by the actuators in the same form as used for the configuration with levers:

$$\tau(q) = p_1 m_{\tau 1}(q) + p_2 m_{\tau 2}(q). \qquad (2.51)$$

A substitution of $r_1' r_{t1}$ in eq. 2.46 by r_1 and combination with τ_2 yields the torque formula in the other familiar form:

$$\tau(q) = F_1 r_1(q) + F_2 r_2(q). \qquad (2.52)$$

In the design stage evaluating the torque output requires numerically solving the linkage equations (see appendix A). Once the design parameters of the configuration have been selected the torque functions are approximated by a fitting function in q.

Compliance characteristic By means of the torque formulas given by eq. 2.33 and eq. 2.32 the stiffness (the inverse of compliance) of the powered joint can be calculated, starting from

$$K = -\frac{d\tau}{dq},$$

and proceeding as was done in section 2.3.4.1. Analogously, stiffness functions can be introduced and, once the design parameters have been selected, these can be approximated by fitting functions in q.

2.3.5.3 Objectives

Three objective functions were retained from the objective vector considered previously for the configuration with levers. As a fourth objective, the minimal perpendicular distance between the input link and the joint axis in O was to be maximised to avoid obstruction. The objective related to stiffness has been omitted on the basis of the results discussed in section 2.3.4.3. The "design for (passive) stiffness" objective and the "design for torque/compactness" objectives are competing objectives leading to opposing design solutions. In a design uniquely for stiffness the active (controlled) compliance cannot be left out of account. Since the prototype is intended for the implementation of different controllers (and not a compliance controller in specific), a detailed simulation study of the controlled actuator system was not considered as supportive to the actuator system design as it is to the controller design, explained in chapter 3.

Hence, the following objectives have been considered:

- $O_1 = (\tau_{MAX} - \tau_{REQ})_{RMS}$: the root mean square of the difference between the required and the maximal torque output characteristic.
- $O_2 = (D_i)_{MAX}$: the maximal diameter of the PPAMs over the range of operation.
- $O_3 = (F_i)_{MAX}$: the maximal force exerted by the PPAMs over the range of operation.
- $O_4 = 1/(d(O, \mathbf{FD_i}))_{MIN}$: the inverse of the minimal distance between the input link and the joint axis in O.

2.3.5.4 Constraints

Several constraints, mainly related to limitations of space and proper operation of the PPAMs, have to be taken into account. The following constraint functions were considered:

- $\| \tau_{MAX} \| \geq \| \tau_{REQ} \|$: the maximal torque characteristic should exceed or at least coincide with the required torque characteristic.
- The four bar linkage equation should have a solution throughout the entire range of operation (see appendix A).
- $\| \mathbf{FD_i} \times \mathbf{BD_i} \| > 0$, $\| \mathbf{OG} \times \mathbf{DG_i} \| > 0$: singular configurations of the actuator and the input link, and the coupler and the output link may not occur in the range of operation.
- $(d(O, \mathbf{FD_i}))_{MIN} \geq c$, $(d(O, \mathbf{DG_i}))_{MIN} \geq c$: the perpendicular distance between the joint axis and the input link or the coupler respectively may not drop below a limit to avoid obstruction.
- $\varepsilon_{i,MIN} \leq \varepsilon_i \leq \varepsilon_{i,MAX}$: contraction has a lower and upper bound, as explained in section 2.3.2.2, the lower bound is typically about 5% , the upper bound, at which forces drop too low, depends on muscle slenderness, as can be seen in fig. 2.10 in section 2.3.2.2.

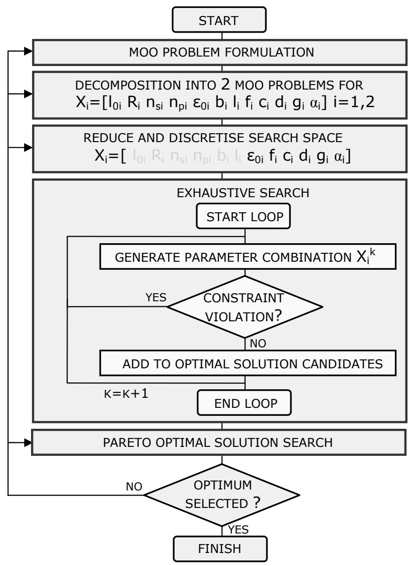

Figure 2.25: Flow chart of the optimisation procedure for the actuator configuration with four bar linkages.

- other spatial constraints: e.g. the PPAMs should fit in a predetermined bounding box and may not be obstructed. These constraints were also verified with the CAD model of the configuration.

2.3.5.5 Parameters

Given the large number of design parameters, the parameter vector in eq. 2.44 was reduced, based on the results of the study of the configuration with levers. As was done previously, the problem is decomposed into two separate optimisation problems, one for each side of the configuration. Since the presence of a four bar linkage narrows down the feasible options for l_{0i}, R_i, n_{si} and n_{pi} because of space limitations, these parameters have been left out of the optimisation procedure. The same conclusion was drawn before for parameters l_i and b_i. Hence, given a feasible parameter set $[l_{0i}\, R_i\, n_{si}\, n_{pi}\, b_i\, l_i]$, the set of remaining design parameters subject to the optimisation procedure is $[\varepsilon_{0i}\, f_i\, d_i\, c_i\, g_i\, \alpha_i]$.

2.3.5.6 Optimisation procedure

The entire procedure, summarised in fig. 2.25, is analogous with the optimisation flow chart of the configuration with levers. After problem decomposition and search

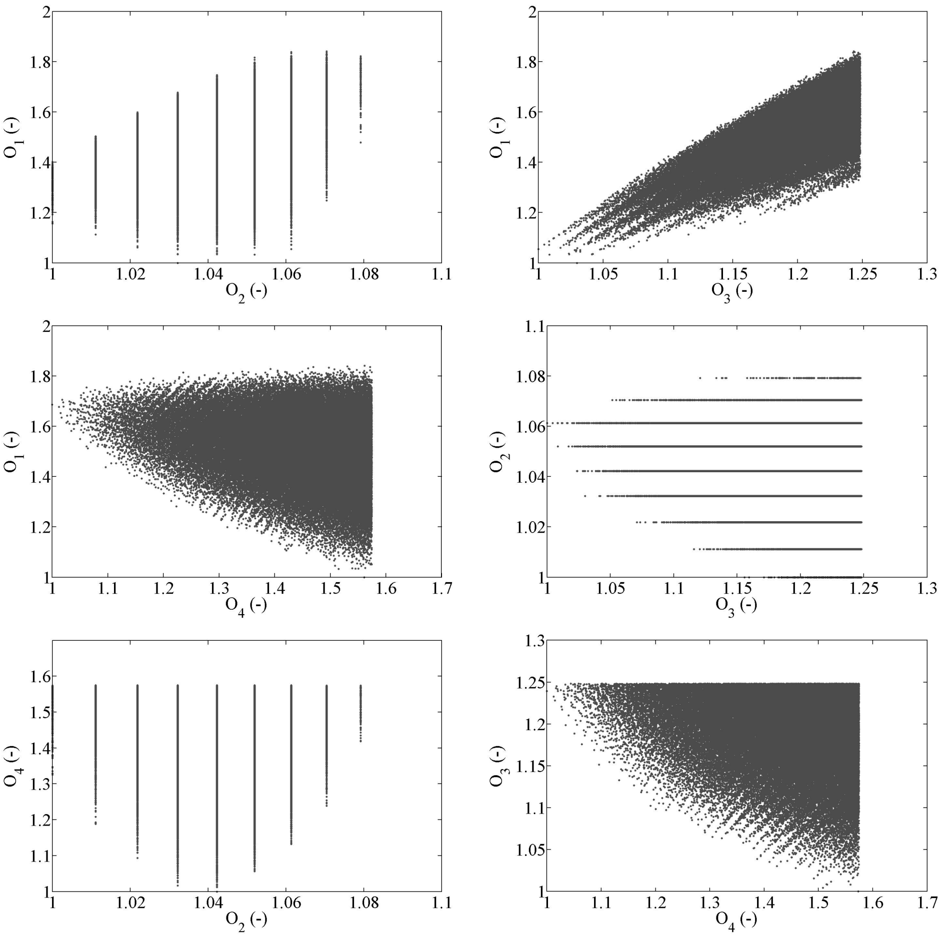

Figure 2.26: Full set of valid solutions represented in $(O_{i,S}, O_{j,S})$-axes with $i, j \in \{1, 2, 3, 4\}$ and $i \neq j$

space reduction, all feasible parameter combinations are checked for constraint violation. Then, the set of valid solutions is searched for Pareto optimal solutions. Knowledge of the set of valid solutions and the set of Pareto optimal solutions and their distribution helps the decision maker either selecting one single solution or redefining the problem in order to change and/or reduce the set of solutions. The code to generate Pareto optimal solutions has been developed in MATLAB. The solver of the four bar linkage equation was programmed in C to speed-up bottleneck calculations.

	f_1	d_1	c_1	g_1	ε_{01}	α_1
	m	m	m	m	%	°
lower bound	0.04	0.04	0.05	0.04	25	20
Δ	0.001	0.001	0.001	0.001	1	1
upper bound	0.06	0.07	0.08	0.07	35	80

Table 2.7: Parameter bounds and step size for the optimisation of the extensor side of the configuration with four bar linkages.

A full set of valid solutions for the design problem related to the extensor side of the configuration is depicted in fig. 2.26. The parameter set assigned prior to optimisation equals $[l_{01} = 0.1\,m\ R_1 = 0.0125\,m\ n_{s1} = 2\ n_{p1} = 1\ b_1 = 0.06\,m\ l_1 = 0.3\,m]$. The bounds and step size for the parameters subject to optimisation are listed in table 2.7. Besides the distribution of solutions in the search space, one can gather how much can be gained by optimisation and whether it is justified to search for an optimal solution. For that purpose, the objective function values in fig. 2.26 are scaled by the respective single objective optima. The scaled objective vector is given by

$$\begin{aligned} O_S(X) &= [O_{1,S}(X)\ \dots\ O_{n,S}(X)] \\ &= [\frac{O_1(X)}{\min(O_1(X))} \cdots \frac{O_n(X)}{\min(O_n(X))}] \end{aligned}$$

Each solution is represented by a dot in $(O_{i,S}, O_{j,S})$-axes, with the objective functions as defined in section 2.3.5.3. Optimal solutions in terms of the represented objectives are found in each graph's bottom left corner. The function value boundaries seen with $O_{2,S}$, $O_{3,S}$ and $O_{4,S}$ are due to constraints and/or parameter bounds. The discretised distribution of $O_{2,S}$ in particular is due to the fact that the maximal diameter is determined exclusively by ε_{0i}. One infers from the graph top right in fig. 2.26, that $O_{1,S}$ and $O_{3,S}$ increase about 80% and 25% respectively, when, instead of the optimal solution, the "worst" feasible solution is chosen. Hence, even in this highly constrained design problem considerable improvement with regard to the objectives can be achieved by optimisation.

Figure 2.27 shows a value path illustration of Pareto optimal solutions, extracted from the full set of solutions. The objective function values have been normalised according to

$$\begin{aligned} O_{NORM}(X) &= [O_{1,NORM}(X)\ \dots\ O_{n,NORM}(X)] \\ &= [\frac{O_1(X) - \min(O_1(X))}{\max(O_1(X)) - \min(O_1(X))} \cdots \frac{O_n(X) - \min(O_n(X))}{\max(O_n(X)) - \min(O_n(X))}]. \end{aligned}$$

Each single objective optimum (coloured value paths in fig. 2.27) is a Pareto optimum. In order to select one single optimal solution out of the set of Pareto

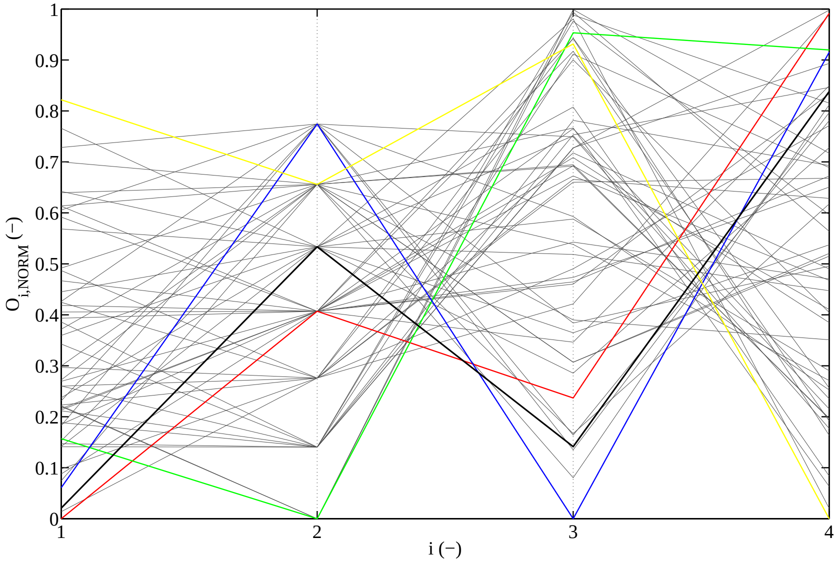

Figure 2.27: Value path illustration of a set of Pareto optimal solutions. Single objective optima are coloured, the selected optimal solution defined by $\min(O_{LC,NORM}(X))$ is marked in black.

optimal solutions, one needs to formulate preferences between objectives. Here, a weighed sum of the normalised objective function values with equal weights was chosen, transforming the normalised objective vector in a scalar objective function given by

$$O_{LC,NORM}(X) = \frac{1}{n}(O_{1,NORM}(X) + \ldots + O_{n,NORM}(X)).$$

The optimal solution that minimises $O_{LC,NORM}(X)$ is represented by the black value path in fig. 2.27. The related design parameters are $[\varepsilon_{01} = 29\%\ f_1 = 0.05\ d_1 = 0.063\ c_1 = 0.072\ g_1 = 0.057\ \alpha_1 = 60°]$.

Figure 2.28 shows $O_{LC,NORM}(X)$ as a function of each parameter, while all other parameters are set equal to the optimal parameter values and held constant. The optimal solution, corresponding to the black value path in fig. 2.27, is indicated by a black dot. In these graphs one observes that the optimal solution lies on the solution space boundary and that separate parameter variations are only feasible in a small range. The slope of each curve corresponds with the partial derivative of the objective function with respect to the respective parameters. As previously mentioned in section 2.3.4.3, this partial derivative is a measure for the sensitivity of the objective function to parameter variations.

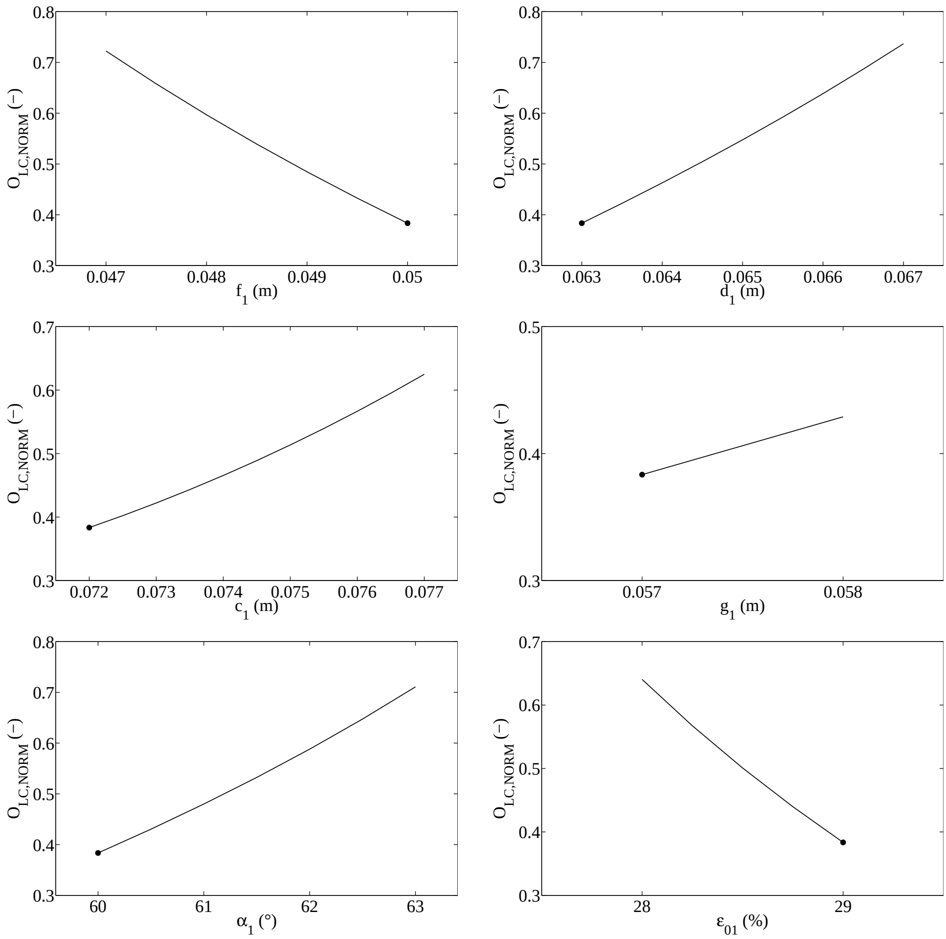

Figure 2.28: Sensitivity of the objective function $O_{LC,NORM}(X)$ near the optimal solution.

Even small parameter changes considerably affect optimality. Non-zero slopes near the selected optimal solution indicate that its optimality is due to the solution space boundary. The constraints defining this boundary impose a limit on the achievable compactness of the design.

For the flexor side, an optimal parameter set was found analogously. The parameters defined prior to optimisation were $[l_{02} = 0.08\,m\ R_2 = 0.0125\,m\ n_{s2} = 2\ n_{p2} = 1\ b_2 = 0.06\,m\ l_2 = 0.3\,m]$. Main differences with the procedure for the extensor side are that the selection of parameter f_1 narrowed down the fea-

	f_i	d_i	c_i	g_i	ε_{0i}	α_i	O_1	O_2	O_3	O_4
	m	m	m	m	%	°	Nm	m	kN	m^{-1}
extensor	0.05	0.063	0.072	0.057	29	60	26.1	0.086	4.23	43.5
flexor	0.068	0.063	0.072	0.03	5	20	12.0	0.075	2.75	18.1

Table 2.8: Parameter and objective function values corresponding with the selected four bar linkage configurations minimising $O_{LC,NORM}(X)$.

sible range for f_2 (see fig. 2.24) and that a solution near the optimal solution ($\min(O_{LC,NORM}(X))$) was ultimately selected so that d_1 and c_1 match d_2 and c_2 respectively to ease manufacturing. The selected design parameters are [$\varepsilon_{02} = 5\%$ $f_2 = 0.068$ $d_2 = 0.063$ $c_2 = 0.072$ $g_2 = 0.03$ $\alpha_2 = 20°$].

All selected design optimisation parameters and their respective objective function values are summarised in table 2.8 for easier comparison with the values in table 2.4 related to the configuration with levers. Even when comparing the selected optimal solution ($\min(O_{LC,NORM}(X))$) of the extensor side with the single objective optima $O_1 \ldots O_3$ of the same side of the configuration with levers, considerable improvement can be observed. Also, by reducing b_1 from $0.12 \rightarrow 0.06$ the four bar linkage configuration is at least twice as compact. For the flexor side improvements are less pronounced: since the requirements and constraints are less critical, a near optimal solution has been selected.

2.3.5.7 Design solution

The theoretical torque characteristics of the actuator system design selected in the previous section are shown in fig. 2.29-2.30.

In fig. 2.29 the maximal actuator torque output (blue) is compared with the maximal required torque (red). The maximal required torque, as introduced in section 2.3.1, is based on gait analysis data of the knee joint measured in unimpaired subjects, taken from (Winter (1991)). A representative torque-angle curve of a subject weighing $75\,kg$ and walking at normal cadence is shown in grey. The design bottleneck for the positive torque characteristic τ_{1MAX} is the large extensor torque required during stance. Hence, in case of small knee joint angles the extensor PPAM is at a high contraction level, generating a low force output. The negative torque characteristic τ_{2MAX} is largely determined by the large required range of motion, rather than by the required flexion torque.

Figure 2.30 shows the torque functions related to the input link (purple) and the output link (blue) of the four bar linkages, as well as their transmission ratios (green) as a function of joint angle. Both transmission ratios are well below one and the relative difference supports the previous observations.

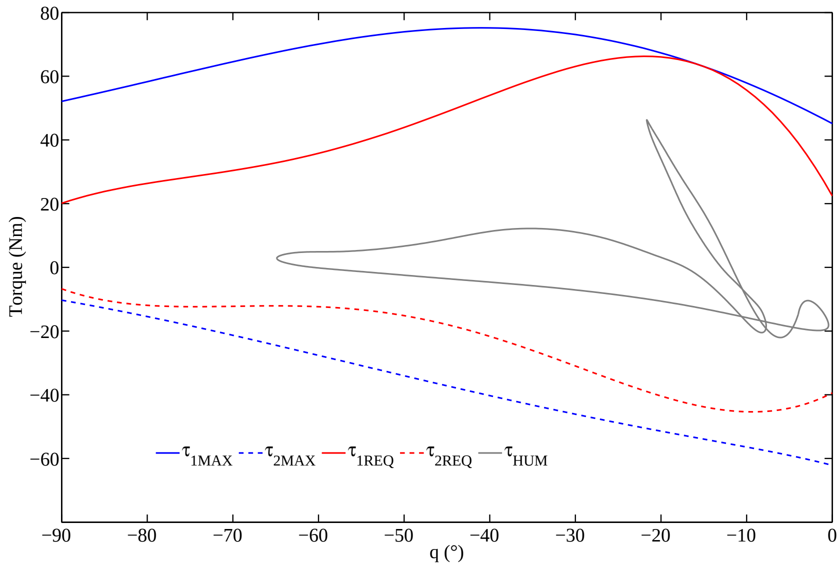

Figure 2.29: Torque characteristic of the actuator system: maximal output torque (blue) and maximal required torque (red) as a function of joint angle, typical moment-angle curve for the knee joint of an unimpaired subject (75kg) walking at a normal cadence (grey, based on data from Winter (1991), see section 2.3.1.

Due to these design bottlenecks and the fact that the transmission ratios cannot be arbitrarily shaped, the actuator system is somewhat overdimensioned in the range corresponding with low muscle contraction levels and high pulling forces. However, due to the use of four bar linkages for force transmission, a design solution has been found that meets the specifications and that is much more compact than a configuration based on levers.

2.3.6 Conclusion

Two key properties of pleated pneumatic artificial muscles make their use as actuators for powering a robotic joint challenging: their nonlinear force-contraction characteristic and their intrinsic compliance.

A force transmission based on four bar linkages was proposed in order to cope with the nonlinear force output and to meet the requirements while satisfying tight constraints. When compared to conventional levers or pulleys, the variable transmission of the linkage allows shaping the torque-angle characteristic of the joint more freely, while extending its range of motion and increasing compactness. To the author's knowledge, this approach has not been used before for pneumatic muscle force transfer to a robotic joint. A methodical approach to the design of

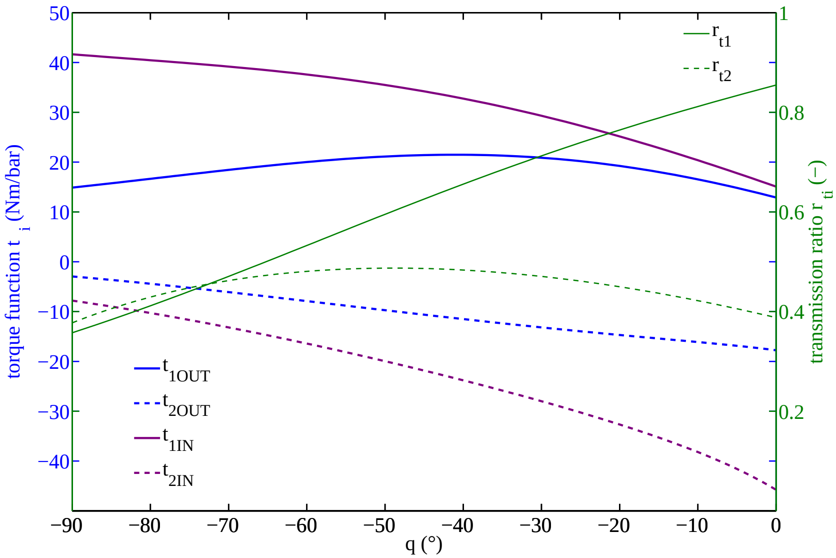

Figure 2.30: Torque functions and transmission ratios of the actuator system: torque functions related to the input link (purple) and output link (blue) of the four bar linkages and transmission ratios (green) of the four bar linkages as a function of joint angle.

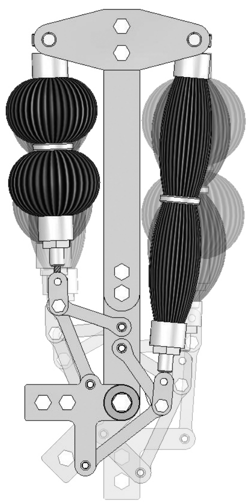

Figure 2.31: Final actuator system design: range of operation.

an actuator system powered by PPAMs was considered indispensable for several reasons. In view of a full lower limb exoskeleton design, such a joint design method could drastically reduce overall design time and improve design quality. Moreover, due to the large number of design parameters and constraints, the design problem tends to grow too complex to find merely feasible solutions by trial and improvement. By means of the mathematical model of the PPAM and the kinematic analysis of the proposed configuration, different design objectives and constraints can be formulated as a function of the design parameters.

The adaptable compliance of the joint has been considered, but it was found difficult to translate into "design for compliance" guidelines, since the passive (intrinsic) compliance range depends on the required torque and the active (controlled) compliance range depends on the behaviour of the controller. A "design for torque/compactness" was considered in the final design. A straightforward optimisation technique based on exhaustive search provided more insight into the multiobjective optimisation problem. The most important observation is that the solution space is highly constrained, in spite of which still considerable improvement can be achieved by searching for an optimal instead of a feasible solution. By reducing the search space, computation time was lowered to an acceptable level. In order not to miss out optimal solution candidates the search space reduction was based on subproblem formulation and sensitivity analysis.

An optimal design solution, meeting the specifications, was selected and has been integrated into the exoskeleton structure, of which the design is addressed in the next section.

2.4 Mechanical structure

2.4.1 Requirements

Although weight minimisation is important in view of wearability, this was not considered the main objective of this design. Emphasis was rather put on robustness and durability, since the device must be capable of safely generating and transferring considerable torques in close contact with a human wearing it. The mechanical structure should be a serial linkage, interconnected by (a) revolute joint(s) and acting in parallel with the human lower limb. Also, the exoskeleton needs to be connected to an external fixed reference, providing weight compensation of the device.

2.4.2 Prototype versions

KNEXO, the current design of the powered knee exoskeleton, is preceded by different intermediate prototypes and test setups.

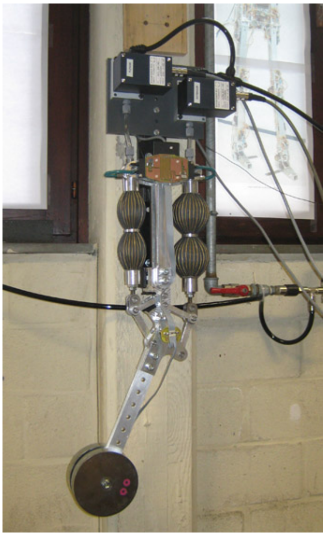

Figure 2.32: 1 DOF pendulum setup.

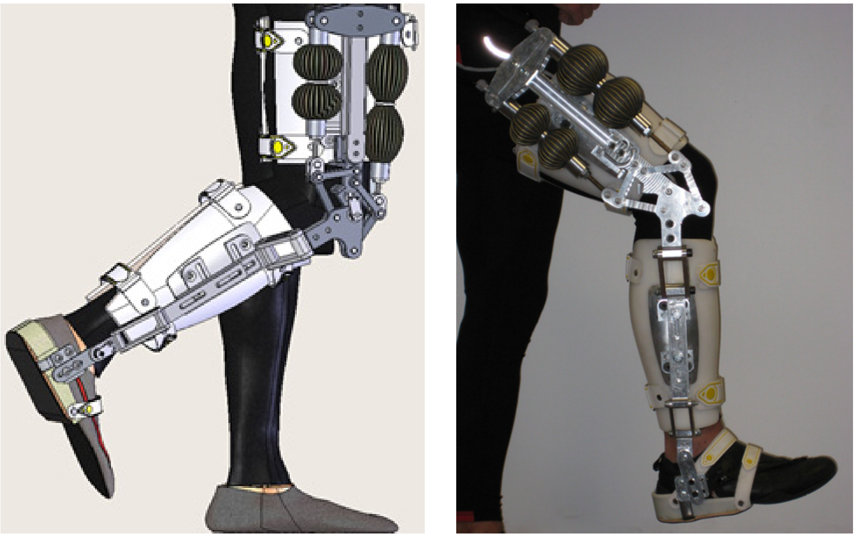

a b

Figure 2.33: Body-grounded exoskeleton with footplate: a) CAD concept model, b) prototype.

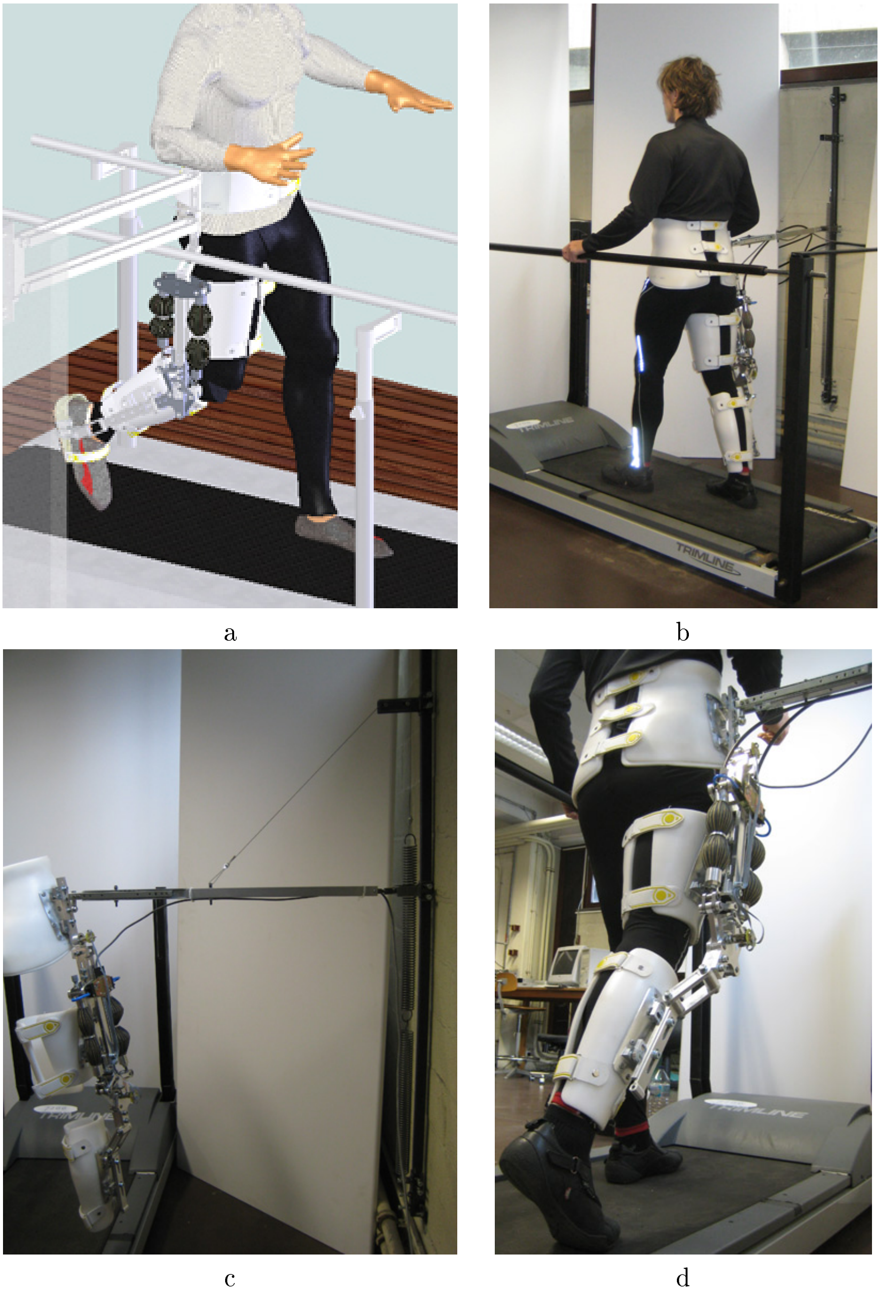

Figure 2.34: Wall-grounded exoskeleton: a) CAD concept model, b) prototype, c) weight compensating arm, d) prototype close up.

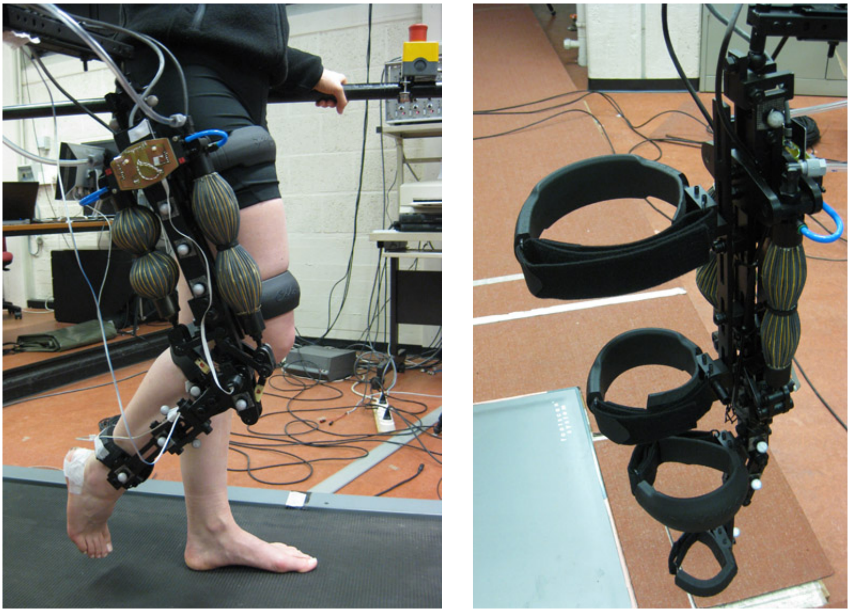

a b

Figure 2.35: KNEXO: a) overview, b) adjustable interface

First a 1 DOF pendulum setup (see fig. 2.32) was built in order to implement and test controllers on the actuator system previously described in section 2.3. Experimental results obtained by means of this set up are presented and discussed in section 3.3-3.4 of chapter 3.

The first exoskeleton-type prototype (see fig. 2.33), adopting the same actuator system, was a powered knee orthosis with a footplate interconnected by a passive ankle joint. Because of the remaining added weight during swing and the influence of the footplate on foot roll, the body-grounded orthosis was adapted into a wall-grounded exoskeleton (see fig. 2.34). The latter did not have a footplate and its structure was extended with an additional upper body link that was connected to a fixed reference by means of a weight compensating arm. The human-robot interface consisted of two-piece thermoplastic cuffs with a foam inlay and Velcro straps at the lower leg, the upper leg and the hips. Their position and orientation with respect to the exoskeleton frame were adjustable by means of slider mechanisms. Pilot experiments performed with this prototype are discussed in section 4.2.2 of chapter 4.

In view of extended testing with unimpaired and impaired subjects, this prototype was adapted into the current prototype version, named KNEXO.

Figure 2.36: Adaptability of the interface: a) cuff with respect to link, b) upper link with respect to lower link.

2.4.3 KNEXO

2.4.3.1 Structure

KNEXO consists of a lower leg link and an upper leg link, each provided with two rigid semi-circular cuffs. The joint is powered by the actuator system, as described in section 2.3. Adjustable mechanical limiters prevent lower link motion beyond the required range of motion, typically $[0-90]^{\circ}$. An upper body link has been omitted to minimise disturbance of pelvic motion. A weight compensating arm is connected to the upper leg link. Most parts of the structure are made of aluminium alloy 6060 (AlMgSi0.5) or 6082 (AlMgSi1), except for small, highly loaded parts made of engineering steel. The weight of KNEXO is about $4.5\,kg$.

2.4.3.2 Interface

In order to fit a wide range of subjects in terms of statures and sizes the structure as well as the cuffs have been made adaptable. Anthropometric data was used as a guideline (NASA (1978)). Figure 2.36 gives an overview of all adjustable degrees of freedom of the cuffs relative to the link (see fig. 2.36.a) and of the links relative to each other (see fig. 2.36.b). A series of rigid cuffs in different sizes was chosen over flexible single sized cuffs to obtain a sufficiently stiff interface, while transferring high torques.

2.4.3.3 Weight compensation

The weight compensating arm, shown in fig. 2.37, is a telescopic arm connected to the upper leg link of KNEXO, near the pelvis, by means of a ball joint and to the fixed reference by means of a universal joint. In this way all translational DOF (forward/backward: $0.3\,m$, other translational: $0.2\,m$) and rotational DOF (flexion/extension: unlimited, other: 40°) are unconstrained within a suitable range to accommodate normal pelvic motion during treadmill walking. The simple weight compensation mechanism is based on gravity balancing theory (Rahman et al. (1995)). It consists of a linear tension spring that acts as a "zero free length spring" between a connection point on the arm and a connection point on the fixed reference, but that is placed remotely by means of a pulley.

For a better understanding a planar force diagram is shown on top of the actual mechanism depicted in fig. 2.37, indicating the external forces acting on the arm. The weight of the exoskeleton is transferred to the arm through the ball joint in E. This load is combined with the arm's own weight, resulting in the vertical force $\mathbf{F_g}$ acting in G. A spring force $\mathbf{F_s}$ acts along $\mathbf{AB}$ in A. In order to have static equilibrium the total moment M_O in O should be zero, which yields

$$\mathbf{M_O} = (\mathbf{OG} \times \mathbf{F_g}) + (\mathbf{OA} \times \mathbf{F_s}) = \mathbf{0}.$$

Denoting the force originating from a spring with zero free length, stiffness k and its end points in A and B by $F_s = kx$ and using the annotations in fig. 2.37, one obtains

$$F_g l sin\theta = kxr,$$

and, since $r = a\sin\beta$ and $x\sin\beta = b\sin\theta$ hold, this simplifies to the following condition for the spring stiffness k:

$$k = \frac{F_g l}{ab}. \tag{2.53}$$

The static equilibrium condition is independent of the angle θ between the arm and the vertical fixed reference. Thus, a spring of which the actual elongation equals the distance between points A and B, and the stiffness complies with eq. 2.53 ideally garantees static equilibrium of the arm loaded by the exoskeleton. Since a physical spring has non-zero free length, these requirements can only be met by placing a spring with the aforementioned stiffness outside segment AB, in this case between

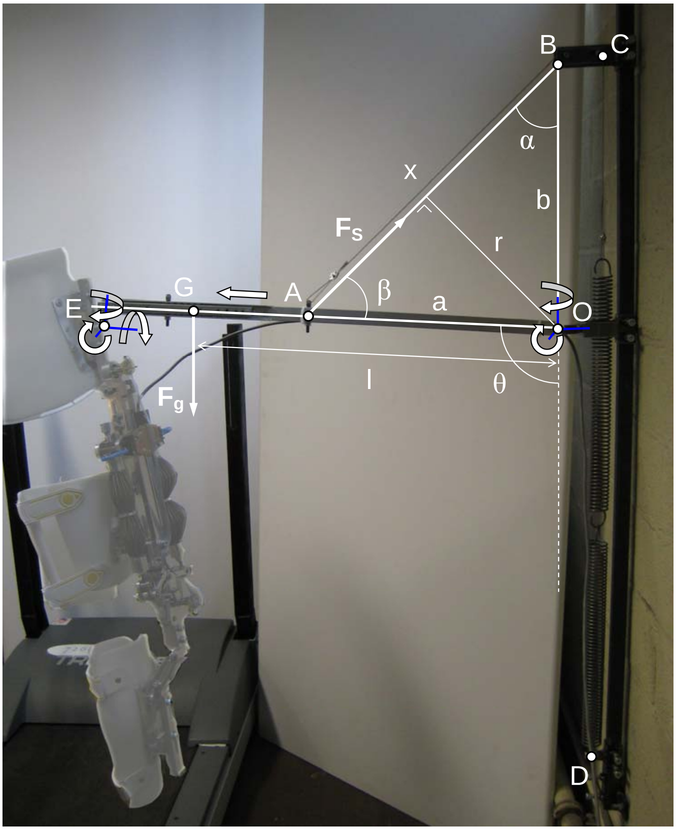

Figure 2.37: Weight compensating arm based on gravity balancing by means of a zero free length spring.

C and D, and setting the pretension such that the actual elongation of the spring equals x. Obviously, in a practical set up nonidealities cause deviations from the ideal force diagram depicted in 2.37: for instance a difference between the line of action of the spring and the path of the cable defining its elongation, variations of l with θ due to the location of E off the arm's centerline and an additional friction force due to the pulleys. Since the telescopic arm is allowed to extend and shorten, these nonidealities are acceptable. During normal operation, within a limited range of θ, the mechanism effectively compensates the exoskeleton's weight (approximate mass $4.5\,kg$), while allowing a sufficient range of motion.

2.5 Instrumentation

2.5.1 Control system

Data-acquisition is performed by a National Instruments PCI-6229 data-acquisition board. All controllers and high-level data-acquisition have been programmed in C/C++. The sampling rate was set at $1\,kHz$. Higher sampling rates appeared not to be feasible without recurring to real-time target software, however, since the valves have minimal opening/closing times of about $1\,ms$, a sampling time of $1\,ms$ was considered sufficient. The data-acquisition board uses hardware-timing for deterministic acquisition.

2.5.2 Actuator output

2.5.2.1 Valves

The gauge pressure of each PPAM is regulated by a Kolvenbach KPS 3/4-00 3/3-way pressure regulating servo valve. An integrated PID controller controls the airflow into or out of the muscle using the desired pressure level, taken from a voltage input, as a reference and the actual pressure inside the valve, measured by an internal pressure sensor, as the system output. Since the valve's internal pressure is used instead of the internal muscle pressure, tubing between the valve and the muscle is kept as short as possible.

2.5.2.2 Pressure sensors

A differential pressure sensor, HCX005D6V by Sensortechnics, is used for gauge pressure measurements in each PPAM. The pressure difference between the two sensing ports of the HCX005D6V is converted to a voltage and amplified to a range of $[0.5-4.5]\,V$ by a built-in signal amplifier. One sensing port is connected to the muscle's interior, whereas the other is subject to atmospheric pressure.

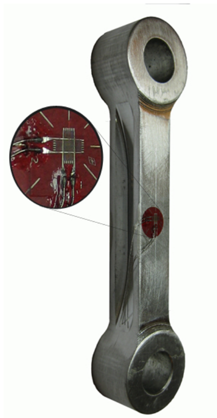

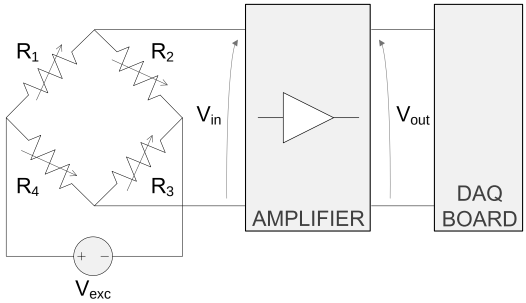

a b

Figure 2.38: Custom-made force sensing: a) coupler equipped with a strain gage Rosette at each of two opposite sides, b) measuring circuit with full Wheatstone bridge.

Differential pressure sensors have been chosen over absolute pressure sensors, since the former are not affected by atmospheric pressure variations.

2.5.2.3 Custom-made force sensors

Due to space limitations, custom-made force sensors were chosen over commercially available force sensors or torque sensors for a more direct torque measurement, that is not based on pressure measurements and the use of the muscle model. The coupler of each four bar linkage is equipped with two pairs of strain gages. Each pair is a 2-element strain gage Rosette consisting of two perpendicular identical single strain gages, as shown on fig. 2.38.a. This particular strain gage configuration has the advantage of a higher measuring sensitivity and the cancellation of bending strain contributions to the measurement, as will be illustrated further.

Ideally, the coupler is loaded purely in tension. For an optimal measurement range of the strain gages the cross section can be sized such that the maximal allowable strain occurs approximately at the maximal load. The minimal cross section area is thus given by

$$\begin{aligned} A_{MIN} &= \frac{F_{MAX}}{E\varepsilon_{MAX}} \\ &\approx 36mm^2 \end{aligned} \tag{2.54}$$

in which E is the modulus of elasticity of the alloy ($70\,GPa$), F_{MAX} the maximal load of the coupler during operation ($2500\,N$) and ε_{MAX} the maximal strain (10^{-3}). The actual I-beam cross section has been conservatively chosen equal to $52\,mm^2$.

The four strain gages are integrated into an electrical circuit, a so called full Wheatstone bridge, to measure the change of resistance due to mechanical strain. Each strain gage is electrically equivalent to a resistor with variable resistance, as indicated in fig. 2.38. The voltage V_{in} is related to the fixed excitation voltage V_{exc} and the resistor values $R_1 \ldots R_4$ as follows:

$$V_{in} = V_{exc}\frac{R_1R_3 - R_2R_4}{(R_1+R_2)(R_3+R_4)}. \tag{2.55}$$

In the unloaded case, the bridge should be balanced, i.e. $V_{in} = 0$, therefore $R_1R_3 = R_2R_4$ is required. Introducing resistance variations $\Delta R_1 \ldots \Delta R_4$ in eq. 2.55 with respect to the balanced condition and omitting second order terms yields

$$\Delta V_{in} = V_{exc}\frac{\frac{R_2}{R_1}}{(1+\frac{R_2}{R_1})^2}\left(\frac{\Delta R_1}{R_1} - \frac{\Delta R_2}{R_2} + \frac{\Delta R_3}{R_3} - \frac{\Delta R_4}{R_4}\right). \tag{2.56}$$

The gage factor k of for instance strain gage 1 relates the variation of its resistance R_1 to its strain ε_1, so $\Delta R_1/R_1 = k\varepsilon_1$ holds, with $k = 2.11$ for all the strain gages used in this setup. Introducing the gage factor in eq. 2.56 and using $R_2/R_1 = 1$, as all strain gages have an identical resistance in the balanced condition ($R = 120\,\Omega$), one obtains

$$\Delta V_{in} = V_{exc}\frac{1}{4}k(\varepsilon_1 - \varepsilon_2 + \varepsilon_3 - \varepsilon_4). \tag{2.57}$$

If one configures the strain gages such that 1 and 3 are aligned longitudinally and 2 and 4 transversally, the sensitivity is effectively increased since the strains of the strain gages relate to the longitudinal extension strain ε of the coupler as given by

$$\begin{aligned}
\varepsilon_1 &= \varepsilon \\
\varepsilon_2 &= -\nu\varepsilon \\
\varepsilon_3 &= \varepsilon \\
\varepsilon_4 &= -\nu\varepsilon,
\end{aligned}$$

in which ν stands for the Poisson ratio of the alloy (0.33). It is also clear from eq. 2.57, that strain due to bending is cancelled out, as bending causes variations of ε_1 and ε_3 with equal amounts, but opposite signs. Equation 2.57 is rewritten as

$$\Delta V_{in} = V_{exc}\frac{1}{4}k(2+2\nu)\varepsilon,$$

and by setting $V_{exc} = 5\,V$, $k = 2.11$, $\nu = 0.33$ and ε equal to the maximal strain (at the maximal load) one obtains the input range of the amplifier circuit $V_{in} \approx [0 - 4.8]\,mV$.

For signal conditioning Futek CSG110 amplifiers are used. By means of gain adjustment and precision shunt resistors the output voltage range is scaled and offset to approximate $V_{out} \approx [0 - 10]\,V$, the required input range of the data-acquisition board. The offset compensates for the initial out-of-balance voltage, due to the fact that the balance condition $R_1R_3 = R_2R_4$ is never exactly satisfied. The entire force sensing circuit has been calibrated in a high precision tensile test bench and tested for stability and repeatability prior to integration into the exoskeleton. The calibration and verification results are discussed in section 3.2.1.3 of chapter 3.

2.5.3 Exoskeleton kinematics

2.5.3.1 Encoder

The knee and hip joint angle of the prototype in fig. 2.34 and the knee joint angle of KNEXO are measured by means of miniature high resolution incremental optical encoders, AEDA-3300 BE1 by Avago Technologies. If both rising and falling edges of the quadrature encoder output signals are taken into account, this encoder type has a maximum of 80000 counts per revolution. The angular resolution, expressed in degrees (°) and radians (rad), equals $\Delta q = 360°/80\,000 = 0.0045° \approx 7.85\,10^{-5} rad$, which outperforms typical requirements.

As for the angular velocity, typical values for the joints are found in the range of $[0 - 10]\,rad/s$. The angular velocity is calculated by counting the amount of encoder pulses detected during a fixed time period. This boils down to using a first order difference approximation with the sampling time T_s as the time step. The angular velocity resolution $\Delta\omega$, expressed in degrees per second (°/s) and radians per second (rad/s), is thus given by $\Delta\omega = \Delta q/T_s = 4.5\,°/s \approx 0.0785\,rad/s$. This is the maximal quantisation error of the angular velocity signal, i.e. the maximal error, due to discretisation by the encoder, between the real and measured angular velocity. Consequently, relative angular velocity errors tend to become high at low speeds. Since the angular velocity resolution is proportional to the angular resolution, the angular resolution has been chosen as small as feasible in view of a higher velocity signal quality. The latter is important for control as it affects the quality of any controller output that consists of a velocity based feedback term.

2.5.3.2 Absolute position measurement

During specific experiments with unimpaired and impaired subjects, absolute position measurements of KNEXO have been performed by means of a Vicon 612 motion analysis system with 7 high speed infrared cameras capturing the position of reflective markers at a frame rate of 250 Hz. These measurements were processed offline to evaluate relative displacements between the exoskeleton and the wearer's body. An absolute position measurement for real-time use in the exoskeleton's control system has been considered as well. Knowledge of the orientation with respect to the gravitational field could be used by a model-based gravity compensation algorithm that outputs a desired support torque to the actuator system. Since either a series of relative position measurements or a combination of accelerometers and gyroscopes would be required, it was decided to omit such absolute position measurement. The support torque generation is therefore based on a different approach, discussed in section 3.4.2.4 of chapter 3.

2.5.4 Gait phase detection

The detection of different phases of gait is important for offline analysis and evaluation of measurements. Moreover, online gait phase detection is essential to achieve a more dedicated and intelligent control of the exoskeleton. Some aspects that make gait phase detection difficult in this particular application are:

- Since only one relative angle measurement (of the knee joint) is available, as explained in section 2.5.3.2, the system lacks information about other joints of both lower limbs.
- Since the device is intended for impaired subject testing, the measurable quantities used for gait phase detection cannot be treated similarly as data originating from unimpaired subjects.

For KNEXO gait phase detection has been limited to foot contact detection for synchronisation purposes, as discussed in section 3.5.2 of chapter 3.

2.5.4.1 Feasibility of accelerometer measurement

Ideally, the foot contact detectors are integrated into the exoskeleton. Treadmill walking experiments performed at different speeds with the exoskeleton equipped with a piezoelectric accelerometer indicated its ineffectiveness in detecting initial contact. Acceleration levels at the instance of heel strike were too low relative to other acceleration peaks during gait to be repeatably distinguishable, because of the absence of direct contact of the exoskeleton with the ground and the compliance of the interface between the wearer and the exoskeleton.

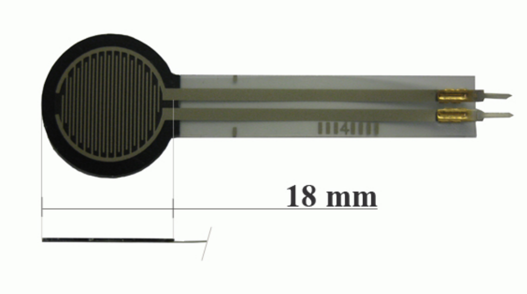

Figure 2.39: Force sensing resistor used for foot contact detection.

2.5.4.2 Force sensing resistors

In spite of the evident drawbacks of foot contact sensors placed on the wearer's foot sole or shoe outsole, these had been ultimately selected as the most simple and reliable solution. A force sensing resistor (FSR, see fig. 2.39) is simply strapped onto the subject's heels. The output signal of each FSR is fed to a voltage divider that determines sensitivity, sampled by the data-acquisition board and passed through a threshold detection with deadband. Especially in subjects with affected gait, tuning of FSR placement and detection is required to cope with unpredictable and variable foot contact.

2.5.5 Safety

Besides mechanical safety measures being provided, such as an overhead fall protection harness and range of motion limiters on the knee joint, a range of safety checks is performed in the control software related to foot contact and actuator state (force, pressure). Manually activated emergency stop buttons cut off the pressure supply of the valves directly, providing a safe bypass in case of control software malfunction.

2.6 Overview

KNEXO, the research prototype developed in this work, is a knee exoskeleton powered by pleated pneumatic artificial muscles, a pneumatic muscle type that outperforms the well known McKibben muscles in terms of stroke length and force output. The actuator system consists of an antagonistic setup of two series PPAMs, each connected to the joint by means of a four bar linkage. The four bar linkage allows a better matching of the required torque and a much more compact design, when compared with conventional mechanisms used in pneumatic muscle systems, such as fixed levers or pulleys. Dimensioning the PPAMs and linkages is a complex design task that benefits from a methodical approach. It was shown that a multiobjective optimisation by means of exhaustive search provides compact solutions, satisfying the torque requirements that were based on gait analysis data of sound knee function. The final actuator system design has a range of motion of 90° and generates peak extension and flexion torques of $75\,Nm$ and $60\,Nm$ respectively. It incorporates custom-made force sensors for actuator torque sensing. KNEXO's mechanical structure and adjustable interface with the wearer have been designed in view of extensive testing. The device is wall-grounded by a gravity-balancing arm in order to compensate its weight during treadmill walking. For gait phase detection force sensing resistors attached to the foot were deemed the most straightforward.

Chapter 3

Control for safe, compliant and adaptable robotic assistance

3.1 Introduction

In the introductory chapter a general overview of the state-of-the-art in robot-assisted gait rehabilitation was given with emphasis on hardware and the concept of assistance-as-needed in the control of gait rehabilitation robots was only briefly discussed. This chapter deals with the study and implementation of different controllers on KNEXO in view of safe, compliant and adaptable robotic assistance of gait. Before passing on to modelling and control of KNEXO, the state-of-the-art in robot control for gait assistance is first looked at in this section, as it provides a framework for understanding different challenges in control of gait rehabilitation robots for the lower limbs. The challenges addressed in this work and the approach followed thereby are discussed.

3.1.1 State-of-the-art

First, a summary restricted to high-level (robot-level) control strategies is given. After that, existing low-level (actuator-level) controllers for pneumatic muscle actuators are discussed briefly.

3.1.1.1 Control strategies for gait assistance

As mentioned in the introductory chapter, various control strategies are being explored for robot-assisted rehabilitation of gait. The principles of motor learning and recovery in robot-assisted neuro-rehabilitation are not yet fully understood and therefore difficult to translate into controller design guidelines (Reinkensmeyer et al., 2007). Control strategy developments therefore tend to be based on general concepts in rehabilitation, neuroscience and motor learning and many advancements are, for the time being, engineering-driven, seeking improvements in robot control to realise those general concepts.

According to Marchal-Crespo and Reinkensmeyer, 2009 the existing high-level controllers can be divided into four categories, depending on the underlying approach to achieve recovery:

- assistance based: the robotic device provides functional assistance, i.e. assistance of a functional task such as supporting the body-weight, advancing the limbs, ... (e.g. Duschau-Wicke et al., 2008; Ekkelenkamp et al., 2007; Aoyagi et al., 2007; Agrawal et al., 2007)
- challenge based: in which a functional task is made more difficult or challenging, as opposed to assistance based strategies envisaged to facilitate a task (e.g. Yoon and Ryu, 2005; Lam et al., 2008; Emken and Reinkensmeyer, 2005).
- virtual-reality based: a haptic interface is used to simulate specific environments and/or activities (e.g. Schmidt et al., 2005b; Zimmerli et al., 2009).
- non-contact coaching based: a mobile robotic coach, making no physical contact, encourages the patient (e.g. Mataric et al., 2007).

For a robotic device the terms assistance and challenge both relate to the way in which the device physically interacts with the patient in order to accomplish a certain task. As such they define a spectrum of possible control strategies that could apply to different patients with different impairment levels or to a single patient throughout his/her recovery. Challenge based strategies in robotic therapy are often based on the device providing resistance against movements or amplifying movement errors with respect to a reference trajectory (Marchal-Crespo and Reinkensmeyer, 2009). These challenge based strategies are likely to be more effective in mildly affected patients and, especially in gait recovery, these would require a combination with an assistance based strategy to safely support patients with unsufficient strength and/or motor control. In this work and in the following overview focus is on assistance based strategies.

A suitable way of differentiating between assistive control strategies is in terms of the activity level of the robot and the human-in-the-robot (Veneman et al. (2007)). At the one side of the spectrum of possible assistive control strategies one can envisage a system that is controlled to minimally interact with the human (patient-in-charge), at the other the system is controlled to, at least partly, take over human function (robot-in-charge). The effectiveness of either strategy will likely depend on the residual strength and motor control of the patient: severely impaired patients would rather require a robot in a robot-in-charge mode to ensure safety and continuity of movements, whereas patients with sufficient walking ability would benefit more from a device in a patient-in-charge mode that only intervenes when required during movements initiated and largely controlled by the patient. The ideal limits of the assistance level scale, namely full assistance (100% robot-in-charge) and zero assistance (100% patient-in-charge), respectively correspond with the robot providing the required power to generate its own and the patient's motion, and with the robot perfectly compensating its own dynamics, such that the presence of the device is not felt. Non-idealities, such as the uncompensated dynamics of the robot, yield negative assistance and cause a shift towards a challenge based situation as explained previously.

As discussed in the introductory chapter some properties of assistance based therapy can negatively affect motor learning and neural recovery. The assistance influences and eases the task to be relearned and as such it may induce a decrease of the patient's effort (Israel et al., 2006) and reduced or altered motor learning (Marchal-Crespo and Reinkensmeyer, 2008). This observation has led to a paradigm shift in robot-assisted rehabilitation of gait towards "assistance-as-needed". In order to maximise assistive therapy outcome the assistive controller should assist as much or little as needed for the specific task, while triggering the patient to maximise his/her own efforts. Initially, assistive controllers were conceived as (high feedback gain) position-based controllers with a fixed target trajectory (Colombo et al., 2001). Such an assisting environment does not promote nor allow patient induced variability of the gait pattern and therefore it can be considered almost equivalent to a pure robot-in-charge mode. With the assistance-as-needed paradigm focus has shifted towards adaptivity of assistance, both in the targeted function/task (task-specificity) and in the assistance level. The adaptivity of assistance is envisaged between different individuals, different phases in therapy and also online, within the individual training session. From the state-of-the-art overview in the introductory chapter it is clear how the paradigm shift has influenced robot design on the hardware level: compliance as a means to provide variability has found its way to actuator design, either in the form of an intrinsically compliant actuator, a passive compliant element in series with a stiff actuator, or a passive compliant element alone. The following non exhaustive overview is aimed at listing some of the different ways of implementing the assistance-as-needed concept on the control level.

Variability in assistance is generally achieved by means of one or a combination of the following concepts:

- task/function specific assistance
- adaptivity of the assistance level
- adaptivity of timing
- adaptivity in space

Task/function specific assistance implies that the assistance is tailored to the gait function(s), joint(s) or limb(s) that need(s) it and in the meantime assistance is reduced where it is useless or adverse. Hybrid force-position control has been used to promote free motion during swing (force control) while using position control during stance (Bernhardt et al., 2005a, Lokomat). A similar approach has been conceived for training of the hemiparetic: position control (Bernhardt et al., 2005a, Lokomat) or impedance control (Vallery et al., 2009, LOPES) of the impaired side and force control of the unaffected side. Another example of task-specific assistance is the use of Virtual Model Control (Ekkelenkamp et al., 2007, LOPES). A virtual model simulates a specific action that needs to be performed on the patient by means of the exoskeleton (eg. foot lift during swing, body weight support, ...). The virtual model control is implemented by means of impedance control (in joint space or task space) defining the interaction between the actual joint/limb motion and a moving or fixed target position. For several reasons different research groups have used force control to apply the zero assistance mode (patient-in-charge mode) also to the entire device: to record unassisted gait for use as target trajectories in a position/impedance control scheme (Aoyagi et al., 2007, PAM, van Asseldonk et al., 2007, LOPES) and as a reference or baseline for the assisted mode (van Asseldonk et al., 2008, LOPES). In order to approximate the ideal zero assistance level the robot's dynamics are modelled and partly compensated. In that case, instead of controlling the actuator output towards zero force/torque, the interaction forces/torques between the robot and the human are minimised.

Adaptivity of the assistance level is often accomplished by using a measure of the patient's effort or a measure of how well the patient performs a task either directly as a feedback control signal or indirectly as a means to scale one or more control parameter(s). Patient-driven motion reinforcement (Bernhardt et al., 2005a, Lokomat) belongs to the first category, since a support torque is calculated as the product of a scale factor and the (modelled) active torque exerted by the patient. In Duschau-Wicke et al., 2008 (Lokomat) the support torque, proportional to the error between the actual and target trajectory, is recalculated at every gait cycle by an iterative learning controller. The second category groups several variations on the parameter scaling approach depending on the underlying control scheme. A forgetting factor is used for instance on the PD gains of a position control scheme (Emken et al., 2008, ARTHuR) and on an error-based learning controller (Emken et al., 2005, ARTHuR) reducing the assistance over time and ensuring the patient is sufficiently challenged. In Riener et al., 2005 (Lokomat) the impedance control parameters are scaled with the patient's effort, such that a larger contribution of the patient allows for larger trajectory deviations.

Adaptivity of timing is always related to adaptivity in space and vice versa, since a gait pattern is defined both in space and time. Moreover, for position based control (eg. position control, impedance control) the timing and the amplitude of the target trajectory affect the assistance level as well. Imposing a target trajectory without imposing a related timing has been done by set point control or path control. In Banala et al., 2007 (ALEX) PD set point control is used in which the target position is only switched to the next set point if the actual position is close enough to the current set point. In Aoyagi et al., 2007 (PAM) the target trajectory of the PD controller is determined on the basis of the actual state of the robot and the target trajectory of the robot defined in state-space. A moving window limits candidate target trajectory points to points close to the actual state. The difference in timing between the two points is fed to a synchronisation algorithm that selects the appropriate target trajectory point. The approach in Duschau-Wicke et al., 2008 (Lokomat) combines impedance control with the aforementioned set point generation method and the use of a moving window. In addition, an automatic treadmill speed adaptation algorithm changes the treadmill speed according to an admittance control scheme, using the measured interaction force between the human and an external fixed reference as an input. Instead of altering time dependent trajectories, some methods generate a position dependent force field or velocity field. The force field controller proposed in Banala et al., 2009 (ALEX) displays a force tangential to a required foot trajectory inside a "virtual tunnel", a normal force towards the target trajectory outside that tunnel and a damping force to limit foot velocity. In Cai et al., 2006 two velocity field controllers are proposed. One has a virtual tunnel with tangential velocity inside and inward spiraling velocity outside, whereas the other has a small moving window with tangential velocity inside and a radial velocity field outside pointed towards the windows center.

Adaptivity in space is either achieved by altering the target trajectory of a position-based controller or it is intrinsic to a non-position-based controller (eg. force controller). The aforementioned force field and velocity field controllers are examples of the latter: the actual position can vary almost freely within the boundaries of the virtual tunnel. The force controllers discussed in the paragraph about task/function specific assistance also allow for patient-induced gait pattern adaptation. The same goes for the impedance controllers used in Lokomat (Riener et al., 2005), LOPES (Veneman et al., 2007) and WalkTrainer (Stauffer et al., 2009) and for the position controllers implemented in devices with intrinsically compliant or backdriveable actuators (ARTHuR, PAM, POGO (Reinkensmeyer et al., 2006)). Different target trajectory adaptation algorithms for position-based control have been proposed in Jezernik et al., 2004. These algorithms calculate a target gait pattern adaptation that minimises the active patient torque. In Vallery et al., 2009 the target trajectory of the impedance controller for the impaired leg is based on the recorded motion of the unimpaired leg fed to a so called "complementary limb motion estimation" algorithm. This allows for a patient-induced adaptation of gait both in space and in timing. The use of surface EMG sensors in a so called proportional myoelectric control should be mentioned as well (Gordon and Ferris, 2007; Lee and Sankai, 2002). Providing an output torque proportional to processed EMG signals indirectly puts the human in control of the timing and the level of assistance. EMG-based torque control thus fits in the previous categories as well.

3.1.1.2 Control of pneumatic muscle actuators

Position and tracking control Most of the research in pneumatic muscle control has been focused on position and tracking control. If the system consists of antagonistically configured muscles, these controllers invariably use some form of the Δp-approach (see section 3.3.1.1) to make the number of controller outputs equal to the number of degrees of freedom. Conventional PID position control has often been used for pneumatic muscle systems (Caldwell et al. (1993); Tondu et al. (1994); Caldwell et al. (2001); Caldwell and Tsagarakis (2002); Šitum and Herceg (2008)), sometimes complemented with a feedforward term in the controller. Modified versions of PID control have been reported in Schröder et al. (2003); Thanh and Ahn (2006a,b). The fact that the muscle parameters are usually not very well known has led several authors to propose adaptive controllers, as in Nouri et al. (1994); Medrano-Cerda et al. (1995); Caldwell et al. (1995). Lilly (2003); Zhang et al. (2007) also propose adaptive controllers for pneumatic muscle systems, but their work is purely simulation based. The difficulty in modelling systems actuated by pneumatic muscles has led to a lot of controllers that use soft computing methods (i.e. neural networks, fuzzy logic, evolutionary algorithms, ...), as reported in Hesselroth et al. (1994); van der Smagt et al. (1996); Eskiizmirliler et al. (2001); Carbonell et al. (2001a); Balasubramanian and Rattan (2003b); Chang and Lilly (2003); Balasubramanian and Rattan (2005); Chang et al. (2006); Yamazaki and Yasunobu (2007). Because of its robustness, sliding mode control has received a lot of attention as well, mostly in simulation based studies (Sira-Ramírez et al. (1996); Cai and Yamaura (1996); Repperger et al. (1998); Cai and Dai (2000); Raparelli et al. (2001); Carbonell et al. (2001b); Cai and Dai (2003); Lilly and Quesada (2004); Lilly and Yang (2005); Yang (2006)), but experimental work has been reported as well (Nouri et al. (1994); Hamerlain (1995); Tondu and Lopez (2000); Chettouh et al. (2006, 2008a,b); Van Damme et al. (2009b)). Computed torque or inverse dynamics control was used in Verrelst (2005); Hildebrandt et al. (2005); Vanderborght et al. (2006b); Verrelst et al. (2006b); Vanderborght et al. (2008a). Various other forms of nonlinear control have also been proposed, see Kimura et al. (1997); Carbonell et al. (2001b); Hildebrandt et al. (2002); Aschemann and Hofer (2006); Schindele and Aschemann (2008). In the work reported in Van Damme et al. (2009a) proxy-based sliding mode control is applied to achieve good trajectory tracking while ensuring a safe response to perturbations.

Force or torque control PID-based torque control based on joint torque measurements has been used in Tsagarakis and Caldwell (2003); Caldwell and Tsagarakis (2002); Costa and Caldwell (2006) for robot-assisted rehabilitation.

Sardellitti et al. (2007) proposes torque control based on pneumatic muscle force measurements, while Schröder et al. (2003) presents a controller with inner torque loop that is entirely model based, i.e. it doesn't use force or torque sensors. Noritsugu and Tanaka (1997) have presented an impedance controller using a force sensor in the tool-center point. Veneman (2007) proposes a linear block-oriented force controller based on feedback linearization.

Compliance control Since in an antagonistic setup two muscles control a single degree of freedom, it is possible to control compliance (the inverse of stiffness) in addition to position or torque. Simultaneous position and compliance control is presented in Clapa et al. (2006); Mao et al. (2006); Vanderborght et al. (2008b), and adaptive simultaneous position and compliance control in Tonietti and Bicchi (2002).

Open loop control As already noted by Inoue (1987), pneumatic muscle systems can be controlled without feedback, using only model-based feedforward control. This idea has been applied in Balasubramanian and Rattan (2003a); Sugar et al. (2007).

3.1.2 Challenges

In this work, controller design is faced with several important challenges related to the application, a powered knee exoskeleton for robot-assisted gait rehabilitation, and to the specific use of pneumatic artficial muscles.

An aspect of primary concern is safety. The general notion of safety covers a broad range of requirements with respect to hardware design, (control) software design and user protocols. The use of actuators with built-in mechanical compliance is an important safety measure on the level of hardware design. Hence, the behavior of the powered joint in response to an external torque will always be inherently compliant, regardless of the bandwidth of the controller. Nonetheless, the controller greatly influences the system's response and overall safety as well. Therefore, it may not counteract the intrinsic compliant behavior of the system. In addition the controller should ensure stability of the combined system of the robot and the human. Treating the stability of this coupled human-robot system is difficult for several reasons. The system is nonlinear and timevarying and it is characterised by large uncertainties due to the human that is part of the system. From the viewpoint of the robot, the environmental conditions (inertial, stiffness and damping properties of the joint, properties of the coupling) determined by the human vary constantly. As a consequence, a definition and analysis of stability is far more complex than it is the case for well-determined, time-invariant linear systems.

Another challenge is synchronising the device's behavior with the human. According to the assistance-as-needed concept the assistance should blend in with the patient's residual strength and motor control. This is especially the case for a unilateral device with a single powered joint, as considered in this work. Such a device (inter)acts locally, but affects the patient's gait globally and thus it should ideally collect global information to tune its assistance. In the case of a position-based control strategy the problem of tuning the level and the timing of the assistance boils down to what the target trajectory should look like, how it should be timed and how the feedback gains are to be set.

A third challenge concerns the translation of control concepts into different functionalities of the device and vice versa such that these concepts become transparent and useful to the device operator. Ultimately, the intended operator of the rehabilitation device, the physiotherapist, should be able to operate it in view of a rehabilitation target without any knowledge of low-level implementation.

The use of pneumatic artificial muscles brings about essential advantages, but also makes controlling the system more challenging. This is mainly due to the actuator's nonlinear characteristics, model uncertainties and the pressure dynamics. More specifically, one is confronted with the following:

- The nonlinear torque-angle characteristic of the PPAM powered joint: the torque output of the PPAM does not only depend on gauge pressure, but also varies nonlinearly with joint angle.

- The nonlinear compliance characteristic of the PPAM powered joint: the compliance of the joint is a nonlinear function of the gauge pressures and the joint angle.

- Hysteresis in the force-contraction relation of a PPAM: PPAMs display, albeit less pronounced compared with McKibben type muscles, hysteresis in the exerted force (the muscle's exerted force is higher during elongation than during contraction). A difference of about 5% is typically observed (Van Damme et al., 2008). In an antagonistic configuration, the hysteresis errors of each side add up, instead of compensating one another, since muscle contraction variations have opposite signs, regardless of the direction of rotation of the joint.

- Uncertainty on the geometrical parameters of the PPAM: the actual uncontracted length l_0 and minimal radius R of a PPAM do not exactly match the design values and they are difficult to determine.

- Inaccurate knowledge of the valve dynamics: the used servo valve is a priori a black-box system.

- Relatively slow pressure dynamics: relatively large time delays (over 100ms for large pressure steps) are observed between a control signal step being fed to the valve and the muscle pressure reaching steady-state. Many factors influence pressure dynamics: the dynamics of the valve, the pneumatic circuit, the supply pressure level, the volume change of the PPAM.

- The coupling between muscle gauge pressure and kinematics of the joint: the gauge pressure inside the muscle changes with inlet/outlet flow, but also with joint angle due to the changing muscle volume.

3.1.3 Approach

In this work two complementary control strategies are investigated. A torque controller is conceived to display an unassisted (patient-in-charge) mode and a trajectory tracking controller to display a safe assisted (robot-in-charge) mode.

Apart from serving as a baseline for evaluating the effects of robotic assistance, the patient-in-charge mode allows for the recording of target trajectories to be used in the trajectory based robot-in-charge mode. Additionally, the torque controller may serve as an inner torque control loop for the outer position control loop of the robot-in-charge mode. The torque control is achieved by means of conventional PI control using force sensor feedback combined with a feed forward term based on the actuator model. This controller is described in section 3.3.

For the robot-in-charge mode a system is envisaged that safely allows for trajectory deviations by combining the actuator's built-in compliance with a suitable trajectory tracking controller. The combination of trajectory tracking and a safe response to perturbations can be achieved with Proxy-based Sliding Control (PSMC, Kikuuwe and Fujimoto, 2006). This has been demonstrated experimentally in Kikuuwe and Fujimoto (2006) for a manipulator powered by electric drives and in Van Damme et al., 2009a for a manipulator arm powered by pleated pneumatic artificial muscles. Section 3.4 explains the characteristics of PSMC and describes the functional interpretation and required modifications when applying PSMC to robot-assisted gait training with KNEXO. The topic of trajectory generation and synchronisation is discussed separately in section 3.5. The models used in the control software and in simulations of the system are explained in section 3.2.

3.2 Modelling

3.2.1 Parameter estimation

Straightforward static models were used to relate the input and output voltage signals of the control software to the physical quantities of interest, namely the muscle gauge pressures, the valve pressures, the forces applied to the force sensors and the actuator torque.

3.2.1.1 Pressure sensors

The differential pressure sensors have a rated output voltage span of $[0.5 - 4.5]\,V$ for a gauge pressure span of $[0 - 5]\,bar$. Since they are susceptible of fabrication offset errors a calibration with a measurement standard has been performed using the standard linear relation between voltage V_p and gauge pressure p:

$$p = c_{1p} V_p + c_{0p}. \tag{3.1}$$

Coefficients c_{0p} and c_{1p} have been determined using a least squares estimate (see table 3.1).

3.2.1.2 Valves

The servo valves produce $1\,bar$ pressure per volt input signal. This gain can be considered constant, but pressure offset variations (up to $0.1\,bar$) are observed depending on the internal operating temperature of the valve. This temperature dependency is not modelled, but dealt with by recalibrating the offset by means of the differential pressure sensor. The relation between the valve output pressure p and the valve control signal voltage V_v is described by

$$V_v = c_{1v} p + c_{0v}, \tag{3.2}$$

and c_{0v} is recalculated in a short calibration procedure prior to every experiment performed with the device to take into account offset variations due to temperature. Coefficient c_{1v} has been determined using a least squares estimate (see table 3.1).

3.2.1.3 Force sensors

The custom made strain gage force sensors have been calibrated in a force test bench (Instron 4505H2267 electro-mechanical, $[0-10]\,kN$, 0.2% relative accuracy). A standard linear model relates the force F_{fs} acting on the sensor to its output voltage V_{fs}:

$$F_{fs} = c_{1fs} V_{fs} + c_{0fs}. \tag{3.3}$$

The output voltage is measured at the output of the signal conditioner/amplifier, set up as explained in section 2.5.2.3. Coefficients c_{0fs} and c_{1fs} have been determined using a least squares estimate based on data originating from several load cycles on the test bench between $[0 - 2500]\,N$ (see table 3.1). In order to verify

	p_1	p_2	$V_{v,1}$	$V_{v,2}$	$F_{fs,1}$	$F_{fs,2}$
c_{1x}	1.272	1.269	1.012	0.998	312	332
c_{0x}	-0.651	-0.658	[0.150... 0.250]	[0.050... 0.150]	$-$[145... 175]	$-$[35... 65]

Table 3.1: Estimated gains and offsets for pressure sensors, valves and force sensors.

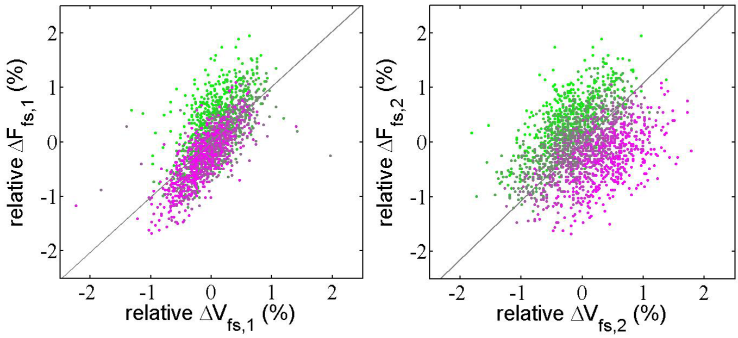

Figure 3.1: Force sensor signal long term stability: relative force deviations and relative voltage deviations with respect to average over a period of 17 hours (colormap indicates evolution in time from green→magenta). For each sensor the estimated gain c_1 is indicated by the slope of the grey line.

the short and long term stability of the voltage signals, measurements have been performed with a constant load (fixed mass) during short (a few minutes after power-on) and long periods (1-3 days). Figure 3.1 shows relative variations of the force measured by the test bench and the sensor output voltage with respect to the average signal values over a period of 17 hours (1 measurement/minute). The time of measurement is indicated by a colour map (green→magenta). Variations should be evaluated with respect to the estimated gain c_{1fs} of the sensor indicated by the grey line. Consecutive measurements tend to lie along virtual lines with similar slope. Long term variations are limited to about 1-2%. Figure 3.2 shows the force sensor signal quality with respect to short term variations at zero load. The large spikes in the blue (unfiltered) signal, which are also apparent from fig. 3.1, are due to high-frequency noise ($> 1\,kHz$) originating from the amplifier circuit. Since the sample frequency is $1\,kHz$, the high frequency noise is downsampled and distributed over the entire measurable frequency range. By means of a passive low pass filter the noise level is reduced significantly (reduction of variance: $0.9\,N^2 \rightarrow 0.06\,N^2$) . The offset parameter c_{0fs} is recalculated in a short calibration procedure prior to every experiment performed with the device.

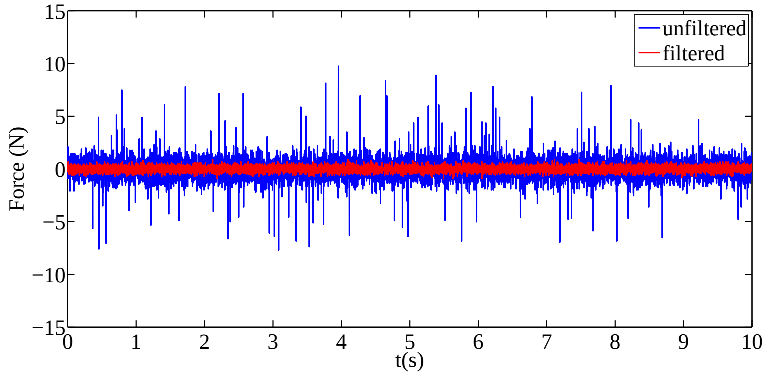

Figure 3.2: Force sensor signal quality: force sensor measurements based on voltage readings fed to eq. 3.3. With (red) and without (blue) passive low pass filter.

3.2.1.4 Actuator torque

It was shown previously in section 2.3.5.2 of chapter 2 that the actuator torque can be written as a function of gauge pressures,

$$\tau(q) = p_1 m_{\tau 1}(q) + p_2 m_{\tau 2}(q), \tag{3.4}$$

with $m_{\tau i}(q)$ the so called torque functions depending on the PPAM's geometry, the configuration and the four bar linkage, and as a function of the muscle forces,

$$\tau(q) = F_1 r_1(q) + F_2 r_2(q), \tag{3.5}$$

with $r_i(q)$ the lever arms depending on the configuration and the four bar linkage. Alternatively, the actuator torque can be written as a function of the forces $F_{fs,i}$, acting on the couplers of the four bar linkages and measured by the force sensors:

$$\tau_{fs}(q) = F_{fs,1} r"_1(q) + F_{fs,2} r"_2(q), \tag{3.6}$$

with $r"_i(q)$ the lever arms of the couplers given by $r"_i(q) = (\mathbf{OD}_\mathrm{i} \times \mathbf{D}_\mathrm{i}\mathbf{G}_\mathrm{i}).\mathbf{1}_z$ (see fig. 2.24 for notations). To avoid solving the linkage equations (see appendix A) the functions $r"_i(q)$ are approximated by a polynomial as given by

$$r"_i(q) = c_5 q^5 + c_4 q^4 + c_3 q^3 + c_2 q^2 + c_1 q + c_0, \tag{3.7}$$

with coefficients $c_0 \ldots c_5$ corresponding with the least squares estimate based on theoretical lever arm data (see table 3.2).

Due to uncertainties on the muscle geometry and on the initial muscle contraction set during the assembly of the actuator system, deviations between the theoretical and the actual torque functions can be expected, as reported in Verrelst (2005);

	c_5	c_4	c_3	c_2	c_1	c_0
$r"_1\,[10^{-3}]$	0.6213	1.396	-4.273	-12.21	13.07	53.74
$r"_2\,[10^{-3}]$	0.1770	0.06602	-3.628	5.177	13.31	-24.43
$m_{\tau 1}$	0.9082	-5.376	-36.46	-71.99	-55.02	5.344
$m_{\tau 2}$	-5.557	-25.80	-41.93	-28.54	-17.36	-17.24

Table 3.2: Estimated polynomial coefficients for lever arm functions and torque functions.

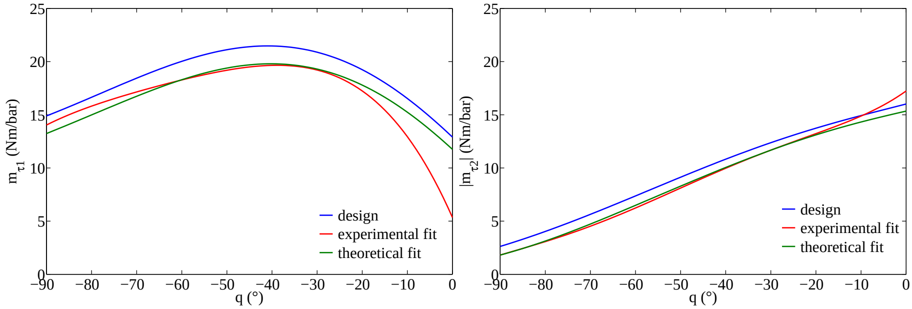

Figure 3.3: Torque function approximation for the extensor (left) and flexor (right) side of the actuator system: theoretical torque function by design (blue), torque function fit (eq. 3.8) based on measurements (red) and theoretical torque function approximation of the experimental fit (green).

Van Damme (2009). To remedy these deviations and to avoid solving the PPAM equations (see section 2.3.2.2) and the linkage equations (see appendix A) each torque function $m_{\tau i}(q)$ is approximated by

$$m_{\tau i}(q) = c_5 q^5 + c_4 q^4 + c_3 q^3 + c_2 q^2 + c_1 q + c_0, \tag{3.8}$$

with coefficients $c_0 \ldots c_5$ corresponding with the least squares estimate based on measured data (see table 3.2). The measured data, i.e. joint angle q, muscle pressure p_i and force $F_{fs,i}$ relate to the torque function $m_{\tau i}(q)$ as given by

$$m_{\tau i}(q) = \frac{F_{fs,i} r"_i(q)}{p_i}.$$

The fitted torque functions (red) are shown in fig. 3.3 and compared with the theoretical torque functions (blue) as calculated in section 2.3.5.

When comparing these functions, one should note that the experimental fit does not account for the hysteresis that is present in the PPAM's output and in the measurement data that has been fitted. As such it provides an underestimation of the output during muscle extension and an overestimation during muscle contraction. The difference in the hysteretic output can typically attain 5%. Accurately modelling this hysteresis effect is difficult, since it requires the hysteretic state of the muscle (initial conditions) to be known at start up (Van Damme, 2009).

Also, it should be noted that the experimental fit is more susceptible to errors in the range of small contraction levels (large flexion angles for the extensor PPAM and small flexion angles for the flexor PPAM) corresponding with high muscle forces and low muscle pressures.

As previously mentioned, the discrepancy between the designed and measured characteristics can be partially attributed to differences between the designed and actual values of muscle geometry (l_0, R) and initial contraction (ε_0). This is illustrated by the theoretical fit (green) that is found by applying small deviations to the aforementioned design parameters underlying the designed characteristic (blue). Both theoretical fits in fig. 3.3 result from a reduction of the parameters with $\triangle\varepsilon_0 = -1\%$, $\Delta l_0 = -0.001\,m$ and $\Delta R \approx -0.001\,m$, which are rather small and thus realistic parameter variations.

The large deviations for the extensor side at small flexion angles cannot be explained on the basis of the previous findings, but are due to a fabrication flaw. In spite of this, it was decided not to manufacture a substitute. Priority was given to implementing control strategies and performing experiments with healthy and impaired subjects with the actuator system as-is.

3.2.2 Simulation models

3.2.2.1 Mechanical model

Although the exoskeleton has one single powered degree of freedom (DOF), the coupling with the human body makes that the combined human-robot system requires quite elaborate and relatively complex models in order to accurately describe its dynamics. A 2D multi-body model of the human body alone that captures bending of the toes for instance, as suggested in fig. 2.3, would require a total of 9 body segments to be included. Besides the number of DOFs, one should decide on how to model the different joint torques or joint movements produced by the (un)impaired human and the interface between the human and the robot as well.

The approach followed in this work puts the focus on the principal functions of the (un-)assisted human knee joint, i.e. toe clearance during swing and limb support during stance, by means of simplified models of the human-robot system. The main objective of the simulations is to gain a qualitative insight into the performance to be expected from the controlled device and into the major points of attention when moving towards experiments.

For the mechanical model two gait phases are considered separately: the swing phase and the single support period of the stance phase of the leg to which the exoskeleton is attached. For both phases under study a 2 DOF link model bound to the sagittal plane is used.

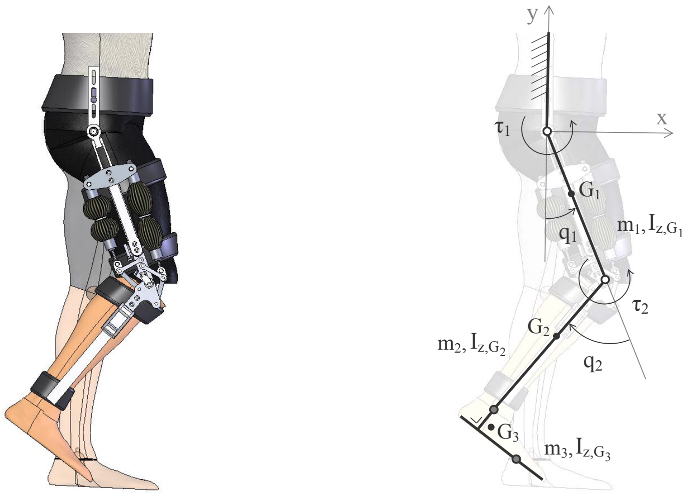

Figure 3.4: Mechanical model for the swing phase: 2 DoF link model (right) of the swing leg and the powered knee exoskeleton (left).

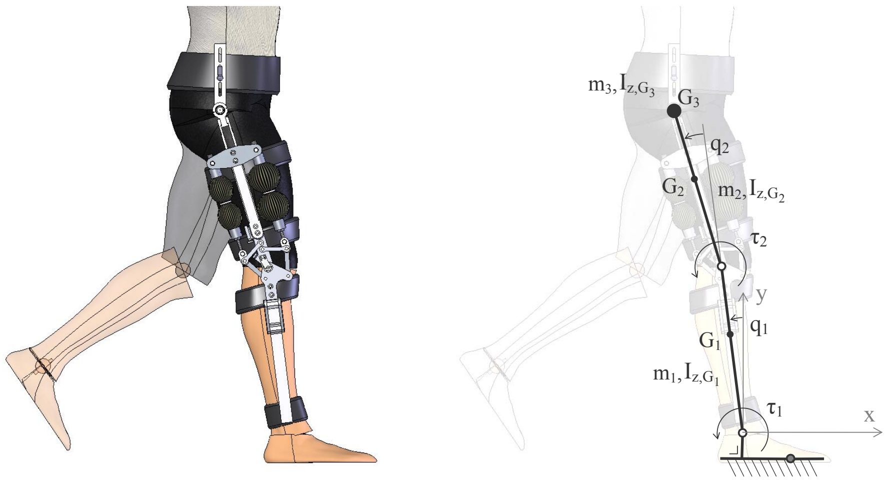

Figure 3.5: Mechanical model for the stance phase: 2 DoF link model (right) of the stance leg and the powered knee exoskeleton (left).

The models applying to the swing phase and the single support phase are illustrated by fig. 3.4 and fig. 3.5 respectively. It is assumed that the human-robot coupling is rigid and that the center of mass G_i of each link is located on the link.

In the model for the swing phase (see fig. 3.4) the upper body link is considered fixed. Motion of the foot relative to the lower leg is not taken into account. The mass, the center of mass and the moment of inertia about $\mathbf{1}_z$ of the upper and lower leg link account for the respective human body segments (anthropometric data taken from NASA (1978)) as well as for the respective exoskeleton segments (estimations based on measurements and CAD). The equations of motion of this 2 DOF link model can be written in the following form:

$$\boldsymbol{H}(\boldsymbol{q})\ddot{\boldsymbol{q}} + \boldsymbol{C}(\boldsymbol{q}, \dot{\boldsymbol{q}})\dot{\boldsymbol{q}} + \boldsymbol{G}(\boldsymbol{q}) = \boldsymbol{\tau}. \tag{3.9}$$

In this equation $\boldsymbol{q} = [q_1\ q_2]^T$ is the vector of joint angles and $\boldsymbol{\tau} = [\tau_1\ \tau_2]^T$ is the vector of "actuator" joint torques as indicated in fig. 3.4, $\boldsymbol{H}(\boldsymbol{q})$ is the inertia matrix, $\boldsymbol{C}(\boldsymbol{q}, \dot{\boldsymbol{q}})$ is the centrifugal matrix and $\boldsymbol{G}(\boldsymbol{q})= [\boldsymbol{G}_1\ \boldsymbol{G}_2]^T$ is the vector of gravitational torques acting in the joints. Each "actuator" joint torque τ_i is the net result of all torques τ_{hum} produced by the human actuators (see section 2.2.2) and all torques τ_{exo} produced by the exoskeletal actuators at that joint. At the hip joint the only contribution is produced by the human ($\tau_1 = \tau_{hum}$), whereas at the knee joint both the human and the exoskeleton contribute to the joint torque ($\tau_2 = \tau_{exo} + \tau_{hum}$).

The model for single support stance (see fig. 3.5) assumes that the foot is fixed in space and considers the lower and upper leg segments as previously explained for the swing phase. Unlike in the previous model, the upper body and the swing leg are simplified into a single point mass located in the hip joint with mass m_3 and moment of inertia I_{z,G_3}. This yields the inverted configuration of the 2 DOF link model depicted in fig. 3.4. The equations of motion of this model can be written in the same form as given by eq. 3.9, using the parameters as defined in fig. 3.5. At the ankle joint the actuator torque is produced by the human ($\tau_1 = \tau_{hum}$) and at the knee joint the actuator torque combines the torque generated by the human and by the exoskeleton.

The exoskeleton torque τ_{exo} is produced by the actuator system according to the approximation described in section 3.2.1. The human torque τ_{hum} is modelled depending on the case under study, as will be explained in the parts dedicated to simulation results in sections 3.3 and 3.4.

3.2.2.2 Pressure dynamics

The pressure dynamics model should at least reflect the principal characteristics of the entire pressure supply system consisting of the muscles, tubing, the valves and the supply buffer.

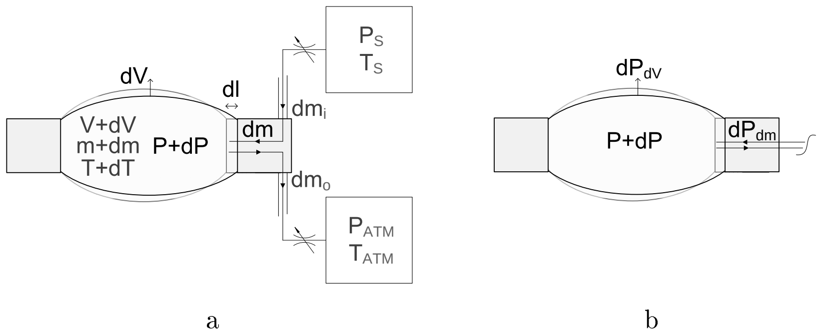

Figure 3.6: Open system pressure dynamics model: white-box model (a) and black-box model (b) of valve-tubing-supply system.

Hence, as mentioned in section 3.1.2, the pressure dynamics are relatively slow and therefore determinant in the dynamics of the actuator system's output. In Verrelst (2005) a thermodynamic model is proposed of a pneumatic system consisting of a PPAM. The system is modelled as an open thermodynamic system, where the control volume is defined as the muscle with tubing and where the orifice of the inlet/outlet valve is defined as the inlet/outlet to the control volume. Figure 3.6.a depicts a schematic of the system. The pressurised air inside the control volume is considered as an ideal gas, uniform over the control volume, and its thermodynamical state is determined by the absolute pressure P, volume V, temperature T and mass m. The variation dP of the pressure P follows from the first law of thermodynamics applied to the control volume, resulting in (Verrelst (2005))

$$dP = \frac{n}{V}(-PdV + rT_s dm_i - rT dm_o), \tag{3.10}$$

where r is the dry air gas constant ($287\,Jkg^{-1}K^{-1}$), T_s the supply air temperature, m_i and m_o the air mass flowing through the inlet and outlet respectively, and n the polytropic coefficient. A valve model should then be added that describes the dynamics of the mass flow(s) through the valve(s).

An alternative approach, reported in Van Damme et al. (2009a), does not rely on a white-box model of the valve-tubing-supply system. It starts from the model in eq. 3.10 and groups the pressure change contributions due to a change of volume (dP_{dV}) and to a change of air mass (dP_{dm}) such that

$$\begin{aligned} dP &= dP_{dV} + dP_{dm} \\ &= -n\frac{P}{V}dV + dP_{dm}. \end{aligned} \tag{3.11}$$

One should note that the contribution dP_{dV} has been introduced previously in the derivation of the compliance characteristic of the PPAM (see section 2.3.2.2).

Replacing infinitesimal variations ($d\bullet$) with time derivatives ($\dot{\bullet}$) in eq. 3.11 and taking into account that $P = p + P_{ATM}$ holds and that the change of the muscle volume is related to the change of the joint angle q, leads to

$$\dot{p} = -n\frac{(p + P_{ATM})}{V}\frac{dV}{dq}\dot{q} + \dot{p}_{dm}. \tag{3.12}$$

The effect on muscle pressure of the servovalve's air mass flow is approximated by a black-box first-order model as given by (Van Damme et al., 2009b)

$$\dot{p}_{dm} = -\frac{p}{T_v} + \frac{p_d}{T_v}, \tag{3.13}$$

where p_d is the desired muscle gauge pressure and T_v is the time constant of the valve system. Combining eq. 3.12 and eq. 3.13 yields the approximated pressure dynamics

$$\dot{p} = -n\frac{(p + P_{ATM})}{V}\frac{dV}{dq}\dot{q} - \frac{p}{T_v} + \frac{p_d}{T_v}. \tag{3.14}$$

3.3 Torque control

3.3.1 PI torque control with model based feedforward

The system output variable to be controlled, the actuator torque, can be written as a function of the system input variables, the gauge pressures, as given by the established torque formula

$$\tau(q) = p_1 m_{\tau 1}(q) + p_2 m_{\tau 2}(q). \tag{3.15}$$

Hence, an infinite number of pressure value pairs satisfies this formula and therefore an additional equation needs to be included that, together with eq. 3.15, yields one single solution for p_1 and for p_2.

3.3.1.1 Δp-approach

An additional equation can be found by considering the intrinsic joint stiffness K (see section 2.3.4.1, eq. 2.40) as an additional system output. The set of equations relating them to the system input variables p_1 and p_2 is given by

$$\begin{cases} \tau & = p_1 m_{\tau 1} + p_2 m_{\tau 2} \\ K & = p_1 K_1 + p_2 K_2 + P_{ATM} K_{ATM} \end{cases}. \tag{3.16}$$

Alternatively, instead of considering an additional system output, a set of intermediate control variables, namely p_m and Δp, can be used such that

$$\begin{cases} p_1 & = p_m + \Delta p \\ p_2 & = p_m - \Delta p \end{cases} \tag{3.17}$$

holds. This so called Δp-approach (Inoue, 1987) defines a mean pressure p_m for both muscles and a pressure difference Δp. The main advantage of this approach is that the pressures can be easily set in a way that the entire allowable pressure range can be covered by the controller. This is the case when $p_m = p_{MAX}/2$. At this set point the controlled system can achieve the entire feasible torque range regardless of the joint angle by means of the proper Δp. The torque τ can thus be set according to

$$\begin{cases} \tau & = p_m(m_{\tau 1} + m_{\tau 2}) + \Delta p(m_{\tau 1} - m_{\tau 2}) \\ p_m & = p_m \end{cases}, \tag{3.18}$$

which, given eq. 3.17, is equivalent with

$$\begin{cases} \tau & = p_1 m_{\tau 1} + p_2 m_{\tau 2} \\ p_m & = \frac{p_1 + p_2}{2} \end{cases}. \tag{3.19}$$

Besides Δp and p_m one could consider other intermediate control variable pairs, as long as they are a function of the system input variables p_1 and p_2. For instance Δp and F_m, the mean pulling force of the muscles (as considered by Sardellitti et al. (2007)), or Δp and C_m, the mean torque amplitude of the muscles. In the case of non-symmetrical muscle configurations (different force/torque characteristics for each side) it is less straightforward to cover the entire torque range with these variables than it is the case with p_m, since their set points need to be adapted with the joint angle and with the required torque. Therefore the Δp-approach has been implemented in all controllers used in this work.

3.3.1.2 Controller

Given a set point for the mean pressure p_m, the torque controller calculates the appropriate Δp such that the actuator torque τ matches the desired torque τ_d. In the absence of modelling errors, the appropriate Δp, denoted by Δp_{FF}, is straightforwardly found by means of the model-based torque formula in eq. 3.20:

$$\Delta p_{FF} = \frac{\tau_d - p_m(m_{\tau 1} + m_{\tau 2})}{(m_{\tau 1} - m_{\tau 2})}. \tag{3.20}$$

A feedback term, denoted by Δp_{PI}, consisting of a proportional and an integral error term, is added to compensate the output for the model errors in eq. 3.20:

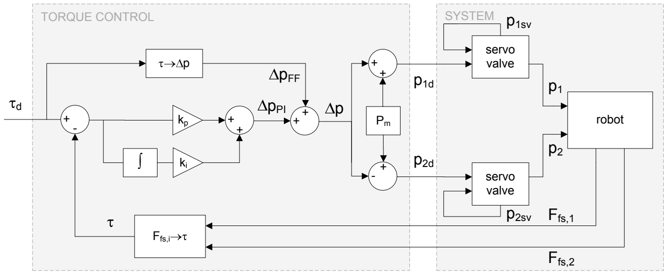

Figure 3.7: Control scheme of the implemented PI torque controller with model-based feedforward.

$$\Delta p_{PI} = k_p(\tau_d - \tau) + k_i \int_{t_0}^{t_1} (\tau_d - \tau)dt, \tag{3.21}$$

where τ is the torque based on force sensor measurements as given by eq. 3.6 and k_p and k_i are the proportional and integral gain respectively. The integral term is bound to avoid integral wind up. Addition of the feedforward and feedback terms yields the control law for the torque controller output:

$$\Delta p = \Delta p_{FF} + \Delta p_{PI}. \tag{3.22}$$

The control scheme is depicted in fig. 3.7.

3.3.2 Performance evaluation

The purpose of the torque controller is twofold: to serve as an inner torque control loop that tracks the torque set point of a trajectory controller and to display an unassisted mode for the exoskeleton by controlling the actuator system output towards zero torque. In the following sections the performance of the controller with regard to torque tracking and displaying zero torque is discussed.

3.3.2.1 Torque tracking

In order to gain insight in the torque tracking performance of the controller, the dynamic response of the controlled actuator system in isometric conditions ($\dot{q} = 0$) has been investigated on the test setup depicted in fig. 3.8.

For linear systems the dynamic response is often characterised by the bandwidth defined on the basis of transfer function measurements (frequency response function (FRF) measurements).

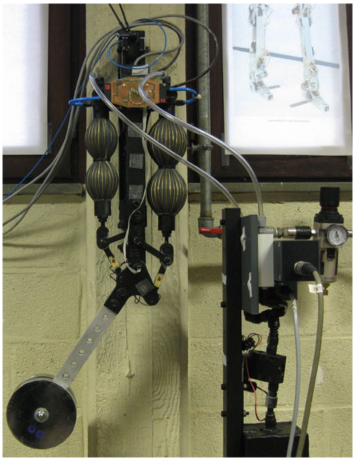

Figure 3.8: Test setup for control performance evaluation.

Provided a known periodic excitation signal with period T, denoted $u(t)$, fed to a linear system $g(t)$ and a measured system output signal $y(t)$, the frequency response function value $G(j\omega_k)$ at frequency f_k is calculated as

$$G(j\omega_k) = \frac{Y(k)}{U(k)}, \tag{3.23}$$

where $U(k)$ and $Y(k)$ are the discrete Fourier transform values at frequency f_k of $u(t)$ and $y(t)$ respectively, $\omega_k = 2\pi f_k$ and $f_k = k/T$ with $k = 1 \dots F \in \mathbb{N}$ (Papoulis, 1962). The bandwidth is the frequency f_k at which the magnitude spectrum of $G(j\omega_k)$, expressed in dB ($20\log_{10}()$), drops by $3\,dB$ relative to the magnitude near $0\,Hz$. The magnitude of $G(j\omega)$ at this $-3\,dB$ point corresponds with 70.7% of the magnitude at $f_k = 0$.

In the case of the controlled actuator system the input signal is a desired torque trajectory $u(t) = \tau_d(t)$ and the output signal is the measured actuator torque $y(t) = \tau(t)$. The system under study is, however, nonlinear: the system's response depends on the amplitude of the input signal $u(t)$ or, in the frequency domain, on the magnitude and phase of the spectral content of $u(t)$ (i.e. $U(k)$, $k = 1 \dots F$). This is due to the underlying nonlinear relationship between valve pressure set point and measured muscle force as reported in Davis et al. (2002) for an isometric setup of a McKibben type muscle and in Versluys et al. (2009b) for an isometric setup of a PPAM. Consequently, the function as calculated by means of eq. 3.23 is not an input-independent characteristic of the system and since the aforementioned $-3\,dB$ point varies with the input signal, it does not characterise the system's dynamic response.

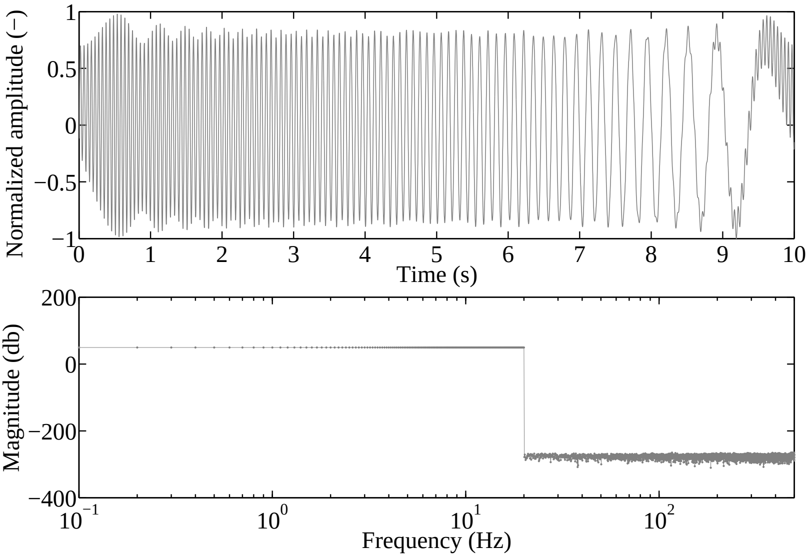

Figure 3.9: Multisine input signal: normalised time domain signal (top) and its magnitude spectrum (bottom) with $\tau_O = 0\,Nm$ and $f_k \in [0.1\;20]\,Hz$.

In order to study the influence of the amplitude of the input signal's spectrum and of the controller settings on the dynamic response of the system eq. 3.23 was still used to capture the input-output relation of the system in the frequency domain. One should bear in mind that these results cannot be generalised, regardless of the input signal. The input signal that was used here is based on a Schroeder multisine signal $s(t)$ given by

$$s(t) = \sum_{k=1}^{F} A\cos(2\pi f_k t + \phi_k), \tag{3.24}$$

where ϕ_k are the Schroeder phases defined by $\phi_k = -k(k+1)\pi/F$ (Pintelon and Schoukens, 2001). This signal has a flat spectrum in the user-defined frequency band $[f_1\;f_F]$, for which $f_k = l_k/T$ with $l_k \in \mathbb{N}$ and T being the period of the multisine signal. The phase relations of the harmonically related sine waves are such that the signal's crest factor (the ratio of the signal's peak value to the signal's rms value) is lower compared with a random phase multisine signal. The frequency lines were chosen according to $l_k = 1\ldots F$, the peak value was scaled to τ_A and an offset τ_O was added to obtain the input signal $\tau_d(t)$ given by

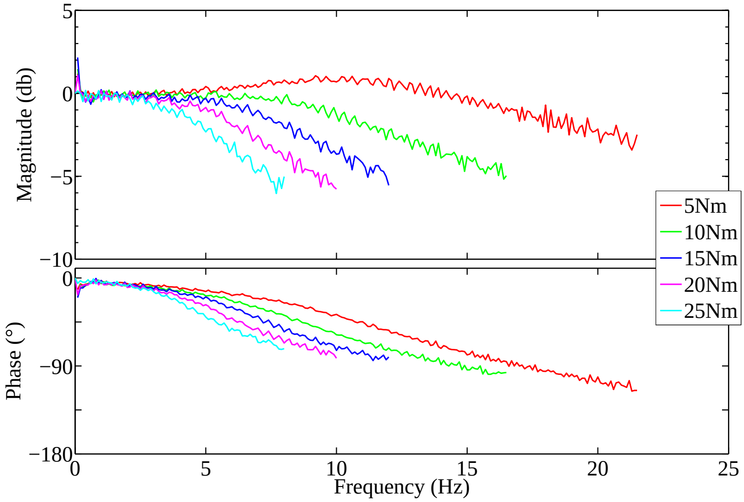

Figure 3.10: Influence of the input signal's amplitude on the system's dynamic response: magnitude spectrum (top) and phase spectrum (bottom) of $G(j\omega)$ for different values of τ_A.

$$\tau_d(t) = \tau_A \frac{s(t)}{\max(\text{abs}(s(t)))} + \tau_O \tag{3.25}$$

(see fig. 3.9). The normalised input signal in fig. 3.9 for instance is obtained by setting $\tau_O = 0\,Nm$ and choosing the period $T = 10\,s$ and $F = 200$ such that $l_k = 1 \ldots 200$ and $f_k \in [0.1\ 20]\,Hz$. In the performed experiments, multiple periods of the multisine signal are fed to the system sequentially and the retrieved output signal is averaged over all periods in the time domain prior to applying the Fourier transformation and calculating the ratio of the averaged output spectrum over the input spectrum according to eq. 3.23. The magnitude of this ratio will be referred to as the (input-dependent) gain of the system. Unless noted otherwise the controller settings during these experiments are $k_p = 0.1\,bar/Nm$, $k_i = 0.05\,bar/Nm.s$ and $p_m = 1.5\,bar$, and the joint angle is fixed at 30°.

As expected the input signal's amplitude indeed influences the gain of the system, as can be seen in fig. 3.10. Ideally, the magnitude (dB) and phase (°) are both zero regardless of the input signal. For frequencies above a certain frequency band the magnitude drops and the phase lag between output and input signal increases more rapidly. This frequency band decreases with increasing input signal amplitude, while the magnitude drop increases. The spikes in the spectra are due to system nonlinearities and not to measurement noise, as the standard deviation on a series of response measurements was found to be around $-[50-60]\,dB$.

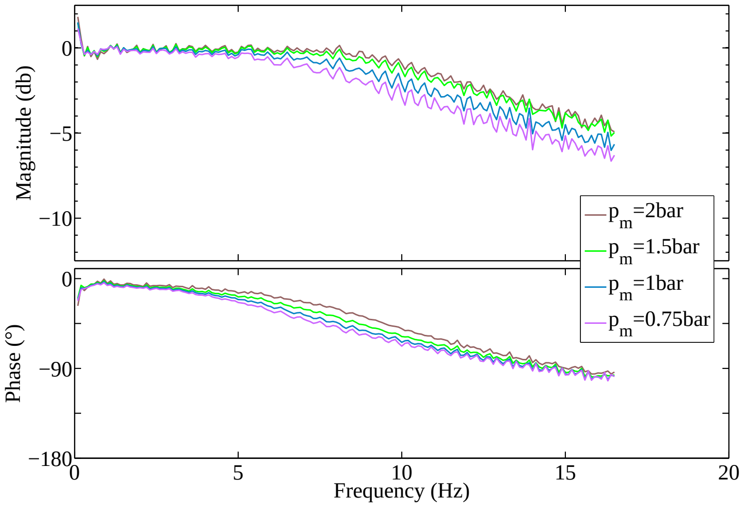

Figure 3.11: Influence of the mean pressure on the system's dynamic response: magnitude spectrum (top) and phase spectrum (bottom) of $G(j\omega)$ for different values of p_m and with $\tau_A = 10\,Nm$.

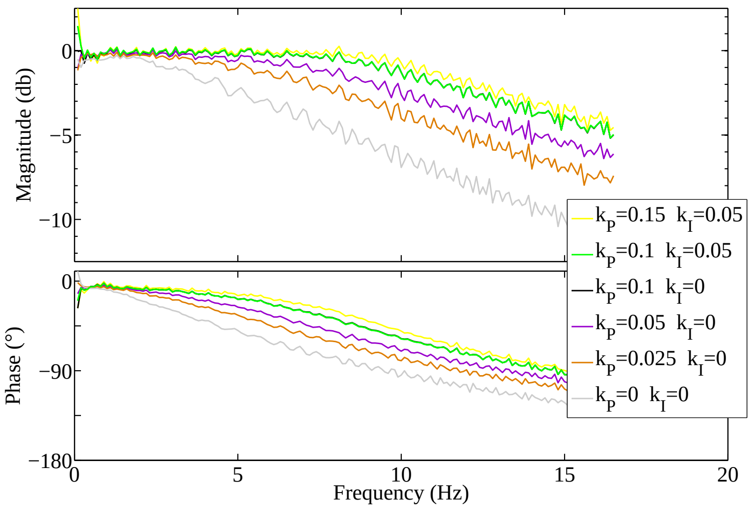

Figure 3.12: Influence of the controller gains on the system's dynamic response: magnitude spectrum (top) and phase spectrum (bottom) of $G(j\omega)$ for different values of k_p and k_i and with $\tau_A = 10\,Nm$. Note: the green curve covers the black one.

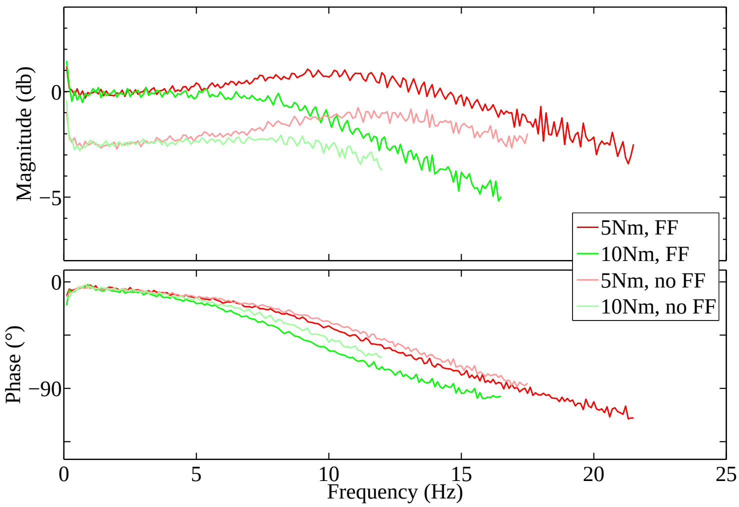

Figure 3.13: Influence of the controller's feedforward term on the system's dynamic response: magnitude spectrum (top) and phase spectrum (bottom) of $G(j\omega)$ in case the feedforward term Δp is turned on (straight line) or off (dotted line).

The influence of the input signal's offset is not illustrated here, since it largely depends on the pressure range that the actuator system covers while responding to the input signal. No significant influence has been observed for small offsets. Control performance does deteriorate if the required muscle pressure approaches zero gauge pressure, since in that case the time needed to deflate the muscle volume increases significantly. This is due to the fact that the pressure difference between the muscle and the exhaust that acts as a driving force for the outlet mass flow becomes small. Since the muscle pressure range is centered around the mean pressure p_m, the latter should be chosen such that pressures close to zero gauge pressure are avoided. This can be inferred from fig. 3.11.

The influence of controller gains k_p and k_i can be observed in fig. 3.12. Omitting the integral term has no significant influence on the system's dynamic response (black curve covered by green curve in fig. 3.12). It does introduce a steady state error, however, which has been observed, but cannot be inferred from this graph. Decreasing the proportional gain k_p adversely affects the system gain. The proportional gain was not increased beyond $0.15\,bar/Nm$, because during prior step response experiments undesired oscillations tended to occur at higher gain settings. The grey curve shows the system's response in the case of a feedforward term only ($k_p = 0$, $k_i = 0$).

The necessity of the model-based feedforward term Δp_{FF} is apparent from fig. 3.13. Especially at low frequencies the gain drops significantly if $\Delta p_{FF} = 0$. This

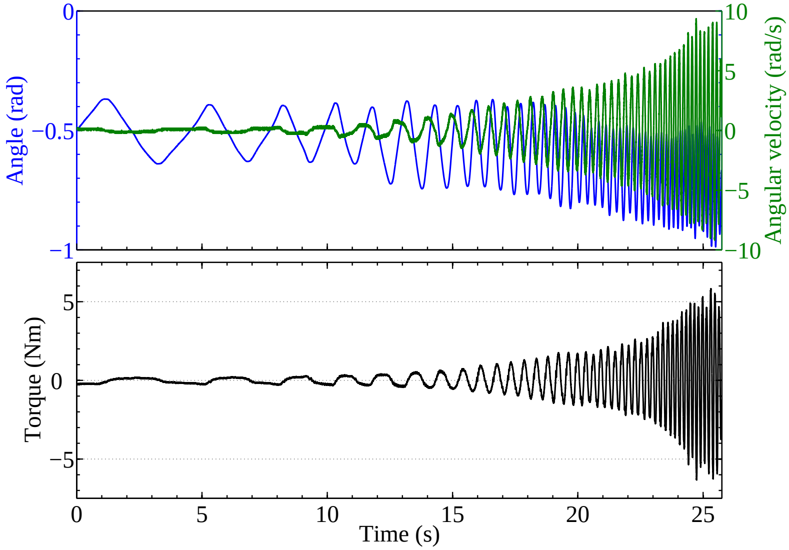

Figure 3.14: Actuator torque resulting from a manually imposed joint angle trajectory: time domain signals of joint angle and angular velocity (top) and actuator torque (bottom) with $p_m = 0.5\,bar$, $k_p = 0.1\,bar/Nm$, $k_i = 0.05\,bar/Nm.s$.

cannot be compensated much by increasing the controller gains since increasing k_p beyond $0.15\,bar/Nm$ causes instability. Since the feedforward term is based on a static model (see eq. 3.20), its added value when compared to PI control alone is more pronounced at low frequencies in terms of the gain and it introduces a small additional phase lag at high frequencies.

The aforementioned results have been obtained in the condition $\dot{q} = 0$. It can be expected that the dynamic response is also dependent of $\dot{q}$ in the case of the joint angle not being constrained. As explained in section 3.2.2.2, the pressure dynamics are influenced by the muscle volume change with the joint angle as well. This influence will be addressed in the following section.

3.3.2.2 Zero torque

In order to evaluate the performance of the torque controller in achieving zero actuator torque, a swept sine like motion has been imposed manually while the torque set point was kept equal to zero. Typical time domain signals resulting from such an experiment are shown in fig. 3.14. Considering the measured joint angle $q(t)$ as the input $u(t)$ to the system and the actuator torque $\tau(t)$ as the measured output $y(t)$, one could study their relationship in the frequency domain,

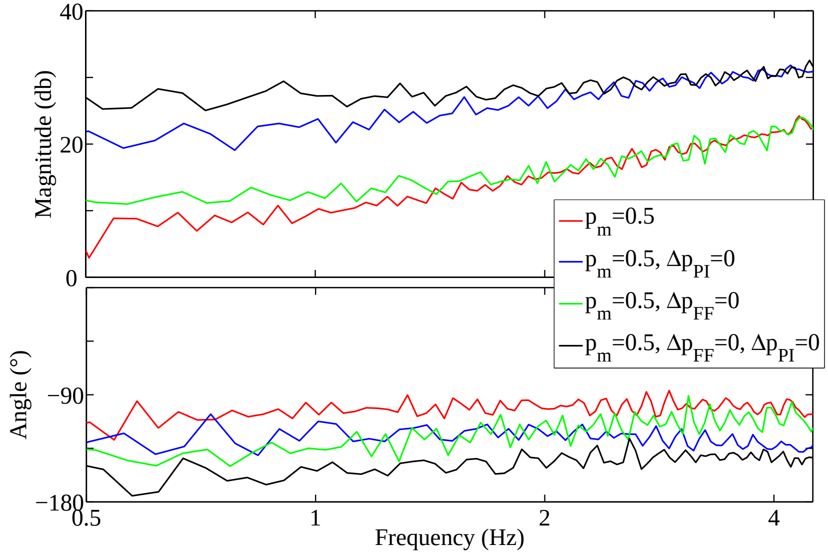

Figure 3.15: Influence of controller settings on the system's dynamic stiffness at $p_m = 0.5\,bar$: magnitude spectrum (top) and phase spectrum (bottom).

as was done previously, by evaluating the ratio of the spectra as given by eq. 3.23. This ratio can be viewed as the system's input-dependent dynamic stiffness. Since the input signal is ill-conditioned (not periodic, no flat power spectrum) the frequency domain analysis is more susceptible to errors when compared with the multisine signal. Most of the input signal's power is concentrated in a frequency band of $[0.5-4.5]\,Hz$ and all results shown are therefore limited to this range. The angular velocities corresponding with these frequencies typically ranged between $[0-10]\,rad/s$, which is the range we expect in our application (see 2.3.1 in chapter 2).

Figure 3.15 and 3.16 show the magnitude and phase spectrum of the system's dynamic stiffness at $p_m = 0.5\,bar$ and $p_m = 1.5\,bar$ respectively. A comparison between the two mean pressure settings is made in fig. 3.17. One should note that all frequency axes are logarithmic.

From these figures it is clear that the torque controller (data in red and orange) achieves a dynamic stiffness reduction of 20→10db (i.e. about a factor 10→3) in this frequency range when compared with the condition in which the controller is switched off (data in gray and black). In that condition the magnitude spectrum is more flat and the phase spectrum lies closer to -180°, indicating that the system rather acts as a pure mechanical stiffness, characterised by a constant magnitude and phase of -180°. The remaining increase of magnitude with frequency is due to the pressure control by the valves (the pressure set points for the valves are in this

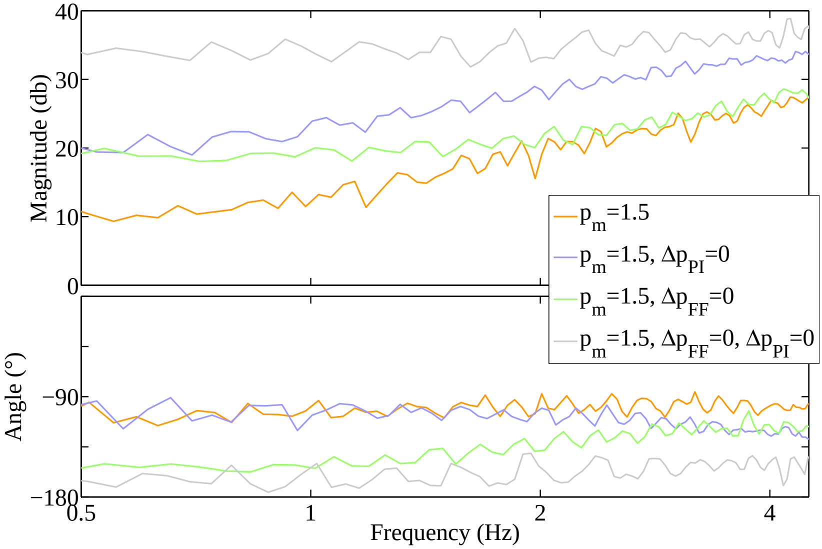

Figure 3.16: Influence of controller settings on the system's dynamic stiffness at $p_m = 1.5\,bar$: magnitude spectrum (top) and phase spectrum (bottom).

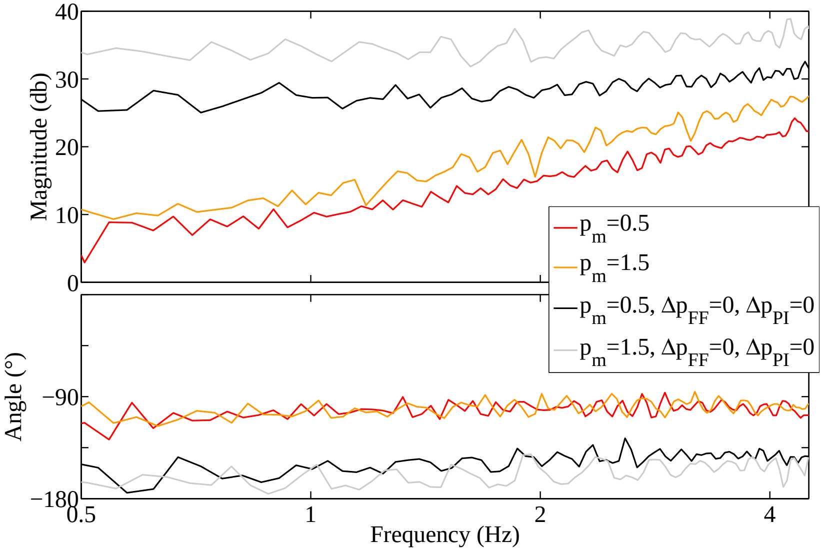

Figure 3.17: Influence of the mean pressure on the system's dynamic stiffness: magnitude spectrum (top) and phase spectrum (bottom) for $p_m = 0.5\,bar$ and $p_m = 1.5\,bar$.

case constant and equal to p_m) and at higher frequencies this increase is expected to saturate at the system's intrinsic stiffness as explained in section 2.3.4.1. Curves associated with the controller (partially) switched on are expected also to approach that same intrinsic stiffness level. The controlled system (data in red and orange) rather acts as a pure damping, characterised by a magnitude increasing linearly with $log(f)$ and a phase of -90°. This can also be inferred from the apparent proportionality of the torque and velocity signals in the time domain in fig. 3.14.

The feedforward term Δp_{FF} appears to be useful at low frequencies only, which is in accordance with the observations made in the previous section. A magnitude decrease of about $10\,dB$ (orange versus green curve in fig. 3.16) at low frequencies proves the feedforward term to be indispensable to the controller's performance in displaying zero torque.

3.3.3 Conclusion

A torque controller was proposed for the robot joint powered by PPAMs, that uses force sensor feedback in a standard PI control scheme and a feedforward term based on a static model of the actuator torque. In view of its use as the inner torque control loop of a trajectory tracking controller on the one hand and as a zero-torque controller on the other hand, the controller's performance has been evaluated experimentally for torque tracking in isometric conditions and zero torque tracking. In both cases the system's dynamic response was analyzed in the frequency domain.

Due to the nonlinearity of the underlying pressure dynamics the system's response is highly dependent of the required torque trajectory. For a multisine input signal with a peak value of $5\,Nm$ gains between required and measured torque of above 70% were found in a frequency band up to $20\,Hz$. In the case of a peak value of $25\,Nm$ gains above 70% were found in a frequency band of $6\,Hz$ (over 90% up to $3\,Hz$). The observed performance is in the range of the actuator system requirements listed in section 2.3.1 of chapter 2, where maximum torque amplitudes up to $25\,Nm$ ($50\,Nm$ peak-to-peak) at $3.5\,Hz$ were stated as a maximum torque rating during slow to moderate walking.

The feedforward term proves to be essential to the controller's performance, especially at low frequencies of the required torque signal, as the feedforward is based on a static actuator model. Since the pressure dynamics govern the system's dynamic response it is important to monitor the pressure range of operation in order to avoid slow outlet flow rates near zero gauge pressure.

Under zero torque tracking the actuator torque amplitude typically stays below $2\,Nm$ at the angular velocities expected during normal operation (up to about $5\,rad/s$ according to the actuator system requirements in section 2.3.1 of chapter 2). With increasing angular velocity (increasing frequency of the input) the system's response is increasingly governed by the intrinsic stiffness of the joint. However, within the velocity range of our interest the torque controller decreases the system's dynamic stiffness by a factor 10. In this range the feedforward term almost equally contributes to the stiffness decrease when compared with the feedback term, proving its necessity for zero-torque tracking as well. In chapter 4 it will be investigated whether the stiffness reduction achieved with the proposed zero-torque controller is sufficient in view of unassisted walking with KNEXO.

3.4 Trajectory control

As pointed out in the introductory section, most gait assistance controllers are essentially trajectory-based (e.g. position control, impedance control). Conventional trajectory control applied to a compliant system in view of gait assistance may lead to a conceptual mismatch. Very accurate tracking is indeed not required. In a typical feedback scheme large perturbations trigger proportionally large restoring actions, which may be undesirable and unsafe in some cases. An exemplary case is the occurrence of spasticity of the leg muscles in persons with neurologic disorders such as spinal cord injury, multiple sclerosis and stroke. Thus, while in some cases, e.g. foot clearance during swing to avoid stumbling, trajectory tracking and safety are compatible objectives, in others they can be competing. Therefore Proxy-based Sliding Mode Control was investigated in this work, as it combines trajectory tracking during normal operation with an appropriately slow and gentle response to large perturbations.

3.4.1 Proxy-based sliding mode control

3.4.1.1 Introduction

Proxy-based sliding mode control (PSMC) was introduced by Kikuuwe and Fujimoto (2006) and tested on a 2 DOF robot powered by electric drives. Van Damme et al. (2009a) implemented PSMC on a 2 DOF manipulator powered by PPAMs. The manipulator is conceived as a device that carries a payload, while interacting closely with a human operator. It was shown that the use of PSMC effectively increases safety in a setting where a human-robot collision can take place (Van Damme et al., 2010). According to Van Damme et al. (2010); Van Damme (2009), intrinsic compliance alone is useful but not sufficient for robot safety in all cases (e.g. large deviations from the desired position) and therefore compliance on the hardware level should be combined with a suitable controller.

In this dissertation the effectiveness of PSMC in safe, compliant and adaptable robotic assistance of gait is investigated and verified experimentally. In what follows, the controller behaviour is explained and the underlying control law is given. The deduction of the discrete time control law is given in detail in appendix B.

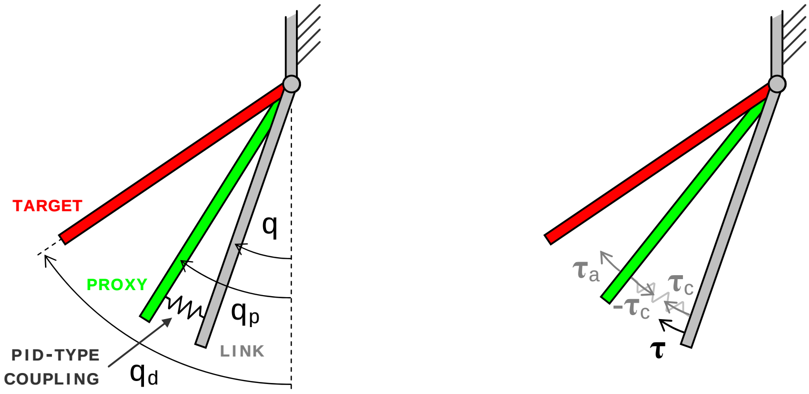

a b

Figure 3.18: Proxy-based sliding mode control applied to a 1 DOF robotic joint: a) proxy (green) and virtual coupling, b) PSMC torque τ acting on the link (grey), ideal sliding mode control torque τ_a acting on the proxy (green), PID-type virtual coupling torque τ_c acting between the proxy and the link.

3.4.1.2 General concept

For easier interpretation, a 1 DOF robotic joint is considered in the horizontal plane as shown in fig. 3.18.a. Apart from the actual link (grey), the target (red) is depicted that defines the desired trajectory. In proxy-based sliding mode control (PSMC) a virtual object or "proxy" is considered that has no mass. The proxy (green), in this case a massless virtual robot link, is connected to the real link by means of a PID-type virtual coupling. This PID-type virtual coupling generates an interaction torque that drives the proxy and the link towards each other. Since there is no mechanically equivalent representation of an element generating a proportional-derivative-integral action, the coupling is represented only by a spring in fig. 3.18.a.

As indicated in fig. 3.18.b, there are two torques acting on the proxy: a virtual actuator torque τ_a, and an interaction torque $-\tau_c$ due to the PID-type virtual coupling. The virtual actuator torque τ_a is set by an ideal sliding mode controller in order to track the target trajectory, while the magnitude of this torque is limited by an adjustable torque limit parameter τ_{LIM}. The interaction torque τ_c exerted by the PID-type virtual coupling on the real link is the actuator torque that is actually set by the proxy-based sliding mode controller and applied to the link. As a result the link is PID controlled towards the proxy, which in turn is controlled by the ideal sliding mode controller in order to track the target.

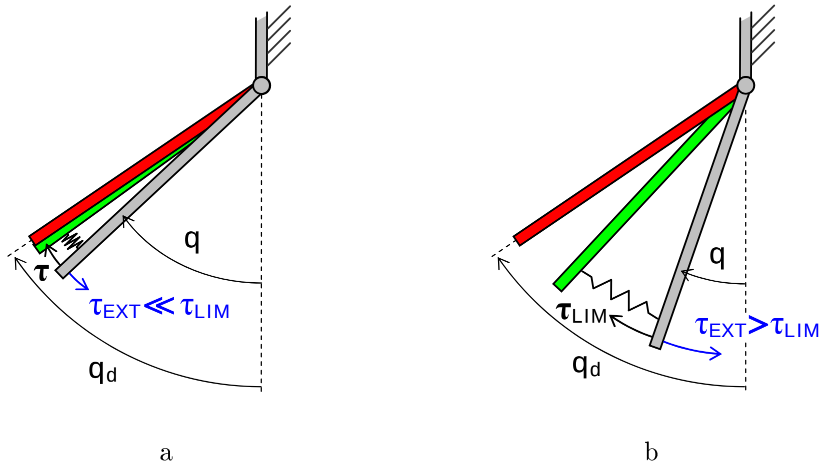

Figure 3.19: Controller behaviour under proxy-based sliding mode control: a) PID-control-like ($\tau_{EXT} \ll \tau_{LIM}$), b) sliding mode control-like ($\tau_{EXT} > \tau_{LIM}$).

3.4.1.3 Controller behaviour

It is clear that a proxy-based sliding mode controller encompasses two different controllers: a PID-type controller acting between the proxy and the link, and an ideal sliding mode controller acting on the proxy. The resulting controller combines the behaviour of both controllers and depending on the target deviation it will either behave largely like a PID controller or rather as a sliding mode controller. In the case of small deviations the proxy is close to the target and, provided that the PID gains are well tuned, the real link tracks the proxy and thus the target closely as if it were PID controlled towards the target. In the case of large deviations the sliding mode controller will dominate and the motion of the proxy will be characterised by a slow and exponential convergence (while being on its, so called, sliding surface; see 3.4.1.4) towards the target without overshoot, which is a key property of sliding mode control. Due to the PID-type coupling the link will follow the proxy and perform a slow recovering motion towards the target.

To gain insight in the role of the actuator torque limit τ_{LIM} in the behaviour of the controller in the event (or absence) of external torques, a 1 DOF robotic link in the horizontal plane is once more considered in fig. 3.19.

If the position error is small and in the absence of any external torque applied to the link, the proxy is on its sliding surface (see 3.4.1.4) and it converges towards the target. Since there is no external torque acting on the link, the link follows the proxy (and the target) closely. If an external torque τ_{EXT} is applied to the link that is working against the actuators (see fig. 3.19.a), the link is deviated from the proxy. As long as τ_{EXT} is such that the PSMC torque τ_{PSMC} stays below the torque magnitude limit τ_{LIM}, the proxy can keep up with the target and the link behaves as if it were controlled towards the target by a PID controller. The controller's response will thus be largely determined by the PID-type virtual coupling and by the PID gains.

If the restoring PSMC torque reaches τ_{LIM} due to an increasing τ_{EXT} and the latter is being further increased the proxy cannot be kept on its sliding surface, since the sliding mode controller torque saturates at τ_{LIM}. The proxy is pulled away from the target and the link is thus further deviated from the target, while undergoing a restoring torque with magnitude τ_{LIM} exerted by the coupling (see fig. 3.19.b). If the external torque is removed in this state, the proxy will be driven towards the target and once the sliding surface is reached it will slowly converge to the target with a convergence rate that is determined by a sliding mode time constant λ. The controller's response will thus be largely determined by the sliding mode controller part and by the time constant λ.

Summarising the aforementioned characteristics, one infers that PSMC combines responsive and accurate PID-like tracking during normal operation with a slow recovery from large deviations from the target trajectory. The advantage of PSMC over conventional PID control is that the response to a large deviation, which results from actuator torque limitation, can be designed independently from the response to a small deviation that can be recovered without torque limitation. In PSMC, the small-scale response can be set as fast as conventional PID or PD control, while the large-scale response can be set arbitrarily slow to ensure safety (Kikuuwe et al., 2010). The transition between these two behavioural modes is determined by a torque magnitude limit τ_{LIM}. If a disturbance exceeds this limit, the link will be pulled away from the target trajectory while resisting the disturbance with a torque that equals τ_{LIM}. Since τ_{LIM} influences the interaction torque with the environment, setting its value may require a trade-off between robustness against tracking disturbances on the one hand and safety of the interaction on the other hand.

3.4.1.4 Control law

Starting from the torque definitions as indicated in fig. 3.18.b and the general concept introduced in the previous sections, the control law can be derived as follows.

The torque exerted by the PID-type virtual coupling, denoted by τ_c, is given by

$$\tau_c = K_p(q_p - q) + K_i \int (q_p - q)dt + K_d(\dot{q}_p - \dot{q}), \tag{3.26}$$

where K_p, K_i and K_d are the respective PID gains. By introducing $a = \int (q_p - q)dt$, the integral can be eliminated from eq. 3.26, which leads to

$$\tau_c = K_p \dot{a} + K_i a + K_d \ddot{a}. \tag{3.27}$$

The proxy's position, on the other hand, is controlled by an ideal sliding mode controller in order to track the target trajectory. The sliding mode control law that is used here is given by

$$\tau_a = \tau_{LIM} \operatorname{sgn}(s), \tag{3.28}$$

with

$$s = (q_d - q_p) + \lambda(\dot{q}_d - \dot{q}_p), \tag{3.29}$$

and the signum function $\operatorname{sgn}(x)$ defined by

$$\operatorname{sgn}(x) \begin{cases} = 1 & if\ x > 0 \\ \in [-1, 1] & if\ x = 0 \\ = -1 & if\ x < 0 \end{cases} . \tag{3.30}$$

The goal of the sliding mode controller is to keep the proxy's state on a line in state space, the so called "sliding surface", such that $s = 0$. Once the proxy's state is on that sliding surface the position error $(q_d - q_p)$ will exponentially decay to zero with time constant $\lambda > 0$, which follows from the error dynamics equation $(q_d - q_p) + \lambda(\dot{q}_d - \dot{q}_p) = 0$. If the proxy is not on the sliding surface the sliding mode controller drives it towards the sliding surface according to eq. 3.28. The torque τ_{LIM} is the maximal torque magnitude output by the sliding mode controller. By introducing $\sigma = (q_d - q) + \lambda(\dot{q}_d - \dot{q})$ eq. 3.28 can also be written as a function of variable a, namely

$$\tau_a = \tau_{LIM} \operatorname{sgn}(\sigma - \dot{a} - \lambda \ddot{a}). \tag{3.31}$$

The torque τ_c exerted by the virtual coupling is the set point, as required by the proxy-based sliding mode controller, for the actuator torque applied to the link. Since the proxy has zero mass, τ_a equals τ_c at all times and the actuator torque τ required by the proxy-based sliding mode controller satisfies

$$\tau = \tau_c = \tau_a. \tag{3.32}$$

Combining eq. 3.32, eq. 3.27 and eq. 3.31 results in the following set of equations for the PSMC torque

$$\begin{cases} \tau & = K_p \dot{a} + K_i a + K_d \ddot{a} \\ \tau & = \tau_{LIM} \operatorname{sgn}(\sigma - \dot{a} - \lambda \ddot{a}) \end{cases} . \tag{3.33}$$

Starting from eq. 3.33 a discrete time control law can be derived that can be implemented on the system. Detailed calculations can be found in appendix B. The resulting set of equations defining the control law at time step n for the torque set point, denoted by τ_{PSMC}, as required by the proxy-based sliding mode controller is given by eq. 3.34-3.37. Here, T stands for the sample time of the controller and ∇ stands for the backward difference operator such that $\nabla x[n] = x[n] - x[n-1]$. Implementing this control law requires the calculation of $\tau^{\star}_{PSMC}[n]$ (eq. 3.35) based on $\sigma[n]$ (eq. 3.34) and on the value at previous time steps of the variable a. $\tau^{\star}_{PSMC}[n]$ is then passed to the saturation condition in eq. 3.36 to obtain the PSMC output torque τ_{PSMC}. Finally, the value of a is updated in view of the iteration at the next time step. It is important to note that the discontinuous $\operatorname{sgn}(\cdot)$ (see eq. 3.33) function does not appear in the controller equations 3.34-3.37. The output is continuous, so the controller does not induce chattering in the proxy's motion (Kikuuwe and Fujimoto, 2006).

$$\sigma[n] = (q_d[n] - q[n]) + \lambda(\dot{q}_d[n] - \dot{q}[n]) \tag{3.34}$$

$$\begin{aligned} \tau^{\star}_{PSMC}[n] &= \frac{K_d + K_pT + K_iT^2}{\lambda + T}\sigma[n] + K_i a[n-1] \\ &+ \frac{(K_p + K_iT)\lambda - K_d}{(\lambda + T)T}\nabla a[n-1] \end{aligned} \tag{3.35}$$

$$\tau_{PSMC}[n] = \begin{cases} \tau^{\star}_{PSMC}[n] & if\ \|\tau^{\star}_{PSMC}[n]\| \le \tau_{LIM} \\ \tau_{LIM}\frac{\tau^{\star}_{PSMC}[n]}{\|\tau^{\star}_{PSMC}[n]\|} & if\ \|\tau^{\star}_{PSMC}[n]\| > \tau_{LIM} \end{cases} \tag{3.36}$$

$$\begin{aligned} a[n] &= \frac{1}{K_d + K_pT + K_iT^2}\big((K_d + K_pT)a[n-1] \\ &+ K_d\nabla a[n-1] + T^2\tau_{PSMC}[n]\big) \end{aligned} \tag{3.37}$$

3.4.1.5 Relation with other controllers

By setting $\lambda = 0$ and $\tau_{LIM} \to \infty$, the controller becomes equivalent to a discrete-time PID controller (Kikuuwe and Fujimoto, 2006). With $K_i = 0$ and $\lambda = K_d/K_p$ the control method can be seen as force-limited PID control, or as sliding mode control with a boundary layer (Kikuuwe and Fujimoto, 2006). Proxy-based sliding mode control can thus be seen as an extension of these conventional methods.

If the virtual coupling is of the PD-type ($K_i = 0$) then it will simulate a spring-damper system as long as the torque stays below the torque limit. One infers that there is a great similarity between PSMC with a PD-type virtual coupling and impedance control (Hogan, 1985) in joint space without an inertial component.

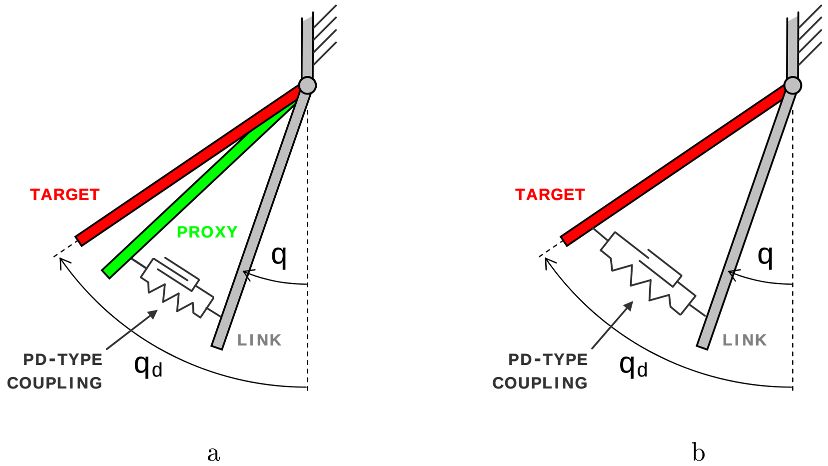

Figure 3.20: Analogy of proxy-based sliding mode control with other controllers implemented in joint space: a) PSMC with PD-type coupling, b) Impedance control.

The difference relies in the fact that the coupling in PSMC is not directly made with the target, but with a virtual object, the proxy, that is controlled towards the target, as illustrated by fig. 3.20. The implementation of impedance control in joint space (see fig. 3.20.b) in turn is similar to PD position control. The similarity with PSMC also applies to the more conventional implementation of impedance control in Cartesian space in the case of an n-link robot ($n \geq 2$). In that case the proxy can be a virtual massless point connected to the robot's end point by a virtual coupling.

3.4.2 Application to robot-assisted gait

3.4.2.1 Human-robot system

When applying PSMC to the powered knee exoskeleton, one is confronted with a system that has more complex dynamics (see fig. 3.21) than the 1 DOF robot joint used as an example in the previous section.

In section 3.2.2.1 two separate 2 DOF link models have been proposed to model the entire system during the swing phase and the single support phase. Extracting from the vectorial dynamics equation (eq. 3.9) the scalar equation that applies to the knee joint yields

$$\boldsymbol{H}_2(\boldsymbol{q})\ddot{\boldsymbol{q}} + \boldsymbol{C}_2(\boldsymbol{q}, \dot{\boldsymbol{q}})\dot{\boldsymbol{q}} + G_2(\boldsymbol{q}) = \tau_{exo} + \tau_{hum}, \tag{3.38}$$

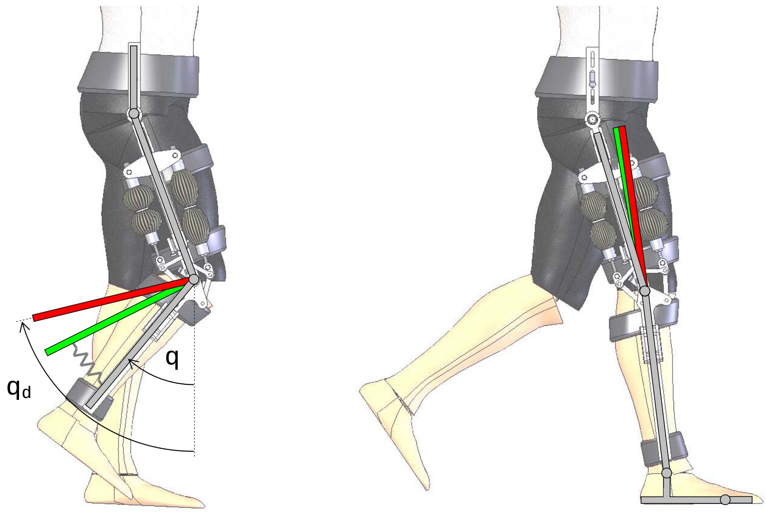

Figure 3.21: Proxy-based sliding mode control applied to a powered knee exoskeleton during swing phase (left) and single support phase (right).

where $\boldsymbol{q} = [q_1\ q_2]^T$ is the vector of joint angles (q_1: ankle joint angle (single support) or hip joint angle (swing), q_2: knee joint angle), G_2 is the gravitational torque acting at the knee joint and $\boldsymbol{H}_2 = [H_{21}\ H_{22}]$ and $\boldsymbol{C}_2 = [C_{21}\ C_{22}]$ are the 2^{nd} row vectors of the inertia matrix $\boldsymbol{H}$ and the centrifugal matrix $\boldsymbol{C}$ of the combined human-robot system respectively. In the right hand side one finds the torque exerted by the actuators (τ_{exo}) and the torque exerted by the human at the knee joint (τ_{hum}).

A consequence of the more complex dynamics is that the functional interpretation of the actuator torque limit in view of gait assistance is not straightforward. One may consider the dynamics of the system consisting of the robot alone, by grouping the left hand side of eq. 3.38 as $\tau_{dyn,exo+hum}$ and rewriting the dynamics equation 3.38 as

$$\begin{aligned} \tau_{dyn,exo+hum} &= \tau_{exo} + \tau_{hum} \\ \tau_{dyn,exo} + \tau_{dyn,hum} &= \tau_{exo} + \tau_{hum} \\ \tau_{dyn,exo} &= \tau_{exo} + \tau_{hum} - \tau_{dyn,hum}. \end{aligned} \tag{3.39}$$

Eq. 3.39 is the dynamics equation related to the exoskeleton's knee joint. In general, the interaction torque $\tau_{hum} - \tau_{dyn,hum}$ exerted by the human on the exoskeleton will differ from the actuator torque because of the exoskeleton's mass and inertia ($\tau_{dyn,exo}$). Having the actuator torque τ_{exo} controlled by a proxy-based sliding mode controller, one could envisage a role for the torque limit parameter τ_{LIM} as a limit on the interaction torque between the human and the robot. Theoretically, this could be achieved by modelling $\tau_{dyn,exo}$ and using the modelled term as a feedforward torque in addition to the feedback torque originating from the proxy-based sliding mode controller. From this example it is clear that the use of a (model-based) feedforward torque changes the role of the torque saturation in PSMC.

Another consequence of the more complex dynamics is that the stability and performance of the controller may not be assured. A common strategy in robot control is to partly linearise the system by adding to the feedback term a feedforward term, that approximates (part of) the dynamic torques required to achieve the target trajectory, as mentioned previously. Here, the actuator torque set point, based on a feedback term τ_{PSMC} and a feedforward term τ_{FF}, is thus given by

$$\tau_{exo} = \tau_{FF} + \tau_{PSMC}. \tag{3.40}$$

In the case of a robot joint subject to the gravitational field for instance, a model-based gravity compensation term is typically used as a feedforward term to compensate the gravitational torque acting on the joint. All unmodelled torque terms and all torques due to modelling errors are considered as disturbances which the feedback term should be able to deal with in view of stability and tracking performance. The use of a model-based feedforward term in the control of a combined human-robot system however is not straightforward for the following reasons:

- the inertia and centrifugal matrices and the gravitational torque vector are different for each model describing a different phase of gait (swing, single support, double. support)
- the inertia and centrifugal matrices and the gravitational torque vector appearing in the system model differ between individuals according to stature and weight.
- the system model is based on simplifying assumptions, e.g. rigid segments, rigid human-robot coupling.
- the human torque τ_{hum} greatly varies between steps and trials of an individual and between different individuals depending on their motor control and strength.

The presence of the unpredictable τ_{hum} yields different scenarios. If $\tau_{hum} \approx 0$ or τ_{hum} is roughly proportional to the required dynamic torques an appropriate model-based feedforward term can effectively decrease the amount of feedback torque (τ_{PSMC}). Spastic leg movements, increased muscle tone and other unpredictable irregularities on the other hand still need to be treated as unmodelled disturbances.

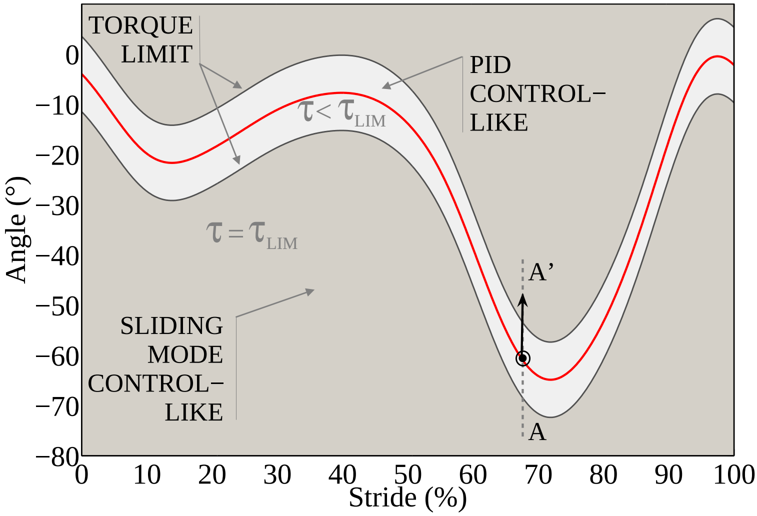

Figure 3.22: Proxy-based sliding mode control applied to gait assistance: simplified illustration of assisted human knee motion (target in red, PID control-like tunnel in light grey, sliding mode control-like torque plateau in dark grey)

3.4.2.2 Control parameters

The application of proxy-based sliding mode control to the powered knee exoskeleton is illustrated by fig. 3.22-3.23. In general, if a PID-type virtual coupling is considered, the PSMC output torque depends on the actual position and velocity errors with respect to the target knee joint trajectory and on previous position errors. For an easier qualitative interpretation, one could consider a tunnel centered around the target knee joint trajectory, in which the exoskeleton displays a PID control-like behaviour and outside of which an actuator torque plateau exists as suggested by fig. 3.22. If the virtual coupling were of the proportional type this representation would have been valid.

In fig. 3.23 a section view is shown along the line AA' as marked on fig. 3.22 and perpendicular to the plane of that figure. It illustrates the variation of the actuator torque magnitude with the deviation from the target at a certain instance of time. Here, the PID control-like output torque as a function of the deviation from the target is represented by an arbitrary curve. In the case of a P-type coupling it would be a straight line with a slope that equals K_p. A change of the PID gains K_p, K_i and K_d (blue curve in fig. 3.23.a) alters the restoring torque as a function of target deviation and generally also the width of the tunnel, whereas a change of the torque limit τ_{LIM} (green curve in fig. 3.23.a) alters the level of the torque plateau and thus also the width of the tunnel.

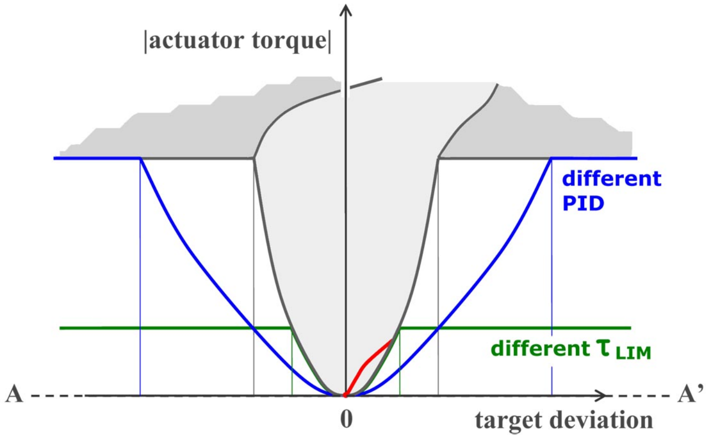

a

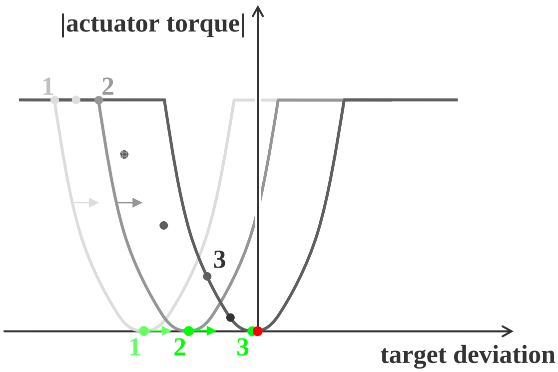

b

Figure 3.23: Proxy-based sliding mode control applied to gait assistance: a) section view along AA' in fig. 3.22 to illustrate the effect of a change of the PID gains (blue) and of a change of the torque limit (green) on the actuator torque. b) illustration of the recovery from large deviations (1→2: reaching the sliding surface while $\tau = \tau_{LIM}$, 2→3: exponential convergence of the proxy (green) towards the target (red) with time constant λ).

Assuming a fixed target and zero initial deviation in fig. 3.23.a, one infers that under a large disturbance the system's state evolves upwards along the tunnel wall and that once $\tau = \tau_{LIM}$ is reached, the proxy is pulled away from the target while the system is dragged further away from the target along the plateau. If at this point, the disturbing torque is removed, the system will recover as illustrated by fig. 3.23.b. From state 1→2 the system is subject to a torque $\tau = \tau_{LIM}$ while the proxy (green) is being driven towards its sliding surface. The actual joint follows the proxy due to the virtual coupling. Once on the sliding surface, the proxy will exponentially converge towards the target with time constant λ from state 2→3. If the proxy coincides with the target again (state 3) the system's state evolves along the tunnel wall towards the target. It should be noted that in general the target is of course not fixed, but varies along the target trajectory as a function of time.

It is clear that the PSMC parameters (K_p, K_i, K_d; τ_{LIM}; λ) provide the system with the ability to display different behavioural modes and that at the same time these parameters need to be set appropriately in view of safe and functional robotic assistance of gait. More specifically the following points of attention should be taken into account with regard to

PID gains ($\boldsymbol{K_p}$, $\boldsymbol{K_i}$, $\boldsymbol{K_d}$) The gains should be appropriately high such that the required amount of assistive torque is provided. The latter implies that trajectory deviations need to be kept within acceptable limits. In practice, feedback gains in systems powered by pneumatic muscles are relatively low to ensure controller stability. In order to provide a sufficient amount of support torque for weight bearing during single support, the PSMC torque should be complemented with an appropriate feedforward torque.

Torque limit ($\boldsymbol{\tau_{LIM}}$) As the torque limit can be seen as a limit on the human-robot interaction torque it could serve as a means to ensure interaction safety and comfort. On the other hand safety also relates to ensuring continuity of the gait pattern and preventing large deviations at crucial gait events such as heel strike. Assigning τ_{LIM} thus implies a trade-off between tracking accuracy and safety of interaction. The use of an appropriate feedforward torque (support torque) can mediate this trade-off by improving tracking accuracy while centering the allowable torque range around the support torque (see section 3.4.2.4).

Sliding mode time constant ($\boldsymbol{\lambda}$) The recovering motion following a large disturbance should be appropriately slow. As for the torque limit a trade-off is required between safety of interaction and tracking accuracy. If the recovering motion is too slow deviations may grow unacceptable in time at crucial phases of gait.

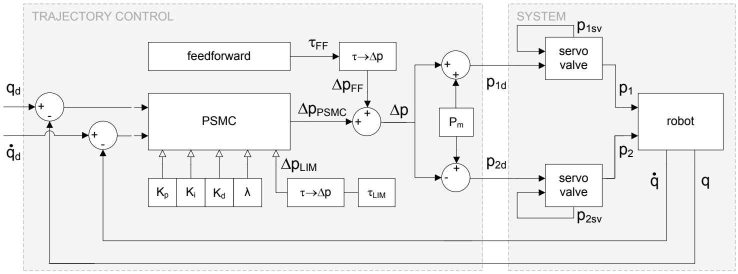

Figure 3.24: Control scheme of the implemented trajectory controller based on PSMC.

3.4.2.3 Controller

Applying PSMC to the exoskeleton's knee joint powered by PPAMs, one is confronted with the fact that the controller generates an actuator torque set point τ_{PSMC} (according to eq. 3.34-3.37) that needs to be met by setting the muscle pressures p_1 and p_2. By means of the Δp-approach (see section 3.3.1.1) the control variable $\triangle p_{PSMC}$ can be introduced such that

$$\begin{cases} \tau_{PSMC} & = p_m(m_{\tau 1} + m_{\tau 2}) + \Delta p_{PSMC}(m_{\tau 1} - m_{\tau 2}) \\ p_m & = p_m \end{cases} \tag{3.41}$$

holds.

As a workaround to the model based torque-to-pressure conversion in eq. 3.41, the control law in eq. 3.34-3.37 can be reformulated so that it generates $\triangle p_{PSMC}$ as an output directly. Provided that the controller can cope with the system's nonlinear torque-pressure relationship, the proxy-based sliding mode control law becomes

$$\sigma[n] = (q_d[n] - q[n]) + \lambda(\dot{q}_d[n] - \dot{q}[n]) \tag{3.42}$$

$$\begin{aligned} \Delta p^{\star}_{PSMC}[n] &= \frac{K_d + K_p T + K_i T^2}{\lambda + T}\sigma[n] + K_i a[n-1] \\ &+ \frac{(K_p + K_i T)\lambda - K_d}{(\lambda + T)T}\nabla a[n-1] \end{aligned} \tag{3.43}$$

$$\Delta p_{PSMC}[n] = \begin{cases} \Delta p^{\star}_{PSMC}[n] & if\ \|\Delta p^{\star}_{PSMC}[n]\| \leq \Delta p_{LIM} \\ \Delta p_{LIM}\frac{\Delta p^{\star}_{PSMC}[n]}{\|\Delta p^{\star}_{PSMC}[n]\|} & if\ \|\Delta p^{\star}_{PSMC}[n]\| > \Delta p_{LIM} \end{cases} \tag{3.44}$$

$$\begin{aligned} a[n] &= \frac{1}{K_d + K_p T + K_i T^2} \left((K_d + K_p T)\, a[n-1] \right. \\ &\quad \left. + K_d \nabla a[n-1] + T^2 \Delta p_{PSMC}[n] \right) \end{aligned} \tag{3.45}$$

The control parameter Δp_{LIM} defines the muscle gauge pressure limits and as such indirectly limits the actuator torque. At a constant Δp_{LIM} the resulting actuator torque limit varies with the joint angle. A feedforward term Δp_{FF} is added to Δp_{PSMC}, originating from eq. 3.42-3.45, which yields

$$\Delta p[n] = \Delta p_{FF}[n] + \Delta p_{PSMC}[n] \tag{3.46}$$

at time step n. The feedforward term Δp_{FF} is based on the feedforward torque τ_{FF} , according to eq. 3.48. The relationship between Δp_{PSMC} and τ_{PSMC} is given by eq. 3.47 so that $\tau = \tau_{FF} + \tau_{PSMC}$ holds. The purpose of the feedforward torque τ_{FF} is to linearise the system in order to improve the stability and the accuracy of the controller. The specific implementation of the feedforward torque in the powered knee exoskeleton is discussed in section 3.4.2.4.

$$\Delta p_{PSMC}[n] = \frac{\tau_{PSMC}[n]}{m_{\tau 1} - m_{\tau 2}} \tag{3.47}$$

$$\Delta p_{FF}[n] = \frac{\tau_{FF}[n] - p_m[n](m_{\tau 1} + m_{\tau 2})}{m_{\tau 1} - m_{\tau 2}} \tag{3.48}$$

Since the actuator torque limit can be seen as a limit on the interaction torque with the environment, it is more appropriate and convenient to work with than a muscle pressure limit. A desired torque limit τ_{LIM} is thus converted to a set value for Δp_{LIM} by means of eq. 3.49 analogously to eq. 3.47.

$$\Delta p_{LIM}[n] = \frac{\tau_{LIM}[n]}{m_{\tau 1} - m_{\tau 2}} \tag{3.49}$$

A workaround to the model-based conversion of eq. 3.49 is discussed in section 3.4.2.4. Figure 3.24 depicts the control scheme of the PSMC-based trajectory controller.

3.4.2.4 Support torque

As mentioned in section 3.4.2.1, a well-chosen model-based feedforward term could improve controller performance, but is difficult to establish for a complex human-robot system with many uncertainties. Therefore the feedforward torque τ_{FF} in eq. 3.48 is not based on a system model, but on actuator torque set point recordings performed while the device is operating under PSMC without feedforward.

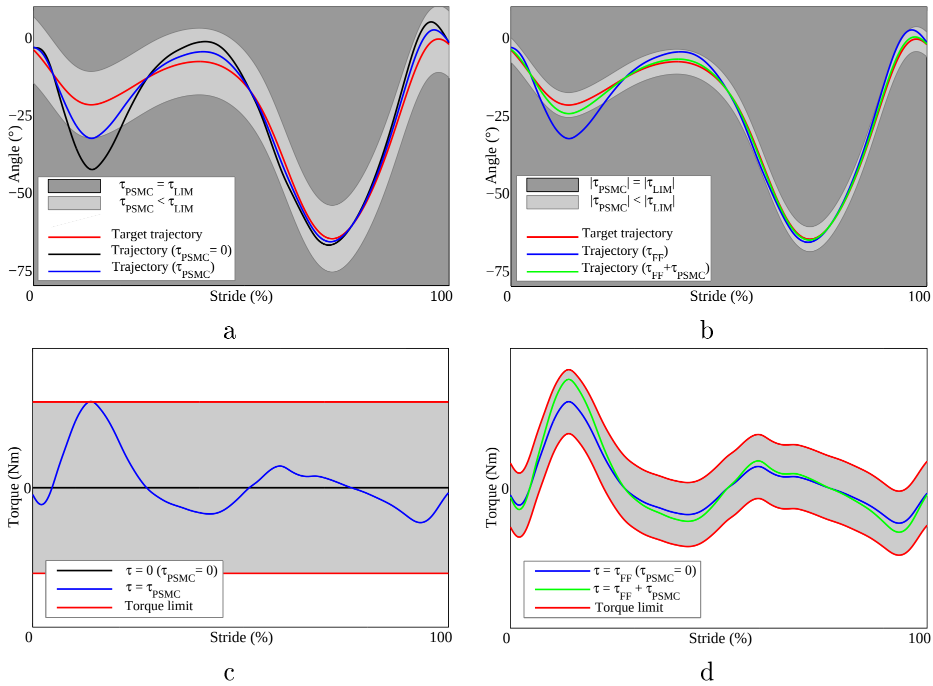

Figure 3.25: Feedforward torque as a support torque: a,c) controller behaviour during feedforward recording (PSMC without feedforward term). b,d) controller behaviour for PSMC with feedforward term taken from c) (i.e. blue torque cycle).

During feedforward torque recording, the gains and torque limit are set appropriately high and τ_{FF} is set to zero. Position errors occurring in this recording mode (high gains, high τ_{LIM}, $\tau_{FF} = 0$) indicate the necessity of a feedforward term. The PSMC output torque τ_{PSMC} is calculated from the controller's set point for Δp_{PSMC} (see eq. 3.47) and recorded. The recorded torque data is sectioned in cycles, by means of heelstrike detection, and averaged over all cycles. The obtained torque cycle represents the average required actuator torque needed to "track" the desired target trajectory according to the controller settings of the recording mode. Figure 3.25.a and 3.25.c illustrate controller behaviour under these settings. The actuator torque set point τ is limited to $[-\tau_{LIM}\ \tau_{LIM}]$. The recorded feedforward torque cycle is depicted in blue in fig. 3.25.c.

During operation under PSMC with feedforward the average required torque cycle is replayed as the feedforward torque τ_{FF} and the control parameter settings can be focused on interaction safety without compromising tracking accuracy as much as without feedforward. Figure 3.25.b and 3.25.d illustrate controller behaviour under such settings. The actuator torque is now bound to $[\tau_{FF} - \tau_{LIM}\ \tau_{FF} + \tau_{LIM}]$ as τ_{LIM} defines a torque range relative to the support torque.

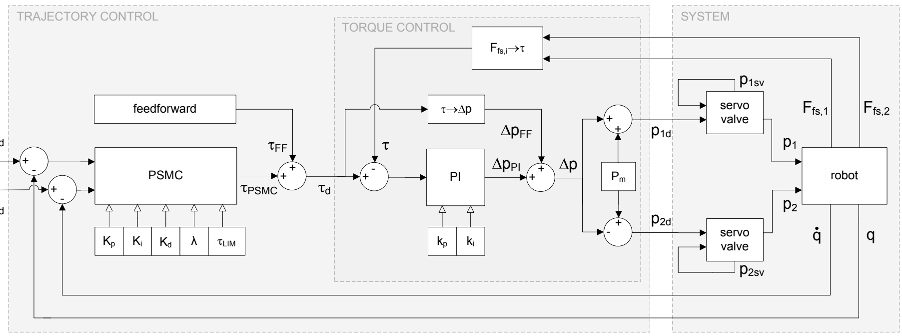

Figure 3.26: Control scheme of the implemented trajectory controller based on PSMC and an inner torque control loop.

3.4.2.5 Inner torque control loop

The control law given in section 3.4.2.3 avoids a model-based torque to pressure conversion of its output, which is beneficial for control performance. However this error-sensitive conversion is still required (see eq. 3.49) for the implementation of the torque limit. Therefore an alternative control scheme has been implemented that combines the explicit PSMC control law (eq. 3.34-3.37 in section 3.4.1.2) with an inner torque control loop (eq. 3.20-3.22 in section 3.3.1.2). The torque set point provided by the trajectory controller, using position and velocity feedback, is combined with a feedforward torque term and fed to the torque controller, using force sensor feedback. The resulting control law is given by eq. 3.50-3.58 and the control scheme is depicted in fig. 3.26.

$$\sigma[n] = (q_d[n] - q[n]) + \lambda(\dot{q}_d[n] - \dot{q}[n]) \tag{3.50}$$

$$\begin{aligned}\tau^{\star}_{PSMC}[n] &= \frac{K_d + K_pT + K_iT^2}{\lambda + T}\sigma[n] + K_i a[n-1] \\ &+ \frac{(K_p + K_iT)\lambda - K_d}{(\lambda + T)T}\nabla a[n-1]\end{aligned} \tag{3.51}$$

$$\tau_{PSMC}[n] = \begin{cases} \tau^{\star}_{PSMC}[n] & if\ \|\tau^{\star}_{PSMC}[n]\| \leq \tau_{LIM} \\ \tau_{LIM}\frac{\tau^{\star}_{PSMC}[n]}{\|\tau^{\star}_{PSMC}[n]\|} & if\ \|\tau^{\star}_{PSMC}[n]\| > \tau_{LIM} \end{cases} \tag{3.52}$$

$$\begin{aligned}a[n] &= \frac{1}{K_d + K_pT + K_iT^2}((K_d + K_pT)a[n-1] \\ &+ K_d\nabla a[n-1] + T^2\tau_{PSMC}[n])\end{aligned} \tag{3.53}$$

$$\tau_d[n] = \tau_{FF}[n] + \tau_{PSMC}[n] \tag{3.54}$$

$$\tag{3.55}$$

$$\Delta p_{FF}[n] = \frac{\tau_d[n] - p_m[n](m_{\tau 1} + m_{\tau 2})}{(m_{\tau 1} - m_{\tau 2})} \tag{3.56}$$

$$\Delta p_{PI}[n] = k_p(\tau_d[n] - \tau[n]) + k_i \sum_{i=0}^{n}(\tau_d[i] - \tau[i])T \tag{3.57}$$

$$\Delta p[n] = \Delta p_{FF}[n] + \Delta p_{PI}[n] \tag{3.58}$$

3.4.3 Performance evaluation

In order to evaluate the performance of the aforementioned controllers prior to implementation on the exoskeleton, experiments have been performed on a 1 DOF pendulum setup consisting of the same actuator system (see fig. 2.32). From now onward and for convenience, the proxy-based sliding mode controller and proxy-based sliding mode controller with inner torque control loop will be referred to by PSMC and PSMC IT respectively. The objectives of the experimental study were:

- to compare the tracking performance of PSMC and PSMC IT with respect to PID control
- to compare the response of PSMC, PSMC IT and PID control to perturbations resulting from physical human-robot interaction

PID control with gravity compensation was used as a reference for comparison, as its feedback gains can be directly compared to those of PSMC and since it is a conventional trajectory tracking control method for a robot joint operating in the gravitational field.

3.4.3.1 PID control with gravity compensation

The PID controller sets the control variable Δp, as defined by the Δp-approach (see section 3.3.1.1), according to the following control law:

$$\Delta p = \Delta p_{FF} + \Delta p_{PID} \tag{3.59}$$

$$\Delta p_{FF} = \frac{\tau_{FF} - p_m(m_{\tau 1} + m_{\tau 2})}{m_{\tau 1} - m_{\tau 2}} \tag{3.60}$$

$$\Delta p_{PID} = K_p(q_d - q) + K_i \int (q_d - q)dt + K_d(\dot{q}_d - \dot{q}) \tag{3.61}$$

The integral term of Δp_{PID} is bound to avoid integral wind up. By choosing Δp as the control variable, the PID controller's feedback gains K_p, K_i, K_d have the same respective dimensions as the PSMC controller's described in section 3.4.2.3, allowing a direct comparison between PSMC and PID control.

The feedforward term Δp_{FF} is used for gravity compensation. The corresponding feedforward torque τ_{FF} required to compensate the gravitational torque acting on the 1 DOF pendulum is calculated by

$$\tau_{FF} = mglsin(q + q_0), \tag{3.62}$$

where m and l are the moving link's mass and distance from its center of mass to the joint axis and q_0 is the offset angle corresponding to the rest position ($\tau = 0$, $\dot{q} = 0$). The expression in eq. 3.62 is reformulated as

$$\begin{aligned} \tau_{FF} &= c_1 \sin(q + c_0) \\ &= c_1 \cos(c_0) \sin(q) + c_1 \sin(c_0) \cos(q) \\ &= A \sin(q) + B \cos(q) \end{aligned}$$

such that it is linear in the unknown coefficients A, B. A least squares estimate of A and B, based on torque measurements, yields the estimated values of $c_0 = 0.02965\,rad$ and $c_1 = 13.88\,Nm$. The torque measurements are based on force sensor readings executed at a grid of joint angles with the link in static equilibrium.

3.4.3.2 Tracking without perturbations

Since accurate tracking is not the most important objective of the envisaged system, focus is on the difference in performance between PSMC and PSMC IT and between both controllers and PID, rather than on absolute tracking accuracy.

Results A linear chirp, i.e. a sinusoid with linearly increasing frequency, with a frequency range of $[0\;1]\,Hz$ and an angular range of $-[10\;60]\,^\circ$ was used as a target trajectory. In all tracking experiments gravity compensation was used for all three controllers and their control parameter settings are summarised by table 3.3. In order to fulfil the condition of unperturbed tracking for PSMC and PSMC IT ($\tau_{LIM} \gg |\tau|$) the torque limit was set sufficiently high such that it would not be reached during tracking ($\tau_{LIM} = 30\,Nm$).

Figures 3.27-3.29 show the target trajectory $q_d(t)$ and actual trajectory $q(t)$ as well as the absolute tracking error $\|q_d(t) - q(t)\|$ for different controllers and control parameter settings. Figure 3.27 compares PSMC with PID for the same gain settings and shows different gain settings for PSMC.

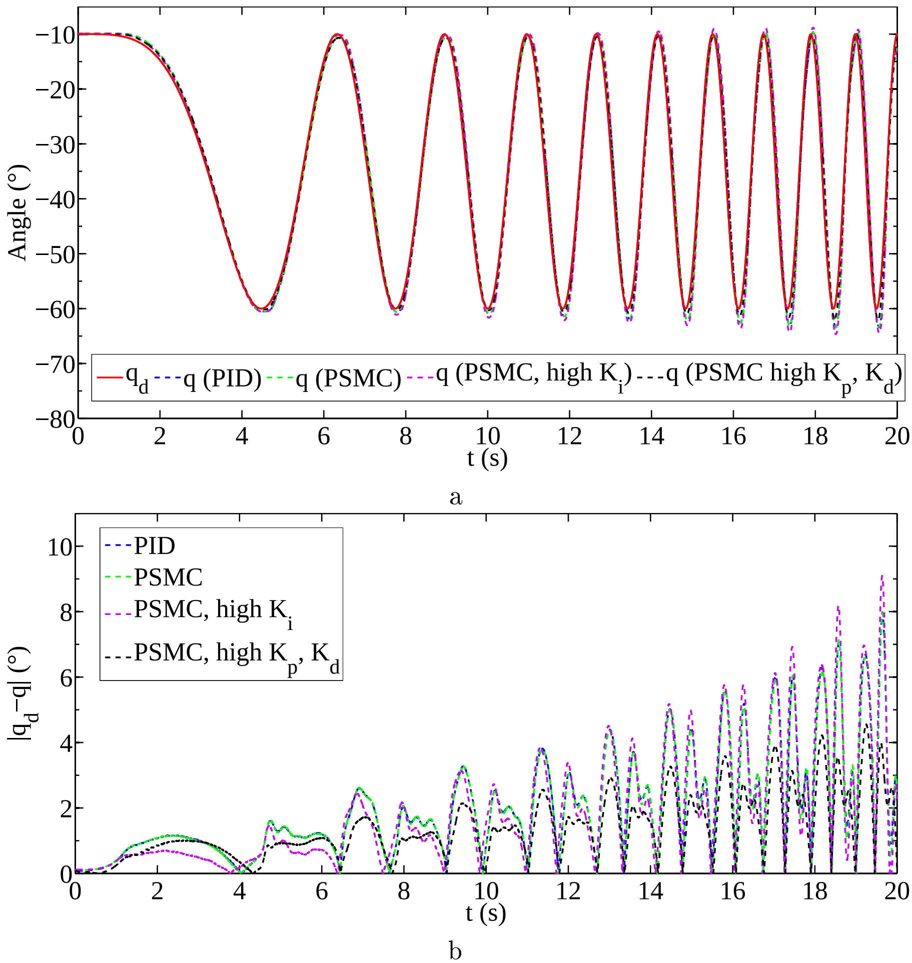

Figure 3.27: Tracking performance of PSMC: a) desired and actual trajectories, b) absolute tracking error. Controller settings are given in table 3.3.

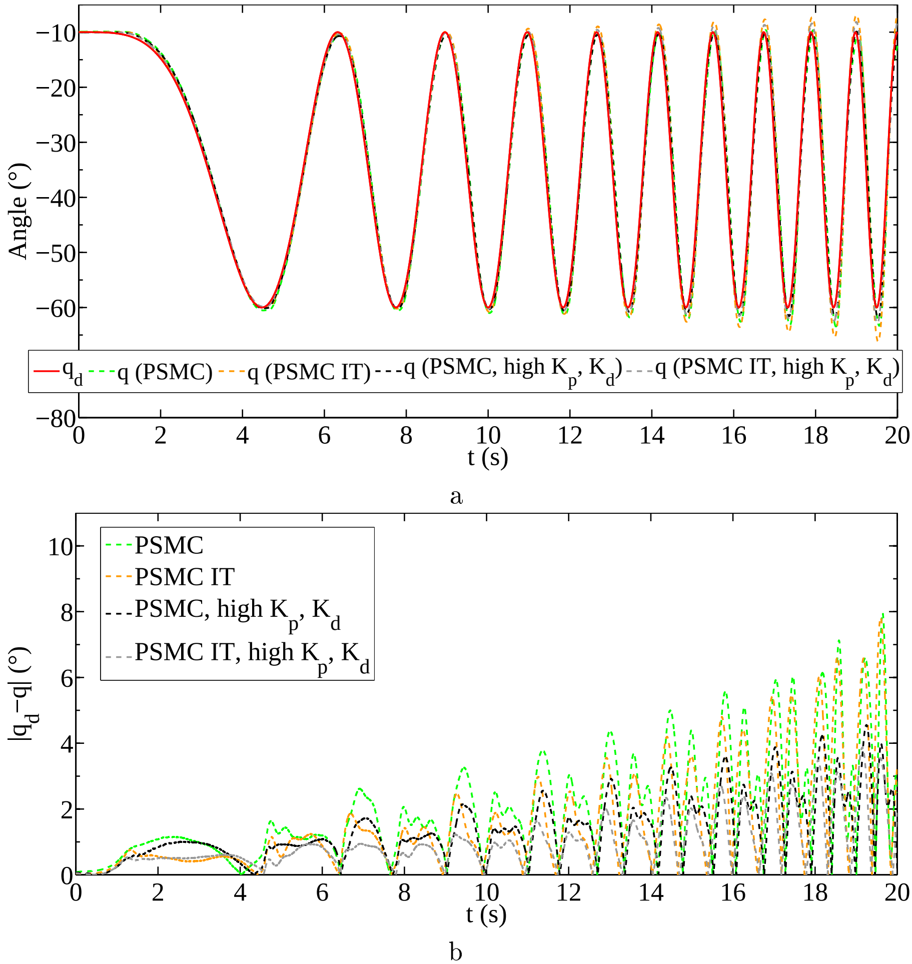

Figure 3.28: Tracking performance of PSMC and PSMC IT: a) desired and actual trajectories, b) absolute tracking error. Controller settings are given in table 3.3.

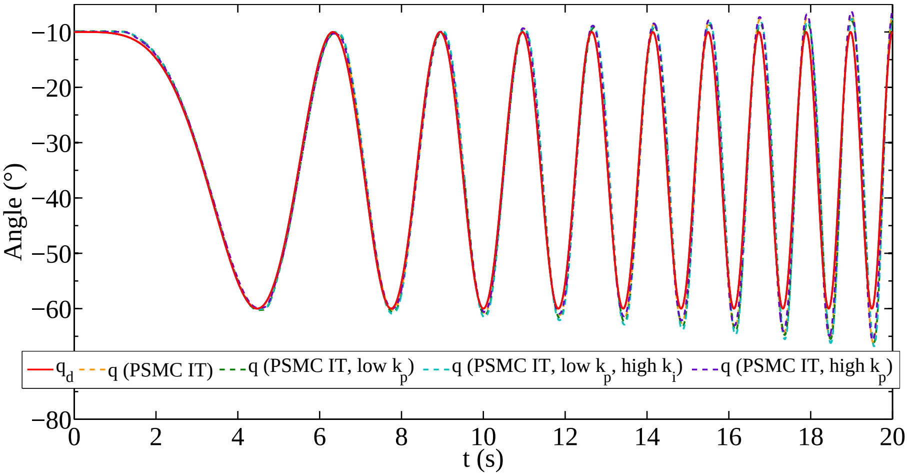

a

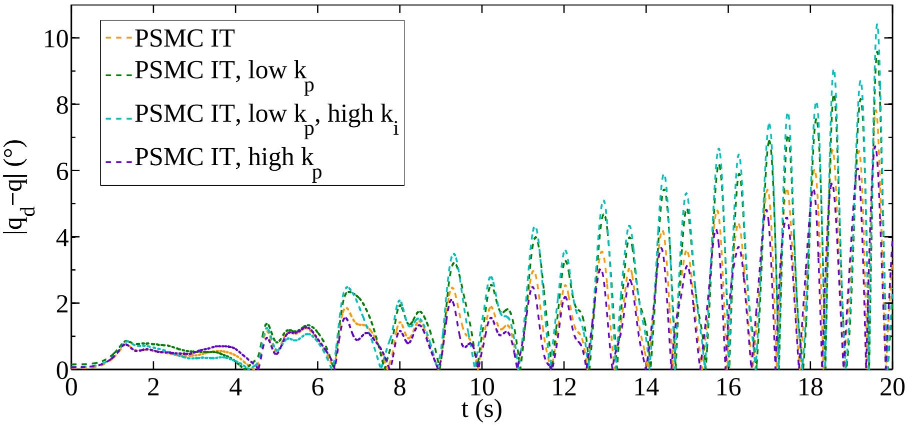

b

Figure 3.29: Tracking performance of PSMC IT at different torque controller gains : a) desired and actual trajectories, b) absolute tracking error. Controller settings are given in table 3.3.

		PID	PSMC			PSMC IT				
				high K_i	high K_p, K_d		high K_p, K_d	low k_p	low k_p high k_i	high k_p
K_p	$\frac{\bullet}{rad}$	4	4	4	**6**	60	**100**	60	60	60
K_i	$\frac{\bullet}{rad.s}$	4	4	**8**	4	60	60	60	60	60
K_d	$\frac{\bullet.s}{rad}$	0.1	0.1	0.1	**0.2**	2	**3**	2	2	2
k_p	$\frac{bar}{Nm}$	-	-	-	-	0.1	0.1	**0.05**	**0.05**	**0.15**
k_i	$\frac{bar}{Nm.s}$	-	-	-	-	0.05	0.05	0.05	**0.1**	0.05

Table 3.3: Controller settings during tracking experiments for PID control, PSMC and PSMC IT. For all controllers $p_m = 1.75\,bar$, and for PSMC and PSMC IT $T_{LIM} = 30\,Nm$ and $\lambda = 0.1$ apply. It should be noted that the dimensions of the gains K_p, K_i, K_d are identical for PID and PSMC ($\bullet = bar$), but different for PSMC IT ($\bullet = Nm$).

Figure 3.28 compares PSMC IT with PSMC for different gain settings (K_p, K_i, K_d) of PSMC IT. Results are shown for a "normal" and "maximum" gain setting of each controller. The maximum settings have been determined on the basis of step response experiments. Further increasing the gains can cause instabilities. Fig. 3.29 compares different gain settings (k_p, k_i, k_d) of the inner torque controller for PSMC IT.

Discussion In the absence of perturbations PSMC displays nearly identical tracking performance when compared with PID control. This is apparent from fig. 3.27 (coinciding blue and green dotted curves). The integral gain K_i can take higher values in the case of PSMC without causing instabilities in the step response, but this serves only as an advantage for slowly varying target trajectories (purple dotted curve). The gains cannot be set much higher than in setting "PSMC high K_p, high K_d" (see table 3.3) without causing instabilities.

As can be inferred from fig. 3.28 PSMC and PSMC IT achieve comparable tracking performance. PSMC IT slightly outperforms PSMC for these specific controller settings, especially at slow speeds, but due to the different dimensions of the gains no firm conclusions can be drawn. The tracking accuracy of PSMC IT at high speeds can be improved by tuning the torque controller gains k_p and k_i (see fig. 3.29). Increasing k_p beyond $[0.05 - 0.1]\,bar/Nm$ can cause high frequency pressure oscillations ($\sim [20 - 25]\,Hz$) at slow speeds that are relatively small in amplitude, but do cause small actuator torque oscillations (typically $\sim 0.5\,Nm$ in amplitude). These oscillations are attributed to the absence of a derivative term in the inner torque control loop. Although hardly affecting tracking accuracy (see fig. 3.29), their occurrence should be avoided in experiments with human subjects.

		Fig. 3.30	Fig. 3.31	Fig. 3.32		Fig. 3.33	Fig. 3.34-3.35	
		PSMC IT	PSMC IT	PSMC	PSMC IT	PSMC IT	PID	PSMC
K_p	$\frac{\bullet}{rad}$	60	60	4	60	60	4	4
K_i	$\frac{\bullet}{rad.s}$	60	60	4	60	60	4	4
K_d	$\frac{\bullet .s}{rad}$	2	2	0.1	2	2	0.1	0.1
k_p	$\frac{bar}{Nm}$	0.1	0.1	-	0.1	0.1	-	-
k_i	$\frac{bar}{Nm.s}$	0.05	0.05	-	0.05	0.05	-	-
λ	s	1	0.1, 1, 2	0.1	0.1	1	-	1
τ_{LIM}	Nm	10, 15, 20	15	15	15	10, 15, 20	-	30
τ_{FF}	Nm	0	0	0	0	GC	GC	GC

Table 3.4: Controller settings during interaction experiments for PID control, PSMC and PSMC IT. GC stands for gravity compensation. For all controllers $p_m = 1.75 bar$ holds. It should be noted that the dimensions of the gains K_p, K_i, K_d are identical for PID and PSMC ($\bullet = bar$), but different for PSMC IT ($\bullet = Nm$).

3.4.3.3 Response to interaction

The main objective of the interaction experiments is to compare the behaviour of PSMC and PSMC IT in view of their implementation on the exoskeleton and highlighting the essential differences of both controllers with PID control.

Results Two types of experiments have been performed. For an easier interpretation the first type involved a fixed target angle, while a perturbing torque was manually imposed on the link and suddenly released. Results are shown in fig. 3.30-3.34. The second type of experiments involved a moving target, while random perturbations were manually exerted on the load. Results are shown in fig. 3.35. Controller settings used during the experiments are summarised in table 3.4.

In fig. 3.30 and fig. 3.31 the influence of the torque limit τ_{LIM} and the sliding mode time constant λ on the system's response is shown for PSMC IT without gravity compensation. The (virtual) proxy angle $q_p(t)$ is also given as it provides a better insight in the underlying control principle. Time instances at which the torque set point τ_{PSMC} saturates at τ_{LIM} are indicated by light gray vertical lines. The accuracy of the actual actuator torque limit with respect to the desired torque limit τ_{LIM} is compared for PSMC and PSMC IT (without gravity compensation) in fig. 3.32. Besides the force sensor based actuator torque $\tau(t)$, the pressure sensor based torque $\tau_p(t)$ is shown that is calculated using the model-based pressure-to-torque conversion given by $\tau_p = p_1 m_{\tau 1} + p_2 m_{\tau 2}$.

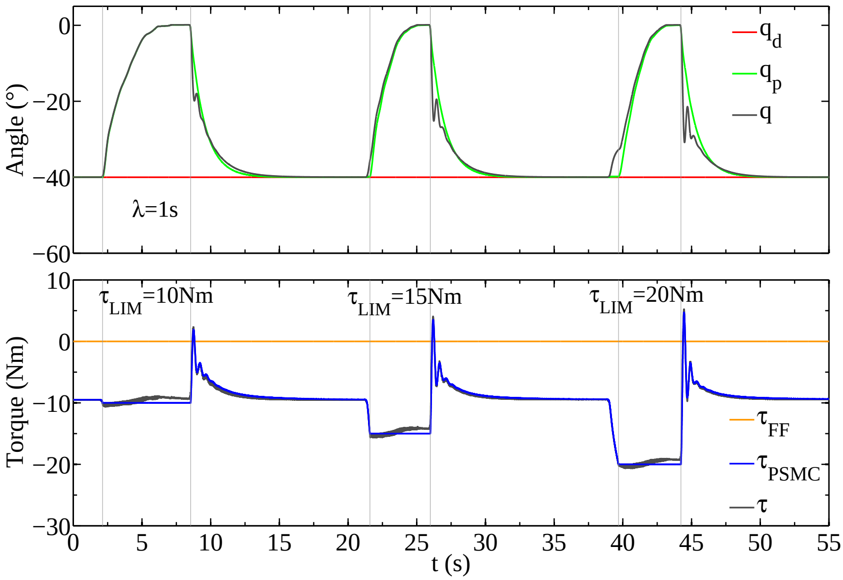

Figure 3.30: Influence of T_{LIM} on the response of PSMC IT to interaction. Controller settings are given in table 3.4.

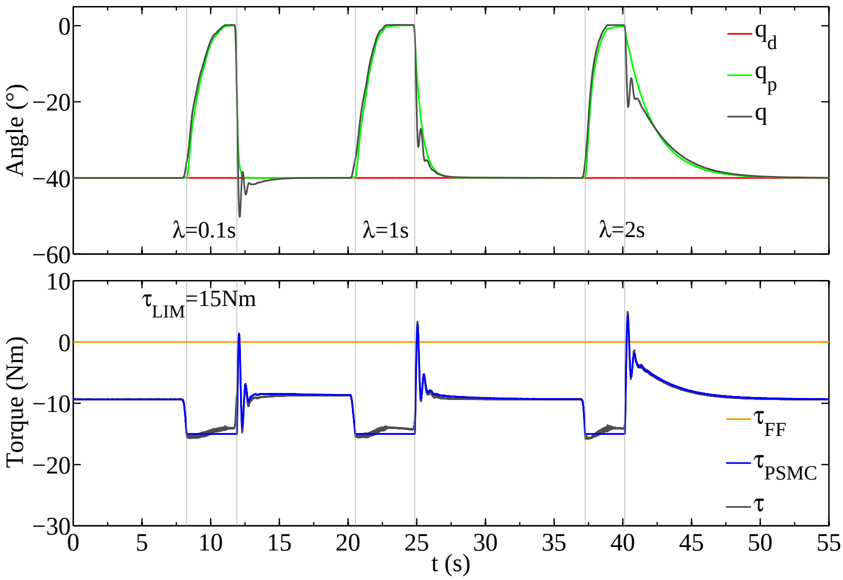

Figure 3.31: Influence of λ on the response of PSMC IT to interaction. Controller settings are given in table 3.4.

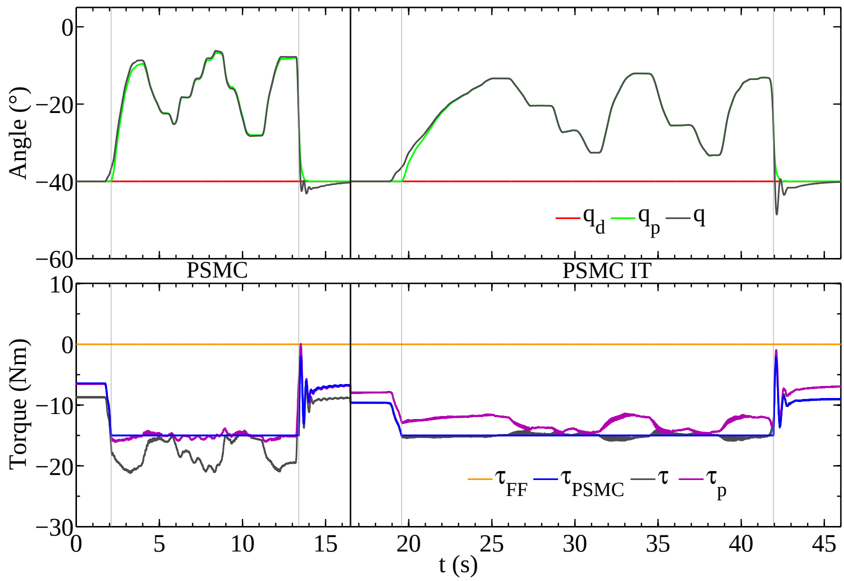

Figure 3.32: Response of PSMC (left) and PSMC IT (right) to interaction. Controller settings are given in table 3.4.

Figure 3.33 clarifies the influence of a feedforward term on the actual actuator torque limit for PSMC IT with gravity compensation. The difference between PID control and PSMC (both with gravity compensation) in the case of identical feedback gains is shown in fig. 3.34 in terms of the joint angle, the angular velocity and the actuator torque under different perturbations. Figure 3.35 compares the results of the same controller settings for a moving target, a sinusoidal target trajectory with a frequency of $0.5\,Hz$, again under different perturbations.

Discussion It is confirmed by fig. 3.30-3.31 that in the case of PSMC IT the actuator torque saturates at the desired torque limit and that the recovering motion can be made appropriately slow.

The main rationale for implementing PSMC IT was the error-sensitive model-based conversion of τ_{LIM} to Δp_{LIM} required by PSMC. As can be seen from fig. 3.32 the pressure-based torque $\tau_p(t)$ differs substantially from the force-based torque $\tau(t)$, and this difference varies with the joint angle. In the case of PSMC τ_{LIM} effectively limits τ_p instead of τ, leading to a less accurate control over the actuator torque limit. Although the accuracy of the model-based conversion could be improved by a more thorough identification of the torque functions $m_{\tau i}(q)$, as explained in section 3.2.1.4, it is rather limited since the underlying model is static and since it does not capture the hysteresis present in the output torque.

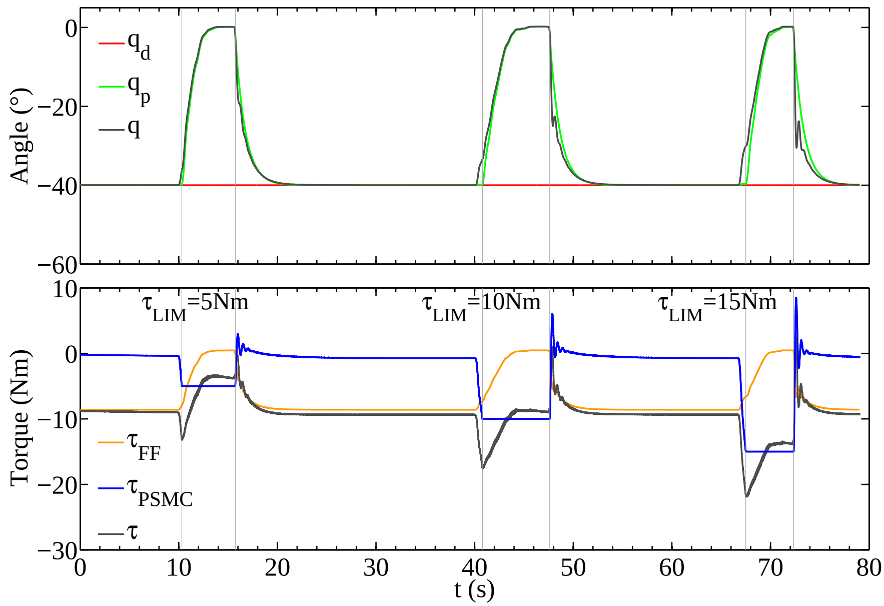

Figure 3.33: Influence of τ_{FF} on the response of PSMC IT to interaction. Separate experiments are plotted consecutively on a single time axis. Controller settings are given in table 3.4.

By contrast, PSMC IT shows much better performance in matching the desired torque limit because of torque feedback.

The addition of a feedforward torque lets τ_{LIM} define an allowable torque range relative to the feedforward torque as illustrated by fig. 3.33. Consequently, the actuator torque magnitude can exceed τ_{LIM} and τ_{LIM} can be set smaller than the actuator torque magnitude required to track the target (e.g. $5\,Nm$ in fig. 3.33). In the case of gravity compensation of the link and a constant deviation from the target, as realised in the experiment covered by fig. 3.33, the restoring actuator torque saturated at τ_{LIM} is approximately the same as the perturbing torque imposed by the human subject. Without gravity compensation (see fig. 3.30) the human subject experiences the saturated restoring torque and the gravitational torque due to the uncompensated weight of the link. As previously explained in section 3.4.2.1 and illustrated here, the choice of the feedforward torque determines the functional interpretation of τ_{LIM}.

The difference between PID control and PSMC in terms of the interaction torque and the recovering motion is apparent from fig. 3.34. In the case of PID control (top graphs) the interaction torque is increased until actuator torque saturation occurs.

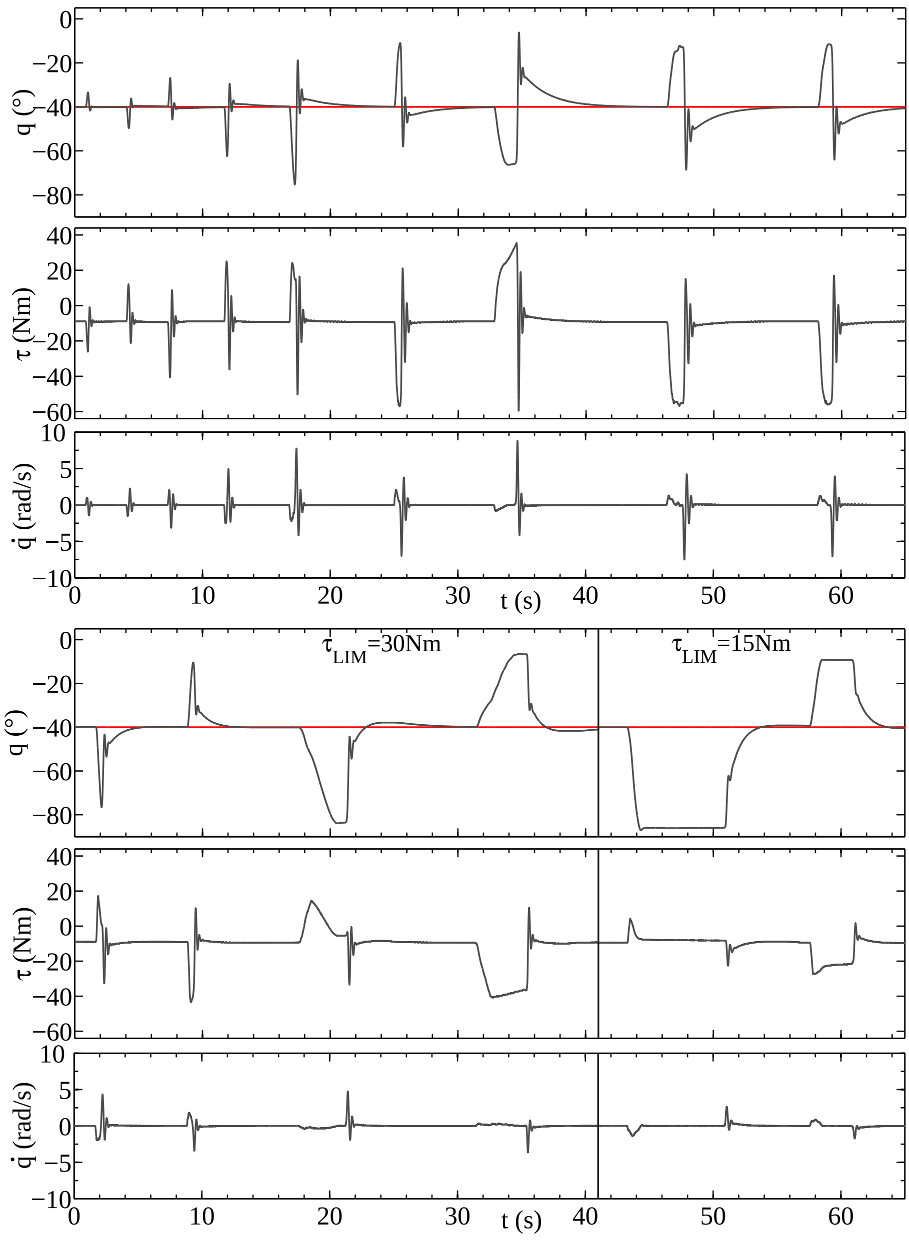

Figure 3.34: Response of PID control (top) and PSMC (bottom) to interaction with a fixed target (red). Gain settings are identical for both controllers. Controller settings are given in table 3.4.

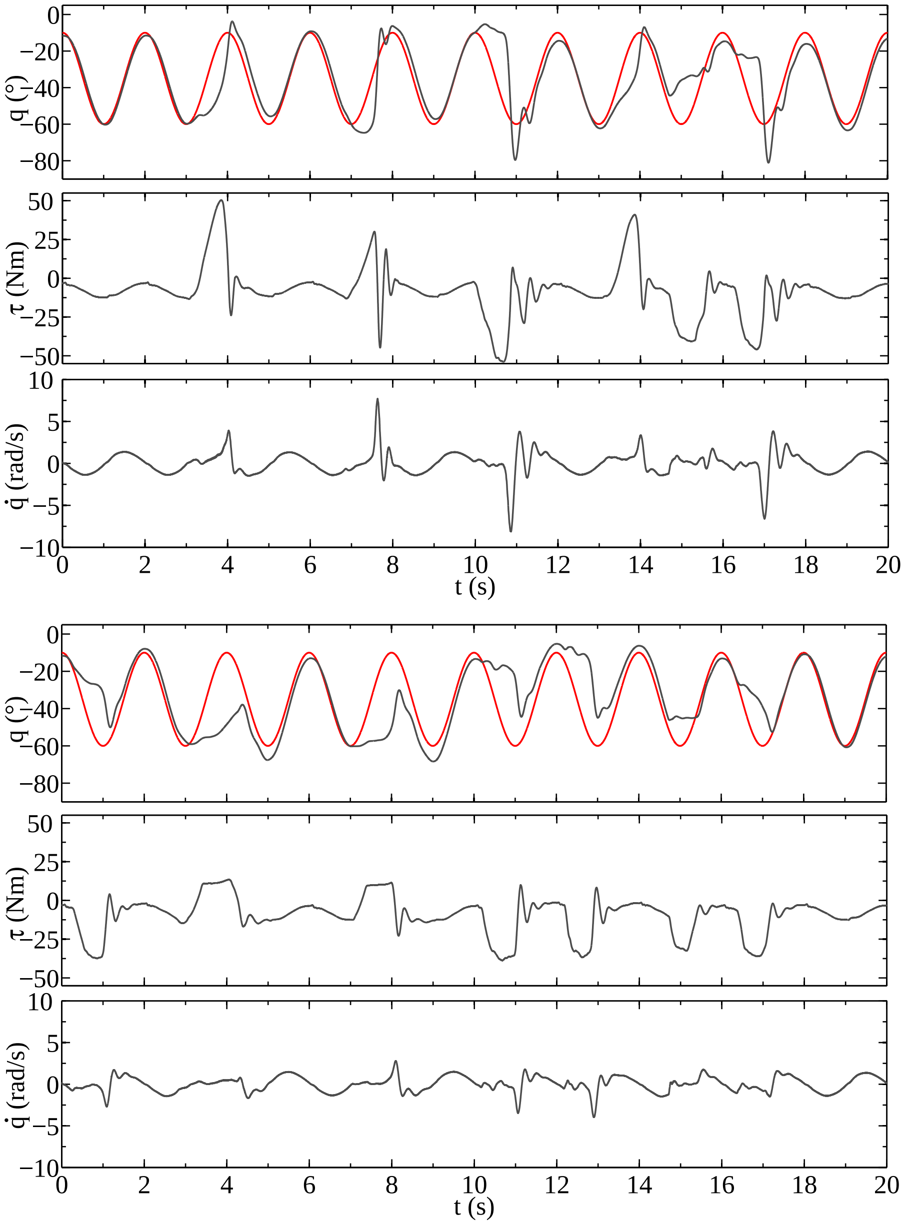

Figure 3.35: Response of PID control (top) and PSMC (bottom) to interaction with a moving target (red). Gain settings are identical for both controllers. Controller settings are given in table 3.4.

Upon removal of the interaction torque the link overshoots the target position, while attaining relatively high angular velocities. In the case of PSMC (bottom graphs) even at a high torque limit ($\tau_{LIM} = 30\,Nm$), corresponding with large interaction torques, the recovering motion can be set appropriately slow resulting in lower angular velocities and a much smaller overshoot compared with PID control. This adaptable recovering motion, as opposed to the torque limit, cannot be provided by torque limited PID control. Similar conclusions can be drawn from the results originating from the experiments with a moving target, depicted in fig. 3.34. Even with a relatively high torque limit ($\tau_{LIM} = 30\,Nm$) the response of PSMC (bottom graphs) is significantly more gentle in terms of torques, angular velocities and overshoots, when compared with PID control (top graphs).

3.4.4 Conclusion

Proxy-based sliding mode control (PSMC) was investigated for the implementation of safe trajectory tracking based gait assistance on a compliantly powered exoskeleton. In prior work by Kikuuwe and Fujimoto (2006); Van Damme et al. (2010) it was shown that PSMC's underlying combination of PID feedback and ideal sliding mode control is beneficial for robot safety in the event of large target deviations and beneficial for human safety against impacts of a robotic manipulator interacting with an operator, suggesting that it is suitable for safe robotic assistance as well.

By comparing PSMC with conventional PID control the need was emphasised of complementing the intrinsic compliance of a robot joint powered by PPAMs with a suitable dedicated control method in order to achieve a gentle response to perturbations, while preserving tracking accuracy in their absence. The response of PMSC is adjustable by means of a torque limit parameter, limiting the actuator torque, and a sliding mode time constant, defining the speed of recovery from a large deviation from the target.

The application of PSMC to gait assistance brings about additional challenges with respect to safety and functionality. From the control viewpoint, achieving a satisfying tracking accuracy with an exoskeleton powered by PPAMs suggests the use of a feedforward torque that partly compensates the dynamics of the combined human-robot system. From the viewpoint of gait assistance, it can be considered as a support torque, that ensures gait continuity in the absence of perturbations. The adjustable torque limit then defines an allowable actuator torque range relative to the support torque. As such, it can be viewed as an approximate limit on the actuator system's torque in response to an active human torque or to a human-robot interaction torque, depending on whether the dynamics of the combined human-robot system or the dynamics of the robot alone are compensated by the support torque.

In order to achieve a more accurate control of the torque limitation, as a crucial element in the envisaged human-robot interaction, an alternative implementation method of PSMC was realised that uses the previously developed torque controller as an inner torque control loop (PSMC IT). Experiments on a 1 DOF pendulum setup have shown that PSMC IT outperforms PSMC in terms of the displayed actuator torque limitation, while achieving comparable tracking performance. Both PSMC and PSMC IT were considered suitable control methods for implementation in KNEXO and subsequent testing with human subjects.

3.5 Trajectory generation and synchronisation

3.5.1 Trajectory generation

The target trajectory is an important determinant of the assistive environment displayed by the device and how it should be defined, is a subject of ongoing research in rehabilitation robotics. Most often gait analysis data taken from unimpaired subjects are used as a reference. Since KNEXO is only intended for testing in mildly impaired subjects, the trajectory recorded during a patient-in-charge mode is used as a starting point. From this point the resulting reference trajectory is edited as needed by means of a dedicated graphical user interface before being used as a target trajectory in the robot-in-charge mode.

3.5.1.1 Record and replay

In the patient-in-charge mode used for reference data recording the actuators are controlled towards zero torque by means of the torque controller described in section 3.3. The recorded data is sectioned in subrecords by means of the heel strike detection signal produced by the FSR sensor attached to the subject's heel. Since the length (i.e. number of data points) of the individual subrecords varies, they are interpolated onto a single reference time base prior to averaging. The obtained averaged trajectory covers one stride or gait cycle and is therefore referred to as "reference cycle". The reference cycle is either edited by software or directly used, "replayed", as a target trajectory for the exoskeleton in the robot-in-charge mode. During online trajectory generation the original or edited reference cycle is interpolated onto the appropriate time base as required by the synchronisation algorithm explained in section 3.5.2.

3.5.1.2 Trajectory customisation

To facilitate the customisation of target trajectories a dedicated graphical user interface was made. The GUI window is depicted in fig. 3.36. Any reference cycle, either originating from gait analysis data or recorded by means of the exoskeleton can be adapted by applying offsets and scale factors to specific areas of the dataset. The tuneable offsets and scale factors are based on polynomials calculated

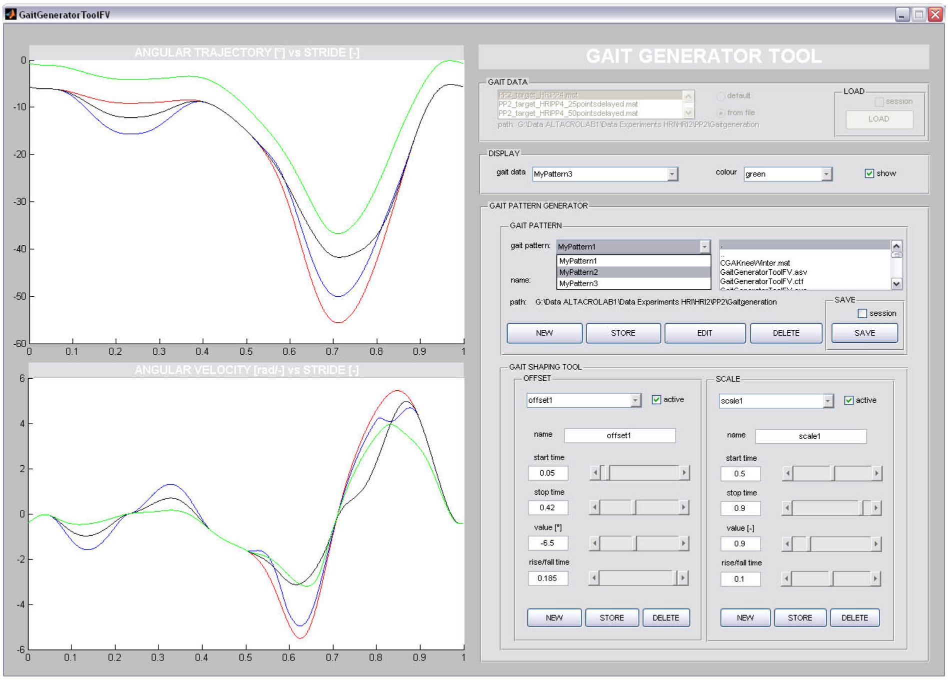

Figure 3.36: Graphical user interface for offline trajectory generation and adaptation.

such that the derivative of the trajectory (i.e. the angular velocity) is continuous. The trajectory adaptation can be tailored to the specific needs of the subject, for instance increased knee flexion during swing to ensure toe clearance.

3.5.2 Synchronisation

Due to the compliance of the device and due to the fact that only the subject's knee joint is externally powered, variations in gait timing generally occur. This variability gives rise to a dynamic interaction with the compliant robotic assistance, resulting in a fluctuating de-synchronisation between the trajectory controlled robot and the wearer. This phenomenon has also been reported in Aoyagi et al. (2007). Since our device has no other actuated DOFs than the knee joint, it was challenging even for unimpaired subjects to keep their cadence synchronised with the exoskeleton in the absence of any synchronisation algorithm, although their personal, previously recorded trajectory was being tracked.

To accommodate for this in view of testing with impaired subjects, both cycle initiation and cycle duration are adapted on a per step basis by a synchronisation

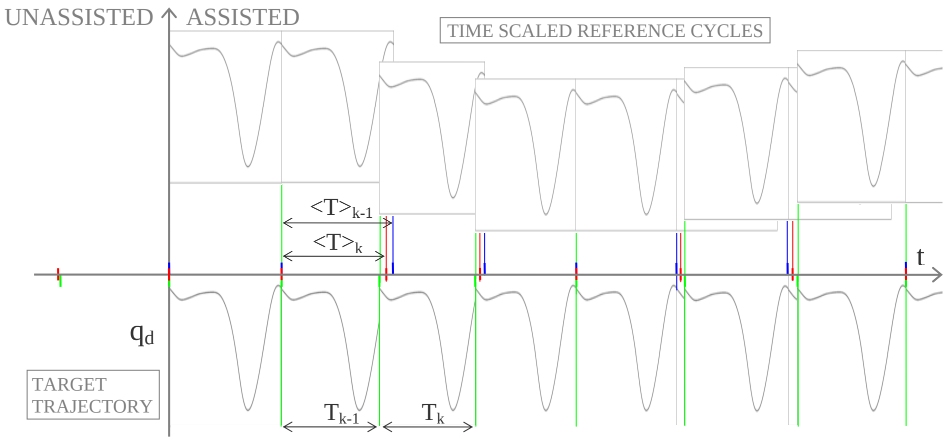

Figure 3.37: Synchronisation of the target trajectory: target trajectory q_d as a function of time consisting of time scaled versions of a reference cycle. Instance of heelstrike marked in green, projected end of a time scaled cycle in blue, projected end of the next replayed cycle based on moving average in red.

algorithm that uses the heel strike detection signals. At the instance of heel strike detection the target knee trajectory is reset to the beginning of the reference cycle. The time period between the two latest consecutive heel strike detections is incorporated into a moving average defining the required duration of the current cycle. The reference cycle is then scaled in time accordingly by interpolation onto the desired time base. If the time base elapses before the next heelstrike detection (decreasing cadence) the target trajectory is reset to the beginning of the reference cycle projected on the same time base, if heelstrike occurs before the end of the time base (increasing cadence) the target trajectory is also reset but the time base is updated by the moving average. The moving average of the stride period for stride k, denoted $< T >_k$, is calculated out of previous stride period measurements according to

$$< T >_k = \alpha T_{k-1} + (1 - \alpha) < T >_{k-1},$$

where α is a factor defining the influence of the last measurement with respect to preceding measurements. The synchronisation procedure is illustrated by fig. 3.37. The adaptation of the exoskeleton to the subject's gait timing can thus be tuned so that only moderate changes in cadence are allowed and excessive changes for instance trigger a safety routine. In order to have the target trajectory synchronised with the subject's gait timing from the very beginning of an assisted walking trial, the device is set to the patient-in-charge mode during the first few steps and switched to robot-in-charge mode when a steady cadence has been reached.

3.6 Conclusion

The state-of-the-art in control of assistance based gait rehabilitation robots has evolved rapidly over the years and has shifted focus on the concept of "assistance-as-needed". Research efforts appear to be concentrated on four strategies to put this concept into practice: task/function specificity of assistance, adaptivity of the assistance level, adaptivity of the timing of assistance and adaptivity of assistance in space.

The knee exoskeleton KNEXO developed and used in this work to implement and test a control strategy for safe, compliant and adaptable gait assistance, uses actuators with built-in compliance. Because of this compliance a certain level of adaptivity is intrinsic to the system. Two complementary control strategies were investigated in order to achieve controlled adaptive assistance: a torque control strategy that displays an unassisted (patient-in-charge) mode and a trajectory tracking based control strategy that displays an assisted (robot-in-charge) mode. The unassisted mode provides a baseline for the evaluation of the effects of assistance and it allows for target trajectory recording for the assisted mode. For the trajectory tracking based control strategy the safety of interaction between the human and the robot was considered of primary concern.

The proposed torque controller combines conventional PI control using force sensor feedback with a feedforward term based on a static actuator model. Its performance was evaluated by means of isometric torque tracking experiments and experiments with the actuator system in zero-torque mode and subject to manually imposed joint motion. Due to the system's underlying nonlinear pressure dynamics, its torque tracking capability proved to be highly dependent on the desired torque amplitude, however, it was found to outperform previously reported results of torque/force tracking of pneumatic muscle based actuator systems. In zero torque mode the system's dynamic stiffness saturates at the intrinsic stiffness at high speed joint motion, but it is significantly reduced at the frequency range of our application. Actuator torques in this mode are limited to a few Nm in the angular velocity range of the joint corresponding with slow to normal walking. The model-based feedforward term is shown to be essential to both torque and zero-torque tracking performance.

The proposed trajectory tracking controller adopts the recently introduced concept of proxy-based sliding mode control (PSMC), a control method that inherits characteristics from both PID control and ideal sliding mode control. PSMC provides the system with an adjustable actuator torque limit and an adjustable slow recovering motion in the event of large deviations from the target. These features ensure an adjustable, gentle response to unforeseen interaction torques between the human and the robot (due to for instance muscle spasms, increased muscle tone or voluntary muscle force), that would otherwise be treated as perturbations by a conventional tracking controller. This essential difference was made clear by comparing PSMC and regular PID control in interaction experiments. The application of PSMC to gait assistance reveals the need of a complementary feedforward torque acting as a support torque. In order to improve the accuracy of the torque limitation an alternative implementation of PSMC was proposed using the torque controller as an inner torque control loop (PSMC IT). Tracking experiments with PSMC, PSMC IT and PID showed comparable overall tracking performance in the absence of perturbations. PSMC IT, however, outperforms PSMC at accurately displaying the interaction torque limit in interaction experiments. These promising results encouraged passing on to assisted walking experiments with unimpaired and impaired subjects.

Chapter 4

Robot-assisted walking with KNEXO

4.1 Introduction

In the previous chapter the controllers implemented on the powered knee exoskeleton were introduced and their performance was evaluated on a simplified test setup. This chapter deals with the evaluation of KNEXO in various treadmill walking experiments. The evaluation of the proposed methods in actual walking experiments with the exoskeleton was first made with unimpaired subjects in different stages before passing on to experiments with impaired subjects. Hence, it was considered of great importance to thoroughly test the device and the proposed methods in view of functionality and safe operation.

First, preliminary assisted walking experiments were performed by a single subject wearing the intermediary prototype (see fig. 2.34). Results are given and discussed in section 4.2.2. Based on these results, the intermediary prototype was adapted into the final prototype, KNEXO (see fig. 2.35), and two important extensions were made to the control software: force sensor based torque control and trajectory synchronisation, both described in the previous chapter in section 3.3 and section 3.5.2 respectively.

Several unimpaired subjects participated in experiments of unassisted and assisted walking with KNEXO. The unassisted mode or zero-torque (ZT) mode was implemented by means of zero-torque control (see 3.3), the assisted mode by means of proxy-based sliding mode control without (PSMC, see 3.4.2.3) or with inner torque control loop (PSMC IT, see 3.4.2.5) and non-model based feedforward torque (see 3.4.2.4).

The main objectives of the unassisted walking experiments were to:

- assess the performance of the unassisted mode
- investigate the effects of unassisted walking with KNEXO on gait

Results are given and discussed in section 4.2.1.

The main objectives of the assisted walking experiments were to:

- verify the feasibility of the record-replay procedure
- investigate the effects of controller settings on compliant guidance
- investigate the effects of controller settings on physical human-robot interaction

Results are given and discussed in section 4.2.3. In order to gain a better insight in the interaction between the human and the robot, and in view of testing with impaired subjects, data from the exoskeleton was combined with gait kinematics data and muscle activity measurements.

Following the successful evaluation with unimpaired subjects, a stroke patient and a Multiple Sclerosis (MS) patient participated in assisted walking trials with KNEXO. These experiments are the final and concluding stage of the work reported in this dissertation and their purpose was to:

- evaluate the effectiveness of the device and the proposed methods in assisting impaired knee function
- evaluate the effects of assistance at the knee on gait
- obtain patient feedback about the perception of assistance and comfort

Results are presented and discussed in section 4.3.

4.2 Unimpaired subjects

4.2.1 Unassisted walking

Unassisted walking experiments were performed with several unimpaired subjects to assess the quality of the exoskeleton's unassisted mode or zero-torque (ZT) mode and its suitability as a gait recording mode for use in a record-replay procedure. Besides the direct effect on knee joint kinematics, the influence of KNEXO on gait kinematics and muscle activity was investigated.

4.2.1.1 Experimental design

Setup and methods Ten unimpaired subjects (age 27.4 ± 6.1, length $1.82 \pm 0.10\,m$, weight $77.5 \pm 11.7\,kg$) participated to the unassisted walking assessment.

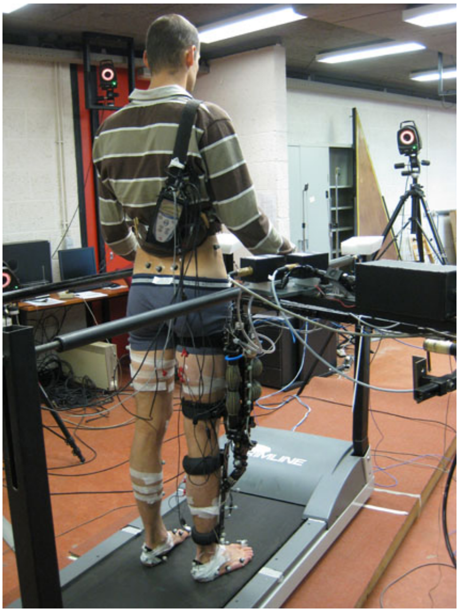

Figure 4.1: Setup for treadmill walking experiments with KNEXO.

In order to evaluate the effects on gait kinematics and muscle activity, motion capturing (Vicon 612 motion analysis system with 7 high-speed (250Hz) infrared cameras) and muscle EMG measurements (Megawin ME6000 Biomonitor, 8 channels) were performed. Figure 4.1 depicts the experimental setup.

Prior to the actual experiments KNEXO was fitted to the subject, followed by a familiarisation period (about 5-10 minutes) of unassisted walking with the device in zero-torque (ZT) mode. This period was kept short, because all subjects participated in preliminary experiments with the device one day or a few hours before. Afterwards EMG electrodes were attached to capture the activity of 5 muscles of the subject's right leg (exoskeleton side): tibialis anterior ("TA", ankle dorsiflexor muscle), gastrocnemius ("GA", ankle plantarflexor muscle), biceps femoris ("BF", knee flexor muscle), rectus femoris ("RF", muscle of the quadriceps, knee extensor and hip flexor muscle) and vastus lateralis ("VL", muscle of the quadriceps, knee extensor muscle). Muscle activity during maximal voluntary contraction (MVC) was measured for normalisation of EMG data (expressed as a percentage of MVC). Reflective markers were attached according to the marker protocol in appendix C. A foot contact sensor (FSR sensor, see 2.5.4.2) was used for right heel strike detection. For more details about the motion capturing as well as the EMG measurements, the reader is referred to appendix C.

The actual walking experiments consisted of a few minutes of treadmill walking without KNEXO and a few minutes of walking with KNEXO in ZT mode, as long as needed to achieve steady state based on visual gait assessment. In both cases, the subject held the treadmill's sidebars. During all walking trials treadmill speed was set to $2.5\,kmph$ ($0.7\,m/s$), which is a common walking speed in robot-assisted treadmill training (see for instance Hornby et al. (2005)).

Data analysis All data captured by the exoskeleton, the motion analysis system and the EMG device were sectioned in cycles according to the heel strike detection signal. The gait analysis based on motion capture data provides the relative rotational motion between the foot and the lower leg, the lower leg and the upper leg and the upper leg and the pelvis for both legs. The discussion of results focuses on the rotations in the sagittal plane (the plane of progression), namely plantarflexion/dorsiflexion of the ankle, flexion/extension of the knee and flexion/extension of the hip. The data was low-pass filtered (4^{th} order butterworth, cut-off frequency of $12.5\,Hz$) to remove motion artefacts. Sudden changes in the standard deviation with respect to stride percentage indicates the presence of these artefacts in the source data. EMG data was full rectified, normalised with respect to maximal voluntary contraction (MVC) and time-averaged (moving window of $100\,ms$). Both gait kinematics data and EMG data were averaged over 4 strides.

4.2.1.2 Results

Figure 4.2 shows KNEXO joint trajectories and actuator torques for all subjects, recorded during ZT mode and averaged over 30 gait cycles. Fitting of the device was done so that a KNEXO joint angle of 0° approximately corresponded with a stretched knee. The average actuator torque cycle over all subjects is marked in red, the average 95% confidence bounds over all subjects are marked in green on top. For two subjects the kinematics of the right and left ankle, knee and hip are compared between "NO KNEXO" (red) and "ZT" (green) in fig. 4.3 (subject A) and fig. 4.5 (subject B). The respective comparison of normalised processed EMG, expressed in % of MVC, is made by fig. 4.4 (subject A) and fig. 4.6 (subject B). It is important to note that a time delay of a few percents of stride (about $2-5\%$, depending on the subject) between the instance of actual initial foot contact after swing and the instance of foot contact detection by the FSR sensor on the heel should be taken into account when analyzing sectioned data.

4.2.1.3 Discussion

In ZT mode KNEXO generates joint torques generally below $2\,Nm$, except during initial swing ($\approx$ 65% of stride), when angular velocities are maximal. This is according to the expectations considering the experimental results discussed in 3.3.2.2. None of the subjects reported experiencing a marked resistance at this specific instance.

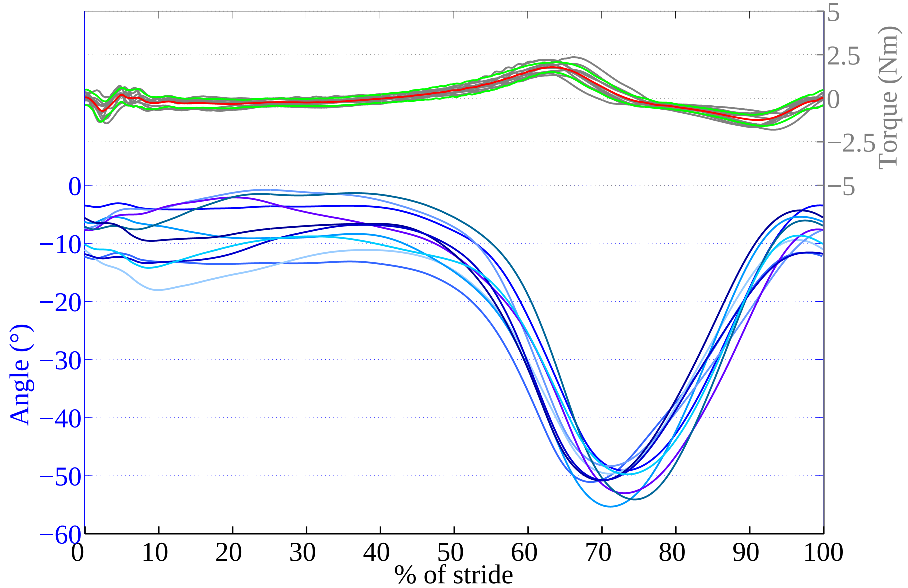

Figure 4.2: Averaged ZT recordings of 10 unimpaired subjects: knee joint trajectories and actuator torques of KNEXO. Average torque cycle over all subjects (red), average 95% confidence bounds over all subjects (green).

In some subjects, however, knee joint kinematics appeared to differ significantly between walking without KNEXO and walking with KNEXO in ZT mode.

In subject A (fig. 4.3) knee excursion is clearly reduced both in flexion and extension, in subject B (fig. 4.5) the effect is less pronounced, but a slightly reduced knee flexion during swing and reduced extension is still observed. The effect of KNEXO on right knee kinematics cannot be attributed entirely to the resisting torque of the actuator, however, since this torque does not comprise the effect of the added inertia and the weight of the exoskeleton's lower leg link for instance nor the possible effect of kinematical misalignments of the human and robotic knee joint. In addition, changes in the kinematics of the other joints affect the right knee joint and vice versa. Both subjects show increased flexion of the right hip, for instance, which could indicate a compensation of the added inertia of the exoskeleton and/or a compensation of the incomplete knee extension at the end of swing. In subject A the range of motion of the hip is conserved and the stride period is hardly affected ($1.413 \pm 0.016\,s \rightarrow 1.423 \pm 0.016\,s$), whereas in subject B the smaller hip excursion leads to a shorter step length and thus a shorter stride period ($1.522 \pm 0.044\,s \rightarrow 1.402 \pm 0.023\,s$).

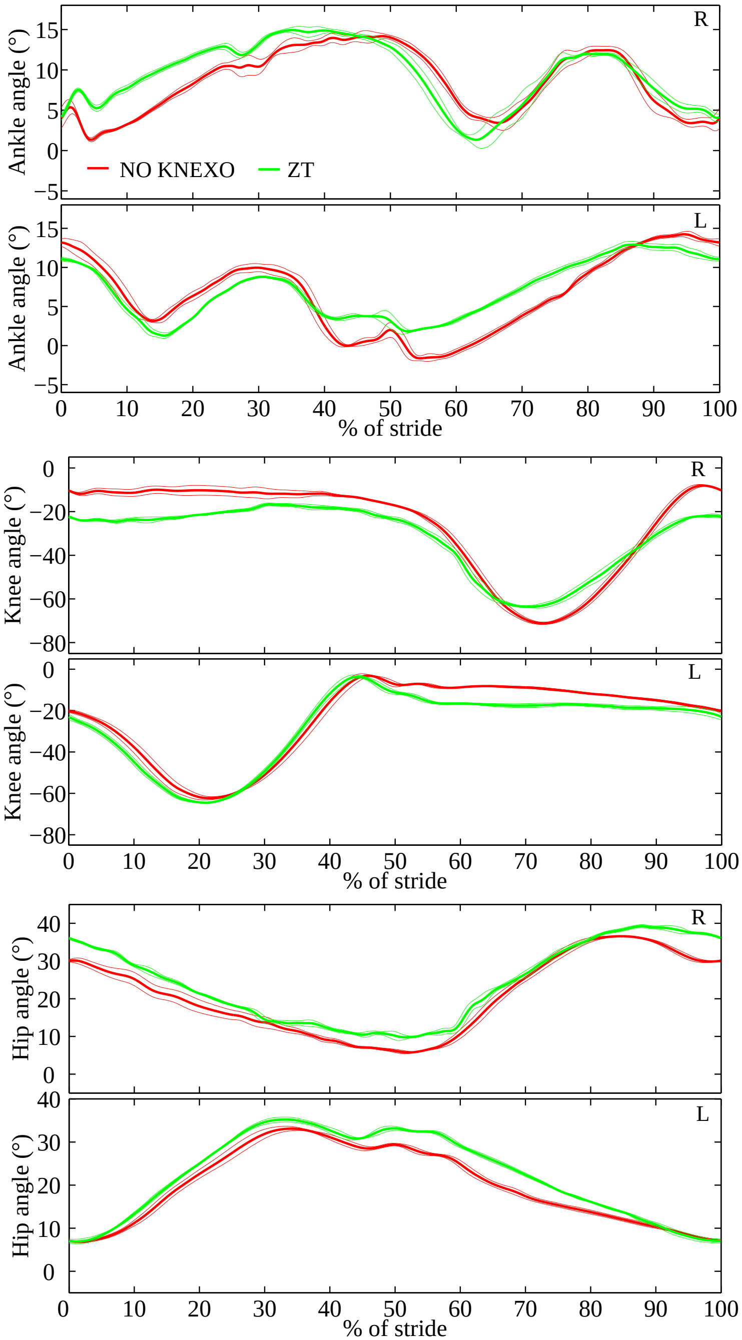

Figure 4.3: Comparison of gait kinematics of subject A with and without KNEXO: flexion/extension angles of the right and left ankle, knee and hip joint without KNEXO (red) and with KNEXO in unassisted (ZT) mode (green).

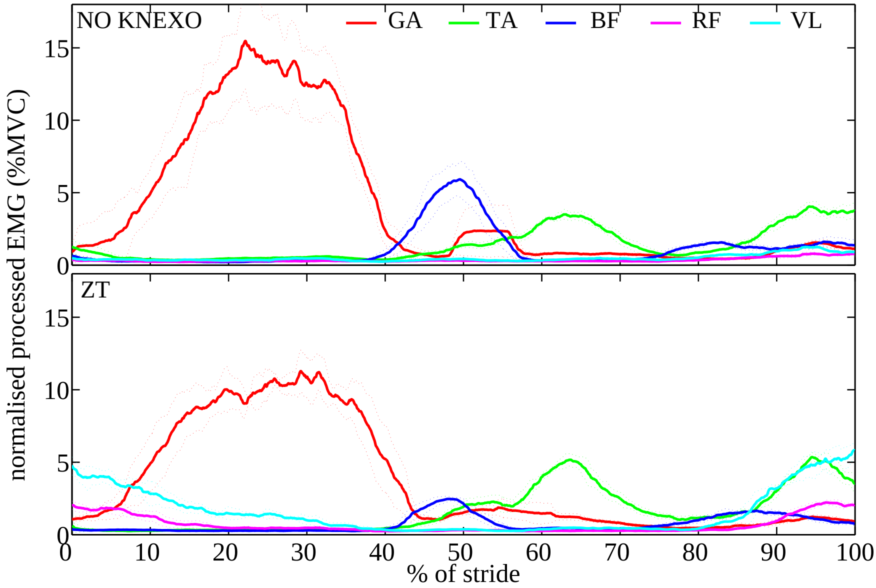

Figure 4.4: Comparison of the muscle activity of subject A with and without KNEXO: normalised processed EMG of five muscles of the right leg of subject A. TA:tibialis anterior, GA: gastrocnemius, BF: biceps femoris, RF: rectus femoris, VL:vastus lateralis.

The EMG data of subject A (fig. 4.4), when compared with subject B (fig. 4.6), shows a marked increase of the activity of the muscles responsible for leg extension (rectus femoris and vastus lateralis) in order to compensate the incomplete extension during swing and to adequately support the body weight while the knee is being more flexed during stance ($80 \rightarrow 20\,\%$ of stride). In both subjects gait kinematics in general show an increased left-right asymmetry.

Summarising these findings, one concludes that wearing KNEXO in unassisted mode has an effect on right knee kinematics, which, combined with the effect of the unilaterally added inertia of the device, leads to asymmetric gait. These effects are dependent on the individual compensatory strategies of the subject. In order to quantify the specific contribution of the resisting torque, experiments could be performed with the actuators mechanically decoupled from the system. It is expected however that further improving the zero-torque controller would have some, but only limited benefit here, since the device is unilateral and has one single powered DOF. It is clear that the induced gait asymmetry should be carefully taken into account when evaluating the effect of gait assistance by KNEXO in persons with gait impairment.

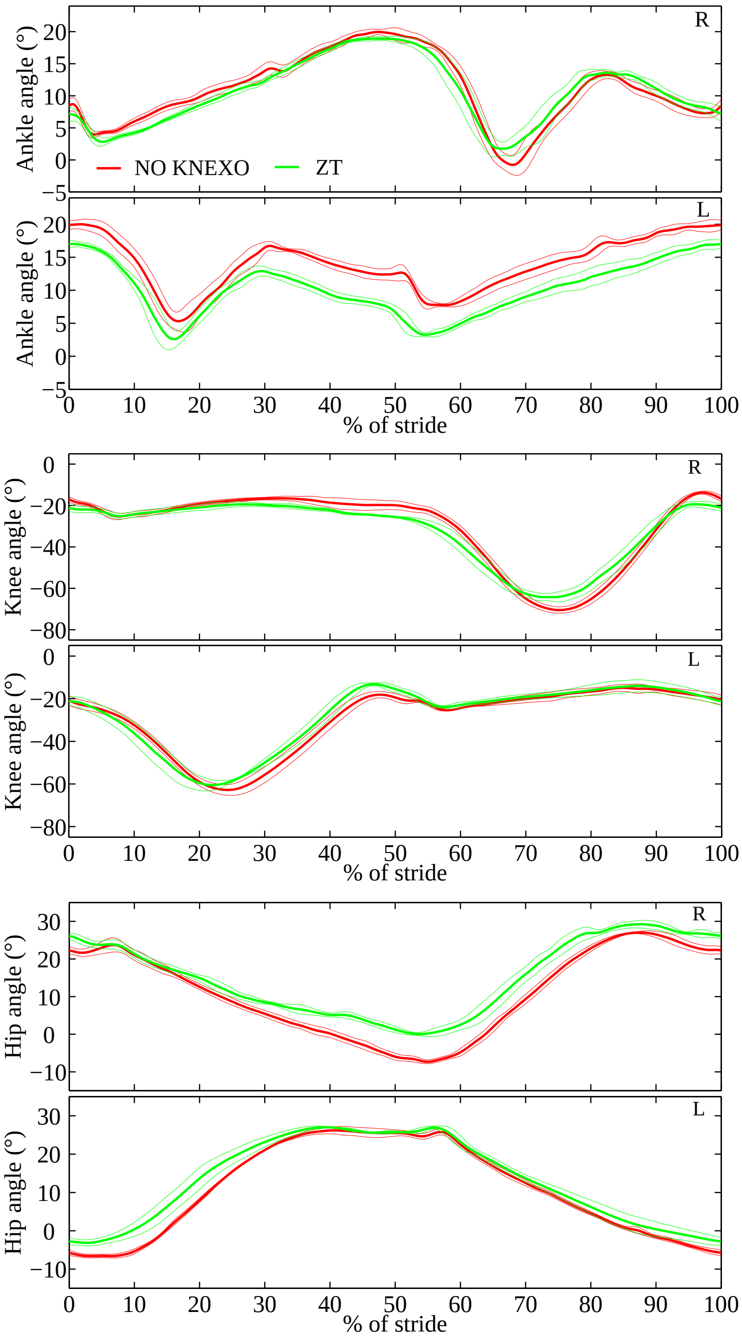

Figure 4.5: Comparison of gait kinematics of subject B with and without KNEXO: flexion/extension angles of the right and left ankle, knee and hip joint without KNEXO (red) and with KNEXO in unassisted (ZT) mode (green).

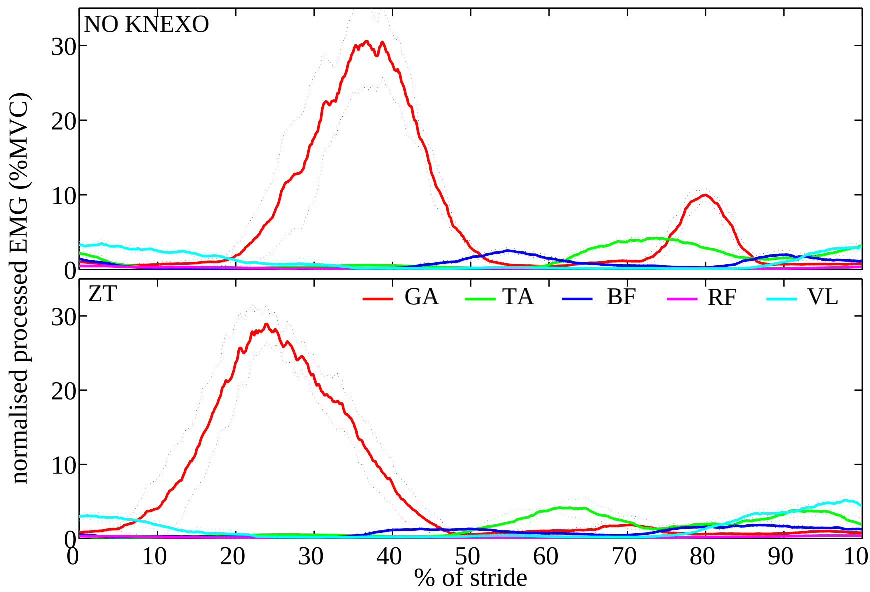

Figure 4.6: Comparison of the muscle activity of subject B with and without KNEXO: normalised processed EMG of five muscles of the right leg of subject B. TA:tibialis anterior, GA: gastrocnemius, BF: biceps femoris, RF: rectus femoris, VL:vastus lateralis.

4.2.2 Assisted walking: preliminary experiments

Pilot experiments with a single unimpaired subject have been performed as a preliminary evaluation of the assistive controller with emphasis on trajectory tracking. More specifically, the aim was to study the influence on allowable controller settings of the "human-as-part-of-the-system" and the influence of a model-based feedforward torque.

4.2.2.1 Experimental design

Setup and methods Pilot walking experiments were performed by a single subject (age 26, $1.80\,m$, $78\,kg$) wearing the intermediary prototype that included a passive hip joint and an upper body segment (see 2.4.2). The experimental setup is depicted in fig. 4.2.2.1. Besides differences in hardware between the intermediary prototype and the final prototype (KNEXO) some differences in the control software should be noted as well. The unassisted mode was implemented by means of pressure control, instead of the torque controller described in 3.3. The assisted mode was implemented by means of the PSMC controller given by 3.4.2.3, but the

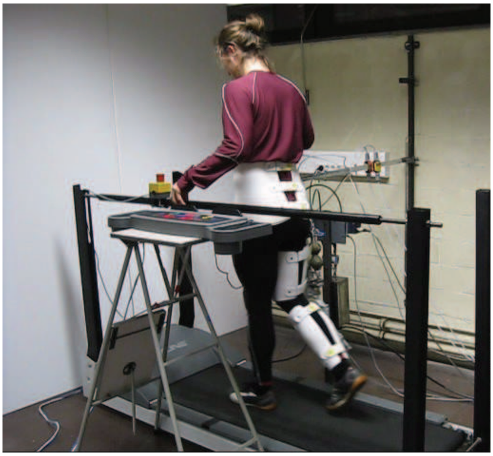

Figure 4.7: Experimental setup for treadmill walking experiments.

pressure limit Δp_{LIM} was set directly, instead of being calculated out of a required torque limit τ_{LIM}. As the synchronisation algorithm described in 3.5.2 was not yet implemented, a fluctuating desynchronisation initially occurred between the actual trajectory and the target trajectory of the exoskeleton during assisted walking. An auditive cue at the start of each gait cycle was therefore used as a preliminary way to help the subject synchronising with the target trajectory. All experiments were carried out at a fixed treadmill speed of $2.5\,kmph$ ($0.7\,m/s$).

A record-replay procedure as described in 3.5 was followed. First hip and knee trajectories were recorded during 25 strides while wearing the exoskeleton in unassisted mode. The recorded data was sectioned in cycles and averaged in order to obtain a single reference cycle for the hip and the knee. The sectioning was based on a search algorithm (similar to the method described in Aoyagi et al. (2007)) that determined for each cycle the point $(q_k, \dot{q}_k, q_h, \dot{q}_h)$ closest to a reference point in state space corresponding with right heel strike. The averaged data were fitted by a 7th order Fourier series in order to obtain a smooth and periodic reference cycle for both knee and hip joint. By selectively scaling the reference knee trajectory different target trajectories were generated for replay during assisted walking trials. Walking trials consisted of 45 seconds of unassisted walking to familiarise with the cadence directly followed by 45 seconds of assisted walking.

The "default" control parameter values of the implemented proxy-based sliding mode controller where: $K_p = 4\,bar/rad$, $K_i = 4\,bar/rad.s$, $K_d = 0.06\,bar.s/rad$, $\Delta p_{LIM} = 1.25\,bar$, $\lambda = 0.3\,s$. During assisted knee flexion/extension experiments feedback gains could be increased further beyond the aforementioned default gain setting and manual tuning pointed out a larger range of stable behaviour, when compared with a configuration of the exoskeleton with a fixed load only. This is due to the additional variable stiffness and damping introduced by the human, which is considered to have a stabilising effect on the system (Vallery (2009)). Gravity compensation was used based on an estimation of the gravitational torque acting on the lower leg segment (i.e. the lower leg and the exoskeleton's lower leg link) during swing. Given an estimation of the lower leg segment's mass, m , and the distance between the center of mass and the knee joint, l, a feedforward torque was calculated of the form $\tau_{FF} = mglsin(q_h + q_k)$ assuming a vertical upper body segment. No gravity compensating support torque was provided for the stance phase. Between trials the target trajectory and/or the control parameters, i.e. the gains K_p, K_i, K_d, the pressure limit parameter Δp_{lim}, the sliding mode time constant λ and the feedforward term τ_{FF}, were adapted to study their influence.

4.2.2.2 Results

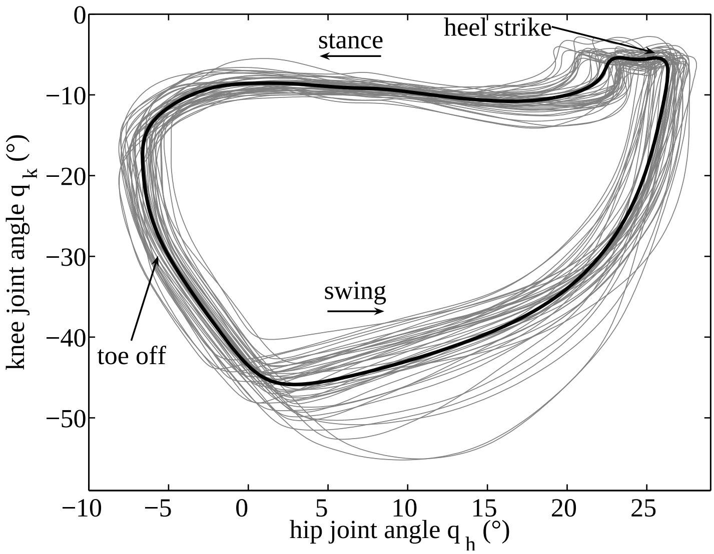

Figure 4.8: Knee and hip joint angles (gray) recorded during unassisted walking and the reference cycle obtained by averaging (black).

The averaged cycles and the unassisted walking data from which they were retrieved are depicted in (q_k,q_h)-axes in fig. 4.8. This combined representation of hip and knee joint angles is used consistently throughout the discussion of results in order to visualise the effect of the assistance at the knee joint on hip joint kinematics.

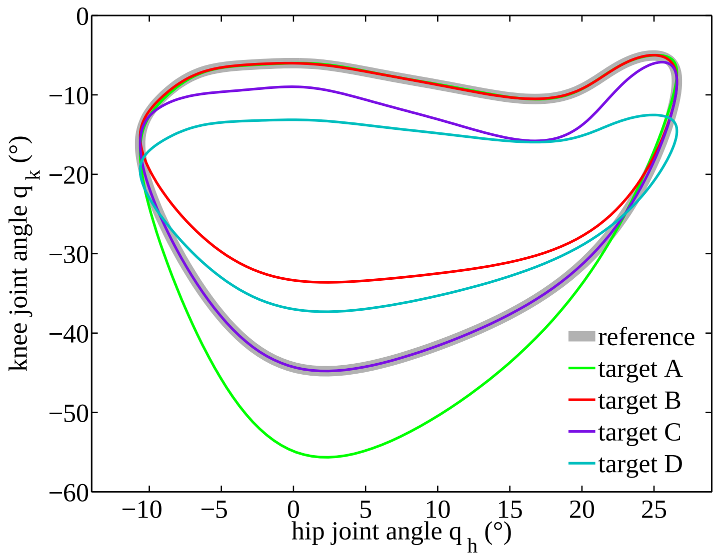

Figure 4.9: Different target trajectories obtained by scaling a reference cycle (gray) fitted on the averaged recorded data shown in fig. 4.8.

Figure 4.9 shows the fitted reference cycle (grey) and the scaled target trajectories (coloured) derived from it. Targets A (green) and B (red) are obtained by applying a scale factor of 1.25 and 0.75 respectively to the reference knee angle during swing phase only (respectively more or less flexion during swing). Target C (purple) is obtained by applying a scale factor of 1.5 during stance phase only (more flexion during stance). Target D (cyan) has a range of motion that is symmetrically decreased by 15°(more flexion during stance, less flexion during swing).

Figure 4.10 illustrates the effect of these target trajectories on the actual knee joint angle during assisted walking. Data recorded a few steps before and after the transition from unassisted (grey) to assisted walking (black) are shown. The knee joint data of assisted gait (black) is plotted against the desired reference hip joint trajectory, setting focus to the deviations from the knee joint target.

In fig. 4.11 the knee-hip pattern obtained in the assisted mode with target B (red) and default control parameter values (black) is compared with the case of a smaller value of the pressure limit parameter Δp_{lim} (dark grey) and a larger value of the sliding mode time constant λ (light gray dashed). Knee joint angles are plotted against actual hip joint angles. The combined influence of the feedforward term τ_{FF} and of Δp_{LIM} on deviations from the desired knee joint trajectory (target A, green) is illustrated by fig. 4.12. Δp_{LIM} is switched between $0.3\,bar$ and $1.25\,bar$ (right-left) and τ_{FF} is either set equal to zero or not (bottom-top). Knee joint angles are plotted against the reference trajectory of the hip.

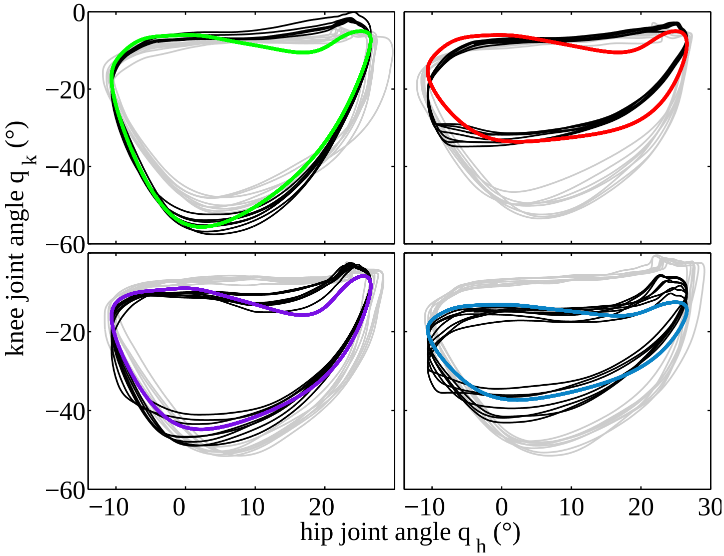

Figure 4.10: Unassisted gait data (gray) and assisted gait data (black) of four walking trials, where patterns A (green), B (red), C (purple) and D (cyan) (see fig. 4.9) were used as target pattern and control parameters were set to default values. Note: the assisted gait data of the knee is plotted against the fixed reference hip trajectory to put focus on knee trajectory tracking.

4.2.2.3 Discussion

According to fig. 4.10, the exoskeleton succeeds in guiding a healthy subject's knee along different trajectories that differ substantially from the reference trajectory recorded during unassisted walking. The compliance of the system ensures variability with respect to the target trajectory, which is believed to be helpful for motor learning and to promote active participation of the user (Reinkensmeyer et al. (2007)).

The indirect actuator torque limit Δp_{LIM} puts a limit on the amount of guidance. A target trajectory that differs substantially from the unassisted knee joint trajectory makes this clear in fig. 4.11. Decreasing Δp_{LIM} results in knee flexion amplitudes closer to those observed during unassisted swing. It is important to note the effect of the time constant λ as well. The experimental results discussed in 3.4.3.3 of the previous chapter stressed the importance of setting this parameter in such a way that the recovering motion is appropriately slow to avoid overshoot and high angular velocities. In the case of assisted gait, a recovering motion that is too slow, however, might impede timely recovery in critical phases of gait. It is clear from fig. 4.11 for instance that a larger time constant hinders full extension of

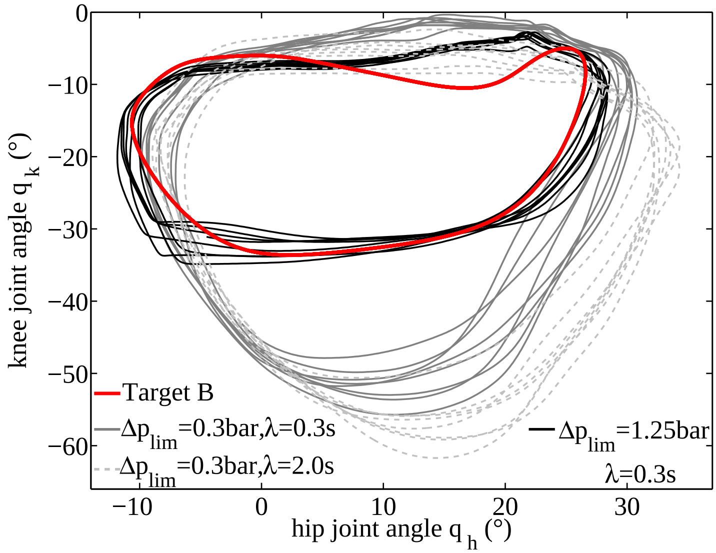

Figure 4.11: Assisted gait data of three trials were target B (red) was used as a target trajectory and control parameters were set to default values (black), Δp_{lim} was set to $0.3\,bar$ (dark gray) and λ was set to $2.0\,s$ (light gray dashed) respectively. Note: the assisted gait data of the knee is plotted against the actual hip joint angles.

the knee prior to heel strike (light grey dashed curve). As a compensatory strategy, the subject increases hip flexion in preparation of proper foot contact. The dual requirement of λ, needing to be large enough to ensure a safe interaction in the event of large deviations from the target and at the same time being small enough to ensure continuity of gait, could be resolved by varying its value throughout the gait cycle. A similar strategy could be applied to the actuator torque limit, as it undergoes the same duality between ensuring safety by closely tracking the target trajectory (e.g. to avoid a fall) and ensuring safety by allowing deviations.

The trade-off related to actuator torque limitation is influenced by the feedforward torque, as can be inferred from fig. 4.12. Tracking during the swing phase is degraded if the feedforward torque is deactivated (bottom vs top) and more importantly, tracking performance is more sensitive to variations of Δp_{LIM} (right vs left) in that case. If the feedforward torque is activated, the torque limit defines an actuator torque relative to the feedforward torque instead of relative to zero torque. Hence, the better the feedforward torque approximates the required torque, the less the torque limit needs to be dedicated to overcoming tracking errors. This observation was the main rationale behind the use of a non-model based feedforward torque, as explained in section 3.4.2.4 of the previous chapter.

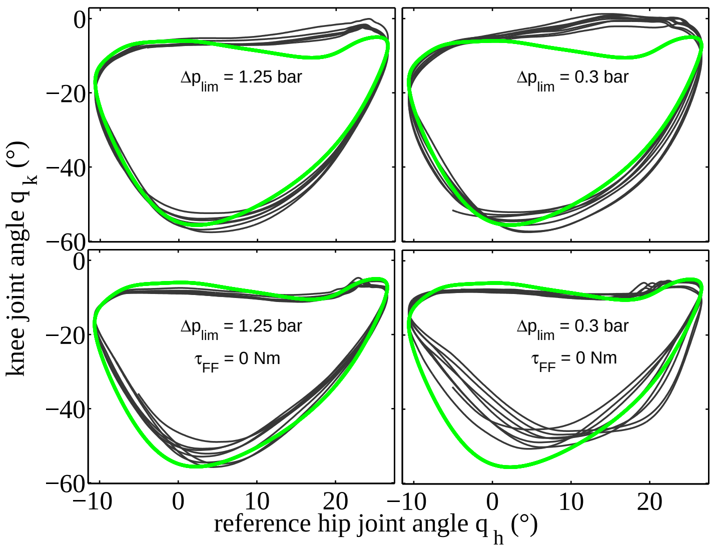

Figure 4.12: Assisted gait data (black) of four walking trials, where target A (green) was used as target trajectory, Δp_{lim} was set to $1.25\,bar$ (left) or $0.3\,bar$ (right) and τ_{FF} was either set zero (bottom) or not (top). Note: the assisted gait data of the knee is plotted against the fixed reference hip trajectory to put focus on knee trajectory tracking.

4.2.3 Assisted walking: human-robot interaction

In order to study physical human-robot interaction during robot-assisted walking, interaction experiments were performed with several unimpaired subjects. Emphasis is put on the robot's response to human-induced perturbations and the influence hereon of the control parameters and of the support (feedforward) torque. Different assistive modes and interaction cases are tested in view and preparation of experiments with impaired subjects.

4.2.3.1 Experimental design

Setup and methods Two types of measurement setups were used. In interaction experiments with focus on controller tuning, the subjects were only fitted with the device and a heel contact detection sensor. Walking trials with the device in assisted mode (PSMC and PSMC IT) were performed during which the subject was requested to walk naturally, reduce effort or resist the target motion imposed by the device. A second type of measurement setup, as depicted in fig. 4.1, also involved camera-based motion capturing and muscle EMG measurements. Maximal voluntary contraction tests and an unassisted walking trial with the device

	A	B	C	D	E	F	G	H
K_p, K_i, K_d (%)	*100*	100	100	100	*100*	100	**25**	100
FF (%)	*0*	0	0	0	*100*	100	100	100
τ_{lim}(Nm)	*20*	20	**10**	**10**	*10*	10	10	**5**
λ (s)	*0.1*	0.1	0.1	**0.5**	*0.1*	0.1	0.1	0.1
disturbance		**x**	**x**	**x**		**x**	**x**	**x**

Table 4.1: Controller settings used in experiments with unimpaired subjects in PSMC mode without feedforward (A-D) and with feedforward (E-H). Changes relative to the italic setting are marked in bold. 100%G corresponds with $K_p = 4.0\,bar/rad$, $K_i = 4.0\,bar/rad.s$, $K_d = 0.04\,bar.s/rad$. 100%FF corresponds with the total feedforward torque reference cycle as recorded in a preceding assisted trial with 0%FF.

in ZT mode to record the individual reference trajectory were followed by assisted walking trials with the subject's own previously recorded reference cycle as a target trajectory. The subject was requested to resist knee flexion during swing en controller settings were varied between trials.

The following discussion of results only covers the assistive mode based on PSMC. As explained in the previous chapter (see 3.4.3.2), the PSMC IT controller was found to be less stable than PSMC. Occasional small and high-frequency pressure oscillations were observed and, although hardly affecting tracking performance, the resulting small torque oscillations were noticed by the person wearing the device. In view of testing with patients it was therefore decided to focus on the performance and implementation of PSMC.

4.2.3.2 Results

A representative overview of the interaction experiments is given by fig. 4.13-4.16. These data are collected from assisted walking experiments with a single subject (age 27, $1.57\,m$, $50\,kg$). Strides of genuine assisted walking are alternated with perturbations induced by the subject in order to achieve larger flexion during swing, smaller flexion during swing or larger flexion during stance. Besides the target trajectory (red) and the knee joint trajectory (blue), the proxy trajectory (green), the actuator torque and the deviation from the target are also shown as they provide a better insight in the system's behaviour in response to perturbations. Figure 4.13-4.14 show data corresponding with assistance without feedforward (0%FF), with high gains (100%G) and respectively with a high torque limit ($\tau_{LIM} = 20\,Nm$) and a low torque limit ($\tau_{LIM} = \{10\,Nm, 7\,Nm\}$). Figure 4.15-4.16 show data corresponding with assistance with feedforward (100%FF), with a low torque limit ($\tau_{LIM} = \{10\,Nm, 5\,Nm, 0\,Nm\}$) and respectively with high gains (100%G) and low gains (25%G). The influence of controller settings on interaction in these experiments is summarised by fig. 4.17.

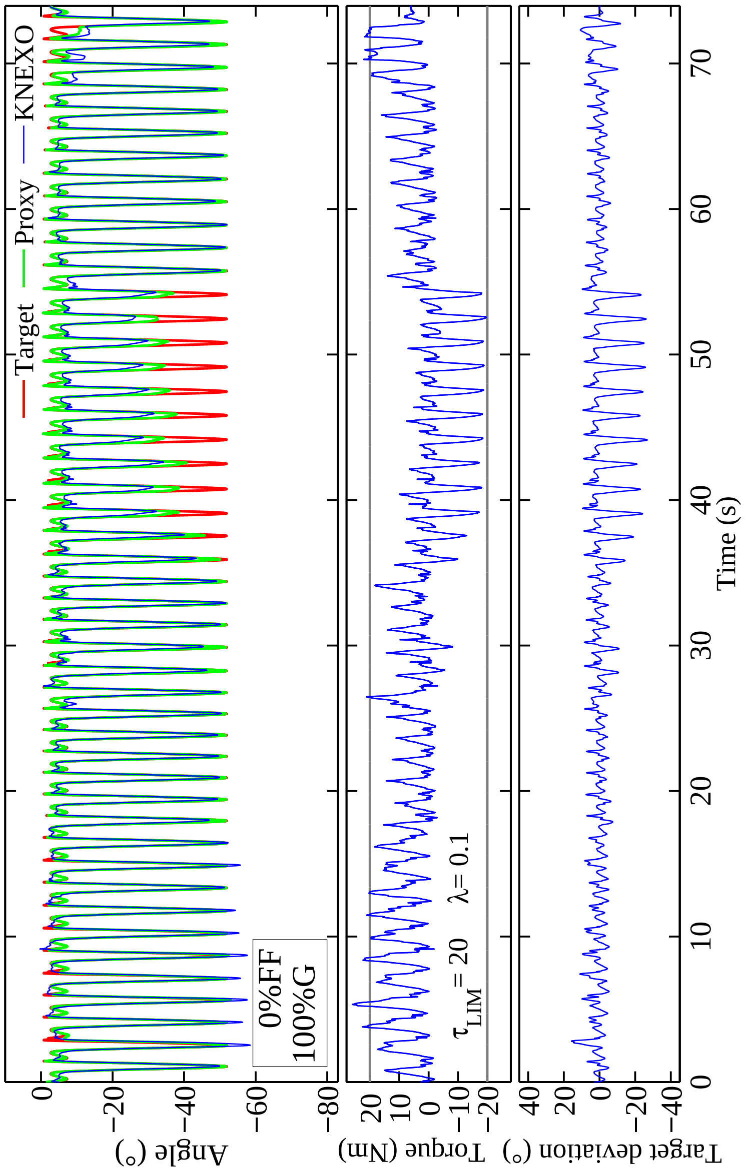

Figure 4.13: Human-robot interaction experiment: system behaviour under perturbations induced by the wearer. Controller setting without feedforward (0%FF), with high gains (100%G), high torque limit ($\tau_{LIM} = 20\,Nm$) and $\lambda = 0.1\,s$

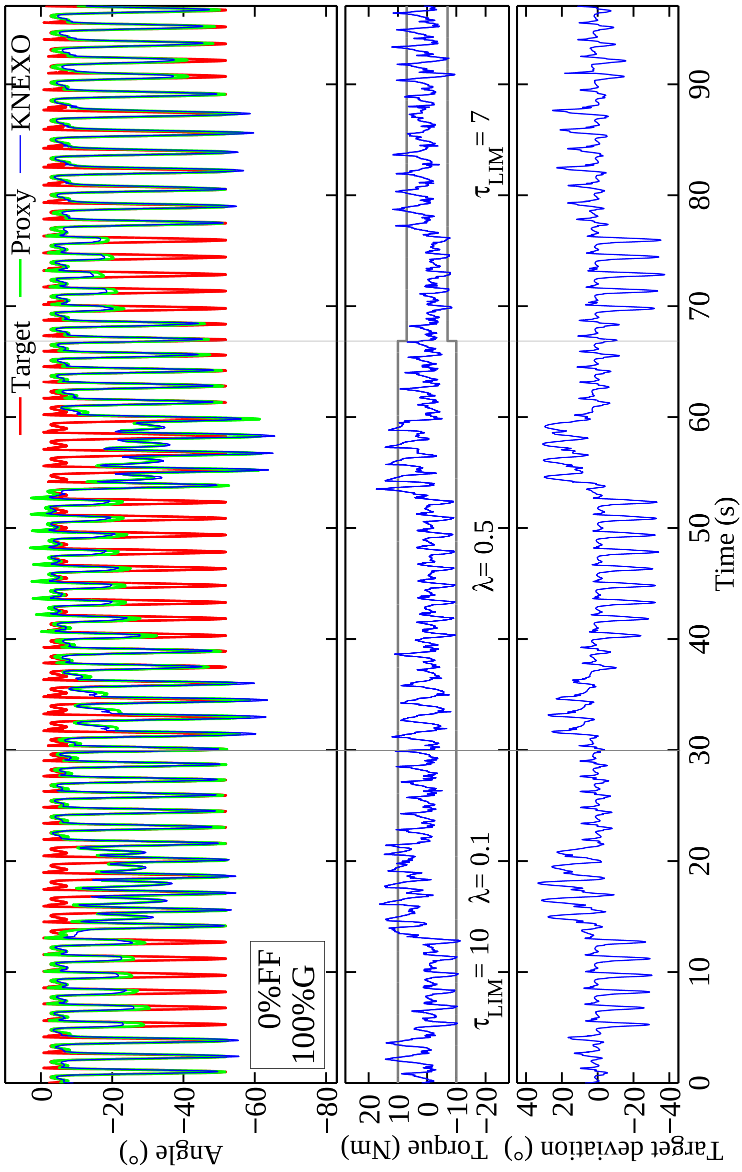

Figure 4.14: Human-robot interaction experiment: system behaviour under perturbations induced by the wearer. Controller setting without feedforward (0%FF), with high gains (100%G), low torque limit ($\tau_{LIM} = 7,\ 10\,Nm$), $\lambda = 0.1,\ 0.5\,s$.

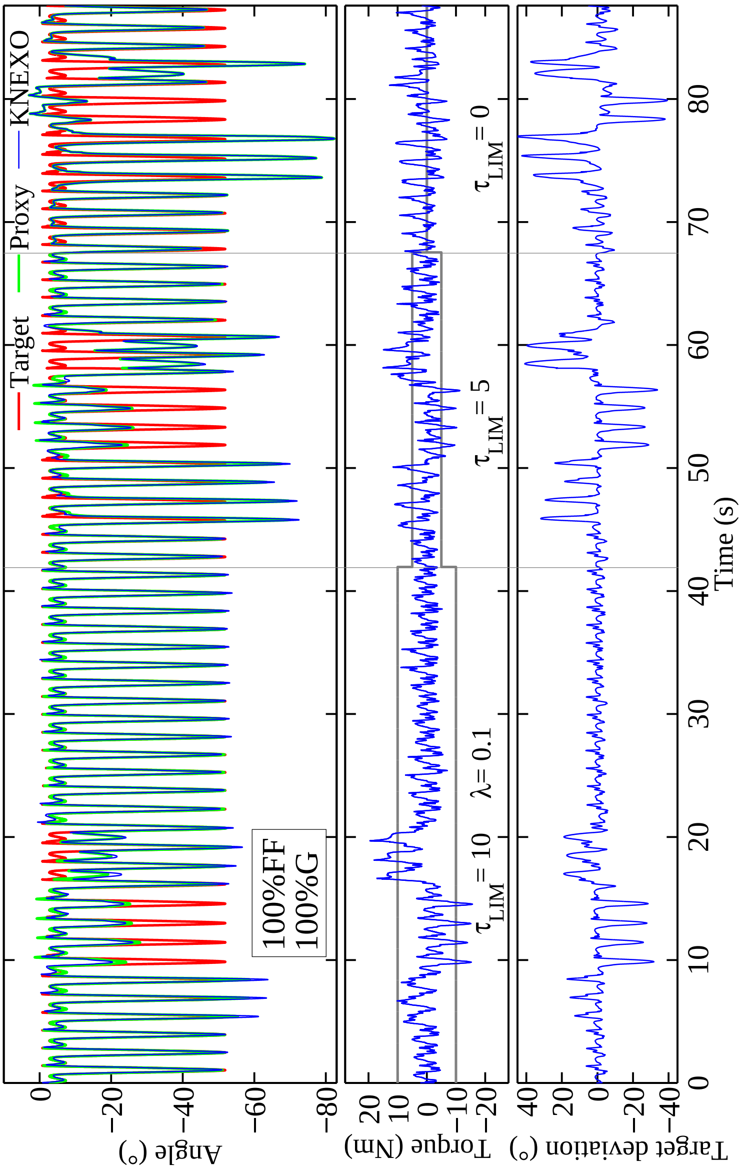

Figure 4.15: Human-robot interaction experiment: system behaviour under perturbations induced by the wearer. Controller setting with feedforward (100%FF), with high gains (100%G) and low torque limit ($\tau_{LIM} = 0,\, 5,\, 10\, Nm$), $\lambda = 0.1\, s$.

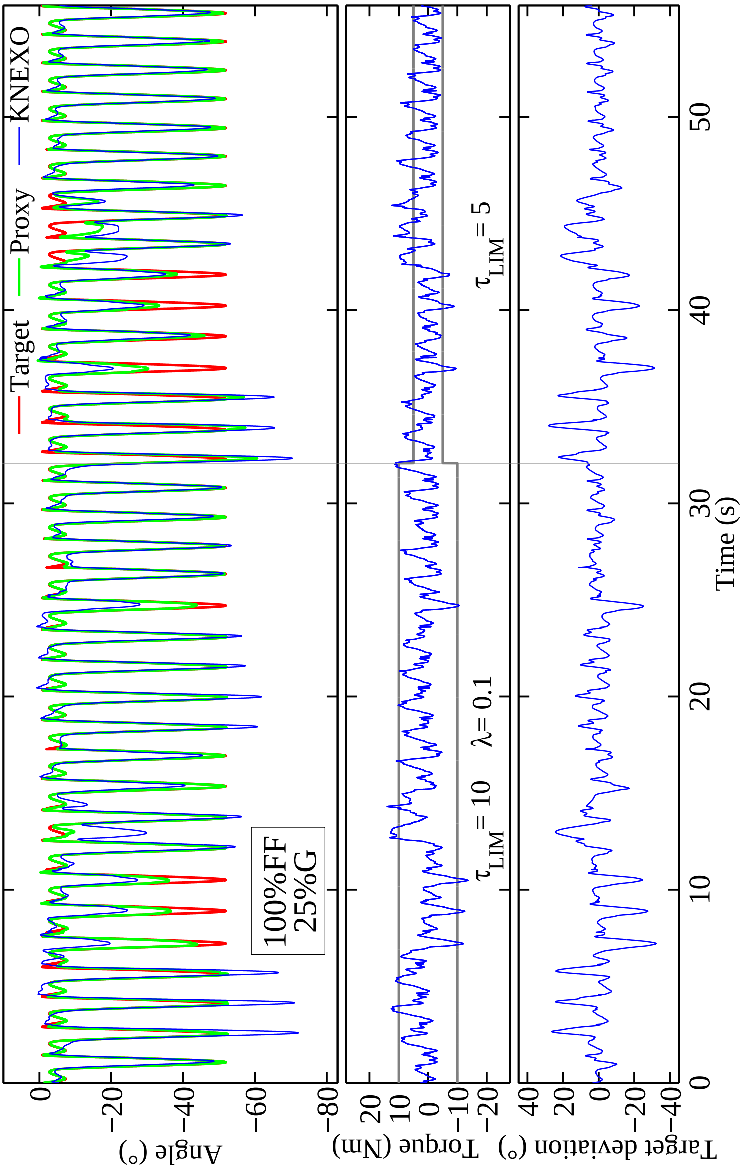

Figure 4.16: Human-robot interaction experiment: system behaviour under perturbations induced by the wearer. Controller setting with feedforward (100%FF), with low gains (25%G) and low torque limit ($\tau_{LIM} = 5,\, 10\, Nm$), $\lambda = 0.1\, s$.

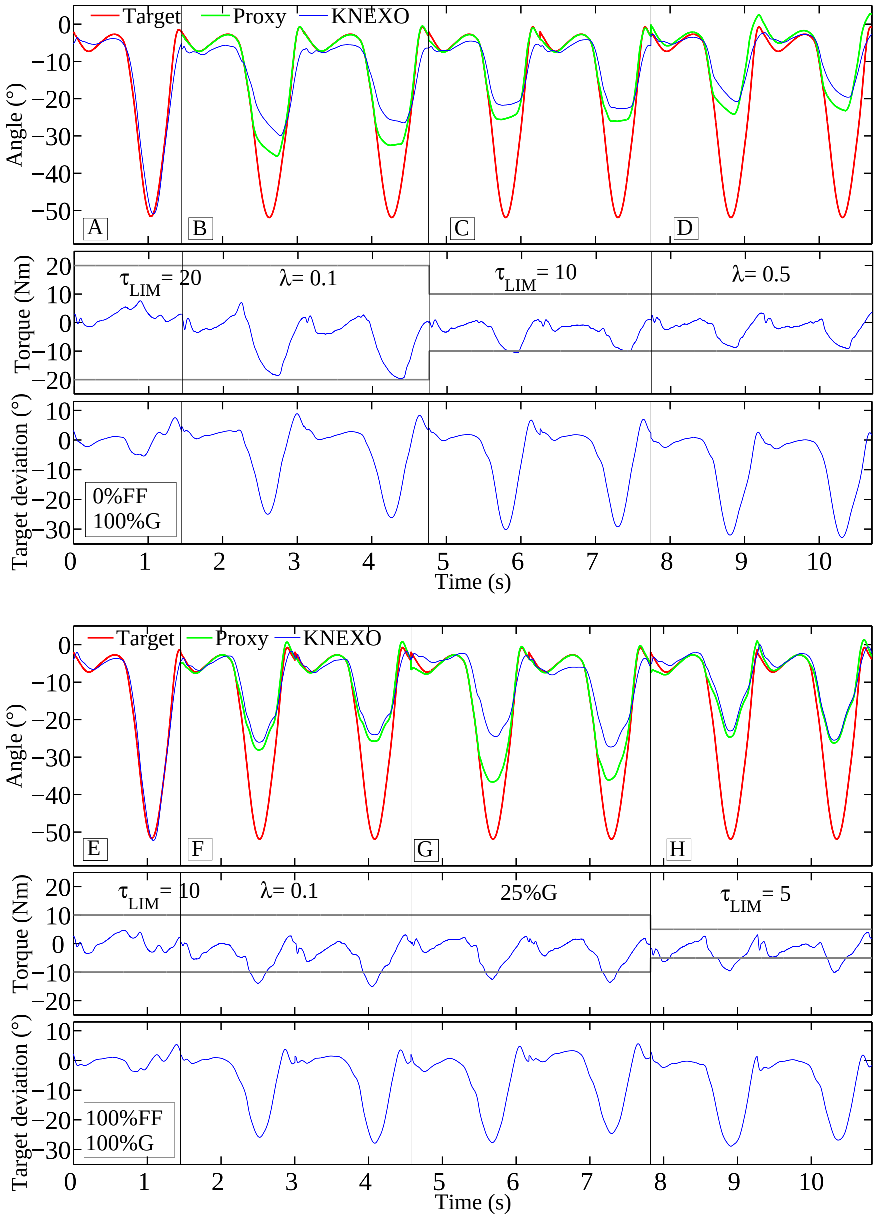

Figure 4.17: Influence of controller settings on human-robot interaction: without (top) and with feedforward torque (bottom) under different controller settings A-H (see also table 4.1). Separate sets of consecutive data are sectioned by gray vertical lines.

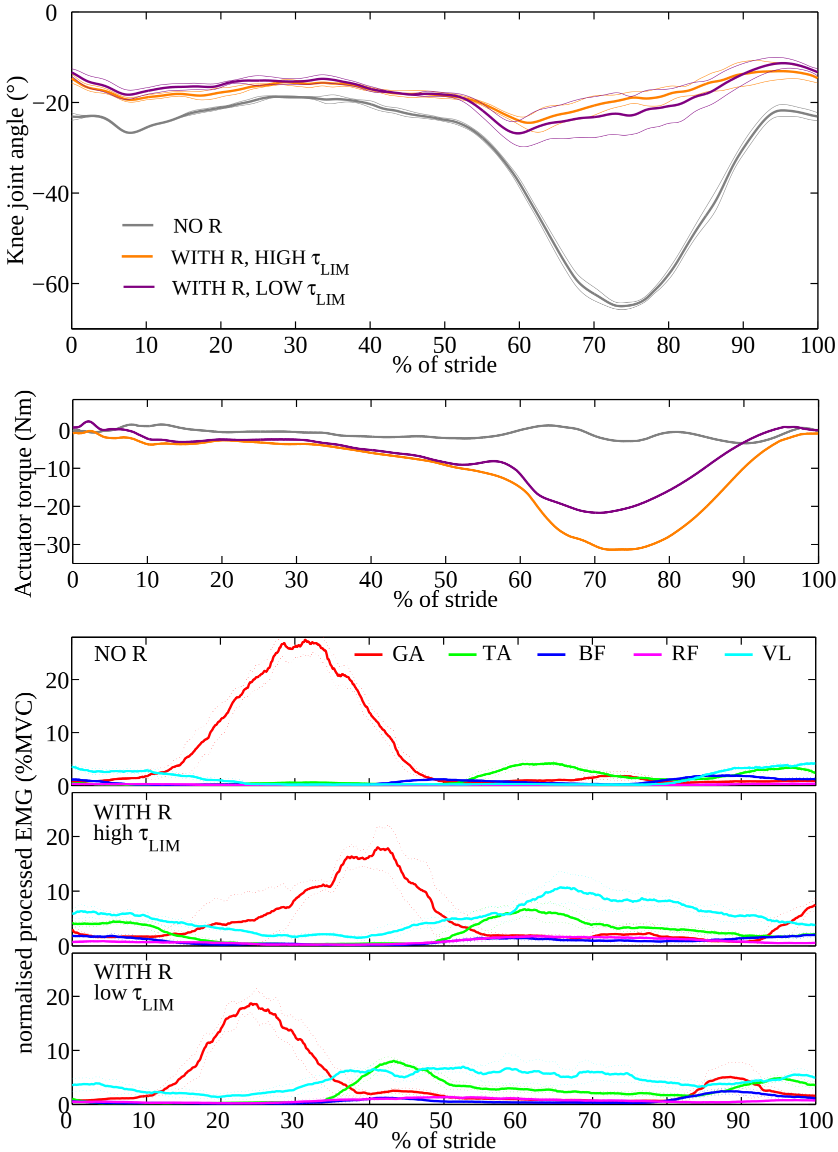

Figure 4.18: Effects on knee kinematics and muscle activity of a human resistance torque during assisted gait: motion capture data of the subject's knee (top), actuator torque (middle) and normalised processed EMG of five muscles of the subject's right leg (bottom) in three cases (grey:without perturbation (NO R), orange: with perturbation (WITH R) and high torque limit, purple:with perturbation and low torque limit).

Cases A and E (data averaged over 10 cycles) represent assisted walking without any deliberate disturbance by the subject, whereas during all other conditions B, C, D, F, G, H (2 consecutive cycles per controller setting) the subject resisted knee flexion during swing phase. Corresponding controller settings A-H are listed in table 4.1.

Figure 4.18 combines knee kinematics, actuator torque and muscle EMG collected from interaction experiments with a different subject (age 37, $1.83\,m$, $83\,kg$). Three cases are compared: assisted walking without deliberate disturbance, assisted walking with resistance against knee flexion during swing with a high value of the torque limit ($\tau_{LIM} = 25\,Nm$) or with a lower value of the torque limit ($\tau_{LIM} = 15\,Nm$). Data was sectioned in cycles according to the heel strike detection signal and averaged over 4 cycles.

4.2.3.3 Discussion

A general comparison of controller settings on the basis of fig. 4.13-4.16 already points out some of the characteristics of the assistive controller.

As expected, in the case of identical control parameter settings, the use of a non-model based feedforward torque decreases deviations from the target during assisted walking without perturbations (see for instance fig. 4.14 and fig. 4.15 around t=20→30s). Regardless of the presence of the feedforward torque, a decrease of the torque limit (τ_{LIM}) results in a decrease of the actuator torque building up against the disturbance induced by the subject. In general, a lower restoring actuator torque yields larger deviations from the target, as the subject tried to generate and maintain the disturbance with equal effort (see fig. 4.13 vs fig. 4.14).

Lowering the feedback gains mostly affects target deviations during unperturbed gait and does not significantly influence large deviations in the case of identical torque limits (see fig. 4.15 vs fig. 4.16).

The time constant of the restoring motion (λ) determines how long the target deviation following a large perturbation is allowed to persist and thus, increasing this time constant leads to increased deviations from the target in some cases. For instance, in the case of increased knee flexion during stance and a larger time constant the target deviation is not timely countered, leading to larger deviations during consecutive swing phases (see fig. 4.14 t=10→20 s vs t=50→60 s). In view of testing with impaired subjects, it was decided to use $\lambda = 0.1s$ to ensure an appropriately slow recovery, that is fast enough not to impede deliberate motion. Kikuuwe et al. (2008) reported $\lambda = 0.1\,s$ as the “optimal” order of magnitude (as opposed to $0.01\,s$ and $0.5\,s$) in the context of experiments with a manipulator applying low-force robotic guidance to a human user. In their study optimality of the time constant was defined as leading to the shortest path and shortest time to reach a target or to the smallest trajectory deviations in the case of a manual positioning/tracking task guided by the end-effector of a manipulator controlled by PSMC in Cartesian space. In the case of gait assistance by the powered knee exoskeleton the suitability of the "optimal" value is assumed to follow from the fundamental frequencies of knee joint motion during gait. Hence, an appropriate response of PSMC during recovery from deviations would be one that induces velocities in a range close to the natural range observed in human walking.

From the more direct comparison of controller settings in fig. 4.17 (top), it is clear that the limitation of the actuator torque qualitatively corresponds with the torque limit τ_{LIM}. Differences between the desired and actual actuator torque limit are due to the model based torque to pressure conversion on the one hand (see 3.4.3.2) and to the difference between the torque set point and the actual torque on the other hand. The added value of the feedforward torque is illustrated by fig. 4.17 (bottom). Although the feedforward torque is rather small in this particular case, the actual trajectory is found to be closer to the target, also in the event of a perturbation acting against the desired motion. This effect would have been more apparent if the target trajectory was such that the recorded feedforward torque was larger.

The combination of the exoskeleton data, the knee joint kinematics and the muscle EMG measurements provides a better insight in the interaction between the exoskeleton and the wearer than exoskeleton data alone as illustrated by fig. 4.18. A torque limit decrease effectively lowers the maximal exerted actuator torque, but the average knee joint pattern seems nearly unaffected. Muscle EMG data points out that the subject shows a lower increase of vastus lateralis activity (knee extensor muscle) compared to assisted walking without resistance, indicating reduced effort.

4.2.4 Conclusion

In preparation of pilot experiments with impaired subjects, KNEXO was evaluated in unassisted and assisted walking experiments with several unimpaired subjects. It was shown that unassisted walking with KNEXO is characterised by a subject-dependent compensation of gait in response to the unilaterally attached device and the small residual resistance torques of the powered knee joint. This should be kept in mind when recruiting impaired subjects and when evaluating the performance of KNEXO on the basis of (un)assisted gait kinematics. From the assisted walking experiments we conclude that the proposed assistive controller achieves compliant guidance in unimpaired subjects and at the same time exhibits a tuneable smooth response to human-robot interaction torques. This response is characterised by an adjustable saturation limit on the interaction torque with the wearer and an appropriately slow recovering motion towards the target trajectory in case of large deviations from the target. The use of a feedforward torque improves guidance and allows dedicated tuning of the torque limit to human resistance torques without compromising guidance. Different settings of the controller's feedback gains, the torque limit, the recovering motion time constant and the feedforward torque enable different assistive modes. The record-replay procedure using trajectory synchronisation proved to be a valuable tool for testing these assistive modes in unimpaired subjects.

4.3 Impaired subjects

Following the successful evaluation of the device and the proposed control concepts in experiments with unimpaired subjects, a stroke patient and a Multiple Sclerosis (MS) patient have been recruited to participate in a pilot study. The goal of the study was to investigate whether KNEXO effectively assists impaired human knee function during walking and to evaluate how the compliant guidance is experienced by these patients. The experimental protocol of the pilot study has been approved by the medical ethics committee of Vrije Universiteit Brussel. Inclusion criteria of the study with regard to the patient's physical condition were:

- right side predominant impairment and affected knee function
- sufficient motor control and strength to walk a few intervals of a few consecutive minutes at $[1.5 - 2.5]$ $kmph$ with or without walking aids such as crutches or a wheeled walker
- familiar with treadmill walking
- sufficient walking ability for short time periods without any orthosis worn at the right leg

The last mentioned criterion had been included to avoid interference or obstruction between the orthosis and KNEXO. Since the device is unilateral and its support is limited to the knee joint, a careful and specific patient selection was mandatory. The patients gave informed consent prior to participation in the study. The results are presented and discussed separately for the stroke patient (section 4.3.1) and the MS patient (section 4.3.2) in the following sections.

4.3.1 Stroke patient

The male stroke patient had a right side hemiparesis and was 1.5 years post-stroke. He was able to walk independently and wore an ankle-foot orthosis. His most prominent gait impairment was weakness of the ankle dorsiflexor muscles resulting in foot drop during swing. He had severely affected speech (aphasia[1]), which made it impossible to obtain feedback about perceived performance and comfort.

4.3.1.1 Experimental design

Setup and methods A treadmill walking assessment was performed first to define comfortable walking speed and to evaluate gait. As the person could not wear his ankle-foot orthosis during experiments, he had to keep his shoes on to maintain sufficient stability at the level of the ankle and the foot. KNEXO was fitted and heel contact detection sensors were attached to the heel region of the shoe soles (FSR sensors, see 2.5.4.2). Walking trials were performed so that the patient could familiarise with the device in the unassisted mode (zero-torque (ZT) mode).

The procedure of experiments involved three consecutive stages. First the subject's individual knee trajectory was recorded with KNEXO in ZT mode. In the second stage a target knee trajectory is tracked by the exoskeleton in the robot-in-charge mode by means of the PSMC controller explained in 3.4.2.3, while the feedforward torque τ_{FF} is set to zero and the controller output τ_{PSMC} is recorded ("PSMC mode"). This recording of τ_{PSMC} is averaged over all cycles to obtain a single feedforward torque cycle. The target trajectory is based on the original reference cycle recorded during ZT mode: it can be an adapted version of this recorded reference cycle or a reference cycle originating from recordings of unimpaired subjects. It is synchronised to the patient's gait by means of the synchronisation algorithm explained in section 3.5.2. Finally, the same target trajectory is again tracked in the robot-in-charge mode, but now τ_{FF} is set to the previously obtained torque reference cycle ("PSMC FF mode"). Each assisted walking trial started with KNEXO in unassisted mode (ZT) during about twenty strides, before switching on-line to assisted mode (PSMC). This covers the treadmill start up phase and allows for the initialisation of the synchronisation algorithm. Between and during the walking trials, the gains (K_p, K_i, K_d) and the feedforward torque (feedforward term τ_{FF}) were scaled to investigate their influence on the knee joint motion and on the provided assistance. The feedforward torque is expressed as a percentage (%FF) of the recorded torque reference cycle and the gains are jointly expressed as a percentage (%G) of the maximum gain setting ($K_p = 4\,bar/rad$, $K_i = 4\,bar/rad.s$, $K_d = 0.04\,bar.s/rad$).

Data analysis The outcome measures, used to evaluate the effect of KNEXO on unassisted and assisted walking, are based on the exoskeleton data and the

[1] Aphasia is a neurological disorder caused by damage to the portions of the brain that are responsible for language. Primary signs of the disorder include difficulty in expressing oneself when speaking, trouble understanding speech, and difficulty with reading and writing. The type and severity of language dysfunction depends on the precise location and extent of the damaged brain tissue (National Institute of Neurological Disorders and Stroke (NINDS).

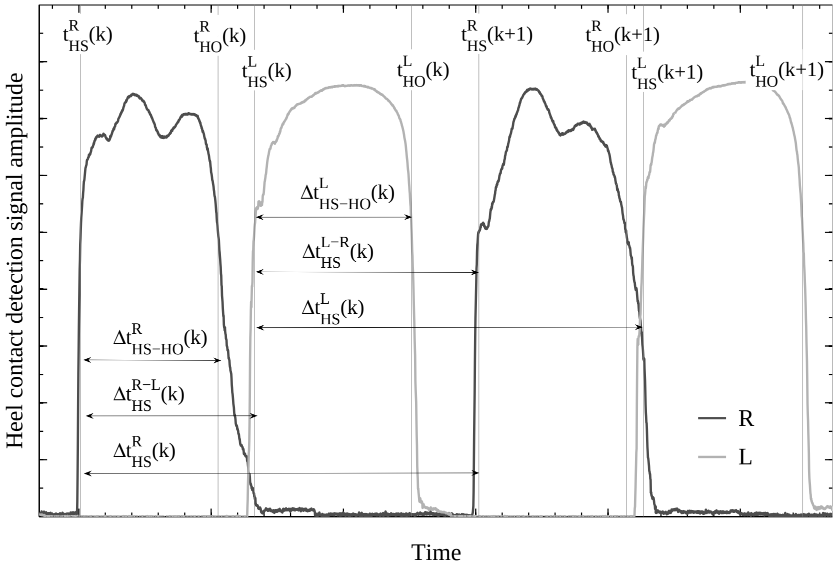

Figure 4.19: Heel contact detection signals of the right (dark gray) and the left side (light gray) with indication of gait phase transitions (vertical lines) and used notations.

heel contact detection signals. The exoskeleton data provides the joint angle, the actuator torque, the instantaneous power generated or absorbed by the actuators (see eq. 2.1) and the corresponding amount of work (see eq. 2.2) performed. These variables are sectioned in cycles by means of the heel contact detection signals and averaged over several cycles.

Besides the start time of each cycle, the heel contact detection signals hold additional gait timing information, as illustrated by fig. 4.19. By means of threshold detection these signals are binarised and as such they yield the approximate time instance of heel strike ($t^R_{HS}(k)$) and heel-off ($t^R_{HO}(k)$) for stride k of the right leg and the time instance of heel strike ($t^L_{HS}(k)$) and heel-off ($t^L_{HO}(k)$) for stride k of the left leg. These time instances allow the calculation of the following gait timing variables:

$$\Delta t^R_{HS}(k) = t^R_{HS}(k+1) - t^R_{HS}(k) \tag{4.1}$$

$$\frac{\Delta t^R_{HS-HO}(k)}{\Delta t^R_{HS}(k)} = \frac{t^R_{HS}(k) - t^R_{HO}(k)}{\Delta t^R_{HS}(k)} \quad * \tag{4.2}$$

$$\frac{\Delta t^{R-L}_{HS}(k)}{\Delta t^R_{HS}(k)} = \frac{t^R_{HS}(k) - t^L_{HS}(k)}{\Delta t^R_{HS}(k)} \quad \circ \tag{4.3}$$

The definitions for the variables related to the left side are found analogously. Equation 4.1 yields the stride period (time period expressed in s), eq. 4.2 yields the period of heel contact with the ground normalised by the stride period (expressed in % of stride) and eq. 4.3 yields the period of foot contact with the ground between successive alternate heel strikes normalised by the stride period (expressed in % of stride). The normalised time periods corresponding with "no heel contact" and "no foot contact" are the respective complements of the aforementioned variables.

Since the FSR sensors only detect heel contact (heel contact/no heel contact), their signals do not provide a direct measure of the stance and swing period. However, the evolution in time of the variables given by eq. 4.2-4.3 (related to stance) and their complements (related to swing) does give a valuable indication of the change of swing and stance period. For easier reference the variable defined by eq. 4.2 (and its complement) is referred to by symbol $*$ and the one defined by eq. 4.3 (and its complement) is referred to by symbol $^\circ$. Hence, the variables related to the right side (left side variables are defined analogously) are:

stance*R the period of right heel contact with the ground divided by the stride period of the right leg (% of stride)

swing*R the period of right heel no-contact with the ground divided by the stride period of the right leg (% of stride)

stance°R the period from right heel contact onset to consecutive left heel contact onset divided by the stride period of the right leg (% of stride)

swing°R the period from left heel contact onset to consecutive right heel contact onset divided by the stride period of the right leg (% of stride)

4.3.1.2 Results

KNEXO was fitted such that its joint angle was a few degrees in flexion with respect to 0° during quiet standing. This was done to capture the frequently occurring hyperextension of the patient's knee joint during stance. The difference between the exoskeleton's zero reference angle (upper and lower link aligned) and the subject's zero reference angle (quiet standing) should be kept in mind when analysing results. The treadmill speed was set at $2\,kmph$ ($0.56\,m/s$).

Figure 4.20 shows exoskeleton data recorded over a period of 20 strides of a walking trial in ZT mode (top) and of a walking trial in PSMC mode (bottom) with maximum feedforward and gains (100%FF 100%G). Averaged data is shown in red and 95% confidence intervals ($[-2\sigma, +2\sigma]$ with standard deviation σ) are indicated in green. One should note that the work is calculated as the accumulated power over each separate cycle and thus it equals zero at the start of each cycle.

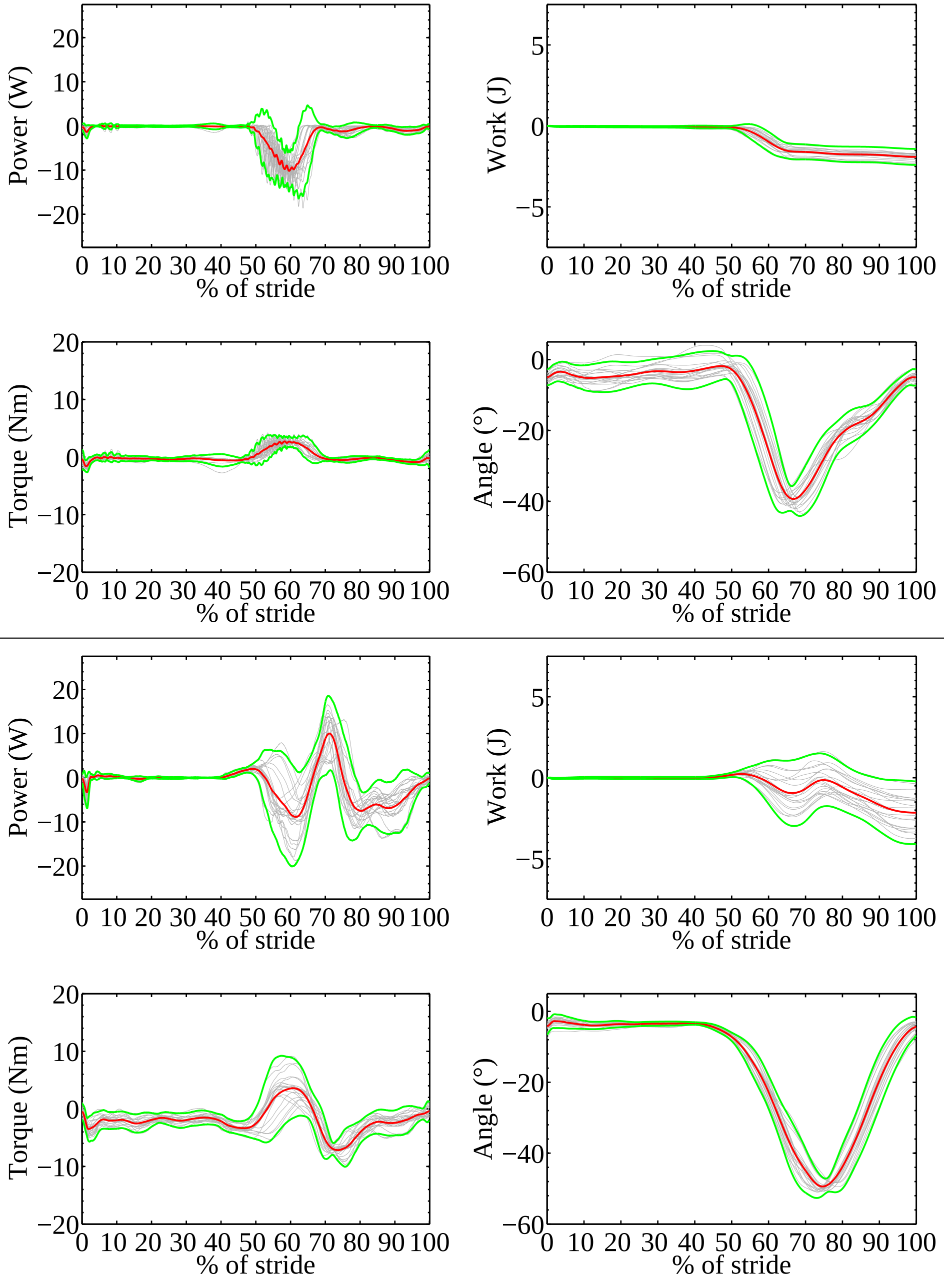

Figure 4.20: Stroke patient wearing KNEXO in ZT mode (top) and in PSMC 100%FF 100%G mode (bottom). Actual joint angle, actuator torque, actuator instantaneous power and actuator work are shown as a function of stride percentage for 20 cycles (gray) together with their average (red) and 95% confidence bounds (green).

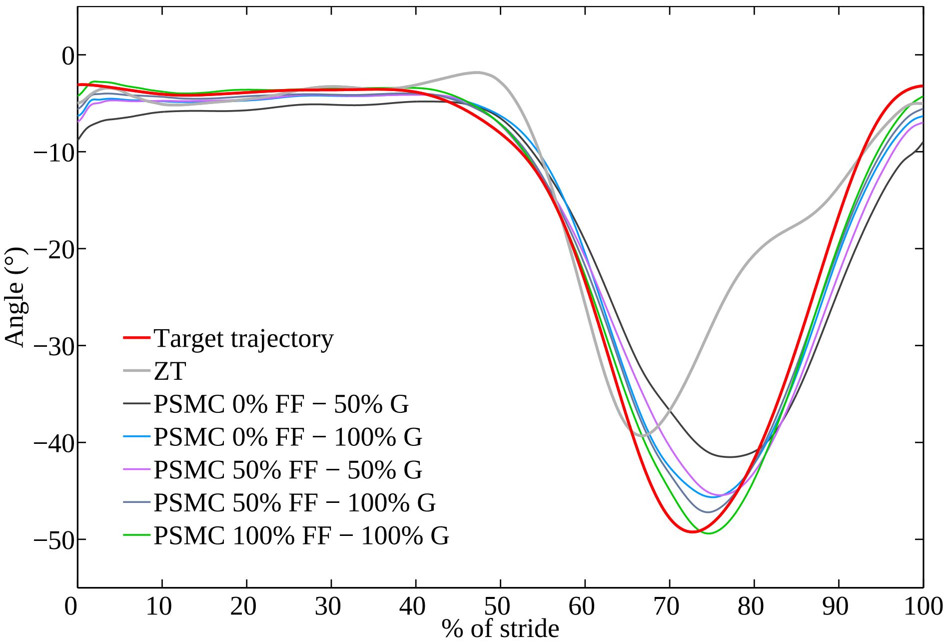

Figure 4.21: Influence of different assistance levels on knee joint angle: target trajectory (red), mean actual trajectories averaged over 20 cycles for different assistance levels from ZT (gray) → PSMC 100% FF 100% G (green).

Figure 4.21 shows the average joint angle trajectory for different levels of assistance ranging from zero assistance (ZT mode; gray curve) to full assistance (PSMC 100%FF 100%G mode; green curve). All trajectories have been rescaled to a common time base. The target trajectory is depicted in red.

The variation of the previously introduced gait timing variables within a walking trial (top) and between walking trials with different assistance levels (bottom) can be observed in fig. 4.22. The top plot shows the transition from ZT mode to PSMC 100%FF 100%G mode. The bottom plot gives the trial means and their respective standard deviations in the order of execution of experiments from left to right.

4.3.1.3 Discussion

According to the exoskeleton's joint angle, the kinematics of the unassisted knee joint are characterised by a lack of stable support during stance and insufficient control over knee flexion and extension during swing as can be observed in fig. 4.20 (top, bottom right graph). Hyperextension of the knee frequently occurred during stance. A relatively fast flexion during pre-swing is followed by a slower and unsmooth extension in mid and late swing.

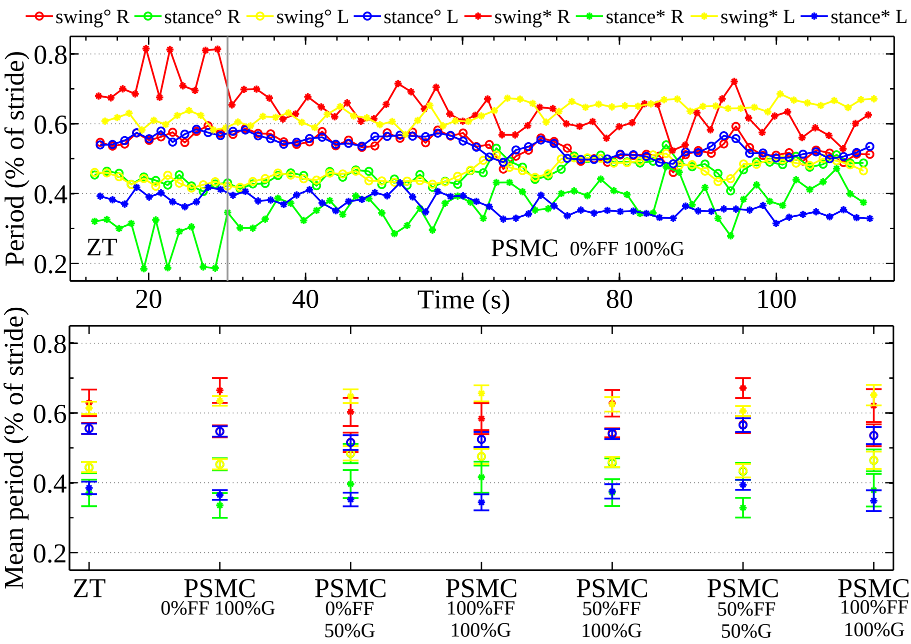

Figure 4.22: Evolution of swing and stance periods (in percentage of stride). Top: evolution in time during PSMC with 100%FF 100%G. Bottom: mean periods $[-\sigma,+\sigma]$ for different assistance levels (in chronological order of execution from left to right).

Since gait kinematics were not captured in these experiments, it is unclear to what extent these characteristics are also found in gait without KNEXO. They were, however, confirmed by the visual gait assessment. During assisted walking (see fig. 4.20, bottom), a small flexion torque prevents hyperextension of the knee during stance and significantly reduces joint angle variability during this phase. A more symmetric and smooth flexion and extension are observed during swing. Extension torques up to 10Nm prevent fast knee flexion (power absorption) followed by a flexion torque in order to reach sufficient flexion during mid swing (power generation). The resulting flexion angle provided more foot clearance when compared with unassisted walking. The overall negative work, combined with the short delay (see fig. 4.21) of the assisted knee trajectory with respect to the unassisted knee trajectory might be an indication that the subject anticipates to the exoskeleton's motion and is therefore slightly resisted, especially during knee extension $(75-100\%$ of stride).

Decreasing the amount of assistance by lowering the feedforward torque and the gains leads to larger deviations from the target trajectory. Timely extension of the knee prior to heel strike is affected in the least supportive mode (PSMC 0%FF

50%G mode). It was difficult to obtain feedback from the patient about his perception of the different settings.

The gait timing variables extracted from the heel contact detection signals show a marked influence of the amount of provided assistance. The stride period appeared to increase from $1.513 \pm 0.050\,s$ to $1.637 \pm 0.030\,s$ when comparing unassisted walking (ZT mode) with assisted walking (PSMC 100%FF 100%G), implying a larger step length. As can be inferred from fig. 4.22 (top and bottom) unassisted walking is characterised by a marked left-right asymmetry. Perfect symmetry corresponds with equal left and right normalised step periods and in that case the variables denoted stance°R, swing°R, stance°L, swing°L should all be equal to 50%. If the stride period is constant, stance°R (green) and swing°L (yellow) on the one hand, and stance°L (blue) and swing°R (red) on the other hand coincide, which follows from their definition (see eq. 4.3 for stance°R). Relative variations of the variables within each pair are due to stride period fluctuations. It can be seen that stance°R is significantly smaller than stance°L without assistance and that increased assistance generally results in increased symmetry (see fig. 4.22 bottom). Figure 4.22 shows that this effect does not set in immediately after switching from ZT mode to PSMC mode. The normalised period of heel contact with the ground shows much greater variation for the affected side (stance*R, green) compared with the left side (stance*L, blue) and this difference persists regardless of assistance (see fig. 4.22 bottom). Generally, the right heel contact period does increase with assistance.

These observations support the conclusion that the subject shows improved knee joint function at the affected side and a more symmetric and stable gait timing while wearing KNEXO in assisted mode when compared with the unassisted mode. The patient's severely affected speech made it impossible, however, to obtain feedback about the perceived assistance and the effect of altering the amount of assistance. An analysis of gait kinematics, comparing gait with and without the device, would also allow more conclusive evidence and was therefore added to the study with the MS patient, discussed in the next section.

4.3.2 MS patient

The participant was a female MS patient ($1,68\,m$, $58\,kg$) with secondary progressive multiple sclerosis (SPMS[2]). Her gait was characterised by a right side predominant loss of strength and coordination, resulting in reduced load bearing on the right leg and gait asymmetry. She was able to walk short distances with a walking cane and wore an ankle-foot orthosis and knee brace for daily activities.

[2]SPMS is one of the four identified subtypes of progression of MS (relapsing-remitting MS, primary progressive MS, secondary progressive MS, progressive relapsing MS). It follows an initial period of relapsing-remitting MS (the most common form of MS in people who are newly-diagnosed). In SPMS, the disease begins to worsen more steadily, with or without occasional attacks, slight remissions, or plateaus (National Multiple Sclerosis Society (US).

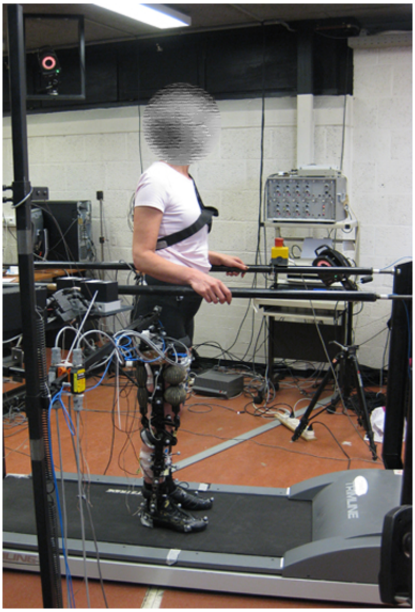

Figure 4.23: Setup for pilot experiments with an MS patient.

4.3.2.1 Experimental design

Setup and methods The experimental setup is shown in fig. 4.23. A treadmill walking assessment was performed to define a comfortable walking speed and to evaluate her gait. The orthosis and brace were not worn during the experiments, but shoes were kept on to provide sufficient stability at the level of the ankle and the foot. KNEXO was fitted and heel contact detection sensors were attached to the heel region of the shoe soles. Reflective markers for camera-based motion capturing were attached to the patient's lower limbs and pelvis and to the exoskeleton according to the protocol in appendix C. Walking trials were performed so that the patient could first familiarise with the device in zero-torque (ZT) mode.

The test procedure was similar to the one followed in the study with the stroke patient. After the familiarisation period, the unassisted knee joint motion and the heel strike detection signals were recorded with KNEXO in ZT mode. Next, suitable target cycles for the assisted mode were selected out of a set of reference cycles of unimpaired subjects. After feedforward torque recording in PSMC mode, the controller settings were tuned in PSMC FF mode, based on gait assessment and patient feedback. Between walking trials the target cycle and the controller settings, i.e. the gain percentage (%G) and the feedforward torque percentage (%FF), were adapted to study their influence. After the experiment, the participant was requested to fill in a questionnaire about her appreciation of the device.

	A	B	C
K_p, K_i, K_d (%)	50	100	50
FF (%)	0	0	100
τ_{lim}(Nm)	20	30	10
λ (s)	0.1	0.1	0.1

Table 4.2: Controller settings used in assisted walking experiments with the MS patient wearing KNEXO in PSMC mode. 100%G corresponds with $K_p = 4.0\,bar/rad$, $K_i = 4.0\,bar/rad.s$, $K_d = 0.04\,bar.s/rad$. 100%FF corresponds with the total feedforward torque reference cycle as recorded in a preceding assisted trial with 0%FF.

Data analysis The outcome measures of the device are the joint angle, the actuator torque, the instantaneous power generated or absorbed by the actuators (see eq. 2.1) and the corresponding amount of work (see eq. 2.2). Exoskeleton data was sectioned in cycles by means of heel contact detection signals and averaged over 25 strides. Additionally, the gait timing variables introduced in 4.3.1.1 are calculated from heel contact detection signals. The gait analysis based on motion capture data (VICON) provides the relative rotational motion between the foot and the lower leg, the lower leg and the upper leg and the upper leg and the pelvis for both legs. The discussion of results focuses on the rotations in the sagittal plane (the plane of progression), namely plantarflexion/dorsiflexion of the ankle, flexion/extension of the knee and flexion/extension of the hip. Joint angle data was sectioned in cycles by means of heel contact detection signals and averaged over 4 strides. The data was low-pass filtered (4^{th} order butterworth, cut-off frequency of $12.5\,Hz$) to remove motion artefacts. Sudden changes in the standard deviation with respect to stride percentage indicate the presence of these artefacts in the source data.

4.3.2.2 Results

KNEXO was fitted so that a joint angle of approximately 0° corresponded with the subject's knee fully stretched. Gait analysis data is zero referenced by means of a static marker measurement during quiet standing. All experiments were performed at a treadmill speed of $1.3\,kmph$ ($0.36\,m/s$).

Figure 4.24 (top) shows 25 cycles of KNEXO data of a walking trial in ZT mode. Averaged data is shown in red and 95% confidence intervals are indicated in green. Based on patient feedback and gait assessment during assisted walking a "best" choice of target (target T1) and of controller settings (setting A, see table 4.2) were selected. Figure 4.24 (bottom) shows 25 cycles of KNEXO data of a walking trial in "best" PSMC mode (PSMC T1 0%FF 50%G). Figure 4.25 (top) compares the average joint angle, the torque, the power and the work for three different target trajectories during assisted mode with fixed controller setting 0%FF 50%G.

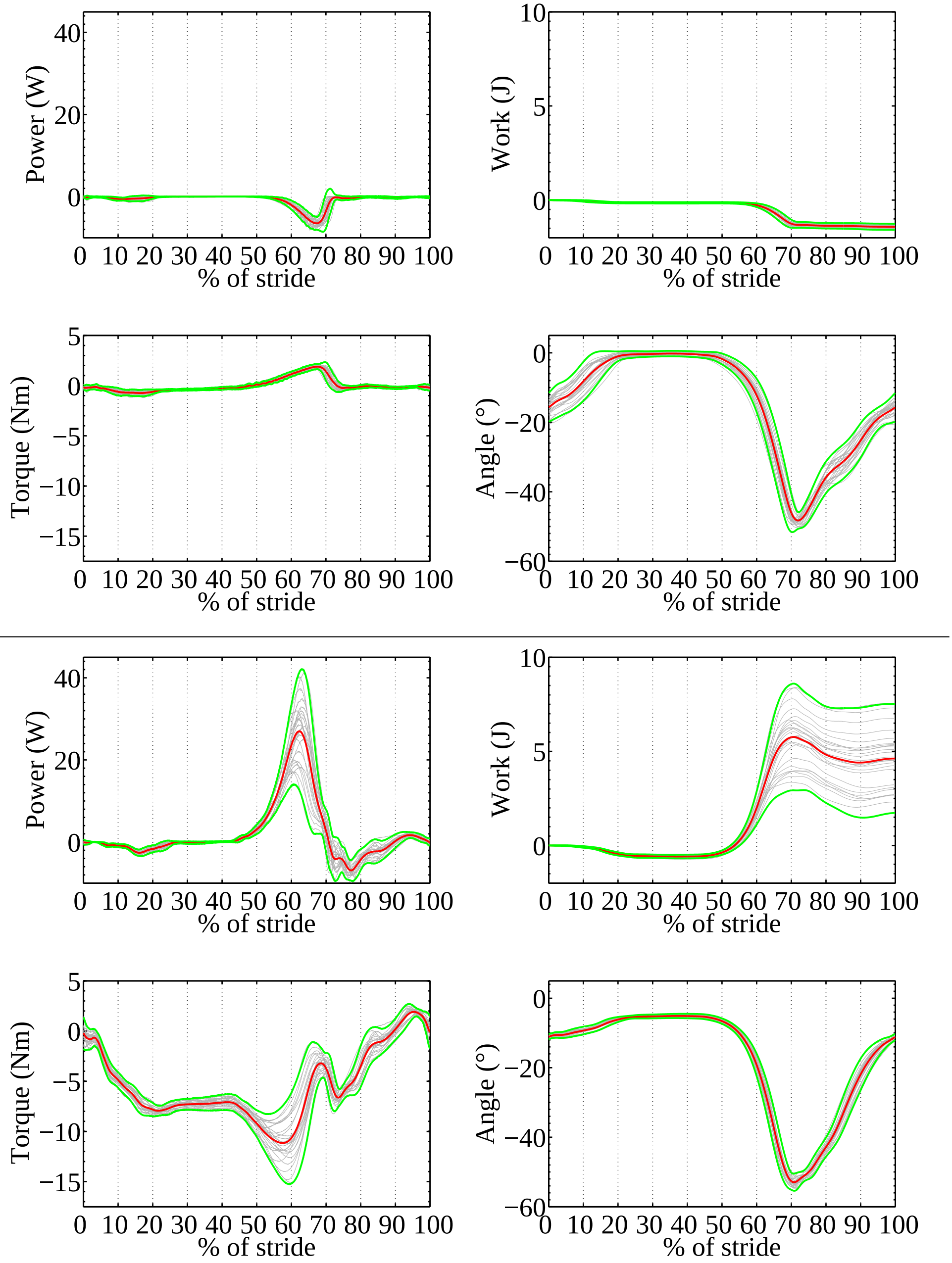

Figure 4.24: Impaired subject wearing KNEXO in ZT mode (top) and in "best" PSMC mode (bottom). Actual joint angle, actuator torque, actuator instantaneous power and actuator work for 25 cycles (gray) and their average (red) and 95% confidence bounds (green) are shown as a function of stride percentage.

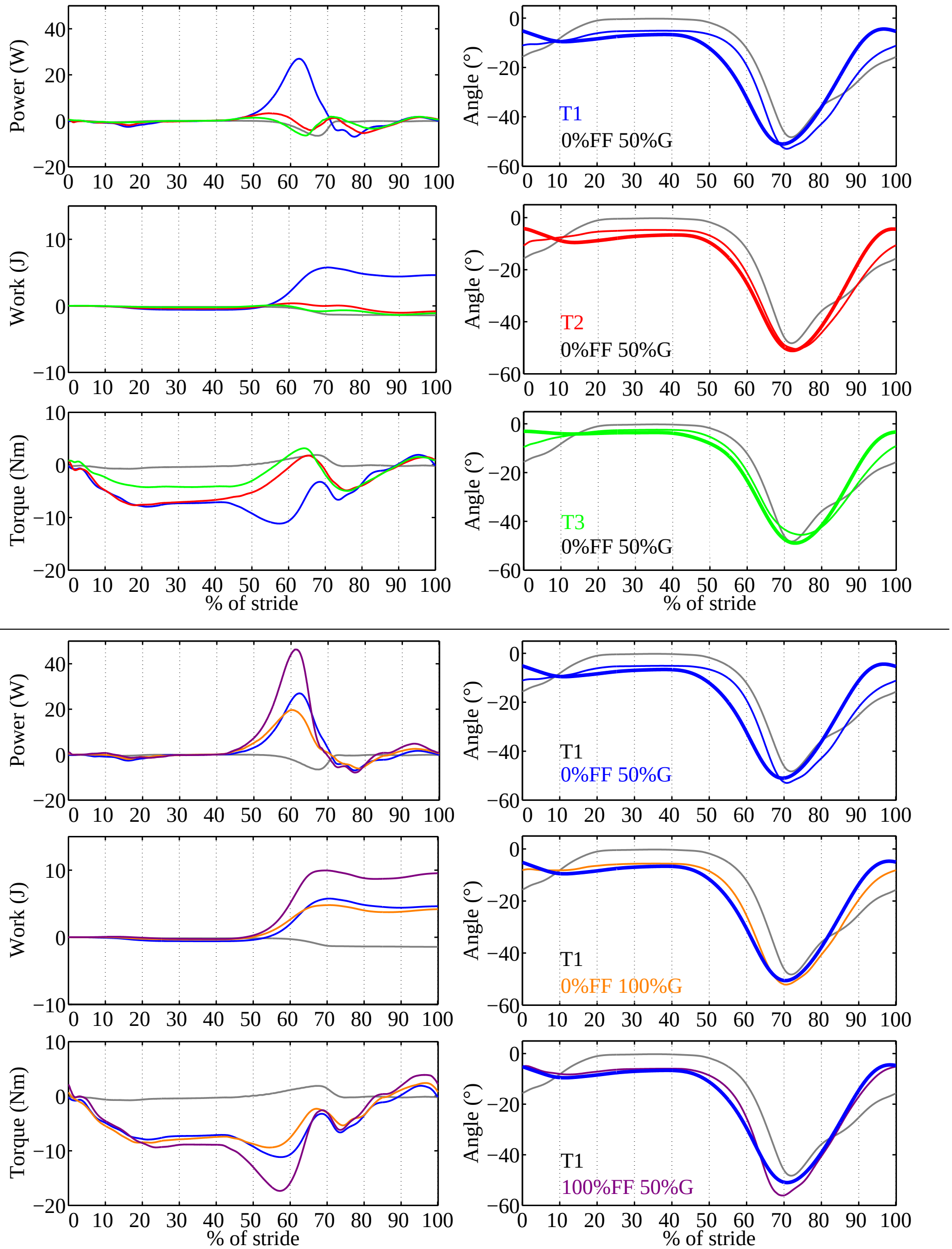

Figure 4.25: Influence of the selected target trajectory (top) and of the controller settings (bottom) on averaged actual joint angle, actuator torque, power and work. ZT data are shown in gray. Top: target trajectory T1 (blue), T2 (red) and T3 (green) and controller setting A were used (see table 4.2). Bottom: controller settings A (blue), B (orange) and C (purple) (see table 4.2) and target trajectory T1 (blue) were used.

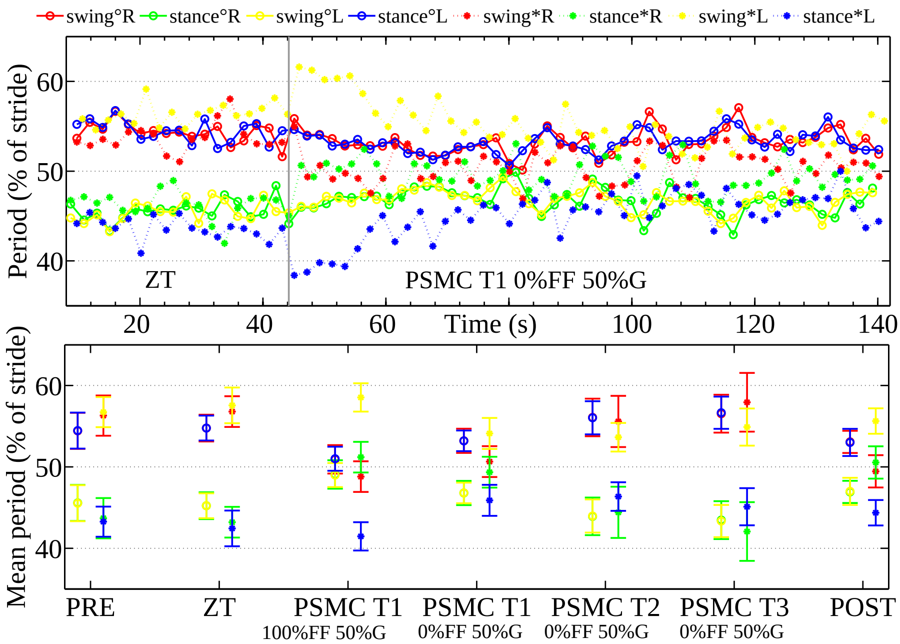

Figure 4.26: Evolution of swing and stance periods (in percentage of stride). Top: evolution in time during a "best" PSMC trial (PSMC T1 0%FF 50%G). Bottom: evolution of trial means $[-\sigma,+\sigma]$ between modes and trials. PRE: without KNEXO before trials, ZT, PSMC T1 100%FF 50%G, PSMC T1-T2-T3 with 0%FF 50%G (see fig. 4.25), POST: without KNEXO after trials.

Target trajectory T1 (blue) and T3 (green) are based on unimpaired subject recordings (see fig. 4.2), T2 (red) is based on T1 with additional 2.5% of stride delay. Figure 4.25 (bottom) compares the average joint angle, the torque, the power and the work for three different controller settings, 0%FF 50%G (blue), 0%FF 100%G (orange) and 100%FF 50%G (purple) during assisted mode with the fixed target trajectory T1 (blue). Average data of a walking trial in ZT mode are given as a reference for comparison. The evolution over time of the gait timing variables during a walking trial with KNEXO in "best" PSMC mode (PSMC T1 0%FF 50%G) is shown in fig. 4.26 (top). The transition from ZT mode to PSMC mode is indicated by a grey vertical line. Figure 4.26 (bottom) compares mean gait timing variables and their standard deviations for different walking trials: without KNEXO before trials (PRE), with KNEXO in ZT mode, with KNEXO in different PSMC modes and without KNEXO after trials (POST). Figure 4.27 shows the mean right and left ankle, the knee and hip joint angle cycles and their respective standard deviations for a walking trial without KNEXO (PRE, red), with KNEXO in ZT mode (ZT, green) and with KNEXO in PSMC 100%FF 50%G mode (purple).

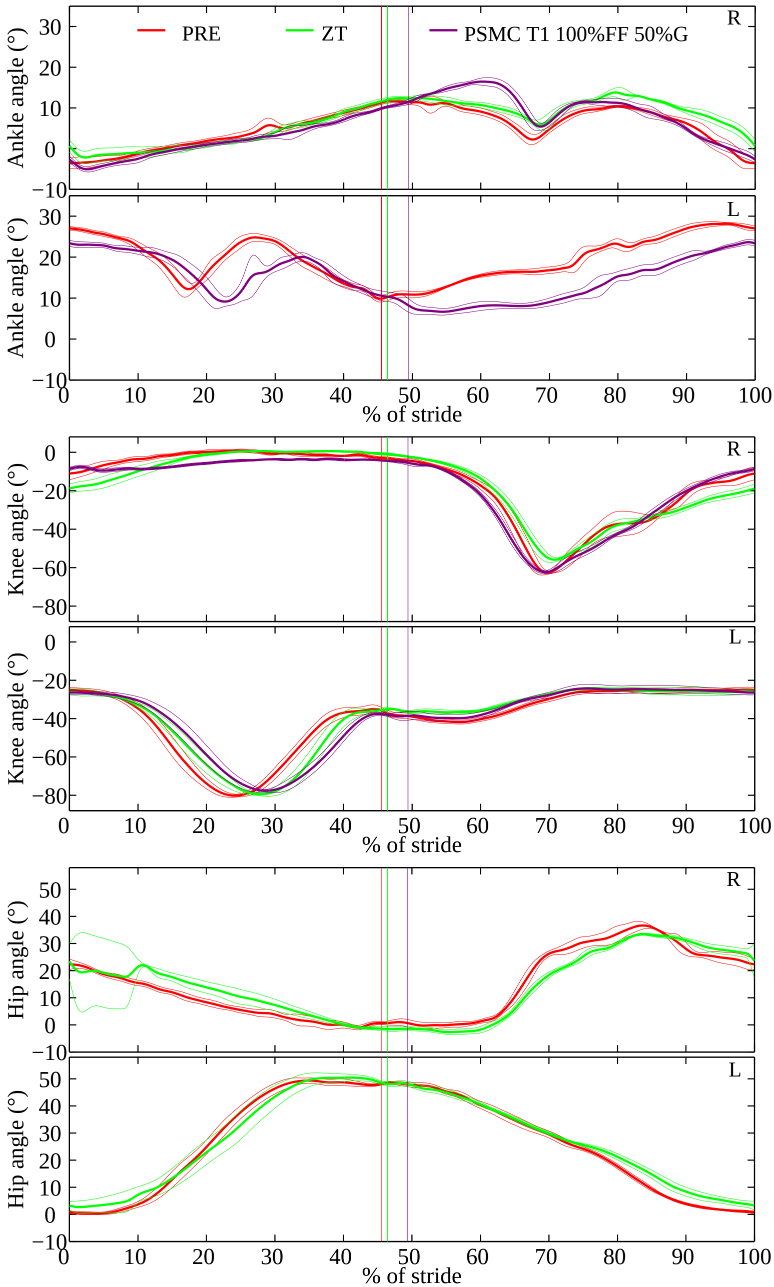

Figure 4.27: Gait kinematics: flexion/extension angles of the patient's right and left ankle, knee and hip joint without KNEXO (PRE, red), with KNEXO unassisted (ZT, green) and assisted (PSMC T1 100%FF 50%G, purple)

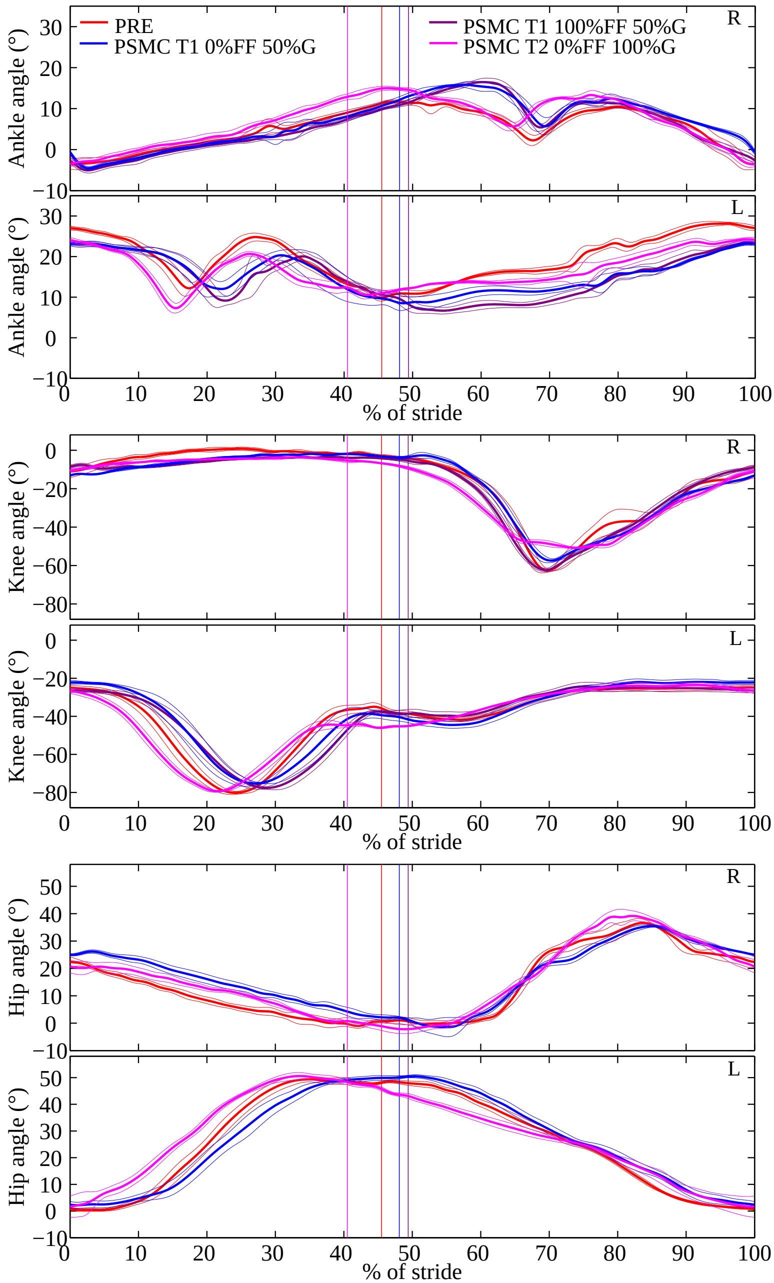

Figure 4.28: Gait kinematics: flexion/extension angles of the patient's right and left ankle, knee and hip joint without KNEXO (PRE, red) and with KNEXO assisted (PSMC T1 100%FF 50%G, purple; PSMC T1 0%FF 50%G, blue; PSMC T2 0%FF 100%G, magenta)

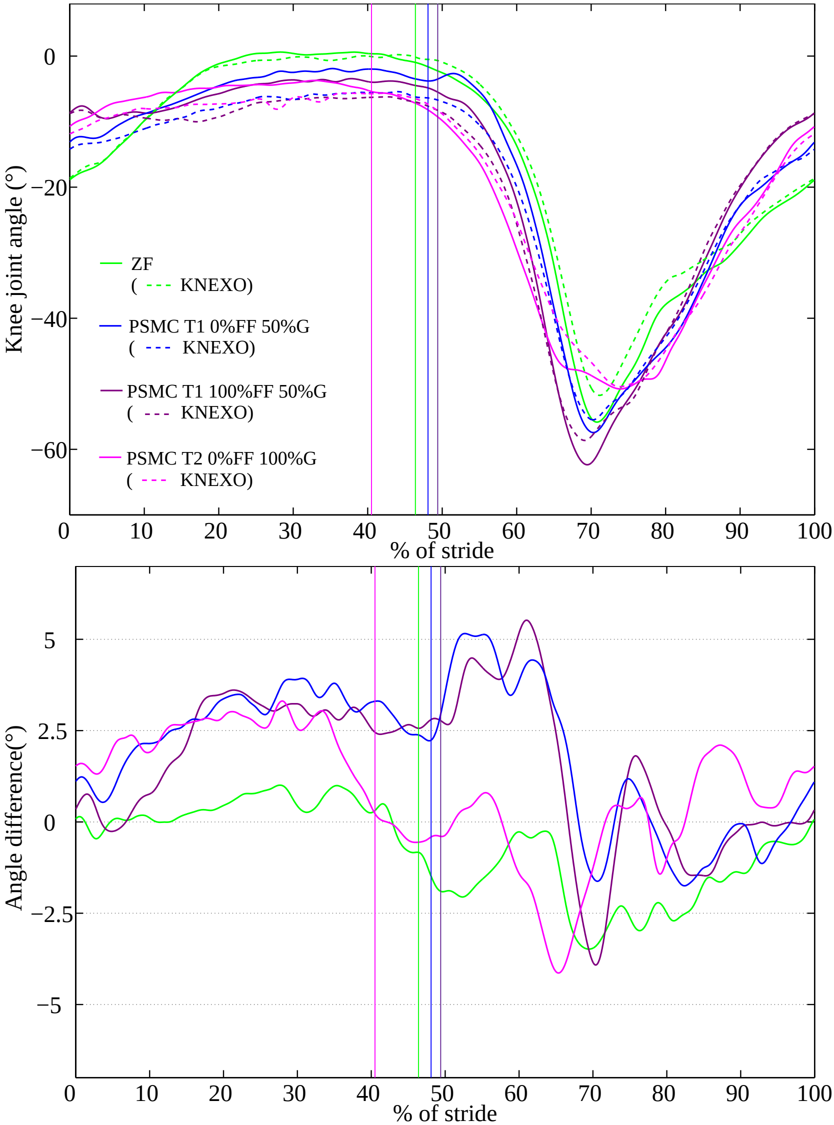

Figure 4.29: Relative motion due to the compliance at the interface, based on VICON data: top) mean flexion/extension angles of the patient's right knee (solid) compared with KNEXO joint angle (dotted) in different modes. bottom) Difference of knee joint angle and KNEXO angle (>0 indicates that the knee is more extended than KNEXO, >0 indicates that the knee is more flexed than KNEXO).

The angles are plotted against the percentage of stride of the right leg (0% corresponds with right heel strike) and the average instance of left heel strike is indicated by a vertical line. Positive angles imply flexion relative to the reference (quiet standing), negative angles imply extension. Data with too many motion artefacts have been omitted (e.g. hip data, assisted (purple)). Figure 4.28 similarly compares a walking trial without KNEXO with walking trials with KNEXO in three different modes: PSMC T1 100%FF 50%G (purple), PSMC T2 0%FF 50%G (blue), PSMC T3 0%FF 100%G (magenta). The mean joint angle cycles of KNEXO (dotted) are compared with the mean human knee joint angle cycles for the same PSMC modes and for ZT mode in figure 4.29 (top). Both human knee angles and KNEXO angles in this figure are based on VICON data. Figure 4.29 (bottom) shows the difference between the knee joint angle and KNEXO angle, where positive and negative angles imply that the human knee joint is respectively more extended or more flexed than the robotic joint.

4.3.2.3 Discussion

The patient's right knee kinematics were marked by a hyperextension (overstretching) during stance and an unsmooth and slow extension during swing, as can be observed in fig. 4.27 (PRE, red). This is in contrast with the left knee, which is significantly more flexed overall and has a smoother flexion/extension course during swing. The left right asymmetry is also clear from the hip joint cycles, showing a marked difference in flexion amplitudes (50° left vs 35° right), and the ankle joint cycles, showing a larger extension range in preparation of swing (from 95%→17.5% of stride) and more flexion overall at the left side. The large hip flexion at both sides can be partly attributed to the subject holding the sidebars of the treadmill for support.

In the unassisted mode (see fig. 4.24(top)) KNEXO generates a small resisting torque ($< 2\,Nm$) and a related energy loss is noticeable in initial swing, but this was not reported by the subject. Similarly to what is observed in unimpaired subjects, a comparison of knee kinematics during unassisted walking with walking without KNEXO in fig. 4.27 (red vs green), shows smaller peak flexion during swing and more incomplete extension. A decrease of the stride period from $2.21 \pm 0.07\,s$ (without KNEXO) to $2.06 \pm 0.05\,s$ (with KNEXO in ZT mode), implying a decrease of the step length (fixed treadmill speed), was also observed.

Three distinctive effects can be pointed out, when comparing assisted walking ("best" PSMC mode, bottom) with unassisted walking (ZT mode, top) in fig. 4.24. During stance a flexion torque ($\approx -8\,Nm$) prevents the knee from overstretching, during pre-swing and initial swing knee flexion is assisted (positive power) and during mid and terminal swing knee extension is guided (reduced variability of the joint angle). This guidance during late swing also induces a larger knee extension in preparation of heel strike and stance. The effects on knee kinematics (VICON) are less pronounced when comparing this PSMC mode (blue) with walking without KNEXO (red) in fig. 4.28. This is not only due to the difference in knee kinematics between walking without KNEXO (red) and with KNEXO in unassisted mode (green), but also due to the compliance of the human-robot interface causing deviations between the knee angle and the exoskeleton's joint angle, as can be inferred from fig. 4.29. The compliance at the interface results from the compliance of the cuffs and the compliance of soft human tissue (i.e. muscles, skin, ...). During the stance phase of assisted walking for instance, the exoskeleton exerts a flexion torque while being more flexed than the patient's knee (positive angle difference in fig. 4.29 (bottom)).

The subject experienced the device as supporting her knee and improving her walking ability. In particular she felt more confident shifting her weight on the right leg when compared with walking in ZT mode and walking without KNEXO. This is confirmed by the gait timing results shown in fig. 4.26. Comparing trial means for PRE/ZT with "best" PSMC in the top graph reveals increased left-right symmetry in terms of heel strike timing (stance°R(swing°L) and swing°R(stance°L) closer to 50%) and longer periods of heel contact with the ground for both sides (increased stance*R and stance*L). The latter, however, turns more asymmetric in the presence of assistance. While similar observations can be made from the top graph in fig. 4.26, the evolution in time of the gait timing variables shows marked fluctuations after the transition to assisted walking that result from the dynamic interaction between the device and the patient adapting to it. The influence of assistance on gait timing symmetry also appears from fig. 4.28. The ankle, knee and hip joint cycles of the left side are time shifted when comparing "best" PSMC (blue) with walking without KNEXO (red).

The selected target trajectory obviously affects the timing and the amount of assistance provided by the device. As can be observed in fig. 4.25(top) PSMC T3 (green) provides a lower flexion torque than PSMC T1 (blue) during stance resulting in increased knee extension, as expected. Comparing PSMC T2 (red) and PSMC T1 (blue), however, reveals similar flexion angles during pre-swing and initial swing (55-65% of stride) and significantly higher flexion torque magnitudes in the case of PSMC T1. This suggests that the patient reduces effort in the latter case, supporting the perception of "best" assistance mode. Both PSMC T2 and PSMC T3 also induce a more pronounced asymmetry in heel strike timing and a larger variability in heel contact with the ground compared with PSMC T1, ZT and PRE (see fig. 4.26(bottom)). These observations underline the importance of the target trajectory and equally show that ultimately its effect is dependent of the wearer's response to the changed assistive environment displayed by the device.

A comparison of different controller settings in fig. 4.25 (bottom) and fig. 4.28 points out that increasing the gains as in PSMC T1 0%FF 100%G (fig. 4.25, orange) results in a better matched target when compared with PSMC T1 0%FF 50%G (blue), without any significant change of torque or power. The difference in joint kinematics suggests a difference in the patient's effort. The addition of a feedforward torque in PSMC T1 100%FF 50%G (purple) yields the most "stiff" controller setting depicted. In this case the torque built up during pre-swing caused a slight overshoot after toe-off at 65%-80% of stride. Heel strike timing appears to be most symmetric in this case, which is also clear from fig. 4.26. Overall, the patient preferred the "softer" PSMC T1 0%FF 50%G controller setting without feedforward, as she felt the assistance was more synchronised to her gait in that case. The torque limit parameter τ_{LIM} was adapted to the amount of %FF in order to have a more or less constant actual actuator torque limit and chosen high enough such that torque saturation would not occur during "normal" assistive walking.

Summarising these observations, one can conclude that KNEXO supports knee joint function and also indirectly improves gait timing symmetry in this patient. Importantly, this was confirmed by the patient's perception and appreciation of the device's performance. The data collected from the exoskeleton enable a qualitative interpretation of its performance during assisted walking, in spite of inevitable relative motion between the human and robot due to the compliance of the interface. Muscle activity measurements could provide a better insight in the patient's response to different assistive modes. These were also included in the study, but the quality of the collected data was insufficient to draw conclusions and therefore these data were not included in the discussion.

4.3.3 Conclusion

A stroke patient and an MS patient with moderate, right side predominant impairment participated in robot-assisted walking experiments with KNEXO. The device's unassisted mode (ZT mode) proved to be a valuable tool for qualitative gait assessment in view of target trajectory selection for the assisted mode. A quantitative comparison of unassisted walking with KNEXO in ZT mode and walking without KNEXO by means of gait analysis pointed out increased gait asymmetry due to the unilateral device, as observed previously in unimpaired subjects.

Given some patient-specific tuning of the assistive mode, KNEXO effectively assists impaired knee function, leading to improved gait symmetry. The improvements observed in the stroke patient were moderate, as his most prominent gait impairment was weakness of the ankle dorsiflexor muscles. Still, the assistance stabilised the knee during stance and provided more foot clearance during swing. In the MS patient, gait analysis confirmed that hyperextension of the knee was prevented and knee extension was smoothly guided in preparation of heel strike. Gait timing symmetry also improved and the subject reported feeling more confident shifting the body weight on the right leg and experiencing a marked but compliant support at the knee.

Due to the compliant guidance and the limitation of assistance to the knee joint a dynamic interaction between the human and the robot takes place that requires gait analysis and muscle EMG measurements in addition to exoskeleton data to provide an in-depth analysis of the influence of robot-assistance on impaired gait. Patients with mild or moderate impairment, that is not related to the right knee function alone, require a more careful selection of the target trajectory and of controller settings with this specific device in order to provide assistance that blends in with the patients' own efforts and leads to more significant improvement.

The potential of the assistive controller was not fully explored in these pilot experiments, since focus was mainly on compliant guidance. However, the torque limitation and slow recovery from large deviations characteristic to the controller, appeared useful during mode transitions (unassisted→assisted, assisted→stop walking) and were felt contributing to the general safety of the test environment. The pilot experiments discussed in this chapter, showing the value of KNEXO and of the proposed methods, encourage future studies in unimpaired subjects focusing more specifically on human-robot interaction.

Conclusion and future research

In the past decade the state-of-the art in robot-assisted rehabilitation of gait has known a steep rise. Research efforts are driven by the need for clinical evidence of the effectiveness of robot-asisted therapy and within the field of gait rehabilition robotics they are focused on the development of novel gait training robots. Newly developped prototypes are aimed at the improvement and diversification of robotic therapies and at gaining insight in the principles underlying motor learning and neural recovery that evidence these therapies. The assistance-as-needed paradigm, that is based on these principles, has put emphasis on a more human-centered approach to robot design and control in which physical human-robot interaction plays a key role.

This dissertation addresses several design and control aspects of a gait rehabilitation exoskeleton powered by compliant actuators with focus on improved physical human-robot interaction. The combination of lightweight, intrinsically compliant, high torque actuators (pleated pneumatic artificial muscles, PPAMs) and safe, adaptable guidance along a target trajectory is investigated for end use in a full lower body exoskeleton. In order to evaluate the proposed design and control concepts a powered knee exoskeleton (KNEXO) has been developed and robot-assisted walking experiments have been performed with unimpaired and impaired subjects. The different stages required to come to this experimental evaluation were tackled: actuator system design, mechanical structure design, system modelling and simulation, controller design and control performance evaluation.

Overview

The mechanical design of KNEXO, presented and explained in chapter 2, finds a logical starting point in the biomechanics of human gait, providing a framework for the actuator system requirements and the kinematics of the mechanical structure.

In view of a generalisation to joints other than the knee a methodical approach to the design of a joint powered by PPAMs was considered indispensable. The design of a conventional antagonistic setup of PPAMs connected to the joint by means of fixed levers was formulated as a multi-objective optimisation problem. An exhaustive search based optimisation method was used to find optimal solutions that are more compact and less overdimensioned than feasible solutions found by trial-and-improvement. In order to come to this level of integration a study of the existing mathematical model of the PPAM was mandatory. Hence, the nonlinear torque-angle relationship of the powered joint that results from the nonlinear force-contraction output of the PPAM is the key characteristic that governs the design problem. A force transmission by four bar linkages was found to possess better torque shaping capabilities than fixed levers while improving compactness. The resulting optimised actuator system design has a maximal torque output of 75Nm and a range of motion of 90°.

Different intermediate prototypes were developed to come to the design of the powered knee exoskeleton KNEXO. Special attention was paid to the adaptability of the interface between human and robot in view of extended testing with different subjects. An external weight compensating mechanism was used for the exoskeleton, that makes it wall-grounded while preserving the degrees-of-freedom of the pelvis in treadmill walking. The device was equipped with custom-made strain gauge based force sensors for use in a torque control scheme.

In chapter 3 the methods and controllers were introduced and discussed to achieve safe, compliant and adaptable robotic assistance by KNEXO. An overview of the state-of-the-art in assistance-based control was given to provide a better insight in the different existing strategies to introduce compliance into the system and to achieve assistance-as-needed. In this work intrinsic compliance on the hardware level (due to the compliant actuators) is combined with proxy-based sliding mode control (PSMC), a control method that combines trajectory tracking with an appropriately slow response to large deviations from the target trajectory. PSMC is known to improve robot safety (against damage due to environmental contact or excessive speed) in robotic manipulator control and to improve impact safety in robots operating in the proximity of humans. One of the main objectives of this thesis was to investigate the suitability of PSMC to improve the safety and adaptability of human-robot interaction in robots that are in close contact with impaired humans.

Two assistive modes were considered: an unassisted mode for trajectory recording and as a baseline for performance evaluation of robot-assistance, and an assisted mode for safe and compliant guidance along a target trajectory. The implementation of these modes required different controllers, that were studied with simulation models of the combined human-robot system and more importantly, experimentally evaluated.

For the unassisted mode, a torque controller was implemented. A PI torque controller with force sensor based feedback and with a feedforward term based on a static actuator model achieved good torque tracking performance compared with other existing pneumatic muscle systems. Dynamic response measurements showed the effects of the nonlinear pressure dynamics underlying the performance of the pneumatic system and revealed the importance of the model-based feedforward term. Zero-torque control effectively reduces the dynamic stiffness of the system and in the velocity range of the application the residual torque levels were found to be acceptable.

For the assisted mode, a proxy-based sliding mode controller with non-model based feedforward torque was implemented. PSMC combines aspects of PID control and sliding mode control into a control method that generates PID-like behaviour with an adjustable actuator torque saturation limit and that provides an adjustable, slow recovering motion from large deviations from the target trajectory. The feedfoward torque, based on measurements of the system under PSMC without feedforward, improves tracking without the need for human-robot system modelling. Interaction experiments on a test setup verified the similarities with PID control in terms of tracking performance without perturbations and the marked differences in the response to human-robot interaction torques. In order to gain a more accurate control over the actuator torque limit an alternative PSMC scheme was proposed that uses the previously developed torque controller as an inner torque control loop, instead of controlling the muscle pressures directly. The resulting controller (PSMC IT) achieved similar tracking performance and more reliable torque saturation, when compared with PSMC, but appeared to be less reliable in terms of stability.

The robot-assisted experiments covered by chapter 4 were designed to evaluate the effectiveness of the proposed controllers and methods. First, by extensive testing with several unimpaired subjects, and after that in pilot experiments with a stroke patient and a Multiple Sclerosis (MS) patient with right side predominant impairment. In the evaluation of the effects of robotic assistance exoskeleton data was combined with gait kinematics measurements and EMG measurements to gain a better insight in human-robot interaction.

Unassisted walking with KNEXO in zero-torque mode was seen to have a subject-dependent adverse effect on overall gait symmetry in (un)impaired subjects due to the unilateral nature of the device. Altered knee joint kinematics at the exoskeleton side were attributed to the combined effect of residual actuator torques, added inertia/weight and possible kinematical misalignment between human and robot. The unassisted mode proved to be indispensable for qualitative (recorded) knee function assesment in preparation of assisted walking trials with impaired subjects.

In assisted walking experiments with unimpaired subjects wearing KNEXO in PSMC mode different interaction scenarios were investigated. Target knee trajectories were generated by a record-replay procedure (with or without trajectory scaling) and synchronised to the subject's gait. According to these experiments KNEXO compliantly guides the knee and is capable of displaying different assistive modes, depending on the control parameters. The control parameters define the amount of assistance during normal guidance (gains and feedforward torque) and the response to human interaction torques (torque limit and time constant of the recovering motion), and their setting implies an important trade-off between safety of guidance and safety of interaction.

Provided a patient-specific controller tuning, the assistive mode of KNEXO effectively assisted impaired knee function and improved gait symmetry in the stroke patient and the MS patient. In the MS patient this was confirmed by gait analysis and also by her feedback on perceived assistance and comfort. She reported improved weight bearing on the most affected leg and an increased confidence in walking. Although the role of the torque saturation and slow recovering motion were not fully explored during guidance in these experiments, these key features of PSMC proved to increase safety during transitions between different assistive modes.

General conclusion

Based on this work some general conclusions can be drawn on the effectiveness of the design and control concepts investigated on KNEXO and on the potential of KNEXO as a research prototype and as a robotic therapy device.

Regarding the compliant actuator implemented in KNEXO, the pleated pneumatic artificial muscle, it is felt that the development of the torque controller, standalone and as part of a trajectory controller with torque-dependent behaviour, has increased the potential of this actuator (and pneumatic muscles in general) to be used as a torque source. In contrast with a pure trajectory controller, an assistive controller aimed at assistance-as-needed requires control over the human-robot interaction torques, which in turn requires actuators to be a good torque source. Provided some hardware adaptations, as will be discussed further, the proposed actuator system may meet the torque requirements that apply to the robot joints of a powered full lower body exoskeleton for gait assistance. However, there are two main disadvantages related to the use of these specific actuators that discourage their use as a torque source. Firstly, due to their nonlinearity, their performance heavily relies on a model-based feedforward term that ideally should take into account the pressure dynamics, as well as the torque-pressure relationship of the PPAM. Improving the relatively slow pressure dynamics requires dedicated modelling and hardware (valves). The PPAM's torque-pressure relationship is complex (e.g. hysteresis) and difficult to model. Secondly, there are some practical issues as well: the manufacturing process of the muscles (manual production, variations in quality and reliability having implications for modelling) and the use of pressurised air as a power source (availability, noise).

Regarding the use of compliant actuators with adaptable intrinsic compliance. Previous work by Vallery et al. (2008); Veneman et al. (2006) on rotational series-elastic actuators with a fixed intrinsic compliance shows that the intrinsic stiffness (the stiffness of the spring in series with the motor) influences torque control performance: a too low stiffness affects the dynamic response because of actuator saturation, a too high stiffness deteriorates stability. According to Vallery et al. (2008) a compliant actuator can not render a higher stiffness than the intrinsic stiffness without compromising stability. In this work it was also shown that the intrinsic stiffness of a PPAM powered joint influences torque control performance. Firstly, performance deterioration at low compliances is also due to saturation-like effects (the underlying pressure dynamics become slow if the mean muscle pressure (which roughly relates to the intrinsic stiffness of the joint) is decreased). Secondly, in zero-torque control it was observed that rendering a minimal dynamic stiffness gives better results in the case of a low intrinsic stiffness, in spite of saturation. These two examples indicate that indirectly (e.g. because of actuator saturation) or directly, the adaptability of intrinsic compliance is a useful means to tune actuator performance according to the needs of the application. Within the ALTACRO project (see 1.2.3), the Mechanically Adjustable Compliance and Controllable Equilibrium Position Actuator (MACCEPA, Van Ham et al. (2007)), a rotational series elastic actuator with adjustable intrinsic stiffness, is investigated in view of implementation in a full lower body exoskeleton. Pin pointing the added value of the adaptability of intrinsic compliance, for instance with respect to robustness against disturbances or against varying conditions (e.g. inertial, stiffness and damping properties of the human as part of the system) remains an important topic of research.

Regarding the suitability of PSMC as an assistive controller, it was shown that the adjustable torque limitation (τ_{LIM}) of PSMC is a useful means to achieve safe and adjustable assistance and that in order to gain control over the human-robot interaction torques with this feature, the exoskeleton's dynamics need to be compensated. The adjustable, slow recovering motion of PSMC should be fast enough to ensure continuity of gait (avoid stumbling or falling) and slow enough to ensure safety of interaction (slow speeds, no overshoot). A value of about $0.1\,s$ for the time constant (λ) of the recovering motion gave the best results in interaction experiments with unimpaired subjects. The combination of the torque limitation and the slow recovering motion allows for a variety of assistive modes. In view of future implementation of PSMC as an assistive control strategy, a higher-level controller is considered indispensable for a methodical, online adaptation of the torque limit τ_{LIM} and the time constant λ.

Regarding the potential of KNEXO as a research prototype and as a robotic therapy device, it is felt that KNEXO is a suitable research prototype for further study of the benefits of intrinsic (adaptable) compliance and of PSMC (and by extension of other control strategies) in different physical human-robot interaction scenarios. In continuation of the evaluation of KNEXO in impaired subjects, focus can be shifted on safety of interaction in the event of considerable resistance against assisted motion (e.g. stiff knee gait in stroke patients, spasticity of the leg muscles). The interaction experiments with unimpaired subjects have already shown the potential of intrinsic compliance and PSMC in such case. Although the prototype was not envisaged as a robotic therapy device, additional patient testing would help defining potential users and therapeutic benefits. From this viewpoint, the absence of assistance at the hip is a current limitation of the device.

Future research

The work reported in this dissertation fits in the scope of a broader ongoing research project (ALTACRO, see 1.2.3) that addresses identified research challenges in robot-assisted rehabilitation of gait and concerns the development of a novel full lower body exoskeleton powered by compliant actuators with intrinsic adaptable compliance. Considering the general conclusions, at least two tracks can be explored starting from this work.

The first, short term track focusing on KNEXO:

- solving the stability issues of the proxy-based sliding mode controller with inner torque control loop. The performance of this controller would benefit from a more accurate model-based feedforward term in the torque control loop. Also the low-level pressure control could be improved by using the internal muscle pressure instead of the valve pressure as the control signal.

- investigating the added value of proxy-based sliding mode control to robotic gait assistance in impaired subjects with significant spasticity of the leg muscles. This would allow to explore assistive modes with emphasis on safety of interaction. Since there is a relationship, although complex, between the occurrence of spasticity and the velocity of joint motion, it could be of interest here to use an alternative PSMC scheme with additional velocity bound as introduced by Kikuuwe et al. (2006).

Some of the concepts proposed and elaborated in this work could be brought to fruition by implementing them on a bilateral exoskeleton with powered joints at the ankle, knee and hip. Therefore the second, long term track focuses on the development of a full lower body exoskeleton:

- investigating the trade-off between safety of interaction and safety of guidance with a joint-level implementation of PSMC. A bilateral multi-DOF exoskeleton allows to explore a higher support torque range and a full robot-in-charge scenario.

- investigating the implementation of PSMC on the robot in cartesian space instead of on a (distributed) joint-level and in which ways human-robot interaction would benefit from this higher level approach.

Publications

Peer-reviewed journal articles:

- **P. Beyl**, K. Knaepen, S. Duerinck, M. Van Damme, B. Vanderborght, D. Lefeber, Safe and compliant guidance by a powered knee exoskeleton for robot-assisted rehabilitation of gait, *Advanced Robotics - Special Issue on Physical Human-Robot Interaction Through Force Interfaces*, vol.25, no.5, 2010, in press.

- M. Van Damme, **P. Beyl**, B. Vanderborght, R. Versluys, R. Van Ham, I. Vanderniepen, F. Daerden, D. Lefeber, The Safety of a Robot Actuated by Pneumatic Muscles : A Case Study, *International Journal of Social Robotics*, vol.2, no.3, pp. 289-303, January 2010.

- **P. Beyl**, M. Van Damme, R. Van Ham, B. Vanderborght, D. Lefeber, Design and control of a lower limb exoskeleton for robot-assisted gait training, *Applied Bionics and Biomechanics*, vol.6, no.2, pp. 229-243, June 2009.

- R. Versluys, **P. Beyl**, M. Van Damme, A. Desomer, R. Van Ham, D. Lefeber, Prosthetic feet: State-of-the-art review and the importance of mimicking human ankle-foot biomechanics, *Disability and Rehabilitation: Assistive Technology,* vol.4, no.2, pp. 65-75, March 2009.

- M. Van Damme, B. Vanderborght, **P. Beyl**, R. Versluys, I. Vanderniepen, R. Van Ham, P. Cherelle, F. Daerden, D. Lefeber, Sliding mode control of a Soft 2-DOF Planar Pneumatic Manipulator, *International Applied Mechanics*, vol.44, no.10, pp. 1191-1199, October 2008.

- B. Vanderborght, B. Verrelst, R. Van Ham, M. Van Damme, **P. Beyl**, D. Lefeber, Development of a compliance controller to reduce energy consumption for bipedal robots, *Autonomous Robots*, vol.15, no. 4, pp. 419-434, February 2008.

- B. Vanderborght, B. Verrelst, R. Van Ham, M. Van Damme, D. Lefeber, B. Meira Y Duran, **P. Beyl**, Exploiting Natural Dynamics to Reduce Energy Consumption by Controlling the Compliance of Soft Actuators, *Internatioal Journal of Robotic Research*, Vol. 25, no. 4, pp. 343-358, April 2006.

Conference papers with full paper review:

- P. Cherelle, V. Grosu, **P. Beyl**, A. Matthys, R. Van Ham, M. Van Damme, B. Vanderborght, D. Lefeber, The MACCEPA Actuation System As Torque Actuator in the Gait Rehabilitation Robot ALTACRO, 2010 BIOROB, *Proceedings of the IEEE International Conference on Biomedical Robotics and Biomechatronics*, Tokyo, Japan, 26-29 September.
- **P. Beyl**, M. Van Damme, P. Cherelle, D. Lefeber, Safe and compliant guidance in robot-assisted gait rehabilitation using proxy-based sliding mode control, 2009 ICORR, *Proceedings of the IEEE International Conference on Rehabilitation Robotics*, Kyoto, Japan, 23-26 June, pp. 277-282.
- **P. Beyl**, P. Cherelle, R. Versluys, I. Vanderniepen, D. Lefeber, A powered knee exoskeleton for gait rehabilitation, 2009 NCTAM, *Proceedings of the 8th National Congress on Theoretical and Applied Mechanics*, Brussels, Belgium, 28-29 May, pp. 188-194.
- **P. Beyl**, P. Cherelle, K. Knaepen, D. Lefeber, A proof-of-concept exoskeleton for robot-assisted rehabilitation of gait, 2008 EMBEC, *Proceedings of the 4th European Conference of the International Federation for Medical and Biological Engineering*, Antwerp, Belgium, 23-27 November, pp. 1825-1829.
- **P. Beyl**, M. Van Damme, R. Van Ham, D. Lefeber, Design and control concepts of an exoskeleton for gait rehabilitation, 2008 BIOROB, *Proceedings of the 2nd Biennial IEEE/RAS-EMBS International Conference on Biomedical Robotics and Biomechatronics*, Scottsdale, AZ, USA, 19-22 October, pp. 103-108.
- R. Versluys, A. Desomer, G. Lenaerts, **P. Beyl**, M. Van Damme, B. Vanderborght, I. Vanderniepen, G. Van der Perre, D. Lefeber, From Conventional Prosthetic Feet to Bionic Feet: A Review Study, 2008 BIOROB, *Proceedings of the 2nd Biennial IEEE/RAS-EMBS International Conference on Biomedical Robotics and Biomechatronics*, Scottsdale, AZ, USA, 19-22 October, pp. 49-54.
- M. Van Damme, **P. Beyl**, B. Vanderborght, R. Van Ham, I. Vanderniepen, R. Versluys, F. Daerden, D. Lefeber, Modeling Hysteresis in Pleated Pneumatic Artificial Muscles Authors, 2008 RAM, *Proceedings of the IEEE International Conference on Robotics, Automation & Mechatronics,* Chengdu, China, 21-24 September, pp. 471-476.

- **P. Beyl**, M. Van Damme, R. Van Ham, R. Versluys, B. Vanderborght, D. Lefeber, An Exoskeleton for Gait Rehabilitation: Prototype Design and Control Principle, 2008 ICRA, *Proceedings of the IEEE International Conference on Robotics and Automation*, Pasadena, CA, USA, 19-23 May, pp. 2037-2042.

- B. Vanderborght, M. Van Damme, R. Van Ham, **P. Beyl**, D. Lefeber, A strategy to combine active trajectory control with the exploitation of the natural dynamics to reduce energy consumption for bipedal robots, Humanoids07, *Proceedings of the IEEE-RAS International Conference on Humanoid Robots*, Pittsburgh, PA, USA, 29 November - 1 December.

- **P. Beyl**, J. Naudet, R. Van Ham, D. Lefeber, Mechanical design of an active knee orthosis for gait rehabilitation, 2007 ICORR, *Proceedings of the IEEE International Conference on Rehabilitation Robotics*, Noordwijk, The Netherlands, 12-15 June, pp. 100-105.

- B. Vanderborght, B. Verrelst, M. Van Damme, R. Van Ham, **P. Beyl**, D. Lefeber, Locomotion Control Architecture for the Pneumatic Biped Lucy Consisting of a Trajectory Generator and Joint Trajectory Tracking Controller, Humanoids06, *Proceedings of the IEEE-RAS International Conference on Humanoid Robots*, Genova, Italy, 4-6 December, pp. 240-245.

- B. Vanderborght, B. Verrelst, R. Van Ham, M. Van Damme, **P. Beyl**, D. Lefeber, Torque and Compliance Control of the Pneumatic Artificial Muscles in the Biped "Lucy", 2006 ICRA, *Proceedings of the IEEE International Conference on Robotics and Automation*, Orlando, FL, USA, 15-19 May 2006, pp. 842-847.

Appendix A

Actuator system design: four bar linkage analysis

A.1 Kinematics

A schematic representation of a four bar linkage with link lengths $L_1 \ldots L_4$ is depicted in fig. A.1. The ground link (segment O_1O_2) is considered fixed. The motion of the input link (segment O_2O_3) is transferred to the output link (segment O_4O_1) by the coupler (segment O_4O_1). The kinematics of the linkage reside in the following simple loop-closure equation:

$$\mathbf{O_1O_2} + \mathbf{O_2O_3} + \mathbf{O_3O_4} + \mathbf{O_4O_1} = \mathbf{0}. \tag{A.1}$$

By means of the angles defined in fig. A.1 the vector eq. A.1 is written as a set of equations:

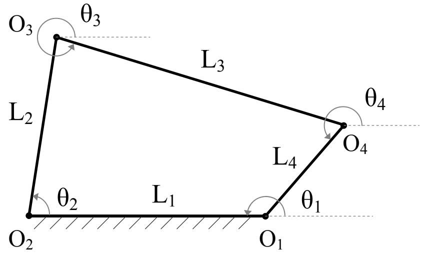

Figure A.1: Four bar linkage

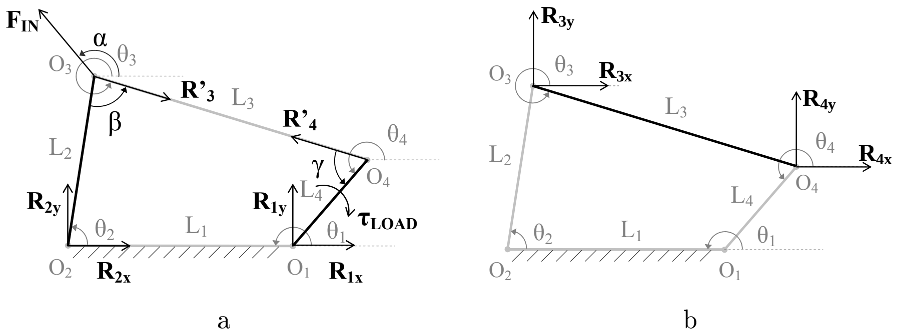

Figure A.2: Free body diagrams: a) input link and output link with known external loads and unknown reaction forces, b) coupler with unknown reaction forces

$$\begin{cases} 0 & = -L_1 + L_2\cos\theta_2 + L_3\cos\theta_3 + L_4\cos\theta_4 \\ 0 & = L_2\sin\theta_2 + L_3\sin\theta_3 + L_4\sin\theta_4 \end{cases} . \tag{A.2}$$

In the actuator configuration with four bar linkages, discussed in section 2.3.5, the output link angle θ_4 is related to the joint angle q. Eq. A.2 is thus solved numerically for θ_2 and θ_3, given θ_4.

A.2 Mechanical advantage and static force analysis

The mechanical advantage of the four bar linkage is defined as the ratio of output torque τ_{OUT} to input torque τ_{IN}, also referred to as transmission ratio (denoted by r_t). If power losses are neglected, the mechanical power P_{IN} at the input link equals the mechanical power P_{OUT} at the output link, which yields

$$\begin{aligned} P_{OUT} &= P_{IN} \\ \tau_{OUT}\dot{\theta}_4 &= \tau_{IN}\dot{\theta}_2 \\ r_t &= \frac{\tau_{OUT}}{\tau_{IN}} = \frac{\dot{\theta}_2}{\dot{\theta}_4}. \end{aligned} \tag{A.3}$$

The transmission ratio r_t can be calculated by taking the derivative of eq. A.2, eliminating $\dot{\theta}_3$ and substituting the far most right hand side of eq. A.3. Alternatively, r_t follows from the static force analysis of the four bar linkage. The forces acting on the links need to be known for strength calculations in the design and in particular for the design of the custom-made force sensors, explained in section

2.5.2.3. Free body diagrams of the input and output link, and of the coupler are shown in fig. A.2.a and fig. A.2.b respectively. In fig. A.2.a the input torque is generated by an external force F_{IN}, whereas the load acting on the output link is represented by an external torque τ_{LOAD}. These loads are external to the linkage and correspond with the loading case found in the configuration depicted in fig. 2.24 and discussed in section 2.3.5. From fig. A.2.b one infers that in order to have force balance the reaction force vectors $\mathbf{R_3}$ $(= \mathbf{R_{3x}} + \mathbf{R_{3y}})$ and $\mathbf{R_4}$ $(= \mathbf{R_{4x}} + \mathbf{R_{4y}})$ should be aligned with the coupler, have equal amplitude and opposite sense. Hence, the same holds for the reaction forces $\mathbf{R_3'}$ $(\mathbf{R_3'} = -\mathbf{R_3})$ and $\mathbf{R_4'}$ $(\mathbf{R_4'} = -\mathbf{R_4})$ shown in fig. A.2.a. The relation between input torque and output torque is found by expressing the condition that the total moment of the external forces acting on the input link and the total moment of the external forces acting on the output link should both be zero:

$$\begin{cases} M_{O_2,input\,link} & = F_{IN} L_2 \sin(\alpha - \theta_2) - R_3' L_2 \sin\beta = 0 \\ M_{O_1,output\,link} & = R_4' L_4 \sin\gamma - \tau_{LOAD} = 0 \end{cases}. \tag{A.4}$$

This set of equations is solved by substituting

$$\begin{aligned} R_4' &= R_3' \\ \tau_{IN} &= F_{IN} L_2 \sin(\alpha - \theta_2) \\ \tau_{OUT} &= \tau_{LOAD} \\ \beta &= \theta_3 - \theta_2 - \pi \\ \gamma &= \theta_4 - \theta_3 + \pi \end{aligned}$$

in eq. A.4, which yields

$$\begin{cases} M_{O_2,input\,link} & = \tau_{IN} - R_3' L_2 \sin(\theta_2 - \theta_3) = 0 \\ M_{O_1,output\,link} & = R_3' L_4 \sin(\theta_3 - \theta_4) - \tau_{OUT} = 0 \end{cases}$$

and by eliminating R_3', which results in

$$r_t = \frac{\tau_{OUT}}{\tau_{IN}} = \frac{L_4}{L_2} \frac{\sin(\theta_3 - \theta_4)}{\sin(\theta_2 - \theta_3)}. \tag{A.5}$$

The longitudinal forces acting on the input link, the output link and the coupler are given by

$$F_{input\,link} = F_{IN} \cos(\alpha - \theta_2) - R_3' \cos\beta$$

$$\begin{aligned} F_{output\,link} &= -R_4' \cos\gamma \\ F_{coupler} &= R_3. \end{aligned} \tag{A.6}$$

in which a positive sign indicates tension and a negative sign indicates compression. The angle α can be determined from the actuator configuration in fig. 2.24. Substituting previous findings in eq. A.6 gives

$$\begin{aligned} F_{input\,link} &= F_{IN}\cos(\alpha-\theta_2) + \frac{\tau_{IN}}{L_2}\cot(\theta_2-\theta_3) \\ F_{output\,link} &= -\frac{\tau_{IN}}{L_2}\frac{\cos(\theta_3-\theta_4)}{\sin(\theta_2-\theta_3)} \\ F_{coupler} &= \frac{\tau_{IN}}{L_2\sin(\theta_2-\theta_3)}. \end{aligned} \tag{A.7}$$

During operation link loading can change from tension to compression or vice versa, depending on the orientation of the linkage and the line of action of the input force.

Appendix B

Proxy-based sliding mode control

B.1 Discrete-time controller

The derivation of the discrete-time control law is explained in what follows. For detailed calculations of the continuous-time and discrete-time control law as well as an in-depth coverage of the characteristics of proxy-based sliding mode control, the reader is referred to Van Damme (2009).

The discrete-time control law is derived from the set of equations that defines the torque τ as required by proxy-based sliding mode control and given by

$$\tau = \tau_{LIM}\,\mathrm{sgn}\left(\sigma - \dot{a} - \lambda\ddot{a}\right) \tag{B.1}$$

$$\tau = K_p\dot{a} + K_i a + K_d\ddot{a} \tag{B.2}$$

where $\sigma = (q_d - q) + \lambda(\dot{q}_d - \dot{q})$ and $a = \int(q_p - q)dt$ and the signum function $\mathrm{sgn}(\cdot)$ defined by

$$sgn(x)\begin{cases} = 1 & if\ x > 0 \\ \in [-1, 1] & if\ x = 0 \\ = -1 & if\ x < 0 \end{cases}. \tag{B.3}$$

The torque τ can be calculated from a discrete-time representation of eq.B.1-B.2.

By writing the value of q at timestep k as $q\,[k]$ (i.e. $q\,[k] = q\,(kT)$, where T is the sampling period) and by introducing the backward difference operator ∇, defined by

$$\nabla q\,[k] = q\,[k] - q\,[k-1]\,, \tag{B.4}$$

one can approximate $\dot{q}$ at timestep k by

$$\dot{q}\,[k] = \frac{\nabla q\,[k]}{T} \tag{B.5}$$

and $\ddot{q}$ by

$$\begin{aligned}\ddot{q}[k] &= \frac{\nabla \dot{q}[k]}{T} \\ &= \frac{\nabla^2 q[k]}{T^2}\end{aligned} \tag{B.6}$$

with

$$\begin{aligned}\nabla^2 q[k] &= \nabla(\nabla q[k]) \\ &= \nabla q[k] - \nabla q[k-1] \\ &= q[k] - 2q[k-1] + q[k-2].\end{aligned}$$

Using these definitions, a discrete time representation of eq. B.1-B.2 is given by

$$\tau[k] = \tau_{LIM}\,\mathrm{sgn}\left(\sigma[k] - \frac{\nabla a[k]}{T} - \lambda\frac{\nabla^2 a[k]}{T^2}\right) \tag{B.7}$$

$$\tau[k] = K_p\frac{\nabla a[k]}{T} + K_i a[k] + K_d\frac{\nabla^2 a[k]}{T^2}, \tag{B.8}$$

with $\sigma[k]$ given by

$$\sigma[k] = (q_d[k] - q[k]) + \lambda(\dot{q}_d[k] - \dot{q}[k]) \tag{B.9}$$

where $\dot{q}_d[k]$ and $\dot{q}[k]$ are known and thus do not need to be approximated by means of finite differences. Eq. B.7-B.8 can be considered as a system of two algebraic equations in two unknowns, $\tau[k]$ and $a[k]$.

A first step in the solution is to solve eq. B.8 for $a[k]$:

$$a[k] = \frac{a[k-1](K_pT + K_d) + K_d\nabla a[k-1] + T^2\tau[k]}{K_iT^2 + K_pT + K_d}. \tag{B.10}$$

Substitution in eq. B.7 gives

$$\tau[k] = \tau_{LIM}\,\mathrm{sgn}(\tau^*[k] - \tau[k]), \tag{B.11}$$

with

$$\tau^*[k] = \frac{K_iT^2 + K_pT + K_d}{T+\lambda}\sigma[k] + K_i a[k-1] + \frac{\lambda(K_iT + K_p) - K_d}{T(T+\lambda)}\nabla a[k-1]. \tag{B.12}$$

Eq. B.11 shows that the discretization has allowed the "closure of a feedback loop" around the signum function within the software of the controller. Since $\tau_{LIM} > 0$ one can rewrite eq. B.11 as

$$\frac{\tau[k]}{\tau_{LIM}} = \mathrm{sgn}(\tau^*[k] - \tau[k])$$

$$= \quad \operatorname{sgn}\left(\frac{\tau^*[k]}{\tau_{LIM}} - \frac{\tau[k]}{\tau_{LIM}}\right).$$

Using the definition of sgn(·) (eq. B.3), Kikuuwe and Fujimoto (2006) show the following equivalence:

$$y = \operatorname{sgn}(x - y) \quad \Longleftrightarrow \quad y = \operatorname{sat}(x), \tag{B.13}$$

with the unit saturation function $\operatorname{sat}(\cdot)$ defined as

$$\operatorname{sat}(x) = \begin{cases} x & \text{if } |x| \leq 1 \\ \operatorname{sgn}(x) & \text{if } |x| > 1. \end{cases} \tag{B.14}$$

Applying this equivalence yields

$$\begin{aligned} \tau[k] &= \tau_{LIM} \operatorname{sat}\left(\frac{\tau^*[k]}{\tau_{LIM}}\right) \\ &= \begin{cases} \tau^*[k] & \text{if } \|\tau^*[k]\| \leq \tau_{LIM} \\ \tau_{LIM} \frac{\tau^*[k]}{\|\tau^*[k]\|} & \text{if } \|\tau^*[k]\| > \tau_{LIM}. \end{cases} \end{aligned} \tag{B.15}$$

Once $\tau[k]$ is known from eq. B.15, it can be used to calculate $\boldsymbol{a}[k]$ using eq. B.10.

The procedure to calculate the output of the proxy-based sliding mode controller at timestep k can thus be summarized as follows:

$$\sigma[k] = (q_d[k] - q[k]) + \lambda(\dot{q}_d[k] - \dot{q}[k]) \tag{B.16}$$

$$\begin{aligned} \tau^*[k] &= \frac{K_i T^2 + K_p T + K_d}{T + \lambda} \sigma[k] + K_i a[k-1] \\ &\quad + \frac{\lambda(K_i T + K_p) - K_d}{T(T + \lambda)} \nabla a[k-1] \end{aligned} \tag{B.17}$$

$$\tau[k] = \begin{cases} \tau^*[k] & \text{if } \|\tau^*[k]\| \leq F \\ F \frac{\tau^*[k]}{\|\tau^*[k]\|} & \text{if } \|\tau^*[k]\| > F. \end{cases} \tag{B.18}$$

$$a[k] = \frac{a[k-1](K_p T + K_d) + K_d \nabla a[k-1] + T^2 \tau[k]}{K_i T^2 + K_p T + K_d}. \tag{B.19}$$

Appendix C

Robot-assisted walking with KNEXO: gait analysis

C.1 Motion analysis

The system used for 3-dimensional motion analysis consists of the Vicon® 612-datastation (Vicon, UK) and seven MX F20 infra-red cameras. These cameras capture the positions of reflective markers at a rate of 250 Hz and they were recalibrated prior to each new motion capturing session.

In unimpaired subjects 45 technical markers were attached to the skin over bony landmarks at the pelvis (7), in three clusters at each foot (12) and in clusters at the anterior aspects of each thigh (4) and shank (4) (see fig. C.1-C.2). Technical markers were also attached to the upper limb segment (4) and lower limb segment (4) of KNEXO in order to capture motion relative to the human limb. All these markers are involved in both static and dynamic measurements. For static reference measurements 10 anatomical markers are attached to specific lateral and/or medial bony landmarks at the hip (1), knee (2) and ankle (2) (see fig. C.2 right). A static reference measurement captures the position and orientation of the technical marker clusters relative to the anatomical markers during static standing. The anatomical markers are removed prior to dynamic measurments.

Data processing and analysis are done by means of Vicon Nexus^{TM} and Vicon BodyBuilder^{TM} software (Vicon Motion Systems Ltd., Vicon, UK) respectively. In the analysis software the marker clusters are correlated with human body segments of a biomechanical multibody model. Here, these segments are the pelvis, the two leg segments (thigh, shank) of each leg and the three foot segments (heel, forefoot, toes) of each foot. The relative motion of these segments is expressed in terms of rotations at the joints between the different segments. The multibody model also includes a two-segment model of the exoskeleton.

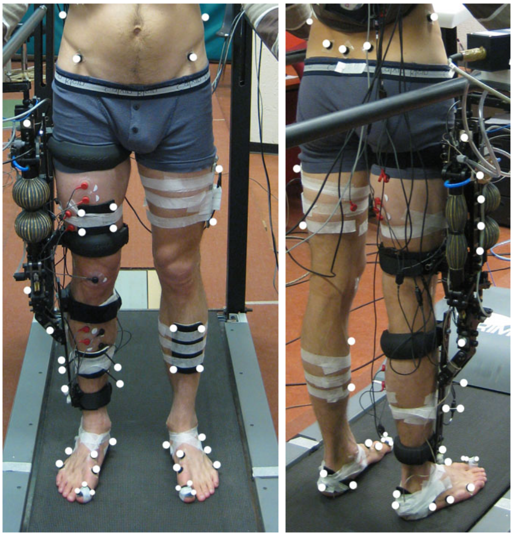

Figure C.1: Reflective marker and EMG electrode placement in unimpaired subject. Only technical markers are shown (white). EMG signal electrode pairs are red, reference electrodes (one per pair) are black.

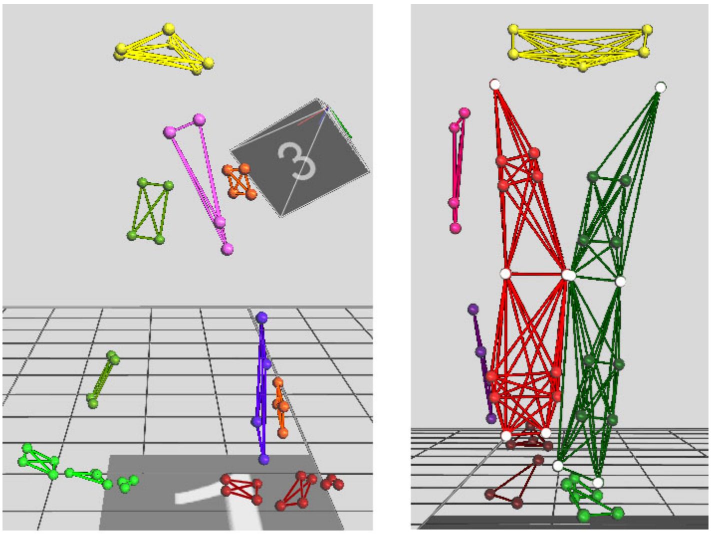

Figure C.2: Marker clusters for motion analysis (views taken from Vicon Nexus^{TM} software): unimpaired subject (left) and impaired subject (right). Anatomical markers are only shown right (white), functional markers are coloured, e.g. pelvis (yellow), upper and lower segment of KNEXO (pink and purple).

This model provides the knee joint angle of KNEXO and the rotations of the exoskeleton's segments relative to the respective human leg segments. In the discussions of results in chapter 4 only rotations in the sagittal plane (flexion/extension) at the hip, knee and ankle are considered. In the MS patient, because of the shoes being kept on, a two-segment model was used for the foot (7 instead of 12 markers for each foot, see fig. C.2 right vs. left), but this has no effect on the data discussed in chapter 4.

C.2 Muscle EMG

In unimpaired subjects muscle activity of five muscles of the right leg (exoskeleton side) was captured: M. Biceps Femoris, M. Vastus Lateralis, M. Rectus Femoris, M. Tibialis Anterior, M. Gastrocnemius Medialis (medial head of Gastrocnemius). A 16-channel Biomonitor ME6000 (Mega Electronics Ltd., Finland) was used with Cleartrace REF1700-03 surface electrodes (ConMed® Corporation, USA). Electrode placement (see fig. C.1) was performed according to SENIAM guidelines (SENIAM (Surface Electromyography for the Non-Invasive Assesement of Muscles). Muscle activity was recorded at a sample rate of 1024 Hz by means of MegaWin 3.0 b2 software (Mega Electronics Ltd., Finland).

Prior to the actual walking experiments muscle activity was measured during maximal voluntary contraction (MVC) executed by the subject according to a fixed and repeatable procedure. The reference used for normalisation was the peak voltage of the signal captured during three trials of a maximal effort test. The raw EMG data recorded during walking trials was full rectified, normalised and time-averaged with a moving window of 100 ms. Processed data was sectioned by means of the heel strike detection signal originating from the FSR sensor and averaged over four cycles.

Bibliography

1. Neurological Disorders: public health challenges. Technical report, World Health Organization, 2006.

2. http://www.ninds.nih.gov/. National Institute of Neurological Disorders and Stroke (NINDS).

3. http://www.nationalmssociety.org/index.aspx. National Multiple Sclerosis Society (US).

4. http://www.seniam.org. SENIAM (Surface Electromyography for the Non-Invasive Assesement of Muscles).

5. Agrawal, S., Banala, S., Mankala, K., Sangwan, V., Scholz, J., Krishnamoorthy, V., and Hsu, W. Exoskeletons for gait assistance and training of the motor impaired. In *Proceedings of the IEEE International Conference on Rehabilitation Robotics*, pages 1108–1113. 2007.

6. Allemand, Y., Stauffer, Y., Clavel, R., and Brodard, R. Design of a new lower extremity orthosis for overground gait training with the WalkTrainer. In *Proceedings of the 2009 IEEE International Conference on Rehabilitation Robotics*, pages 550–555. 2009.

7. Aoyagi, D., Ichinose, W., Harkema, S., Reinkensmeyer, D., and Bobrow, J. A robot and control algorithm that can synchronously assist in naturalistic motion during body-weight-supported gait training following neurologic injury. *IEEE Transactions on Neural Systems and Rehabilitation Engineering* 15(3):387–400, 2007.

8. Aschemann, H. and Hofer, E. P. Nonlinear Trajectory Control of a High-Speed Linear Axis Driven by Pneumatic Muscle Actuators. In *Proceedings of the 32nd Annual Conference on IEEE Industrial Electronics*, pages 3857–3862. 2006.

9. Balasubramanian, K. and Rattan, K. Trajectory tracking control of a pneumatic muscle system using fuzzy logic. In *Proceedings of NAFIPS 2005 - Annual Meeting of the North American Fuzzy Information Processing Society*, pages 472–477. 2005.

10. Balasubramanian, K. and Rattan, K. S. Feedforward control of a non-linear pneumatic muscle system using fuzzy logic. In *Proceedings of The 12th IEEE International Conference on Fuzzy Systems*, volume 1, pages 272–277. 2003a.

11. Balasubramanian, K. and Rattan, K. S. Fuzzy logic control of a pneumatic muscle system using a linearing control scheme. In *Proceedings of NAFIPS 2003 - 22nd International Conference of the North American Fuzzy Information Processing Society*, pages 432–436. 2003b.

12. Banala, S. K., Agrawal, S. K., Fattah, A., Krishnamoorthy, V., Hsu, W., Scholz, J., and Rudolph, K. Gravity-Balancing Leg Orthosis and Its Performance Evaluation. *IEEE Transactions on Robotics* 22(6):1228–1239, 2006.

13. Banala, S. K., Kim, S. H., Agrawal, S. K., and Scholz, J. P. Robot Assisted Gait Training With Active Leg Exoskeleton (ALEX). *IEEE transactions on neural systems and rehabilitation engineering* 17(1):2–8, 2009.

14. Banala, S. K., Kulpe, A., and Agrawal, S. K. A Powered Leg Orthosis for Gait Rehabilitation of Motor-Impaired Patients. In *Proceedings of IEEE International Conference on Robotics and Automation*, pages 4140–4145. 2007.

15. Barbeau, H. and Rossignol, S. Enhancement of locomotor recovery following spinal cord injury. *Current Opinion in Neurology* 7:517–524, 1994.

16. Behrman, A. and Harkema, S. Locomotor training after human spinal cord injury: a series of case studies. *Physical Therapy* 80(7):688–700, 2000.

17. Bernhardt, M., Frey, M., Colombo, G., and Riener, R. Hybrid force-position control yields cooperative behaviour of the rehabilitation robot Lokomat. In *9th International Conference on Rehabilitation Robotics (ICORR 2005)*, pages 536–539. 2005a.

18. Bernhardt, M., Lutz, P., and Frey, M. Physiological Treadmill Training with the 8-DOF Rehabilitation Robot LOKOMAT. In *BMT 2005, Jahrestagung der deutschen Gesellschaft für biomedizinische Technik*. 2005b.

19. Bharadwaj, K. and Sugar, T. G. Kinematics of a Robotic Gait Trainer for Stroke Rehabilitation. In *Proceedings of the 2006 IEEE International Conference on Robotics and Automation*, pages 3492–3497. 2006.

20. Blaya, J. A. and Herr, H. Adaptive control of a variable-impedance ankle-foot orthosis to assist drop-foot gait. *IEEE Transactions on Neural Systems and Rehabilitation Engineering* 12(1):24–31, 2004.

21. Blum, C. and Roli, A. Metaheuristics in combinatorial optimization: Overview and conceptual comparison. *ACM Comput. Surv.* 35(3):268–308, 2003.

22. Cai, D. and Dai, Y. A sliding mode controller for manipulator driven by artificial muscle actuator. In *Proceedings of the 2000 IEEE International Conference on Control Applications*, pages 668–673. 2000.

23. Cai, D. and Dai, Y. A Sliding Mode Controller for Manipulator Driven by Artificial Muscle Actuator. *Electronics and Communications in Japan* 86(11):57–64, 2003.

24. Cai, D. and Yamaura, H. A robust controller for manipulator driven by artificial muscle actuator. In *Proceedings of the 1996 IEEE International Conference on Control Applications*, pages 540–545. 1996.

25. Cai, L. L., Fong, A. J., Otoshi, C. K., Liang, Y., Burdick, J. W., Roy, R. R., and Edgerton, V. R. Implications of assist-as-needed robotic step training after a complete spinal cord injury on intrinsic strategies of motor learning. *Journal of Neuroscience* 26(41):10564–8, 2006.

26. Caldwell, D. G., Medrano-Cerda, G. A., and Goodwin, M. J. Braided Pneumatic Actuator Control of a Multi-Jointed Manipulator. In *International Conference on Systems, Man and Cybernetics*, pages 423–428. 1993.

27. Caldwell, D. G., Medrano-Cerda, G. A., and Goodwin, M. J. Control of pneumatic muscle actuators. *IEEE Control Systems Journal* 15(1):40–48, 1995.

28. Caldwell, D. G. and Tsagarakis, N. Biomimetic actuators in prosthetic and rehabilitation applications. *Technology and Health Care* 10:107–120, 2002.

29. Caldwell, D. G., Tsagarakis, N., Medrano-Cerda, G. A., Schofield, J., and Brown, S. A pneumatic muscle actuator driven manipulator for nuclear waste retrieval. *Control Engineering Practice* 9(1):23–36, 2001.

30. Carbonell, P., Jiang, Z. P., and Repperger, D. W. A Fuzzy Backstepping Controller for a Pneumatic Muscle Actuator System. In *Proceedings of the 2001 IEEE International Symposium on Intelligent Control*, pages 353–358. 2001a.

31. Carbonell, P., Jiang, Z. P., and Repperger, D. W. Nonlinear control of a pneumatic muscle actuator: backstepping vs.sliding-mode. In *Proceedings of the 2001 IEEE International Conference on Control Applications*, pages 167–172. 2001b.

32. Chang, M.-K., Yen, P.-L., and Yuan, T.-H. Angle Control of a one-Dimension Pneumatic Muscle Arm using Self-Organizing Fuzzy Control. In *Proceedings of the 2006 IEEE International Conference on Systems, Man, and Cybernetics*, pages 3834–3838. 2006.

33. Chang, X. and Lilly, J. H. Fuzzy Control for Pneumatic Muscle Tracking via Evolutionary Tuning. *Intelligent Automation and Soft Computing* 9(4):227–244, 2003.

34. Chettouh, M., Toumi, R., and Hamerlain, M. Derivative control in sliding mode of a robot driven by artificial muscles. In *Proceedings of the 1st IEEE International Conference on E-Learning in Industrial Electronics*. 2006.

35. Chettouh, M., Toumi, R., and Hamerlain, M. A 2-sliding control for pneumatic artificial muscles. In *Proceedings of the 5th International Multi-Conference on Systems, Signals and Devices*. 2008a.

36. Chettouh, M., Toumi, R., and Hamerlain, M. Chatter Reduction in an Artificial Muscles Robot Application. *International Journal of Robotics and Automation* 23(2):88–97, 2008b.

37. Chou, C. P. and Hannaford, B. Measurement and modelling of McKibben Pneumatic Artificial Muscles. *IEEE Transactions on Robotics and Automation* 12(1):90–102, 1996.

38. Chu, A., Kazerooni, H., and Zoss, A. On the Biomimetic Design of the Berkeley Lower Extremity Exoskeleton (BLEEX). In *Proceedings of the 2005 IEEE International Conference on Robotics and Automation*, pages 4356–4363. 2005.

39. Clapa, D. J., Croft, E. A., and Hodgson, A. J. Equilibrium Point Control of a 2-DOF Manipulator. *Transactions of the ASME - G - Journal of Dynamic Systems Measurement Control* 128:134–141, 2006.

40. Colombo, G., Wirz, M., and Dietz, V. Driven gait orthosis for improvement of locomotor training in paraplegic patients. *Spinal Cord* 39:252–253, 2001.

41. Costa, N. and Caldwell, D. Control of a biomimetic "soft-actuated" 10 DoF lower body exoskeleton. In *Proceedings of the IEEE/RAS-EMBS International Conference on Biomedical Robotics and Biomechatronics*, pages 495–501. 2006.

42. Daerden, F. *Conception and realization of pleated pneumatic artificial muscles and their use as compliant actuation elements.* Ph.D. thesis, Vrije Universiteit Brussel, 1999.

43. Daerden, F. and Lefeber, D. The concept and design of pleated pneumatic artificial muscles. *International Journal of Fluid Power* 2(3):41–50, 2001.

44. Daerden, F. and Lefeber, D. Pneumatic artificial muscles: actuators for robotics and automation. *European Journal of Mechanical and Environmental Engineering* 47(1):10–21, 2002.

45. Davis, S., Canderle, J., Artrit, P., Tsagarakis, N., and Caldwell, D. Enhanced dynamic performance in pneumatic muscle actuators. In *IEEE International Conference on Robotics and Automation (ICRA 2002)*, volume 3, pages 2836–2841. 2002.

46. Dietz, V., Colombo, G., and Jensen, L. Locomotor activity in spinal man. *Lancet* 44:1260–1263, 1994.

47. Dollar, A. and Herr, H. Lower extremity exoskeletons and active orthoses: challenges and state-of-the-art. *IEEE Transactions on Robotics* 24(1):144–158, 2008.

48. Duschau-Wicke, A., v. Zitzewitz, J., Lünenburger, L., and Riener, R. Patient-driven cooperative gait training with the rehabilitation robot Lokomat. In *ECIFMBE-IFMBE Proceedings 22*, pages 1616–1619. 2008.

49. Ehrgott, M. and Gandibleux, X. A survey and annotated bibliography of multiobjective combinatorial optimization. *OR Spectrum* 22(4):425–460, 2000.

50. Ekkelenkamp, R., Veltink, P., Stramigioli, S., and van der Kooij, H. Evaluation of a Virtual Model Control for the selective support of gait functions using an exoskeleton. In *Proceedings of the IEEE 10th International Conference on Rehabilitation Robotics*, pages 693–699. 2007.

51. Elbert, T., Flor, H., Birbaumer, N., Knecht, S., Hampson, S., Larbig, W., and Taub, E. Extensive reorganization of the somatosensory cortex in adult humans after nervous system injury. *Neuroreport* 5(18):2593–2597, 1994.

52. Emken, J., Bobrow, J., and Reinkensmeyer, D. Robotic movement training as an optimization problem: designing a controller that assists only as needed. In *Proceedings of 9th International Conference on Rehabilitation Robotics*, pages 307–312. 2005.

53. Emken, J. L., Benitez, R., and Reinkensmeyer, D. J. Human-robot cooperative movement training: Learning a novel sensory motor transformation during walking with robotic assistance-as-needed. *Journal of NeuroEngineering and Rehabilitation* 4(8), 2007.

54. Emken, J. L., Harkema, S. J., Beres-Jones, J. A., Ferreira, C. K., and Reinkensmeyer, D. J. Feasibility of manual teach-and-replay and continuous impedance shaping for robotic locomotor training following spinal cord injury. *IEEE Transactions on Biomedical Engineering* 55(1):322–334, 2008.

55. Emken, J. L. and Reinkensmeyer, D. J. Robot-Enhanced motor learning: accelerating internal model formation during locomotion by transient dynamic amplification. *IEEE Transactions on Neural Systems and Rehabilitation Engineering* 13:33–39, 2005.

56. Emken, J. L., Wynne, J. H., Harkema, S. J., and J., R. D. A Robotic Device for Manipulating Human Stepping. *IEEE Transactions on Robotics* 22(1):185–189, 2006.

57. Eskiizmirliler, S., Tondu, B., and Darlot, C. Motor control of a limb segment actuated by artificial muscles. In *Proceedings of the 23rd Annual International Conference of the IEEE Engineering in Medicine and Biology Society*, volume 1, pages 865–868. 2001.

58. Farris, R. J., Quintero, H. A., Withrow, T. J., and Goldfarb, M. Design of a Joint-Coupled Orthosis for FES-Aided Gait. In *2009 IEEE International Conference on Rehabilitation Robotics*, pages 246–252. 2009.

59. Gordon, K. E. and Ferris, D. P. Learning to walk with a robotic ankle exoskeleton. *Journal of Biomechanics* 40:2636–2644, 2007.

60. Guglielmelli, E., Johnson, M. J., and Shibata, T. Guest Editorial Special Issue on Rehabilitation Robotics. *IEEE Transactions on Robotics* 25(3):477–480, 2009.

61. Hamerlain, M. An anthropomorphic robot arm driven by artificial muscles using a variable structure control. In *Proceedings of the 1995 IEEE/RJS International Conference of Intelligent Robots and Systems*, volume 1, pages 550–555. 1995.

62. Harkema, S. J. Neural plasticity after human spinal cord injury: application of locomotor training to the rehabilitation of walking. *The Neuroscientist* 7(5):455–468, 2001.

63. Hesse, S., Bertelt, C., Jahnke, M. T., Schaffrin, A., Baake, P., and Malezic, M. Treadmill Training with partial body weight support compared with physiotherapy in nonambulatory hemiparetic patients. *Stroke* 26:976–981, 1995.

64. Hesse, S. and Uhlenbrock, D. A mechanized gait trainer for restoration of gait. *Journal of Rehabilitation Research and Development* 37(6):701–708, 2000.

65. Hesselroth, T., Sarkar, K., van der Smagt, P. P., and Schulten, K. Neural Network Control of a Pneumatic Robot Arm. *IEEE Transactions on Systems, Man, and Cybernetics* 24(1):28–38, 1994.

66. Hidler, J., Hamm, L. F., Lichy, A., and Groah, S. L. Automating activity-based interventions: The role of robotics. *Journal of Rehabilitation Research & Development* 45(2):337–344, 2008.

67. Hidler, J. M. What is next for locomotor-based studies? *J Rehabil Res Dev.* 42(1):xi–xiv, 2005.

68. Hildebrandt, A., Sawodny, O., Neumann, R., and Hartmann, A. A Flatness Based Design for Tracking Control of Pneumatic Muscle Actuators. In *Proceedings of the 7th International Conference on Control, Automation, Robotics and Vision.*, pages 1156–1161. 2002.

69. Hildebrandt, A., Sawodny, O., Neumann, R., and Hartmann, A. Cascaded control concept of a robot with two degrees of freedom driven by four artificial pneumatic muscle actuators. In *Proceedings of the 2005 American Control Conference*, pages 680–685. Portland, OR, USA, 2005.

70. Hitt, J., Oymagil, A. M., and Sugar, T. Dynamically controlled ankle-foot orthosis (DCO) with regenerative kinetics: incrementally attaining user portability. *2007 Proceedings of the IEEE International Conference on Robotics and Automation Roma, Italy* pages 1541–1546, 2007.

71. Hogan, N. Impedance control: an approach to manipulation, parts I-III. *Journal of Dynamics Systems, Measurements and Control Eng. Practice* 107:1–24, 1985.

72. Hornby, T., Zemon, D., and Campbell, D. Robotic-assisted, body-weight-supported treadmill training in individuals following motor incomplete spinal cord injury. *Physical Therapy* 85(1):52–66, 2005.

73. Inoue, K. Rubbertuators and Applications for Robots. In *Proceedings of the 4th International Symposium on Robotic Research*, pages 57–63. 1987.

74. Israel, J., Campbell, D., Kahn, J., and Hornby, T. Metabolic costs and muscle activity patterns during robotic- and therapist-assisted treadmill walking in individuals with incomplete spinal cord injury. *Physical Therapy* 86(11):1466–78, 2006.

75. Jezernik, S., Colombo, G., and Morari, M. Automatic gait-pattern adaptation algorithms for rehabilitation with a 4-DOF robotic orthosis. *IEEE Transactions on Robotics and Automation* 20(3):574–582, 2004.

76. Kazerooni, H. and Steger, R. The Berkeley Lower Extremity Exoskeleton. *Journal of Dynamic Systems, Measurement and Control* 128:14–25, 2006.

77. Kikuuwe, R. and Fujimoto, H. Proxy-based sliding mode control for accurate and safe position control. In *Proceedings of the IEEE International Conference on Robotics and Automation*, pages 25–30. 2006.

78. Kikuuwe, R., Yamamoto, T., and Fujimoto, H. Velocity-Bounding Stiff Position Controller. *Proceedings of the 2006 IEEE/RSJ International Conference on Intelligent Robots and Systems* pages 3050–3055, 2006.

79. Kikuuwe, R., Yamamoto, T., and Fujimoto, H. A Guideline for Low-Force Robotic Guidance for Enhancing Human Performance of Positioning and Trajectory Tracking: It Should Be Stiff and Appropriately Slow. *IEEE transactions on systems, man, and cybernetics - part A:systems and humans* 38(4):945–957, 2008.

80. Kikuuwe, R., Yasukouchi, S., Fujimoto, H., and Yamamoto, M. Proxy-Based Sliding Mode Control: A Safer Extension of PID Position Control. *IEEE Transactions on Robotics* 26(4):670–683, 2010.

81. Kimura, T., Hara, S., Fujita, T., and Kagawa, T. Feedback Linearization for Pneumatic Actuator Systems with Static Friction. *Control Eng. Practice* 5(10):1385–1394, 1997.

82. Kong, K. and Jeon, D. Design and Control of an Exoskeleton for the Elderly and Patients. *IEEE/ASME Transactions on Mechatronics* 11(4):428–423, 2006.

83. Krut, S., Benoit, M., Dombre, E., and Pierrot, F. MoonWalker, a Lower Limb Exoskeleton able to Sustain Bodyweight using a Passive Force Balancer. In *2010 IEEE International Conference on Robotics and Automation*, pages 2215–2220. 2010.

84. Lam, T., Wirz, M., Lünenburger, L., and Dietz, V. Swing phase resistance enhances flexor muscle activity during treadmill locomotion in incomplete spinal cord injury. *Neurorehabil Neural Repair* 22(5):438–446, 2008.

85. Lance, J. The control of muscle tone, reflexes, and movements: Robert Wartenberg Lecture. *Neurology* 30:1303–1313, 1980.

86. Lee, S. and Sankai, Y. Power assist control for leg with HAL-3 based on virtual torque and impedance adjustment. In *IEEE International Conference on Systems, Man and Cybernetics*, volume 4, pages 6–9. 2002.

87. Lilly, J. H. Adaptive Tracking for Pneumatic Muscle Actuators in Bicep and Tricep Configurations. *IEEE Transactions on Neural Systems and Rehabilitation Engineering* 11(3):333–339, 2003.

88. Lilly, J. H. and Quesada, P. M. A Two-Input Sliding-Mode Controller for a Planar Arm Actuated by Four Pneumatic Muscle Groups. *IEEE Transactions On Neural Systems and Rehabilitation Engineering* 12(3):349–359, 2004.

89. Lilly, J. H. and Yang, L. Sliding Mode Tracking for Pneumatic Muscle Actuators in Opposing Pair Configuration. *IEEE Transactions On Control Systems Technology* 13(4):550–558, 2005.

90. Lotze, M., Braun, C., Birbaumer, N., Anders, S., and Cohen, L. G. Motor learning elicited by voluntary drive. *Brain* 126(4):866–872, 2003.

91. Low, K. H., Liu, X., and Yu, H. Development of NTU Wearable Exoskeleton System for Assistive Technologies. In *Proceedings of the 2005 IEEE International Conference on Mechatronics & Automation*, pages 1099–1106. 2005.

92. Mankala, K. K., Banala, S. K., and Agrawal, S. K. Passive Swing Assistive Exoskeletons for Motor-Incomplete Spinal Cord Injury Patients. In *Proceedings of the 2007 IEEE International Conference on Robotics and Automation*, pages 3761–3766. 2007.

93. Mao, Y., Wang, J., Li, S., and Han, Z. Energy-Efficient Control of Pneumatic Muscle Actuated Biped Robot Joints. In *6th World Congress on Intelligent Control and Automation*, pages 8881–8885. 2006.

94. Marchal-Crespo, L. and Reinkensmeyer, D. Haptic guidance can enhance motor learning of a steering tasks. *Journal of motor behaviour* 40(6):545–557, 2008.

95. Marchal-Crespo, L. and Reinkensmeyer, D. J. Review of control strategies for robotic movement training after neurologic injury. *Journal of NeuroEngineering and Rehabilitation* 6(20):–, 2009.

96. Martin, J., Pollock, A., and Hettinger, J. Microprocessor Lower Limb Prosthetics: Review of Current State of the Art. *Journal of Prosthetics & Orthotics* 22(3):183–193, 2010.

97. Mataric, M. J., Eriksson, J., Feil-Seifer, D. J., and Winstein, C. J. Socially assistive robotics for post-stroke rehabilitation. *Journal of NeuroEngineering and Rehabilitation* 4(5), 2007.

98. Medrano-Cerda, G. A., Bowler, C. J., and Caldwell, D. G. Adaptive position control of antagonistic pneumatic muscle actuators. In *Proceedings of the International Conference on Intelligent Robots and Systems*, volume 1, pages 378–383. 1995.

99. Merletti, R. Standards for reporting EMG data. Technical report, International Society of Electrophysiology and Kinesiology, 1999.

100. Miettinen, K. *Nonlinear multiobjective optimization*. Kluwer Academic Publishers, 1999.

101. NASA. *Anthropometric source book, volume I: anthropometry for designers*. Webb Associates, 1978.

102. Neckel, N., Wisman, W., and Hidler, J. Limb Alignment and Kinematics Inside a Lokomat Robotic Orthosis. *Proceedings of the 28th IEEE EMBS Annual International Conference New York City, USA* pages 2698–2701, 2006.

103. Noritsugu, T. and Tanaka, T. Application of a Rubber Artificial Muscle Manipulator as a Rehabilitation Robot. *IEEE/ASME Transactions on Mechatronics* 2(4):259–267, 1997.

104. Nouri, A. S., Gauvert, C., Tondu, B., and Lopez, P. Generalized variable structure model reference adaptive control of one-link artificial muscle manipulator in two operating modes. In *Proceedings of the 1994 IEEE International Conference on Systems, Man, and Cybernetics*, volume 2, pages 1944–1950. 1994.

105. Papoulis, A. *The Fourier Transform and Its Applications*. McGraw-Hill, New York, 1962.

106. Perry, J. *Gait analysis Normal and pathological function*. SLACK Incorporated, 1992.

107. Pintelon, R. and Schoukens, J. *System identification a frequency domain approach*. IEEE press, 2001.

108. Rahman, T., Ramanathan, R., Seliktar, R., and Harwin, W. A simple technique to passively gravity-balance articulated mechanisms. *Trans. of the ASME- J of Mechanical Design* 117(4):655–658, 1995.

109. Raparelli, T., Beomonte Zobel, P., and Durante, F. The Design of a 2-dof Robot for Functional Recovery Therapy driven by Pneumatic Muscles. In *Proceedings of 10th Int. Workshop on Robotics In Alpe-Adria-Danube Region*. 2001.

110. Reinkensmeyer, D., Aoyagi, D., Emken, J., Galvez, J., Ichinose, W., Kerdanyan, G., Maneekobkunwong, S., Minakata, K., Nessler, J., Weber, R., Roy, R., de Leon, R., Bobrow, J., Harkema, S., and Edgerton, V. Tools for understanding and optimizing robotic gait training. *Journal of Rehabilitation Research & Development* 43(5):657–670, 2006.

111. Reinkensmeyer, D., Galvez, J., Marchal, L., Wolbrecht, E., and Bobrow, J. Some key problems for robot-assisted movement therapy research: a perspective from the University of California at Irvine. In *Proceedings of the IEEE 10th International Conference on Rehabilitation Robotics*, pages 1009–1015. 2007.

112. Reisman, D. S., Wityk, R., Silver, K., and Bastian, A. J. Locomotor adaptation on a split-belt treadmill can improve walking symmetry post-stroke. *Brain* 130(7):1861–1872, 2007.

113. Repperger, D. W., Johnson, K. R., and Philips, C. A. A VSC Position Tracking System Involving a large Scale Pneumatic Muscle Actuator. In *Proceedings of the 37th IEEE Conference on Decision & Control*, pages 4302–4307. 1998.

114. Ridding, M. C. and Rothwell, J. C. Afferent input and cortical organisation: a study with magnetic stimulation. *Experimental Brain Research* 126(4):536–544, 1999.

115. Riener, R. and Edrich, T. Identification of passive elastic joint moments in the lower extremities. *Journal of Biomechanics* 32(5):539–544, 1999.

116. Riener, R., Lunenburger, L., Jezernik, S., Anderschitz, M., Colombo, G., and Dietz, V. Patient-cooperative strategies for robot-aided treadmill training: first experimental results. *IEEE Transactions on Neural Systems and Rehabilitation Engineering* 13(3):380–394, 2005.

117. Saglia, J. A., Tsagarakis, N. G., Dai, J. S., and Caldwell, D. G. Control Strategies for Ankle Rehabilitation using a High Performance Ankle Exerciser. In *Proceedings of the 2010 IEEE International Conference on Robotics and Automation*, pages 2221–2227. 2010.

118. Sardellitti, I., Park, J., Shin, D., and Khatib, O. Air muscle controller design in the distributed macro-mini (DM^2) actuation approach. In *Proceedings of the 2007 IEEE/RSJ International Conference on Intelligent Robots and Systems*, pages 1822–1827. 2007.

119. Sawicki, G., Gordon, K., and Ferris, D. Powered lower limb orthoses: applications in motor adaptation and rehabilitation. In *9th International Conference on Rehabilitation Robotics (ICORR 2005)*, pages 206–211. 2005.

120. Schiele, A. An Explicit Model to predict and Interpret Constraint Force Creation in pHRI with Exoskeletons. In *Proceedings of the IEEE International Conference on Robotics and Automation*, pages 1324–1330. 2008.

121. Schiele, A. and van der Helm, F. Kinematic Design to Improve Ergonomics in Human Machine Interaction. *IEEE Transactions on Neural Systems and Rehabilitation Engineering* 14(2):456–469, 2006.

122. Schindele, D. and Aschemann, H. Nonlinear Model Predictive Control of a High-Speed Linear Axis Driven by Pneumatic Muscles. In *Proceedings of the 2008 American Control Conference*, pages 3017–3022. 2008.

123. Schmidt, H., Hesse, S., and Bernhardt, R. Haptic Walker - A novel haptic foot device. *ACM Transactions on Applied Perception* 2:166–180, 2005a.

124. Schmidt, H., Piorko, F., Bernhardt, R., Kruger, J., and Hesse, S. Synthesis of perturbations for gait rehabilitation robots. In *Proceedings of the 2005 IEEE International Conference on Rehabilitation Robotics*, pages 74–77. 2005b.

125. Schröder, J., Kawamura, K., Gockel, T., and Dillmann, R. Improved control of a humanoid arm driven by pneumatic actuators. In *Proceedings of Humanoids 2003*. 2003.

126. Schulte, H. F. The characteristics of the McKibben artificial muscle. In *The Application of External Power in Prosthetics and Orthotics*, Publication 874, pages 94–115. National Academy of Sciences - National Research Council, Washington DC, 1961.

127. Sergi, F., Accoto, D., Tagliamonte, N., Carpino, G., Pathiyil, L., and Guglielmelli, E. A systematic graph-based method for the kinematic synthesis of non-anthropomorphic wearable robots. In *2010 IEEE Conference on Robotics Automation and Mechatronics (RAM)*, pages 100–105. 2010.

128. Sinkjaer, T. and Popovic, D. B. Trends in the Rehabilitation of Hemiplegic Subjects. *Journal of Automatic Control* 15:1–10, 2005.

129. Sira-Ramírez, H., Lopez, P., and Tondu, B. On the robust stabilization and tracking for robotic manipulators with artificial muscles. *International Journal of Systems Science* 27(11):1067–1075, 1996.

130. Šitum, Ž. and Herceg, S. Design and Control of a Manipulator Arm Driven by Pneumatic Muscle Actuators. In *Proceedings of the 16th IEEE Mediterranean Conference on Control and Automation*, pages 926–932. 2008.

131. Soderberg, G. L. and Knutson, L. M. A Guide for Use and Interpretation of Kinesiologic Electromyographic Data. *Physical Therapy* 80(5):485–498, 2000.

132. Stauffer, Y., Allemand, Y., Bouri, M., Fournier, J., Clavel, R., Metrailler, P., Brodard, R., and F, R. The WalkTrainer - A new generation of walking reeducation device combining orthoses and muscle stimulation. *IEEE Transactions on neural systems and rehabilitation engineering* 17(1):38–45, 2009.

133. Stienen, A. H. A., Hekman, E. E. G., van der Helm, F. C. T., and van der Kooij, H. Self-Aligning Exoskeleton Axes Through Decoupling of Joint Rotations and Translations. *IEEE Transactions on Robotics* 25(3):628–633, 2009.

134. Sugar, T. G., He, J., Koeneman, E. J., Koeneman, J. B., Herman, R., Huang, H., Schultz, R. S., Herring, D. E., Wanberg, J., Balasubramanian, S., Swenson, P., and Ward, J. A. Design and Control of RUPERT: A Device for Robotic Upper Extremity Repetitive Therapy. *IEEE Transactions on Neural Systems and Rehabilitation Engineering* 15(3):336–346, 2007.

135. Sulzer, J., Roiz, R., Peshkin, M., and Patton, J. A Highly Backdrivable, Lightweight Knee Actuator for Investigating Gait in Stroke. *IEEE Transactions on Robotics* 25(3):539–548, 2009.

136. Surdilovic, D., Zhang, J., and Bernhardt, R. STRING-MAN: Wire-robot technology for safe, flexible and human-friendly gait rehabilitation. In *Proceedings of the 2007 IEEE 10th International Conference on Rehabilitation Robotics*, pages 446–453. 2007.

137. Thanh, T. D. C. and Ahn, K. K. Intelligent phase plane switching control of pneumatic artificial muscle manipulators with magneto-rheological brake. *Mechatronics* 16:85–95, 2006a.

138. Thanh, T. D. C. and Ahn, K. K. Nonlinear PID control to improve the control performance of 2 axes pneumatic artificial muscle manipulator using neural network. *Mechatronics* 16(9):577–587, 2006b.

139. Tondu, B., Boitier, V., and Lopez, P. Naturally compliant robot-arms actuated by McKibben artificial muscles. In *Proceedings of the 1994 IEEE International Conference on Systems, Man and Cybernetics*, volume 3, pages 2635–2640. 1994.

140. Tondu, B. and Lopez, P. Modeling and Control of McKibben Artificial Muscle Robot Actuators. *IEEE Control Systems Magazine* 20(2):15–38, 2000.

141. Tonietti, G. and Bicchi, A. Adaptive Simultaneous Position and Stiffness Control for a Soft Robot Arm. In *Proc. IEEE Int. Symp. Intelligent Robots and Systems*, pages 1992–1997. 2002.

142. Tsagarakis, N. G. and Caldwell, G. Development and Control of a "Soft-Actuated" Exoskeleton for Use in Physiotherapy and Training. *Autonomous Robots* 15:21–33, 2003.

143. Vallery, H. *Stable and user-controlled assistance of human motor function*. Ph.D. thesis, Technischen Universität München, 2009.

144. Vallery, H., van Asseldonk, E., Buss, M., and van der Kooij, H. Reference trajectory generation for rehabilitation robots: complementary limb motion estimation. *IEEE Transactions on Neural Systems and Rehabilitation Engineering* 17(1):23–30, 2009.

145. Vallery, H., Veneman, J., Van Asseldonk, E., Ekkelenkamp, R., Buss, M., and van der Kooij, H. Compliant Actuation of Rehabilitation Robots. *IEEE Robotics & Automation Magazine* 15(3):60–69, 2008.

146. van Asseldonk, E., Ekkelenkamp, R., Veneman, J., Van der Helm, F., and van der Kooij, H. Selective control of a subtask of walking in a robotic gait trainer(LOPES). In *IEEE 10th International Conference on Rehabilitation Robotics*, pages 841–848. 2007.

147. van Asseldonk, E. H. F., Veneman, J. F., Ekkelenkamp, R., Buurke, J. H., van der Helm, F. C. T., and van der Kooij, H. The Effects on Kinematics and Muscle Activity of Walking in a Robotic Gait Trainer During Zero-Force Control. *IEEE Transactions on Neural Systems and Rehabilitation Engineering* 16(4):360–370, 2008.

148. Van Damme, M. *Towards safe control of a compliant manipulator powered by pneumatic muscles*. Ph.D. thesis, Vrije Universiteit Brussel, 2009.

149. Van Damme, M., Beyl, P., Vanderborght, B., Van Ham, R., Vanderniepen, I., Versluys, R., Daerden, F., and Lefeber, D. Modeling Hysteresis in Pleated Pneumatic Artificial Muscles. In *Proceedings of the 2008 IEEE International Conference on Robotics, Automation & Mechatronics*, pages 471–476. 2008.

150. Van Damme, M., Beyl, P., Vanderborght, B., Versluys, R., Van Ham, R., Vanderniepen, I., F., D., and Lefeber, D. The Safety of a Robot Actuated by Pneumatic Muscles: A Case Study. *International Journal of Social Robotics* 2(3):289–303, 2010.

151. Van Damme, M., Vanderborght, B., Van Ham, R., Verrelst, B., Daerden, F., and Lefeber, D. Proxy-based sliding mode control of a planar pneumatic manipulator. *International Journal of Robotics Research* 28(2):266–284, 2009a.

152. Van Damme, M., Vanderborght, B., Van Ham, R., Verrelst, B., Daerden, F., and Lefeber, D. Sliding Mode Control of a 2-DOF Planar Pneumatic Manipulator. *Transactions of the ASME - Journal of Dynamic Systems, Measurement, and Control* 131(2):–, 2009b.

153. van der Smagt, P., Groen, F., and Schulten, K. Analysis and control of a rubbertuator arm. *Biological Cybernetics* 75:433–440, 1996.

154. Van Ham, R., Vanderborght, B., Van Damme, M., Verrelst, B., and Lefeber, D. MACCEPA, the Mechanically Adjustable Compliance and Controllable Equilibrium Position Actuator: Design and Implementation in a Biped Robot. *Robotics and Autonomous Systems* 55(10):761–768, 2007.

155. Vanderborght, B., Van Ham, R., Verrelst, B., Van Damme, M., and Lefeber, D. Overview of the Lucy Project: Dynamic Stabilization of a Biped Powered by Pneumatic Artificial Muscles. *Advanced Robotics* 22(25):1027–1051, 2008a.

156. Vanderborght, B., Verrelst, B., Van Damme, M., Van Ham, R., Beyl, P., and Lefeber, D. Locomotion Control Architecture for the Pneumatic Biped Lucy Consisting of a Trajectory Generator and Joint Trajectory Tracking Controller. In *IEEE-RAS International Conference on Humanoid Robots*, pages 240–245. 2006a.

157. Vanderborght, B., Verrelst, B., Van Ham, R., and Lefeber, D. Controlling a Bipedal Walking Robot Actuated by Pleated Pneumatic Artificial Muscles. *Robotica* 24(4):401–410, 2006b.

158. Vanderborght, B., Verrelst, B., Van Ham, R., Van Damme, M., Beyl, P., and Lefeber, D. Development of a compliance controller to reduce energy consumption for bipedal robots. *Autonomous Robots* 24(4):419–434, 2008b.

159. Veneman, J. *Design and evaluation of the gait rehabilitation robot LOPES*. Ph.D. thesis, University of Twente (The Netherlands), 2007.

160. Veneman, J., Ekkelenkamp, R., Kruidhof, R., van der Helm, F., and van der Kooij, H. Design of a series elastic- and Bowden cable-based actuation system for use as torque-actuator in exoskeleton-type training. In *9th International Conference on Rehabilitation Robotics (ICORR 2005)*, pages 496–499. 2005.

161. Veneman, J., Ekkelenkamp, R., Kruidhof, R., van der Helm, F., and van der Kooij, H. A Series Elastic- and Bowden-Cable-Based Actuation System for Use as Torque Actuator in Exoskeleton-Type Robots. *The International Journal of Robotics Research* 25(3):261–281, 2006.

162. Veneman, J., Kruidhof, R., Hekman, E., Ekkelenkamp, R., Van Asseldonk, E., and van der Kooij, H. Design and evaluation of the LOPES exoskeleton robot for interactive gait rehabilitation. *IEEE Transactions on Neural Systems and Rehabilitation Engineering* 15(3):379–386, 2007.

163. Verrelst, B. *A dynamic walking biped actuated by pleated pneumatic artificial muscles: Basic concepts and control issues.* Ph.D. thesis, Vrije Universiteit Brussel, 2005.

164. Verrelst, B., Van Ham, R., Vanderborght, B., Lefeber, D., Daerden, F., and Van Damme, M. Second generation pleated pneumatic artificial muscle and its robotic applications. *Advanced Robotics* 20(7):783–805, 2006a.

165. Verrelst, B., Vermeulen, J., Vanderborght, B., Van Ham, R., Naudet, J., Lefeber, D., Daerden, F., and Van Damme, M. Motion Generation and Control for the Pneumatic Biped 'Lucy'. *International Journal of Humanoid Robotics (IJHR)* 3(1):1–35, 2006b.

166. Versluys, R., Beyl, P., Van Damme, M., Desomer, A., Van Ham, R., and Lefeber, D. Prosthetic Feet: State-of-the-art Review and the Importance of Mimicking Human Ankle-Foot Biomechanics. *Disability and Rehabilitation: Assistive Technology* 4(2):65–75, 2009a.

167. Versluys, R., Deckers, K., Van Damme, M., Van Ham, R., Steenackers, G., Guillaume, P., and Lefeber, D. A study on the bandwidth characteristics of pleated pneumatic artificial muscles. *Applied Bionics and Biomechanics* 6(1):49–55, 2009b.

168. Villegas, D., Vanderborght, B., Van Damme, M., Beyl, P., and Lefeber, D. Third Generation Pleated Pneumatic Artificial Muscles for Robotic Applications: Development and Comparison with the McKibben Muscle. *Advanced Robotics* page (submitted), 2010.

169. Walsh, C. J., Endo, K., and Herr, H. A Quasi-passive Legacy Exoskeleton for load-carrying augmentation. *International Journal of Humanoid Robotics* 4(3):487–506, 2007.

170. Weinberg, B., Nikitczuk, J., Patel, S., Patritti, B., Mavroidis, C., Bonato, P., and P., C. Design, Control and Human Testing of an Active Knee Rehabilitation Orthotic Device. In *Proceedings of 2007 IEEE International Conference on Robotics and Automation*, pages 4126–4133. 2007.

171. Winter, D. *The biomechanics and motor control of human gait: normal, elderly and pathological*. University of Waterloo Press, second edition, 1991.

172. Yamazaki, M. and Yasunobu, S. An Intelligent Control for State-Dependent Nonlinear Actuator and Its Application to Pneumatic Servo System. In *Proceedings of the SICE Annual Conference 2007*, pages 2194–2199. 2007.

173. Yang, J. F. and Gorassini, M. Spinal and Brain Control of Human Walking: Implications for Retraining of Walking. *Neuroscientist* 12(5):379–389, 2006.

174. Yang, L. *Sliding Mode Control of Robotics Systems Actuated by Pneumatic Muscles*. Ph.D. thesis, University of Louisville, 2006.

175. Yoon, J. and Ryu, J. A Novel Reconfigurable Ankle/Foot Rehabilitation Robot. In *Proceedings of the 2005 IEEE international Conference on Robotics and Automation*, pages 2301–2306. 2005.

176. Zhang, L., Xie, J., and Lu, D. Adaptive Robust Control of One-Link Joint Actuated by Pneumatic Artificial Muscles. In *Proceedings of the 1st IEEE International Conference on Bioinformatics and Biomedical Engineering*, pages 1185–1189. 2007.

177. Zimmerli, L., Duschau-Wicke, A., Mayr, A., Riener, R., and Lunenburger, L. Virtual reality and gait rehabilitation augmented feedback for the lokomat. In *Proceedings of the 2009 IEEE Virtual Rehabilitation International Conference*, pages 150–153. 2009.